NBSIR 85-3182(R)

Validation Metrology of the Large Optics Diamond Turning Machine

W. Tyler Estler and Edward B. Magrab

U.S. DEPARTMENT OF COMMERCE
National Bureau of Standards
Center for Manufacturing Engineering
Automated Production Technology Division
Gaithersburg, MD 20899

June 1985

Final Report

Sponsored by:
Defense Advanced Research Projects
1400 Wilson Boulevard
Arlington, VA 22209

NBSIR 85-3182(R)

VALIDATION METROLOGY OF THE LARGE OPTICS DIAMOND TURNING MACHINE

W. Tyler Estler and Edward B. Magrab

U.S. DEPARTMENT OF COMMERCE
National Bureau of Standards
Center for Manufacturing Engineering
Automated Production Technology Division
Gaithersburg, MD 20899

June 1985

Final Report

Sponsored by:
Defense Advanced Research Projects
1400 Wilson Boulevard
Arlington, VA 22209

U.S. DEPARTMENT OF COMMERCE, Malcolm Baldrige, *Secretary*
NATIONAL BUREAU OF STANDARDS, Ernest Ambler, *Director*

ABSTRACT

We present the results of field validation measurements designed to test the positioning accuracy and kinematic performance of the Large Optics Diamond Turning Machine (LODTM), constructed at Lawrence Livermore National Laboratory. Field measurements were performed during January-February and November, 1984, and are sufficient to characterize the capabilities of LODTM when used as a measuring machine. No part cutting tests were done. Measured errors include those due to machine drift, position repeatability, laser length scales, slide straightness, tool bar angular motions, axis geometry, and spindle motion. The static and dynamic performance of the Fast Tool Servo was assessed by bench tests at NBS. We also identify those aspects of machine behavior which are potentially problematic in fabrication of large optics with figure errors within the design specifications of LODTM.

TABLE OF CONTENTS

Introduction and Measurement Summary.................................... 1

Areas of Concern.. 8

1. Static X-Z Drift Tests... 15

2. Positioning Repeatability Tests...................................... 21

3. Tests for Polarization Mixing Errors................................. 25

4. X-Axis Scale Errors.. 26

5. Z-Axis Scale Errors.. 31

6. Angular Motions.. 34

    6.A. X-Axis Pitch Motion.. 34

    6.B. Z-Axis Pitch Motion.. 36

7. Slide Straightness Errors.. 49

    7.A. Z-Straightness of the X-Axis................................... 50

    7.B. X-Straightness of the Z-Axis................................... 53

8. Axis Geometry.. 72

    8.A. X-W Squareness Error... 74

    8.B. X-Z Squareness Error... 84

    8.C. Remarks on Axis Geometry....................................... 91

9. Spindle Errors... 95

    9.A. Radial Error Motion... 96

    9.B. Axial Error Motion... 116

    9.C. Tilt Error Motion.. 122

    9.D. Spindle Capacitance Gauges..................................... 126

    9.E. Spindle Random Motion / Capacitance Gauge Noise................ 134

    9.F. Dynamic Z-W Parallelism Error.................................. 144

10. Fast Tool Servo Tests... 145

10.A. NBS Capacitance Gauges 146

10.B. Static Displacement Tests 152

10.C. Dynamic Displacement Tests 157

10.D. Discussion 164

Acknowledgements 164

References 168

Appendices 169

INTRODUCTION AND MEASUREMENT SUMMARY

This report presents the results of field tests designed to validate the positioning accuracy of the Large Optics Diamond Turning Machine (LODTM), constructed at Lawrence Livermore National Laboratory (LLNL). The geometry, design details, and performance goals of this machine are described in References (1-3). With the exception of the Fast Tool Servo validation, all testing was performed at LLNL during two validation periods: 9 January - 17 February and 5 November - 2 December, 1984.

Table 1 shows a list of the error measurements which are needed in order to characterize the tool-to-workpiece positioning performance of LODTM. We stress that no cutting tests or sample part metrology were performed by NBS, so that we concern ourselves here only with those elements of machine error which affect workpiece form, or figure, and neglect such important considerations as dynamic tool-workpiece interaction and surface finish.

In this Introduction we summarize the results of machine validation for quick reference purposes. Detailed measurement procedures and discussions are presented in the following sections.

1. Drift Tests

Machine drift ≤1 microinch in each axis, for a time of 24 hours or less.

NBS/LODTM FIELD METROLOGY

REQUIRED ERROR MEASUREMENTS:

1. Static/Dynamic Drift Tests
2. Repeatability Tests
3. Scale Errors
4. Straightness Errors
5. Tool Bar Angular Motion Errors
6. Squareness/Parallelism Errors
7. Axis of Rotation Errors
8. Fast Tool Servo Performance

Table 1

2. Repeatability Tests

Both unidirectional and bi-directional repeatability of the tool point position, when commanded to the same point, is ≈0.5 microinches or better for the X-axis. Due to a thermal hysteresis problem, described in Appendix A, the Z-axis repeatability may be fixture-dependent; maximum observed non-repeatability was ≈2 microinches.

3. Scale Errors

a. Periodic error due to polarization mixing in the position interferometers: <0.1 microinch in each axis.

b. X and Z-axis displacement errors: <1 part in 10^7 of commanded displacement. This upper limit is set by the calculated accuracy of the interferometer system used to measure displacement errors.

4. Straightness Errors

a. Z (vertical) straightness of the X-axis: <4 microinches peak-valley in a 40-inch range of travel. This upper limit is set by our ability to compute the figure error of the reference artifact used for this measurement.

b. X (horizontal) straightness of the Z-axis: <4 microinches peak-valley in 19.5 inches of travel. This error is dominated by thermal hysteresis in the LODTM tool bar.

5. Tool Bar Angular Motion Errors

a. X-axis pitch motion: the physical rotation of the tool bar about the machine Y-axis is ≈3 arc-seconds (15 microradians) in 40 inches of X-axis travel. The control software corrects the X-position of the tool point to within the accuracy of the NBS metrology interferometer (≈1 part in 10^7), provided that the tool Z-offset is specified to within ≈0.25 inches. With this proviso, it is correct to state that the combined X-axis positioning error due to length scale and X-pitch is <1 part in 10^7 of commanded displacement.

b. Z-axis pitch motion: the physical rotation of the tool bar about the machine Y-axis is ≈1.6 arc-second (8 microradians) in 19 inches of Z-axis travel. After software correction the Z-position of the tool point is compensated to within the accuracy of the NBS interferometer. Due to thermal hysteresis in the tool bar, however, there is ≈3 microinches peak-valley Z-axis non-repeatability with an X-offset of 10 inches.

6. Squareness / Parallelism Errors

a. X-Z squareness error: -0.46 ±0.3 microradians after software correction. The negative sign indicates an acute angle between the X and Z axes.

b. X-W (spindle) squareness error: +0.40 ±0.12 microradians, measured by reversal with the spindle rotor at rest. The sign is such that the tool point moves up in Z as the X-slide moves to the South.

c. Z-W parallelism error: this error was measured both statically and dynamically. For the static (spindle at rest) case, the measured error is +5.30±0.22 microradians. At spindle speeds of 25 and 50 RPM the measured errors are, respectively, +2.6±0.4 microradians and +2.9±0.4 microradians. The sign is such that the spindle axis is tilted to the South with respect to the Z-axis. There is evidence, explained in the text, that this parallelism error is a function of tool bar position upon closing the machine positioning loops.

7. Axis of Rotation Errors

a. Spindle radial error motion: the inherent, uncompensated radial motion was measured at 25 and 50 RPM at two axial locations, Z=7.5 inches and Z=21.5 inches above the rotor surface. The observed peak-valley radial motions are, approximately,

$$Z=7.5\text{ inches:}\quad\begin{cases}3.5\text{ microinches, 25 RPM}\\[2ex]4\text{ microinches, 50 RPM}\end{cases}$$

and

$$Z\text{=21.5 inches: }\begin{cases} \text{7 microinches, 25 RPM} \\ \\ \text{9 microinches, 50 RPM} \end{cases} .$$

In each case the dominant contribution to the measured error is due to a second harmonic (or twice per revolution) radial motion.

b. Spindle axial error motion: the inherent, uncompensated axial motion was measured at 25 and 50 RPM. The peak-valley error at these two spindle speeds are, respectively, ≈3 microinches and ≈2 microinches. This axial error is predominantly second harmonic in nature.

c. Spindle tilt motion: measured tilt motion, computed from the radial motion data, is ≈0.04 arc-seconds (0.2 microradians) peak-valley, at both 25 and 50 RPM.

d. Spindle capacitance gauges: the output levels of the spindle capacitance gauges change significantly with spindle speed. Between 2 RPM and 50 RPM the measured peak-valley change in signal levels corresponds to 30-40 microinches apparent motion for the X-axis gauges and 15-20 microinches for the Z-axis gauges.

e. Spindle random motion / capacitance gauge noise: peak-valley non-repeatability of each of the four spindle capacitance gauges is ≈2 microinches. For the X-axis gauges this behavior appears to be dominated by inherent gauge noise, making radial error correction problematic. Gauge noise and tool bar vibration preclude meaningful estimates of the "random", or non-repeatable component of the spindle error motions.

8. Fast Tool Servo Performance

a. Static behavior: the FTS static displacement versus command voltage is linear to better than 0.05 microinches for commands in the range of ±10 VDC. Static repeatability error is also <0.05 microinches.

b. Dynamic behavior: FTS dynamic repeatability error is <0.05 microinches. In a bandwidth of 100 Hz, the dynamic positioning error is <1 microinch for peak displacement of 28 microinches and is <2 microinches for peak displacement of 46 microinches.

AREAS OF CONCERN

During our field measurements at LODTM we observed several aspects of machine behavior which may potentially limit the achievable figure and surface finish characteristics of diamond turned optics. In addition to these observations, there are tests and measurements which could not be performed due to schedule constraints. In this section we briefly present these matters for consideration, with no attempt to order them according to their ultimate impact on finished part quality.

(1) Tool Set Station

The LODTM tool set station, which defines the origin of the tool point coordinate system, was installed prior to our second series of field measurements but was not tested for drift and repeatability errors. Since our experience indicates that machine emergency stops are plausible events, part production planning must include the possibility of interrupted cutting passes which require re-zeroing of the tool coordinates. In our opinion it would be very worthwhile to test the repeatability of this process in order to assess the accuracy with which an interrupted cut could be picked up and continued following a loss of servo control.

(2) Tool Bar Vibration

The LODTM tool bar has an oscillation, primarily along the X-axis, with a frequency of ≈100 Hz and peak-valley amplitude of 3-5 microinches depending upon fixturing and Z-axis position. This behavior is most likely a resonance of the tool bar excited by the Z-axis air bearings and the amplitude of the effect changes with bearing supply pressure. The presence of this vibration made it nearly impossible to draw meaningful conclusions about non-repeatable spindle radial motion relative to the tool bar. With respect to machined optics such vibration may have an objectionable effect upon achievable surface finish.

(3) Tool Bar Thermal Distortion

Joule-Thompson expansion of the air supplying the tool bar air bearings causes these bearings to cool below ambient temperature. Much of our measurement data was characterized by systematic, hysteresis-like behavior as the tool bar cycled through the machine work volume. Prior to the installation of in-line supply air heaters we were able to understand these effects, and to correlate them with temperature changes of the tool bar mounting plate to which our fixtures were attached. A simple thermal model enabled us to plausibly demonstrate that essentially all of the observed systematic errors could be attributed to dimensional changes in the gauging fixtures themselves.

After installation of the heaters, we verified that their effect was to render the tool bar mounting plate isothermal and in addition, we replaced all aluminum and steel fixtures with Invar components. In spite of these improvements, we still observed systematic, presumably thermally-related, non-repeatability in much of our data. The exact cause of this behavior is not known. We were able to rule out any asymmetric motion of the Z-axis straightedges, so that the most probable explanation is a "warping" or distortion of the tool bar as it changes position with respect to the heaters. The tool bar structure contains a capacitance gauge designed to detect bending, but it was not functioning during these measurements.

Tool point positioning errors caused by thermal distortion are not well characterized at this time, and can only be crudely estimated for any particular machining operation. In our opinion, with Super-invar tooling and small (<5 inches) X-axis tool offsets, the maximum thermally-induced error would be ≈2 microinches for tool motion anywhere in the machine work volume, with the air line heaters on. With these heaters off, and the same tooling, the error would probably be smaller.

(4) Z-Axis - Spindle Axis Parallelism Error

In the stacked-slide design of LODTM, angular motions of the X-carriage change the direction in space of the Z-axis. Because of this coupling the parallelism error between the spindle axis and the Z-axis is a function of the position of the X-carriage upon closing the machine positioning loops. Thus, there is apparently no single number which characterizes this axis alignment error. Since the pitch error of the

X-carriage is greater than 3 arc-seconds (15 µrad), very large systematic positioning errors are possible without modification of the LODTM start-up procedures. In Section 8.C. we suggest several such modifications.

(5) Spindle Error Correction

The results of our measurements of the error motions of the LODTM spindle rotor and the correction signals from the spindle capacitance gauges suggest a careful review of the hardware design, calibration procedures, and the error correction algorithms as currently implemented on the real-time computer (RTC). In particular, with respect to possible degradation of workpiece azimuthal figure error, we make the following observations.

(a) Capacitance Gauge Noise

The LODTM spindle capacitance gauges appear to have significant noise components in their outputs when the spindle turns at cutting speed (50 RPM). Using nominal gauge calibration data as supplied by the LODTM staff, the signal noise is equivalent to about ±1 microinch apparent random motion for each gauge. The effect is most directly demonstrated for the X-axis gauges, for which the signal noise is roughly 1% of the DC output level. The reason for this behavior is not known but could possibly be caused by turbulence-induced changes in the dielectric constant of the air within the gauge sensing gaps. Our data is not conclusive, and we stress that these remarks are, at this time, speculative. We would strongly urge, however, further testing of the dynamic behavior of the capacitance gauges prior to their use in error correction, since noise levels of the magnitude suggested here would yield false correction data comparable in size to any real spindle error motion.

(b) Capacitance Gauge Calibrations

Calibration factors for the spindle capacitance gauges were supplied by the LODTM staff and used in our analyses of the gauge output signals. Centering error computations for the X-axis gauges suggest that the relative calibrations were in error by ≈30%. A similar analysis was not possible for the Z-axis gauges, but these results, which were derived from only one set of data, are a cause for concern. In our opinion, it is clearly necessary to re-calibrate the spindle capacitance gauges and to consider a program of periodic checks on these calibrations in order to minimize errors caused by drift.

(c) Capacitance Gauge Groove Errors

The apparent motion seen by any of the LODTM spindle capacitance gauges is a mixture of form error of the groove in which it rides and actual error motions of the axis of rotation. Once the latter have been accurately measured it is straightforward to compute an "error map" for each of the capacitance gauge grooves in the form of a lookup table. Our measurements have demonstrated that it is crucial for this procedure to be carried out at actual machining rotation rates, since the gauge outputs are significantly dependent upon spindle speed.

(d) Spindle Error Correction Software

In every case, when spindle error motions were measured with software correction on, the effect was to increase the measured error. With respect to radial error motion, we can understand this behavior since it was later discovered that one of the X-axis capacitance gauges was operating with the wrong polarity. Furthermore, as described in (b) above, we believe that the calibration of at least one of these gauges was in error. We do not understand the observed degradation of the spindle axial error motion, which depends for its correction only upon the Z-axis gauges. The most likely explanation is a faulty procedure for filling the groove error lookup tables.

In order to fully implement and validate spindle error correction on LODTM, it is necessary to accurately determine the X and Z groove errors, fill the lookup tables, and then perform a complete re-measurement of the spindle error motions. If this is not done, the effect of the correction algorithms will likely cause objectionable workpiece errors, over and above those due to inherent errors in the LODTM spindle.

(e) Metrology Frame Stability

In one of our last exercises during fieldwork at LODTM we observed a periodic component in the output of the North-X capacitance gauge, with the spindle rotor at rest. The displacement amplitude was 1-2 microinches and the frequency near 60 Hz. Discussions with the LODTM technical staff have raised the possiblity of an oscillation of the North end of the machine metrology frame. We would urge a careful investigation of this matter and its possible influence on spindle error correction.

(f) Fast Tool Servo Integration

We raise this subject only because we were not able to test the FTS as an integrated sub-system of LODTM. Prior to any use for final part machining it would be highly desirable to validate the FTS with respect to its performance under cutting conditions and its interface with the position correction software.

1. Static X-Z Drift Tests

Drift tests are designed to test the basic stability of the machine against environmental and other changes, for a time commensurate with the time required to machine a part. Any measurable changes in the machine enclosure air temperature can be expected to change the relative position of the tool point with respect to a workpiece. For this reason, all measurements of machine performance were accompanied by careful monitoring of the enclosure air temperature.

Our goal was to measure the static drift of LODTM for a period of at least 24 hours, employing two NBS capacitance gauges to test stability in both machine axes simultaneously. After a series of shorter tests which were aborted due to machine emergency stops from various causes, one such test was completed. Because an earlier machine crash had damaged one of the NBS capacitance gauges, this test employed one NBS gauge and a pair of LLNL-designed gauges.

The test object in these tests was a 2-inch diameter tungsten carbide ball with excellent surface finish. The ball was epoxied to a small stand, which was in turn mounted on the machine spindle face plate using an LLNL-designed vacuum chuck normally used to fixture small flats for test machining. The capacitance gauges were mounted to the machine tool bar using an Invar fixture. This fixture was modified to hold one of the LLNL gauges (X-axis) as well as an NBS gauge (Z-axis). Since the LLNL gauges are differential devices, the second gauge of the pair was mounted in a Super-invar reference fixture of LLNL design. A diagram of the setup is shown in Fig.(1).

Prior to actual drift testing, all of the capacitance gauges were tested for any inherent drift due to electronics and/or fixturing. Results of these "cap" tests showed the NBS gauges to be stable within about 1 microinch, and the LLNL gauges within about 2 microinches in a 24 hour period. We believe the greater drift of the LLNL gauges to be caused by mechanical creep in the fixtures designed to implement these tests, but time did not allow a detailed investigation of this behavior.

The results of the 24 hour X-Z static drift test are shown in Figs. (2-4). Figure (2) shows the average machine enclosure air temperature as measured by eight calibrated thermistors placed at various points near the machine. The apparent 24-hour cyclic behavior of the air temperature with a peak-valley amplitude of about 0.01°C (0.018°F) was observed on several occasions during our early validation work at LODTM. Investigation by J. Roblee of the LODTM staff revealed that this behavior was caused by radiative coupling of the enclosure control thermistor to a diurnally-varying source of thermal radiation. Shielding of the control thermistor with reflective metal foil was sufficient to bring the machine enclosure air temperature to within the design specifications. Subsequent measurements have shown temperature control to be 0.005°C (0.01°F) or better during 24 hour time periods.

Figures (3) and (4) display the measured drift of LODTM along Z and X, respectively. The diurnal behavior of the enclosure air temperature is

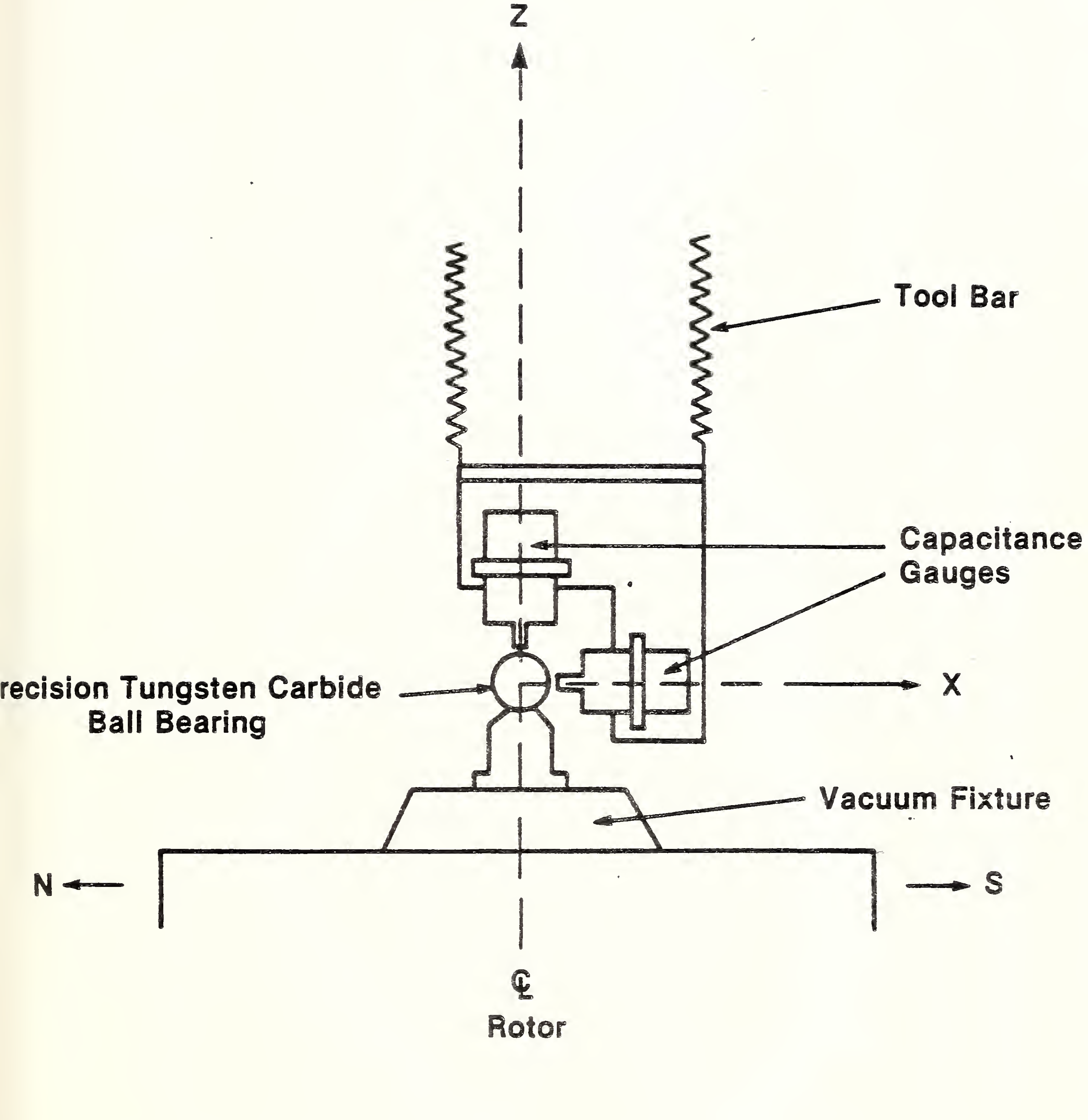
Z
Tool Bar
Capacitance
Gauges
recision Tungsten Carbide
Ball Bearing
X
Vacuum Fixture
N
S
℄
Rotor

Figure 1

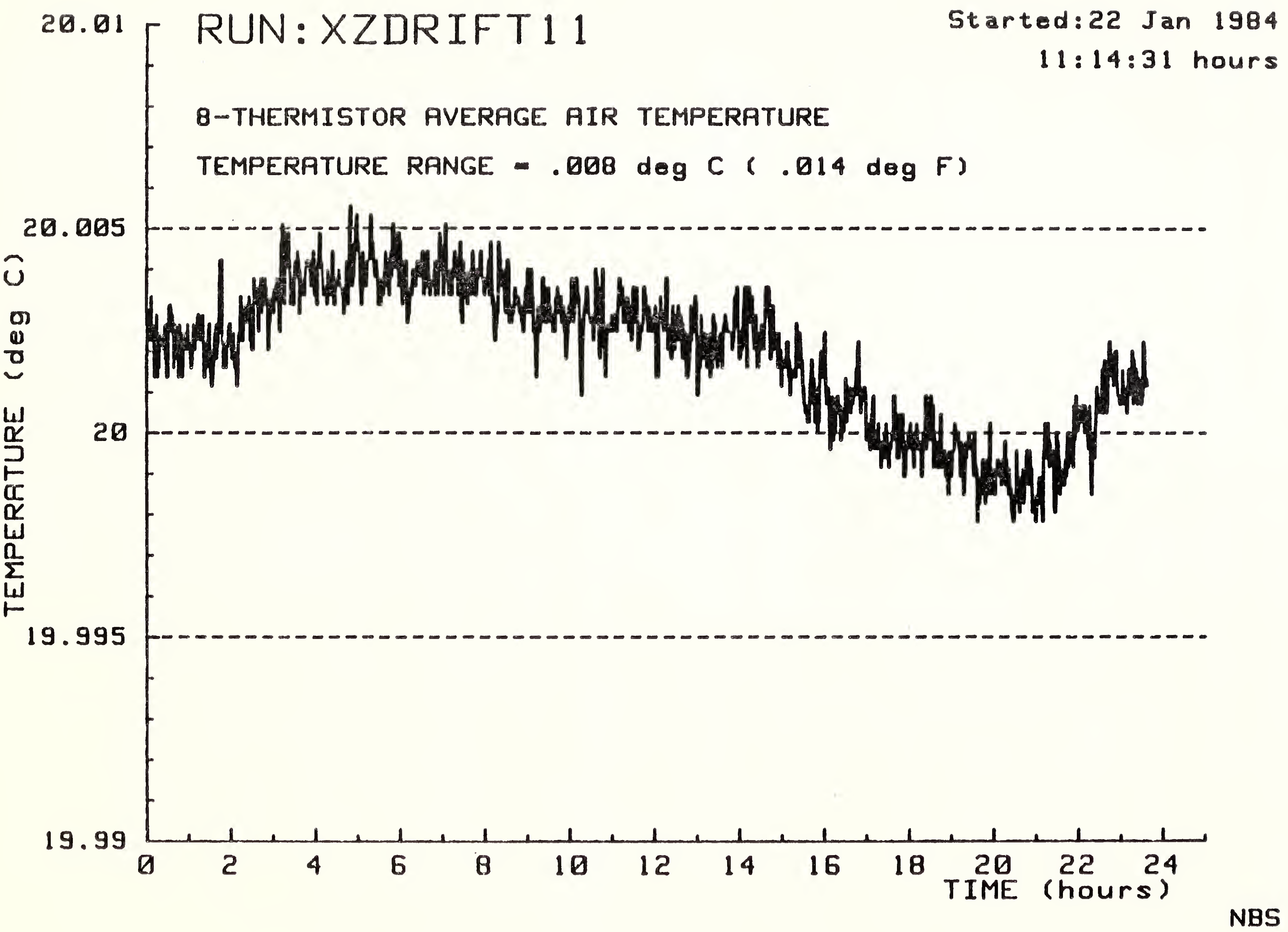
RUN: XZDRIFT11
Started:22 Jan 1984
11:14:31 hours
8-THERMISTOR AVERAGE AIR TEMPERATURE
TEMPERATURE RANGE = .008 deg C (.014 deg F)
TEMPERATURE (deg C)
20.01
20.005
20
19.995
19.99
0
2
4
6
8
10
12
14
16
18
20
22
24
TIME (hours)
NBS

Figure 2

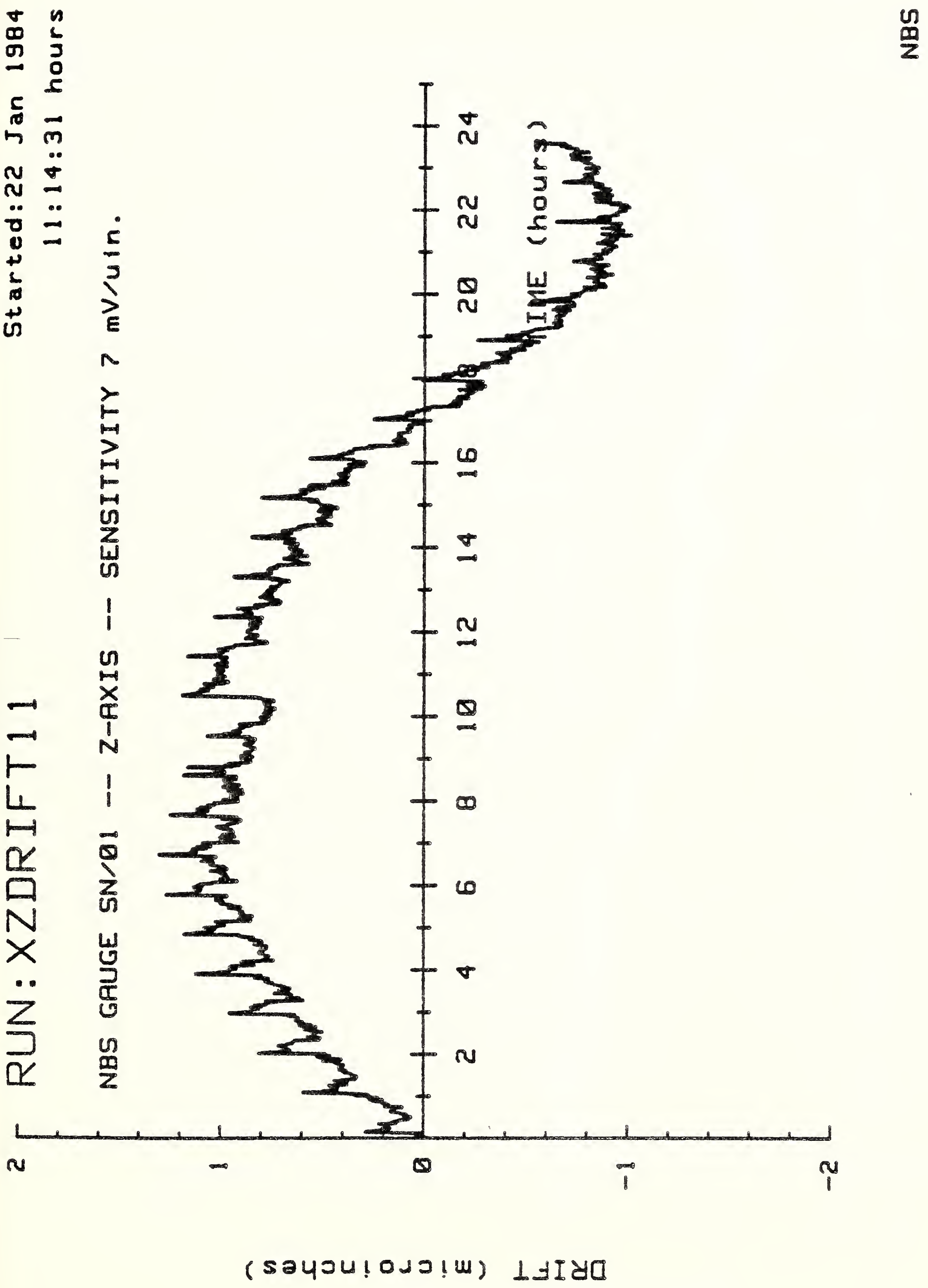
RUN:XZDRIFT11
Started:22 Jan 1984
11:14:31 hours
NBS GAUGE SN/01 -- Z-AXIS -- SENSITIVITY 7 mV/uin.
DRIFT (microinches)
2
1
0
-1
-2
2
4
6
8
10
12
14
16
18
20
22
24
TIME (hours)
NBS

Figure 3

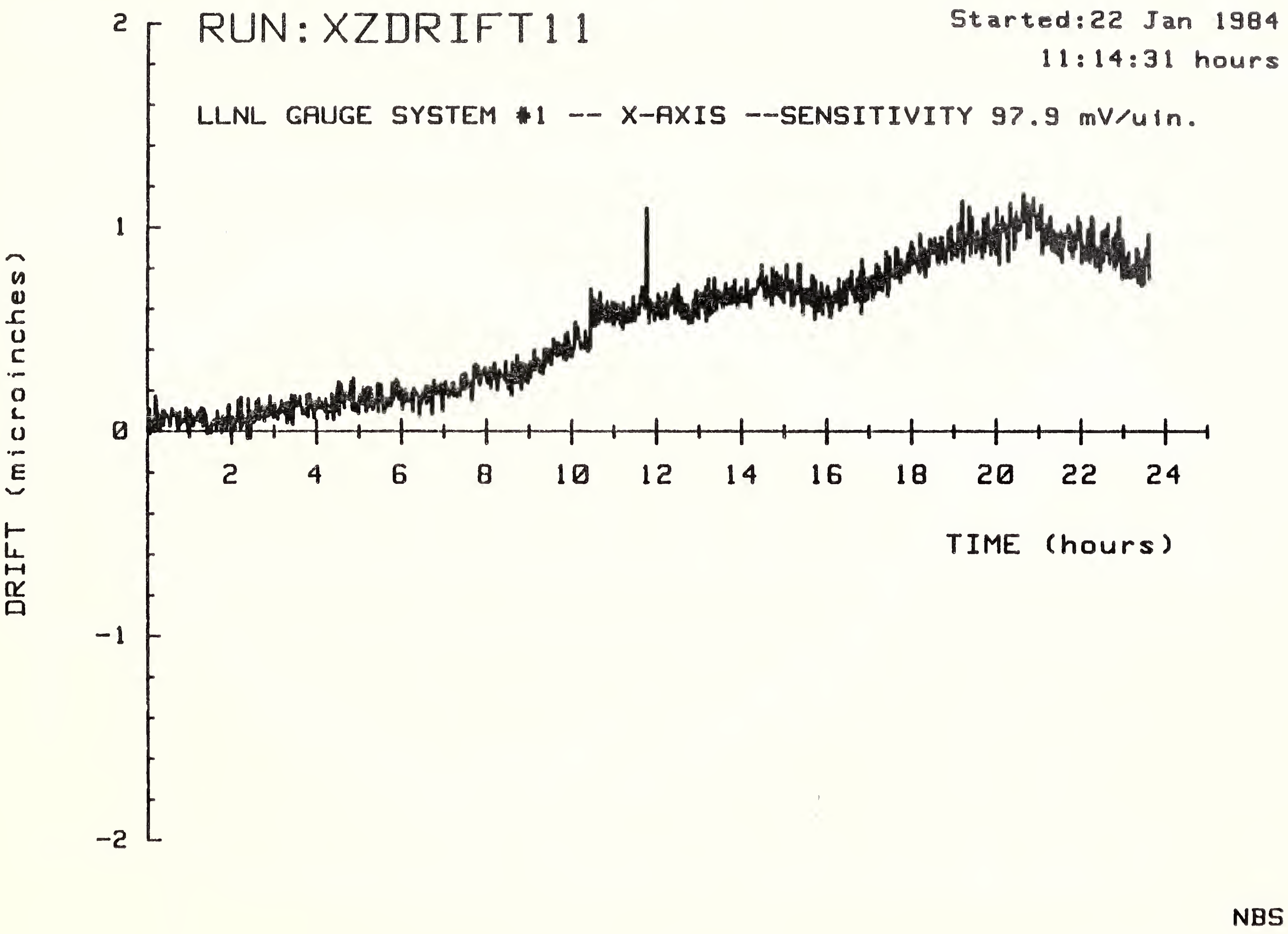
RUN: XZDRIFT11
Started:22 Jan 1984
11:14:31 hours
LLNL GAUGE SYSTEM #1 -- X-AXIS --SENSITIVITY 97.9 mV/uin.
DRIFT (microinches)
2
1
0
-1
-2
2
4
6
8
10
12
14
16
18
20
22
24
TIME (hours)
NBS

Figure 4

clearly coupled into the Z-axis drift data; no such correlation is observed in the X-axis data. The small-amplitude (≈0.4 microinch) periodic disturbances in the Z-axis data are fixturing artifacts, caused by mechanical flexing of the top mounting plate of the vacuum chuck. During the re-cycle sequence of the oil supply for the LODTM spindle thrust bearing, the vacuum pressure fluctuates with the opening and closing of solenoid valves. Such pressure fluctuations beneath the vacuum chuck cause mechanical deformations which couple directly to the test ball. These variations in spindle oil pressure were monitored during drift testing [see Fig.(5)] and are readily correlated with the small peaks in the Z-axis data.

The peak-valley drifts in the X and Z axes are approximately 1 microinch and 2 microinches in the 24 hour period measured. In the absence of periodic temperature variations, and taking into account inherent gauge stability, machine static drift stability appears to be better than 1 microinch P-V in both axes for 24 hours or less.

Figure (6) shows the state of air temperature control within the LODTM machine enclosure, as measured over a period of 36 hours during November, 1984. The machine thermal environment is exceptional and is within the specifications of the machine designers.

2. Positioning Repeatability Tests

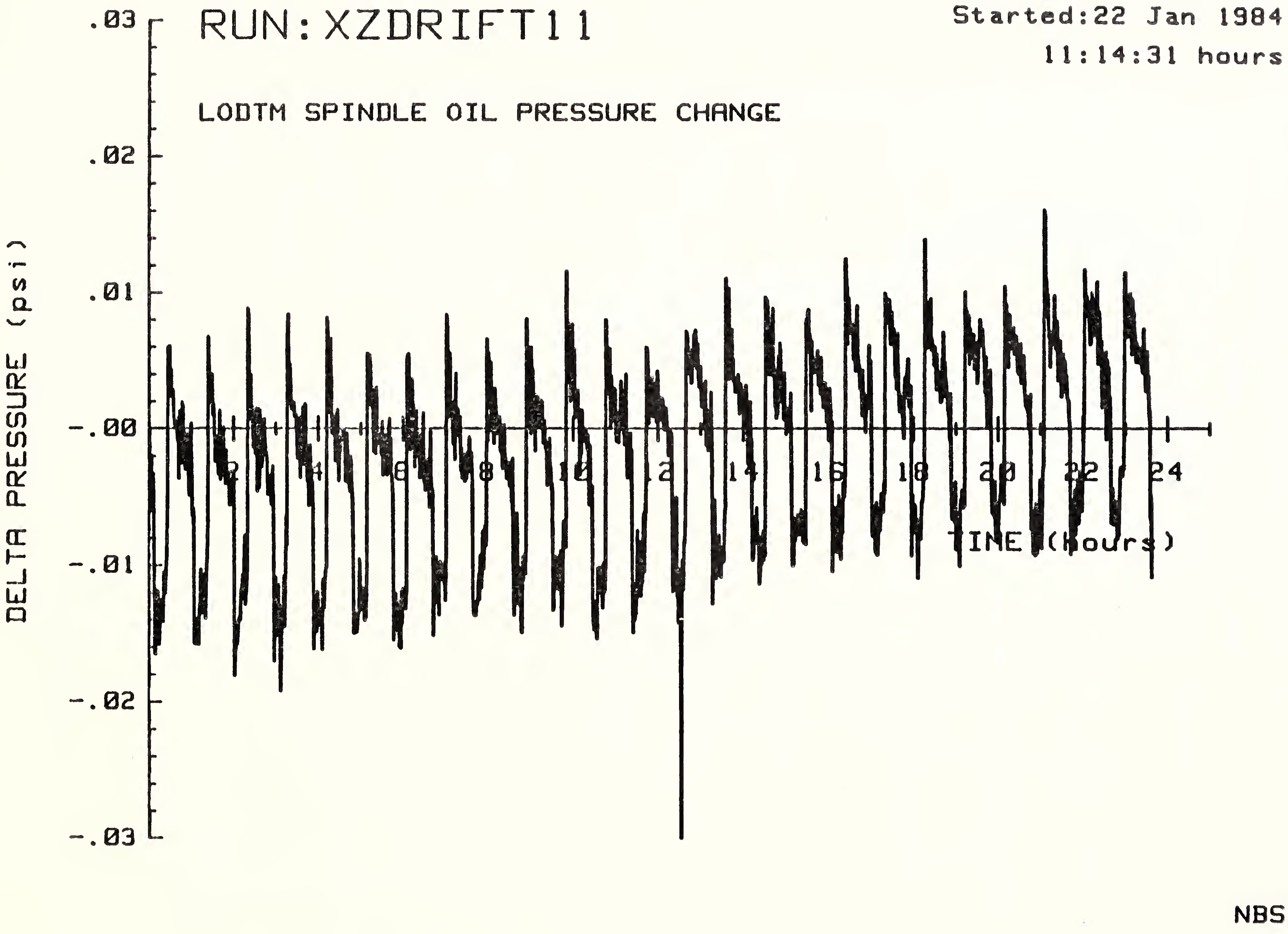
RUN:XZDRIFT11
Started:22 Jan 1984
11:14:31 hours
LODTM SPINDLE OIL PRESSURE CHANGE
DELTA PRESSURE (psi)
.03
.02
.01
-.00
-.01
-.02
-.03
2
4
6
8
10
12
14
16
18
20
22
24
TIME (hours)
NBS

Figure 5

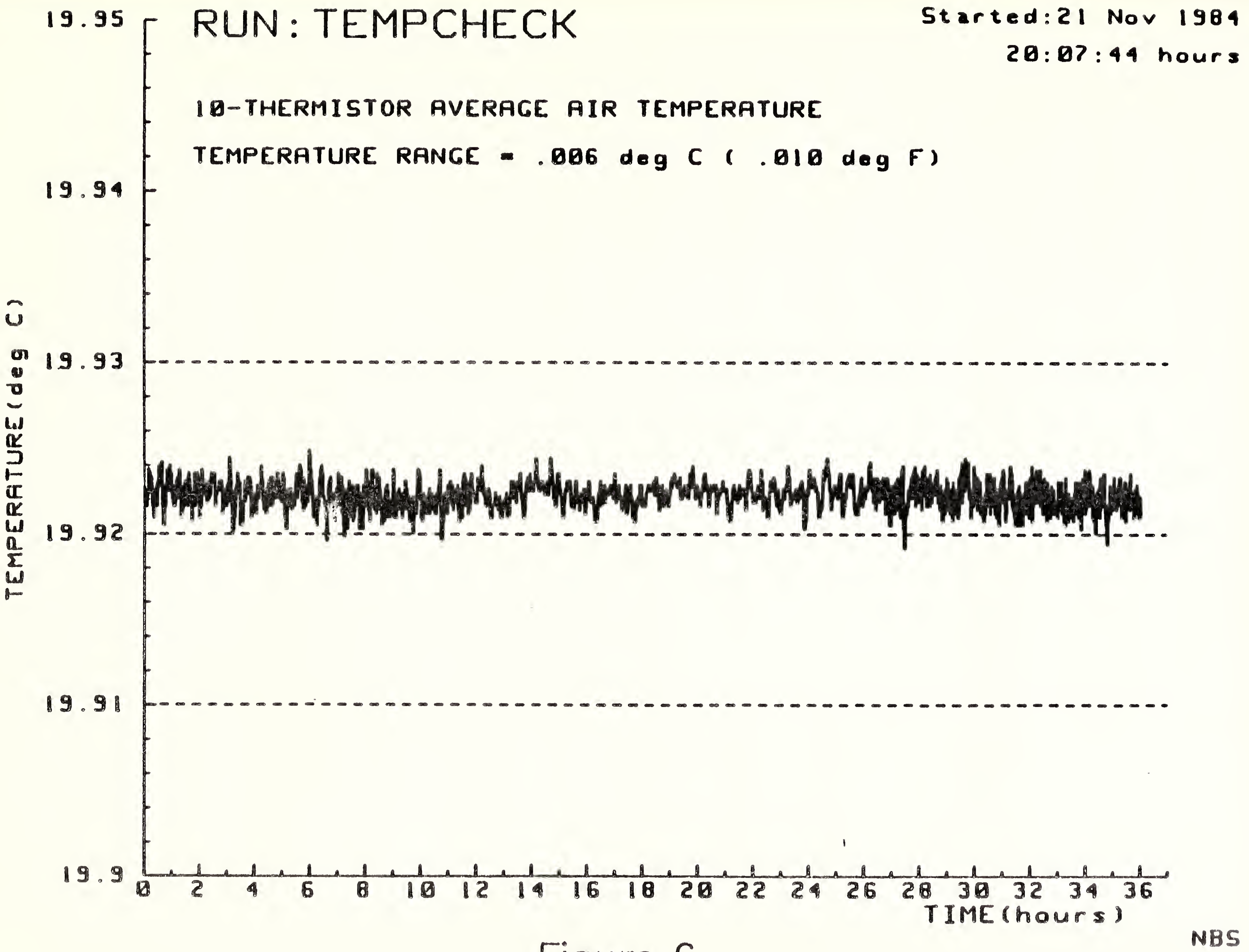
RUN: TEMPCHECK
Started:21 Nov 1984
20:07:44 hours
10-THERMISTOR AVERAGE AIR TEMPERATURE
TEMPERATURE RANGE = .006 deg C (.010 deg F)
19.95
19.94
19.93
19.92
19.91
19.9
TEMPERATURE(deg C)
0
2
4
6
8
10
12
14
16
18
20
22
24
26
28
30
32
34
36
TIME(hours)
NBS

Figure 6

Several tests were performed to check the reproducibility of machine positioning, in order to discover any effects due to "drive heating" or temperature gradients within the LODTM work volume. These tests were performed using the X and Z axis capacitance gauges and the 2-inch tungsten carbide ball described above.

During our early repeatability tests, we discovered that while the Z-axis repeated to better than 0.5 microinches (for short moves), the X-axis was highly erratic. Upon moving the tool bar manually 0.1 inches away from the test ball and back in the X-direction, the positioning repeatability varied in an unpredictable fashion from better than 0.5 microinches to as much as 60 microinches. A systematic investigation of this behavior revealed the source of the problem to be a faulty printed circuit board in one X-axis channel of the LODTM laser resolution electronics. The problem was subsequently eliminated by completely replacing all four PC boards in that particular channel.

The time required to isolate and repair the above hardware failure precluded testing machine repeatability as extensively as originally planned. The results and conclusions of the tests ultimately completed may be summarized as follows:

(a) Short moves: (0.1 inches in X and Z). X and Z both repeat to within 0.5 microinches or better, based upon approximately 10 trials.

(b) Intermediate move: (5 inches in X and Z). One trial only; X repeated to <0.5 microinches, Z repeated to <0.1 microinches.

(c) Long move: (15 inches in X and 10 inches in Z). One trial only; X repeated to <0.3 microinches, Z returned 2 microinches short of initial position.

Two points should be stressed with respect to these results. First, the presence of a 2-3 microinch, ≈100Hz vibration of the LODTM tool bar in the X-direction caused the sampling repeatability of the X-axis capacitance gauge to be inherently worse than for the Z-axis, which was free from this "noise" component. For this reason the "true" average X-axis tool bar repeatability is probably better than the 0.5 microinch figure we are able to quote.

The second comment concerns the comparatively poor repeatability of the Z-axis after the "long" move described in case (c). We now believe that this behavior was caused by dimensional changes in the capacitance gauge mounting fixture due to a position-dependent cooling of the tool bar mounting plate. This effect is described in Appendix A.

3. Tests for Polarization Mixing Errors

The slide positioning systems of LODTM were tested for the existence of polarization mixing errors. Such errors may occur in interferometers in which polarization is used to separate the information and reference beams. Because of the plane-mirror geometry employed in the LODTM interferometers, any such errors would appear as sinusoidal positioning errors with a period of ≈6 microinches.

These tests employed the same fixtures and gauges described above. For each axis, the machine moved under computer control for a total displacement of 10 microinches, in 0.1 microinch steps. Gauge resolution on both axes was better than 0.1 microinch.

The results of these tests are conclusive: if periodic errors exist in the LODTM slide positioning systems, they are smaller than 0.1 microinch in amplitude and thus of negligible importance to part machining accuracy.

4. X-axis Scale Errors (0-40 inches)

The linear positioning error (scale error) of the LODTM X-axis was measured over 40 inches of its approximately 44 inches of travel. We define the scale error as the difference between actual (measured) slide position and the position commanded by the NC machine controller.

Scale error measurements were performed with the NBS-developed laser interferometer system described in detail in Appendix B. Because of schedule delays and time constraints, we used a retroflector target rather than plane-mirror optics which resulted in a factor of two decrease in interferometer resolution. In addition, our extensive experience with the commercial laser head used in these tests revealed it to be remarkably stable (frequency drift <1 part in 10^9 in any 24-hour period measured). For this reason, the iodine-stabilized He-Ne laser was used for frequency checks before and after the scale measurements, rather than being used as a real-time component of the interferometer system.

There are two sources of systematic errors which must always be considered in this type of displacement interferometry. The first is a length-dependent error which arises when the measurement laser beam is not parallel to the machine motion axis. Such a misalignment will cause the interferometer to measure a displacement smaller than the actual machine motion by an amount proportional to the cosine of the angle between the two axes, and the resultant error is thus known as "cosine error". In the NBS measurements, beam alignment was accomplished using a 2-axis lateral-effect photodiode position detector which enabled the direct measurement of the relevant angle. This result was used to correct the measured data for the effects of cosine error.

The second systematic error occurs when the environmental conditions change during a measurement cycle. The interferometer system is zeroed at the start of a run with the retroreflector at some small, but finite (≈1/4 inch) distance from the beam splitter and reference reflector. If the refractive index of the air within the machine enclosure changes then the position of the zero point will wander by an amount proportional to such a change. If not corrected, this zero drift causes what are referred to as "deadpath" errors in the interferometer system. Since environmental parameters are routinely sampled and stored during laser measurements, deadpath errors are calculated and removed by the data analysis software.

The LODTM X-axis scale errors were measured at 1 inch intervals, with each point sampled twice (once for each direction of slide motion). The machine moved to its commanded positions under computer control, and was linked to the NBS metrology system by means of a 0→5 VDC "in-position" signal from the computer, followed by a pause (≈10 seconds) for data sampling.

The results of our first X-axis scale measurement are shown in Fig.(7). The large (≈160 microinch) systematic error is a consequence of our basic unfamiliarity with LODTM start-up procedures, which require the operator to enter the tool point coordinates into the real-time computer (RTC). In this run (XDISP6) this information was entered at the wrong point in the sequence and caused a 10-inch error in the vertical position of the tool point (retroreflector) used by the RTC for real-time software correction. Combined with the observed 160 microinch error, this 10-inch offset indicates an approximately 3 arc-second pitch motion of the X-axis carriage.

Figure (8) shows the measured X-axis scale error with the tool point position entered correctly into the control software. The solid curve connects points sampled with X increasing and the dashed curve corresponds to decreasing X. This data displays an approximately linear systematic error of 8 parts in 10^8. While this is smaller than the estimated 1 part in 10^7

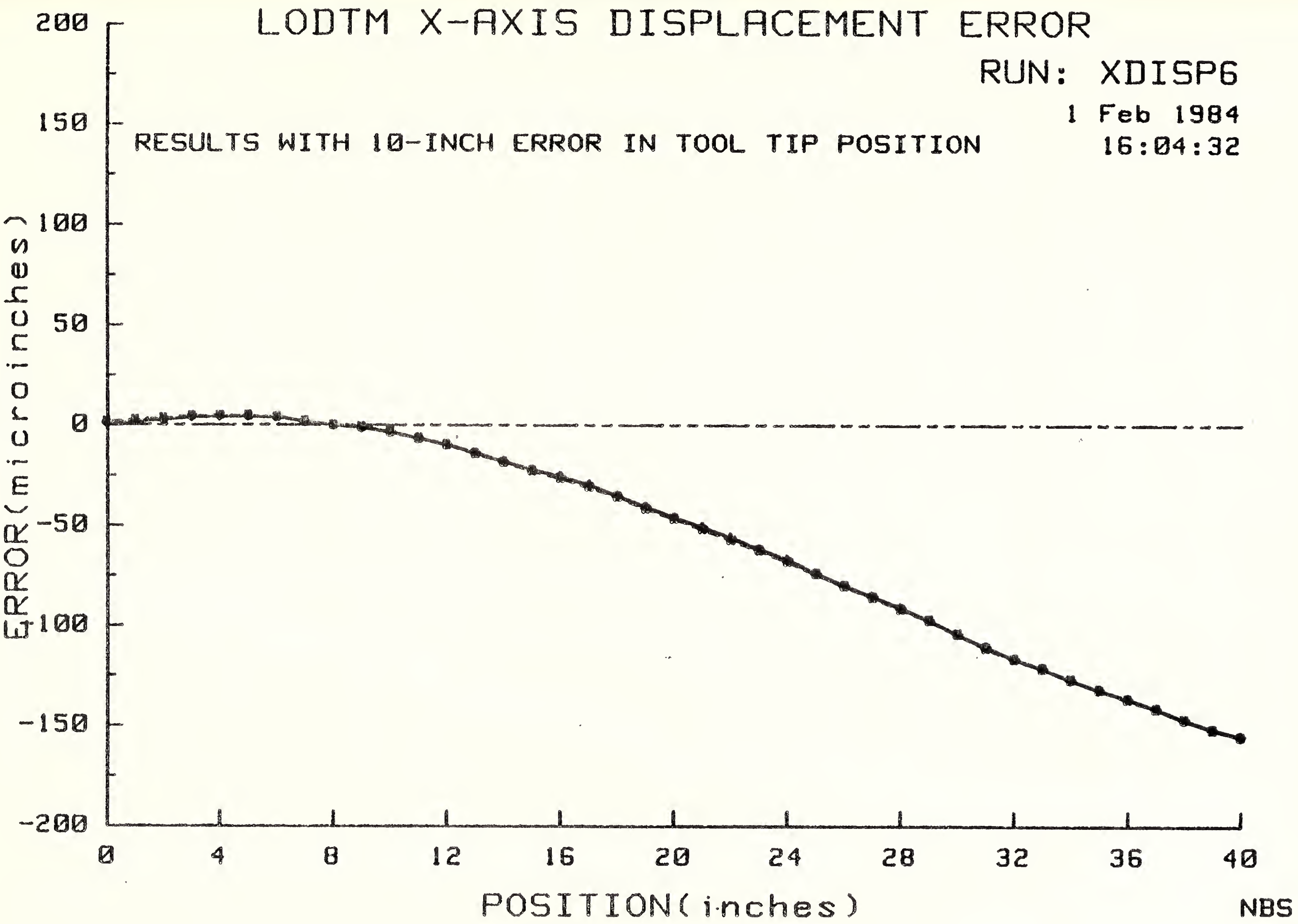
LODTM X-AXIS DISPLACEMENT ERROR
RUN: XDISP6
1 Feb 1984
16:04:32
RESULTS WITH 10-INCH ERROR IN TOOL TIP POSITION
ERROR(microinches)
200
150
100
50
0
-50
-100
-150
-200
0
4
8
12
16
20
24
28
32
36
40
POSITION(inches)
NBS

Figure 7

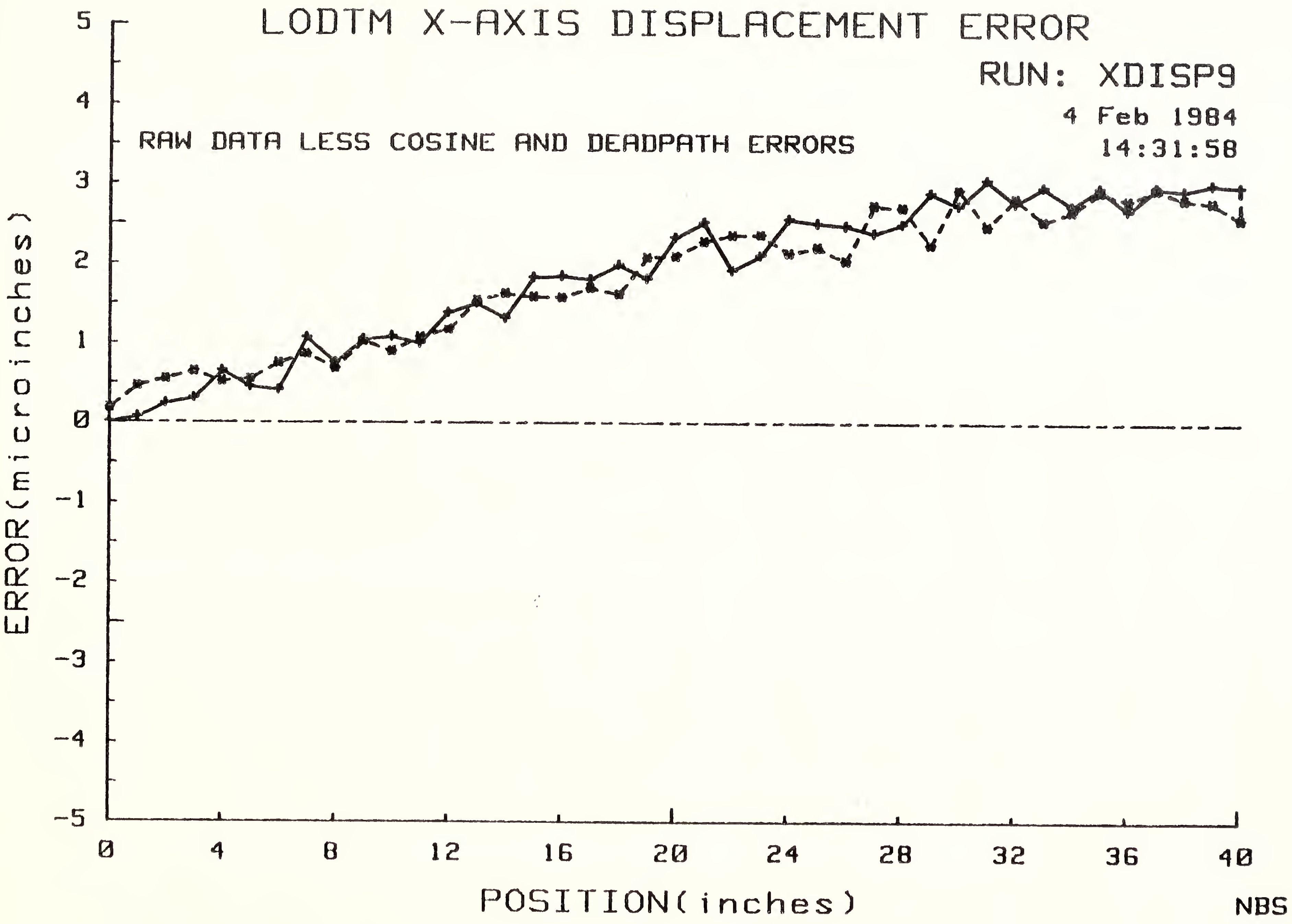
LODTM X-AXIS DISPLACEMENT ERROR
RUN: XDISP9
4 Feb 1984
14:31:58
RAW DATA LESS COSINE AND DEADPATH ERRORS
ERROR(microinches)
5
4
3
2
1
0
-1
-2
-3
-4
-5
0
4
8
12
16
20
24
28
32
36
40
POSITION(inches)
NBS

Figure 8

accuracy of the NBS interferometer system, we discovered that the LODTM metrology laser was operating 30 MHz below the frequency coded into the RT computer. More than one-half of the observed slope of the data may be attributed to this frequency error, and the data was subsequently re-analyzed with the appropriate frequency correction.

The final results, corrected for all known systematic errors, are shown in Fig.(9). As is evident from this data, LODTM is more accurate than an interferometer operating in air can measure. All data is within the systematic uncertainty in the NBS interferometer system. The lack of exact position repeatability is due to air turbulence and a 2-3 microinch vibration of the machine tool bar. This effect could be reduced by longer averaging but time constraints precluded this improvement.

5. Z-Axis Scale Errors (0-19.5 inches)

The scale error of the LODTM Z-axis was measured over 19.5 inches of its approximately 20-inch range of travel. Data was taken at 1-inch intervals using essentially the same optics used in the X-axis measurements.

The raw data (less cosine and deadpath errors) is shown in Fig.(10). The marked systematic non-repeatability in the data was traced to a position-dependent thermal gradient in the LODTM tool bar. This effect is described in detail in Appendix A. For the present it suffices to say that a simple

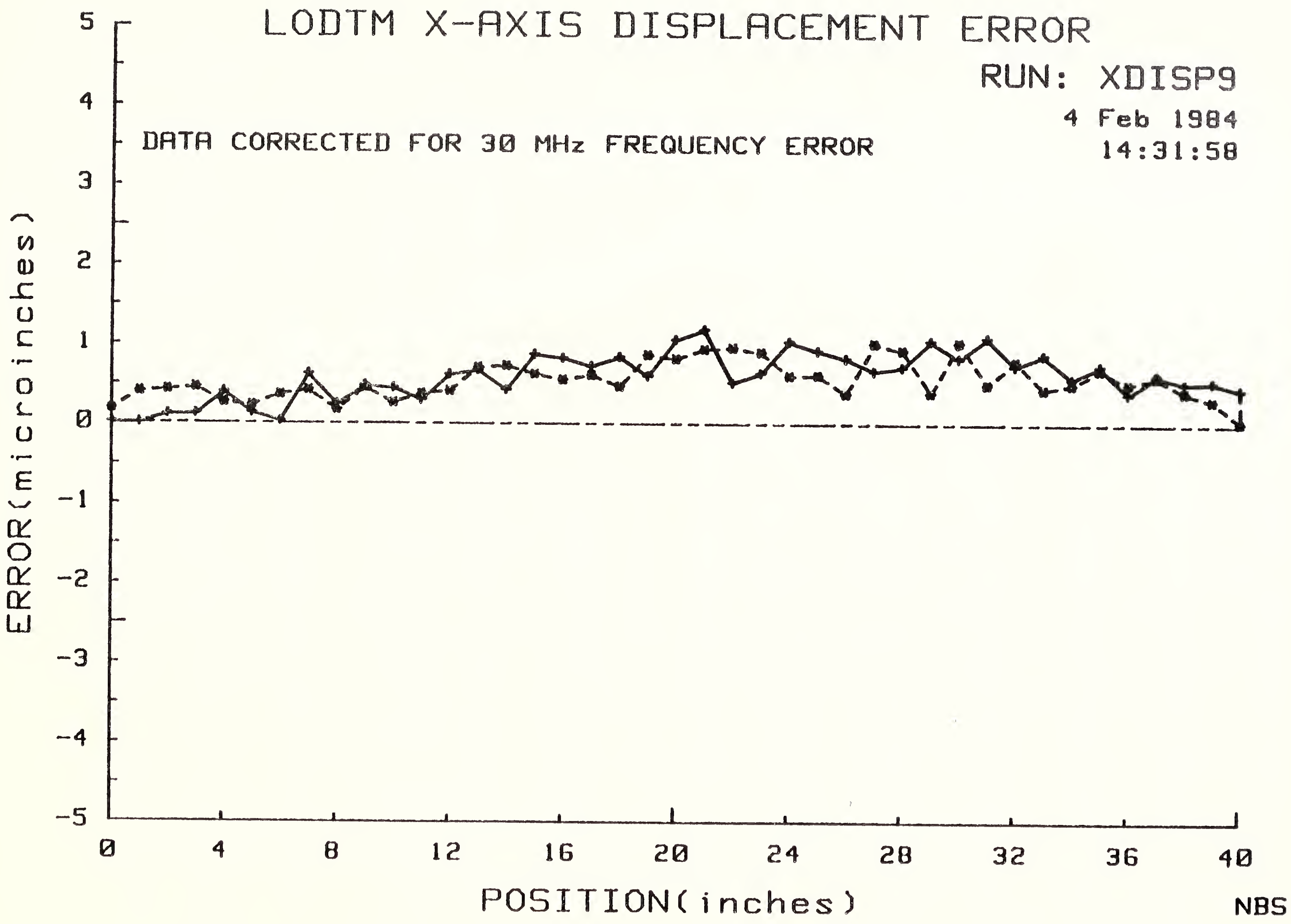
LODTM X-AXIS DISPLACEMENT ERROR
RUN: XDISP9
4 Feb 1984
14:31:58
DATA CORRECTED FOR 30 MHz FREQUENCY ERROR
ERROR(microinches)
5
4
3
2
1
0
-1
-2
-3
-4
-5
0
4
8
12
16
20
24
28
32
36
40
POSITION(inches)
NBS

Figure 9

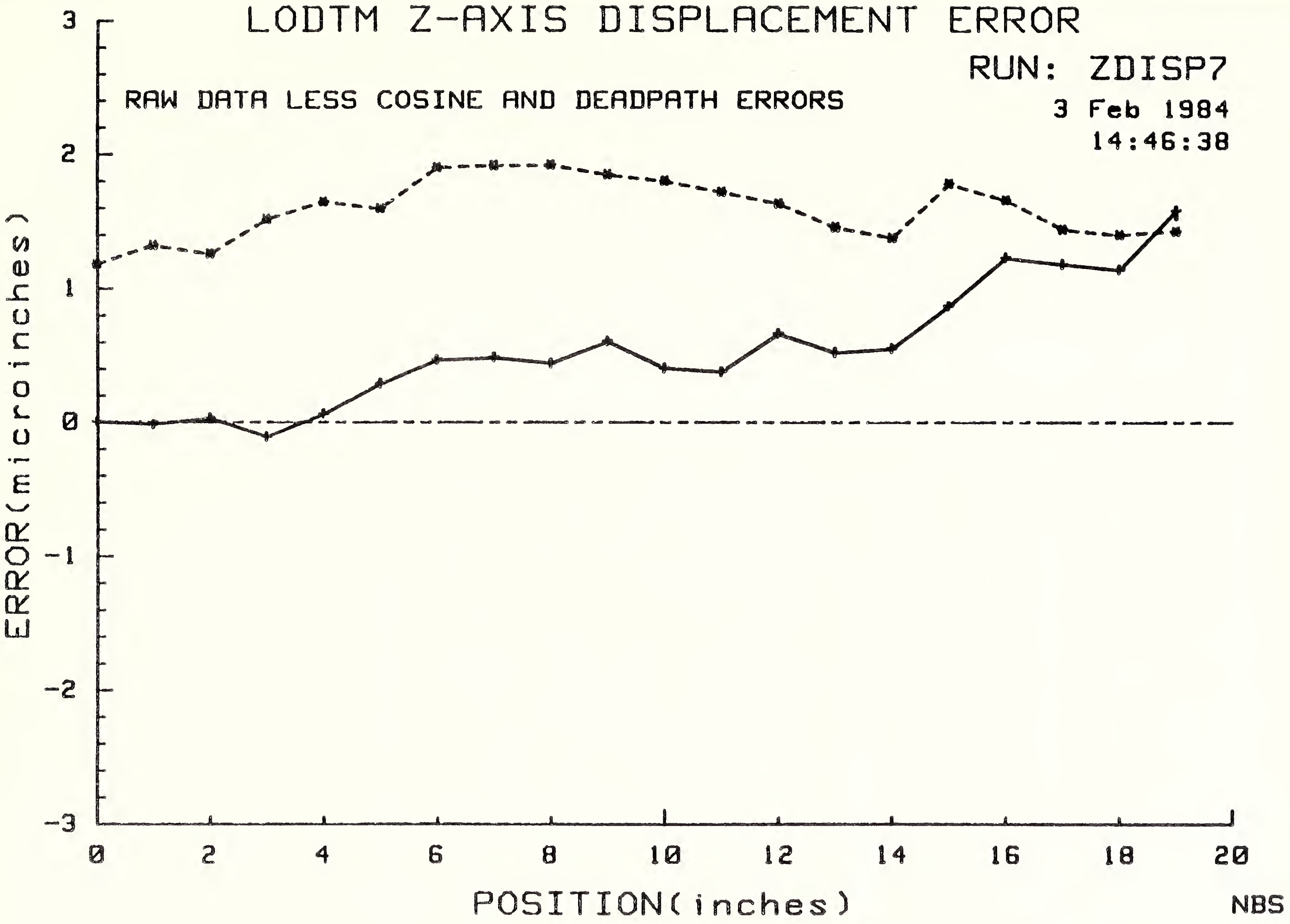
LODTM Z-AXIS DISPLACEMENT ERROR
RUN: ZDISP7
3 Feb 1984
14:46:38
RAW DATA LESS COSINE AND DEADPATH ERRORS
ERROR(microinches)
3
2
1
0
-1
-2
-3
0
2
4
6
8
10
12
14
16
18
20
POSITION(inches)
NBS

Figure 10

model afforded a satisfactory way to correct measurement data for the effects of thermal drift.

The corrected data is shown in Fig.(11). As was the case for the X-axis measurements, the observed Z-axis scale errors are completely within the systematic uncertainty of the NBS interferometer system.

6. Angular Motions

The four X-axis interferometers on LODTM are designed to detect rotations of the tool bar about the machine Y-axis and to provide error signals for real-time position correction. In order to measure the actual angular motions (pitch errors) of the machine slides and the degree to which the RTC software is able to compensate for them, it was necessary to enter a fictitious tool tip position into the RTC at startup, thus disabling the pitch compensation portion of the control software. The actual measurements employed the NBS laser interferometer system, since with appropriate tool offsets pitch motions cause apparent scale errors (i.e.,"Abbe errors").

6.A. X-Axis Pitch Motion [$\varepsilon_y(X)$]

The real-time correction of errors due to pitch motion of the LODTM X-axis carriage is well illustrated by Figs.(7) and (8). The only difference between these two runs was the vertical distance between the effective tool

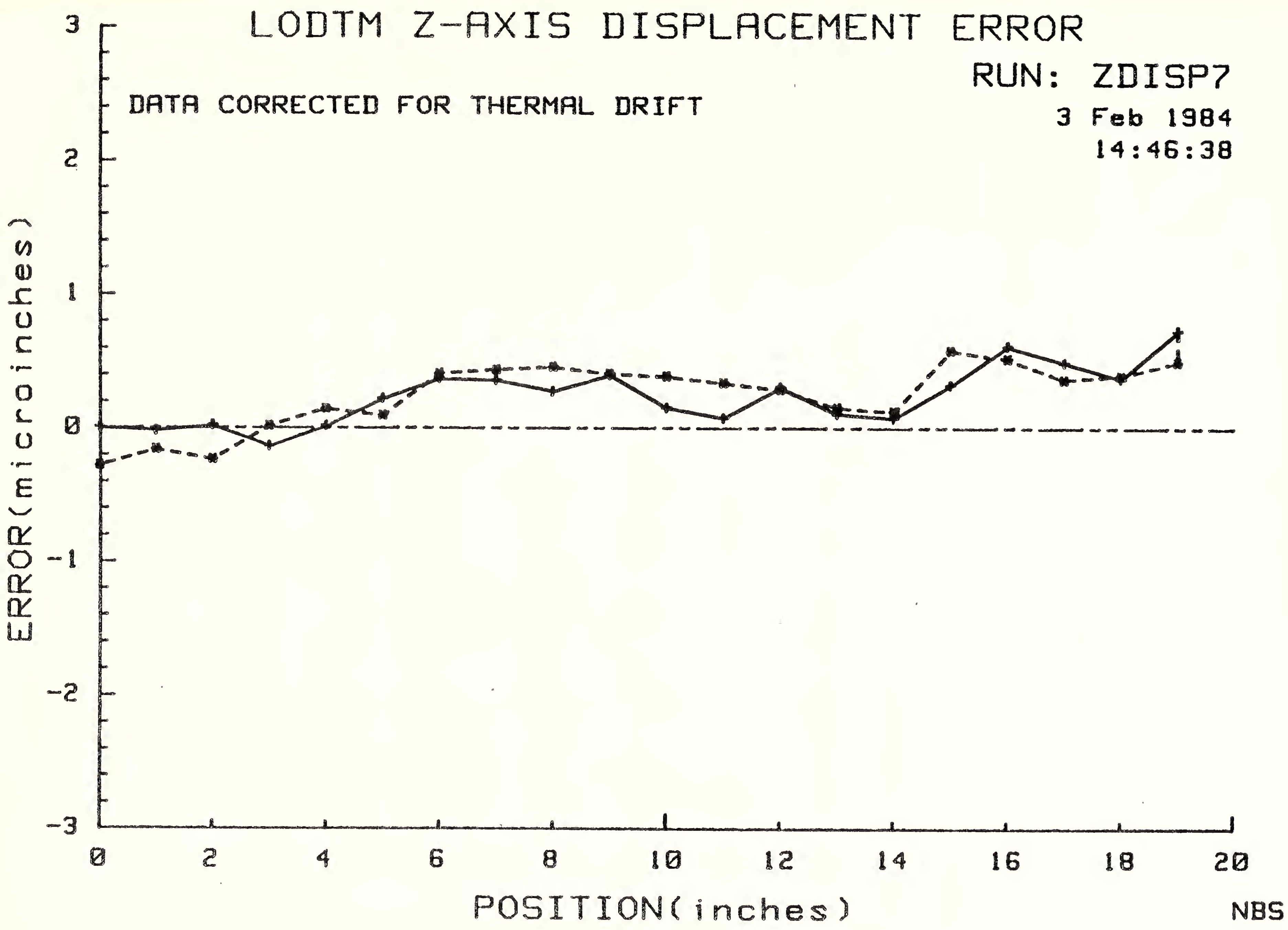
LODTM Z-AXIS DISPLACEMENT ERROR
RUN: ZDISP7
3 Feb 1984
14:46:38
DATA CORRECTED FOR THERMAL DRIFT
ERROR(microinches)
3
2
1
0
-1
-2
-3
0
2
4
6
8
10
12
14
16
18
20
POSITION(inches)
NBS

Figure 11

point and the tool bar mounting plate which was entered into the RTC. In the first case [Fig.(7)] this offset was in error by 10 inches. After entering this distance correctly [Fig.(8)] the large systematic error disappeared, indicating that the real-time correction software was functioning correctly. Any residual angular motions cause position errors within the systematic uncertainty of the NBS interferometer system.

6.B. Z-Axis Pitch Motion [$\varepsilon_y(Z)$]

The rotation of the LODTM tool bar about the machine Y-axis, as a function of Z-position, was measured in the following manner. Using the NBS laser interferometer system, the displacement error of the target reflector (corner cube) was measured with the reflector offset from the center line of the tool bar in the X-direction. In this configuration, if the RTC is given a zero X-axis offset at start-up, then the machine will move in the Z-direction with no correction for rotational motion (Z-positioning errors due to Y-axis rotations are of second order when the tool point is on the tool bar center line). Real pitch errors of the tool bar then appear as scale errors to the interferometer system, with magnitude equal to the angular motion multiplied by the reflector offset.

By repeating the above measurements with the correct X-axis offset entered into the RTC, the effect is to toggle, or turn on, the pitch correction part of the position correctioning software. These measurements were performed for two different tool offsets: +9.3 inches (runs ZDISP5 and ZDISP6) and

-4.65 inches (runs ZDISP8 and ZDISP9). For each offset, one run was made with software correction off followed by a run with software correction on. [Note: the signs of the offsets refer to the offset directions relative to the center of the tool bar. By convention, positive offsets are to the North.]

During our January-February, 1984 validation measurements it was necessary to correct all Z-axis pitch measurement data for the effects of the tool bar thermal gradient, as described in Appendix A.

The results of the two runs with software correction off (ZDISP5 and ZDISP8) are shown in Figs.(12) and (13). It is clear from these figures that the LODTM tool bar possesses a systematic rotation about the machine Y-axis of magnitude 0.4 microradians/inch of Z-travel. The total rotation in 20 inches of travel is approximately 1.64 arc-seconds (7.95 μrad), and the sense of rotation is clockwise when viewed from the West. We stress that this is the inherent, or uncorrected, pitch error and its magnitude is typical of a precision machine tool of the size of LODTM.

By entering the correct tool offsets, we then effectively turn on the LODTM Z-axis pitch correction software, resulting in Figs.(14) and (15) [runs ZDISP6 and ZDISP9]. If the Z-axis reference straightedges were perfectly straight and if the pitch correction calculation was properly implemented, we would expect the resultant errors to be zero, within the measurement uncertainty. As the data indicate, however, with the pitch compensation turned on there is a residual apparent pitch error of approximately 0.097

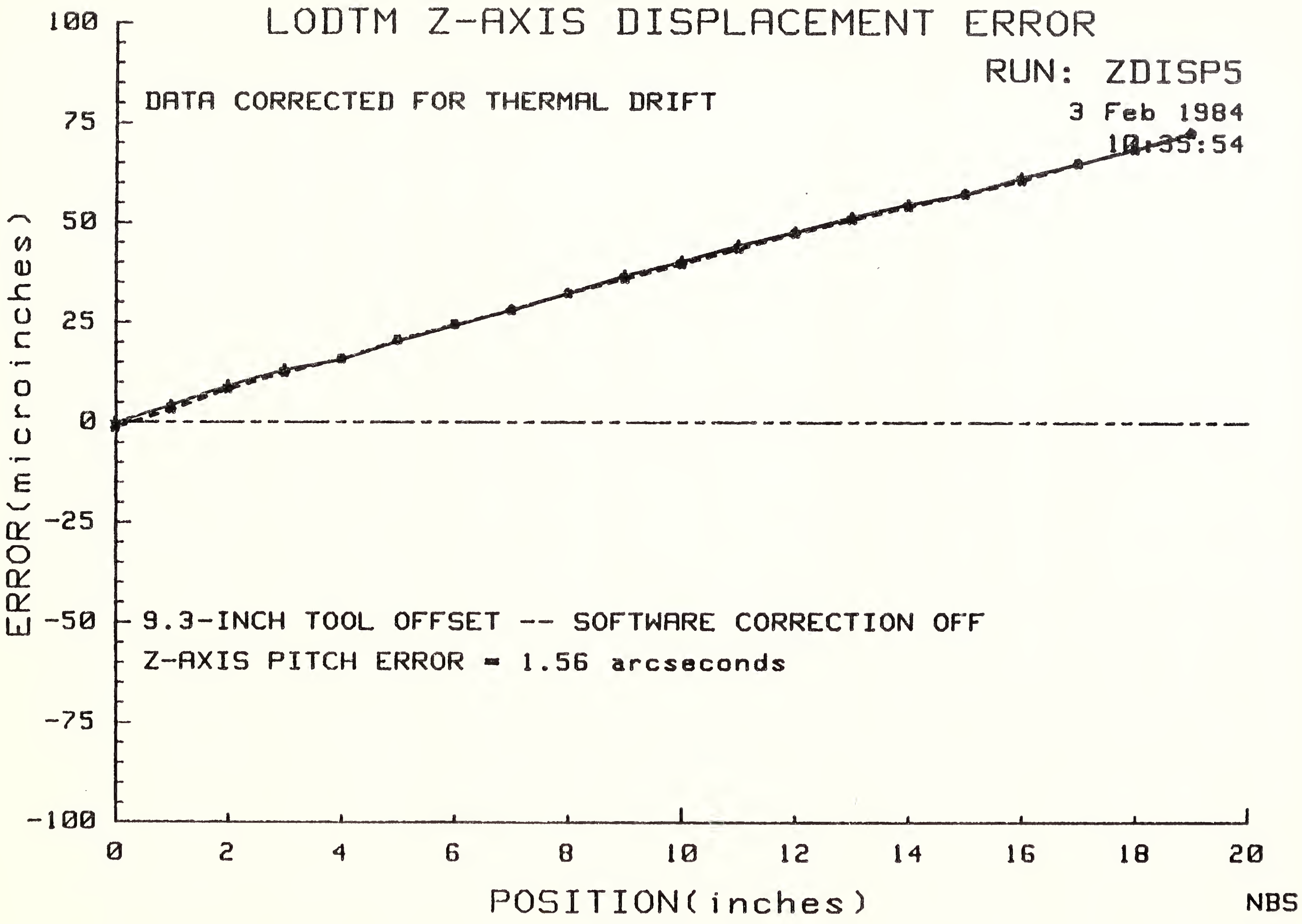
LODTM Z-AXIS DISPLACEMENT ERROR
RUN: ZDISP5
3 Feb 1984
10:35:54
DATA CORRECTED FOR THERMAL DRIFT
9.3-INCH TOOL OFFSET -- SOFTWARE CORRECTION OFF
Z-AXIS PITCH ERROR = 1.56 arcseconds
ERROR(microinches)
100
75
50
25
0
-25
-50
-75
-100
POSITION(inches)
0
2
4
6
8
10
12
14
16
18
20
NBS

Figure 12

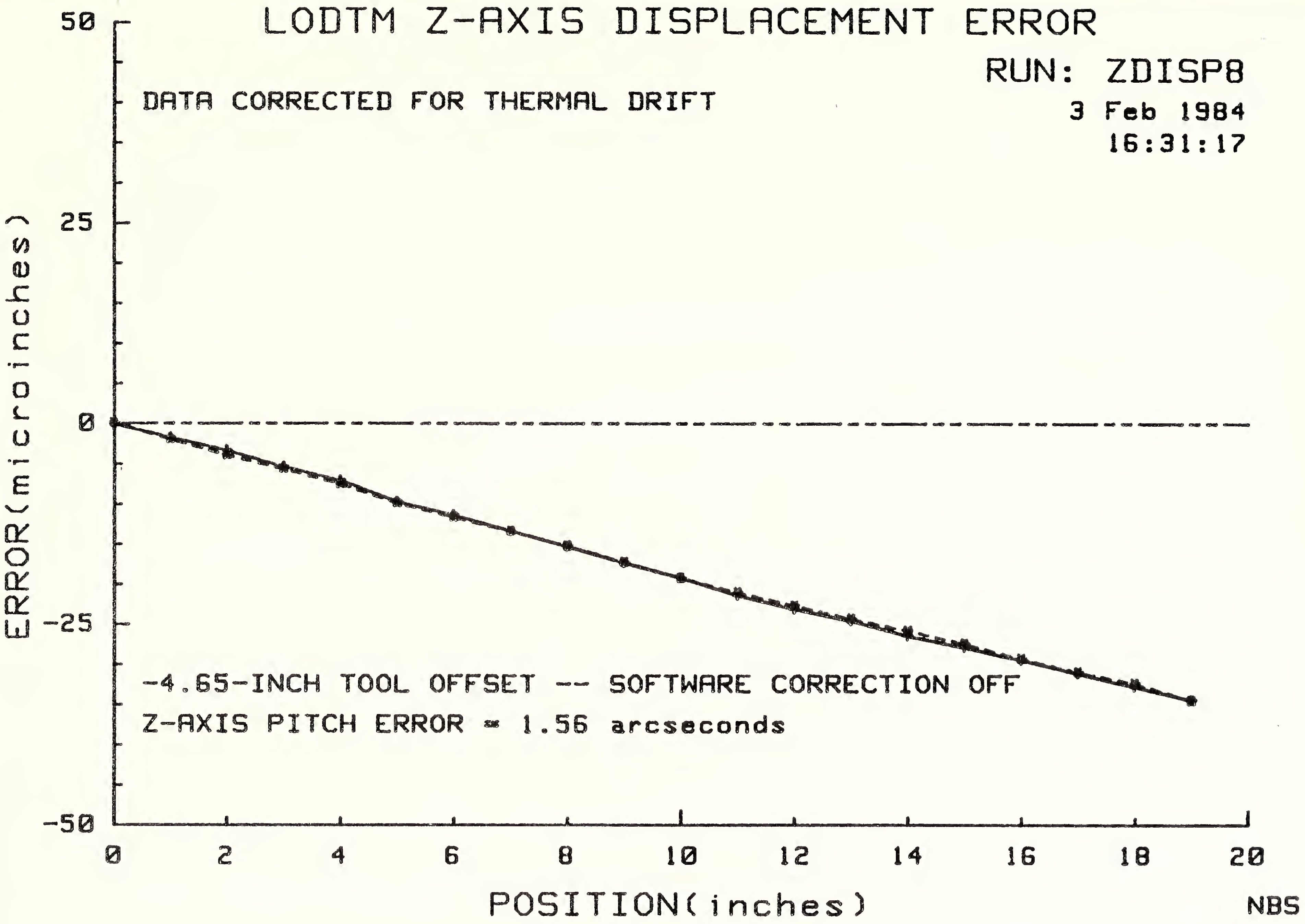
LODTM Z-AXIS DISPLACEMENT ERROR
RUN: ZDISP8
3 Feb 1984
16:31:17
DATA CORRECTED FOR THERMAL DRIFT
-4.65-INCH TOOL OFFSET -- SOFTWARE CORRECTION OFF
Z-AXIS PITCH ERROR = 1.56 arcseconds
ERROR(microinches)
50
25
0
-25
-50
POSITION(inches)
0
2
4
6
8
10
12
14
16
18
20
NBS

Figure 13

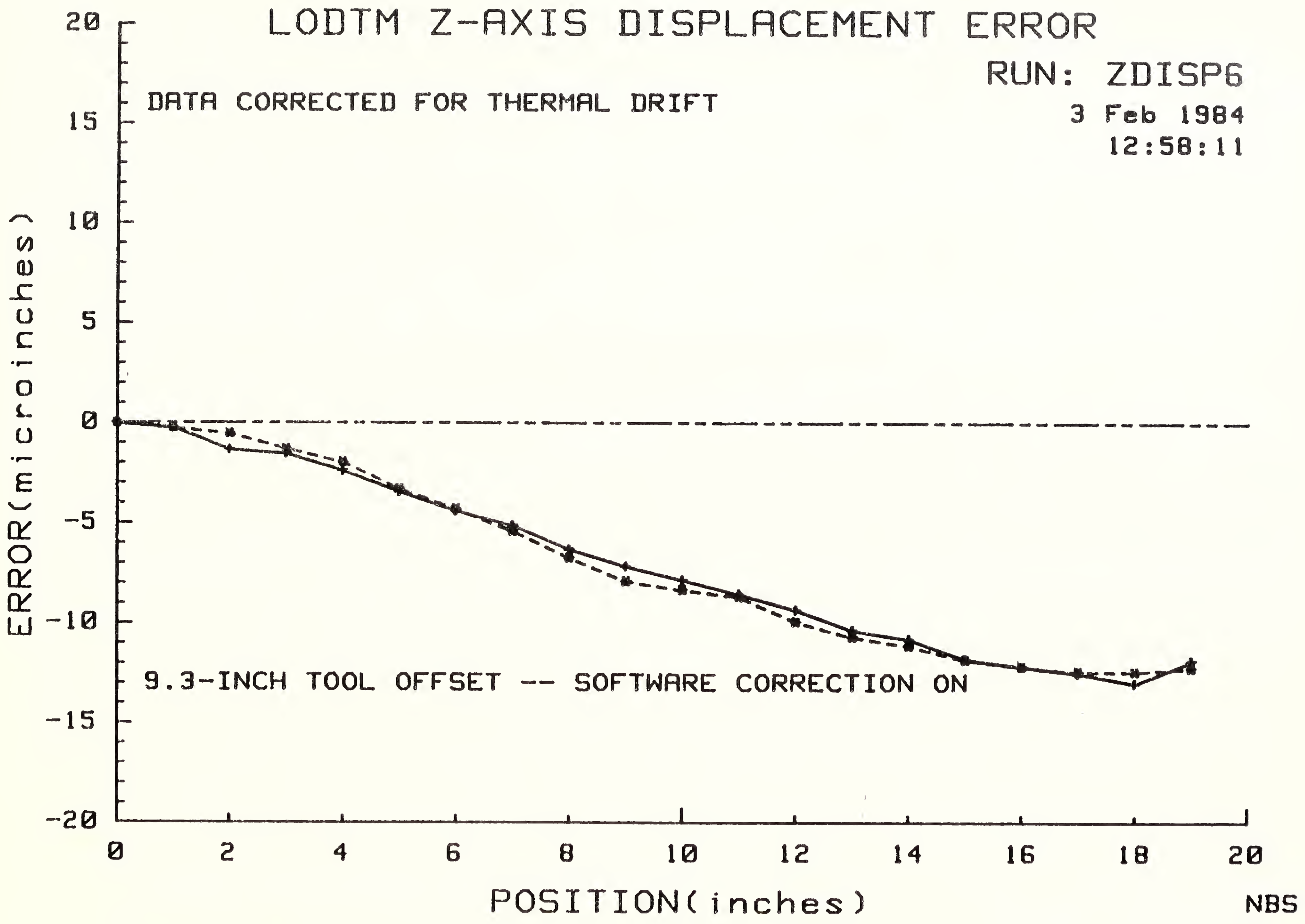
LODTM Z-AXIS DISPLACEMENT ERROR
RUN: ZDISP6
3 Feb 1984
12:58:11
DATA CORRECTED FOR THERMAL DRIFT
9.3-INCH TOOL OFFSET -- SOFTWARE CORRECTION ON
ERROR(microinches)
20
15
10
5
0
-5
-10
-15
-20
POSITION(inches)
0
2
4
6
8
10
12
14
16
18
20
NBS

Figure 14

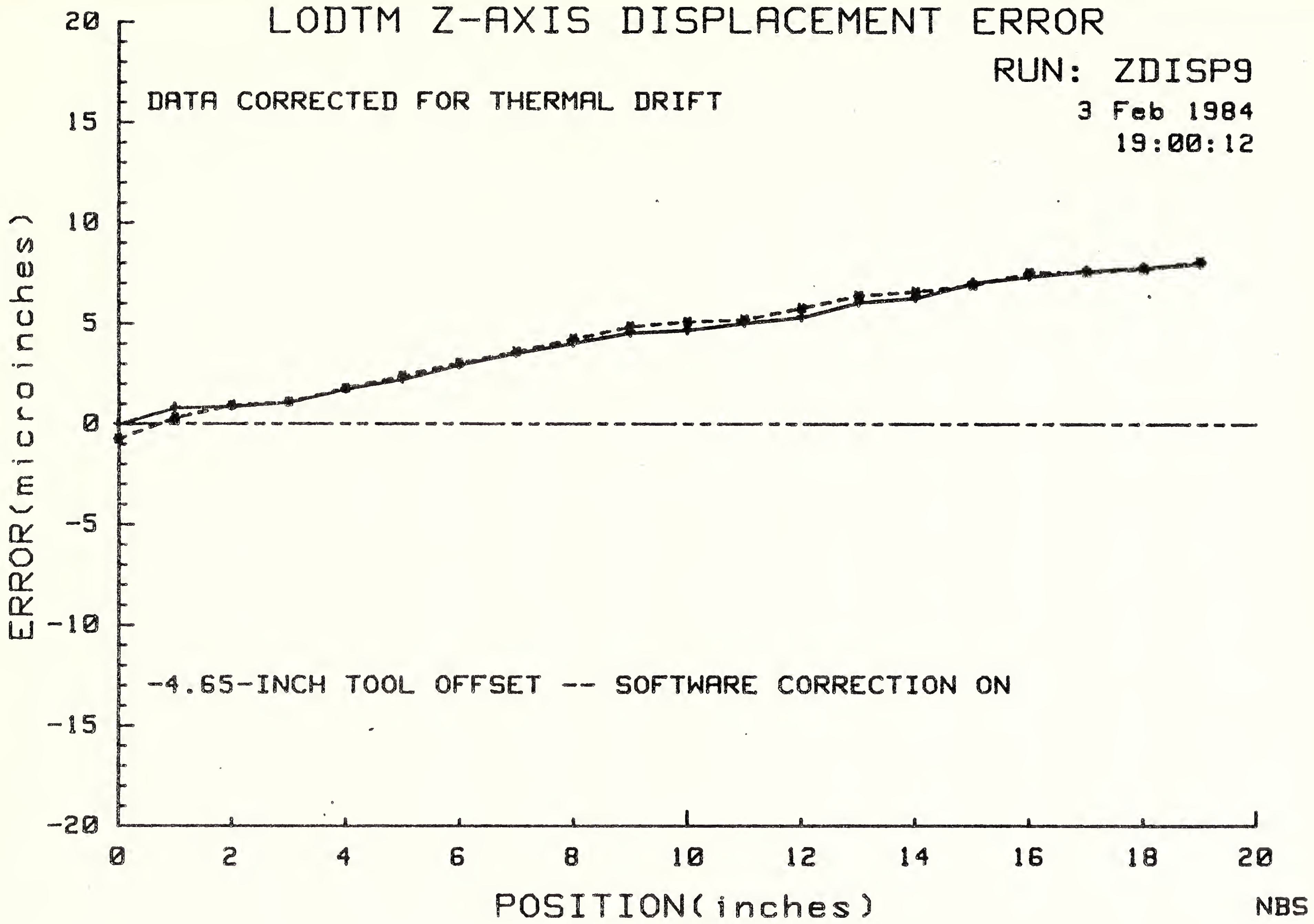
LODTM Z-AXIS DISPLACEMENT ERROR
RUN: ZDISP9
3 Feb 1984
19:00:12
DATA CORRECTED FOR THERMAL DRIFT
-4.65-INCH TOOL OFFSET -- SOFTWARE CORRECTION ON
ERROR(microinches)
20
15
10
5
0
-5
-10
-15
-20
0
2
4
6
8
10
12
14
16
18
20
POSITION(inches)
NBS

Figure 15

μrad/inch of Z-travel with direction counter-clockwise when viewed from the West. In other words, the control system over-corrected for the effects of Z-axis pitch. In our opinion, this over-correction is due to the differences in the shapes of the two Z-axis reference straightedges.

During our return validation period in November, 1984, we undertook the re-measurement of the Z-axis pitch error in order to assure that the linear term in the Z-straightedge look-up tables was properly assigned. This linear term arises due to the shape errors of the tool bar straightedges and should have the effect of removing the apparent residual pitch error described in the preceding paragraph. These new measurements were performed in a manner similar to that of the original series, except that we used only a -10-inch offset fixture together with on-axis scale measurements.

It should be noted that these measurements were done with the air line heaters, as described in Appendix A, turned on and operating at approximately 50% of full power. Direct measurements showed that the tool bar face plate temperature was constant within ±0.01°C over the full range of Z-axis travel under these conditions, so that the simple thermal model used to correct the original data could not be applied to the re-measurements. As will be seen, there is a significant amount of thermally-related hysteresis remaining in the Z-axis displacement/pitch data which is not related to any real dimensional changes in the fixtures. The detailed cause of this behavior is not understood at this time.

Figure (16) displays the results of our re-measurement of the Z-axis displacement error (run ZSCALE9). The lack of bi-directional repeatability is due to the thermal hysteresis mentioned above. A comparison of this data with our original measurement [Fig.(11)] shows somewhat larger systematic error than we calculate for the NBS interferometer system (1 part in 10^7). Prior to this measurement we made a very careful determination of the frequency reference chain and the subsequent frequency-to-wavelength conversion algorithm used by the LODTM control computer to set the length scale of the machine. The only uncertainty associated with this system was the frequency of the reference laser. Shortly after the January-February, 1984 validation period, the reference iodine-stabilized He-Ne laser on LODTM failed and due to lack of a spare was replaced with the commercial metrology laser used in the NBS interferometer system. This laser had been calibrated at NBS and at Livermore prior to its use in field measurements, but the last calibration was performed in January, 1984. The long-term frequency stability of this laser is specified to be ±1 part in 10^7; a drift of this magnitude could account for 2 microinches of observed displacement error. While such a frequency drift is in principle possible, our experience with frequency calibrations of the metrology laser leads us to believe that a drift of such magnitude is very unlikely.

In our opinion, a more likely explanation of the measured displacement error is a drift of some component of the NBS interferometer system. The metrology laser used for the November, 1984 measurements was frequency calibrated approximately one week prior to the start of field testing, so that we

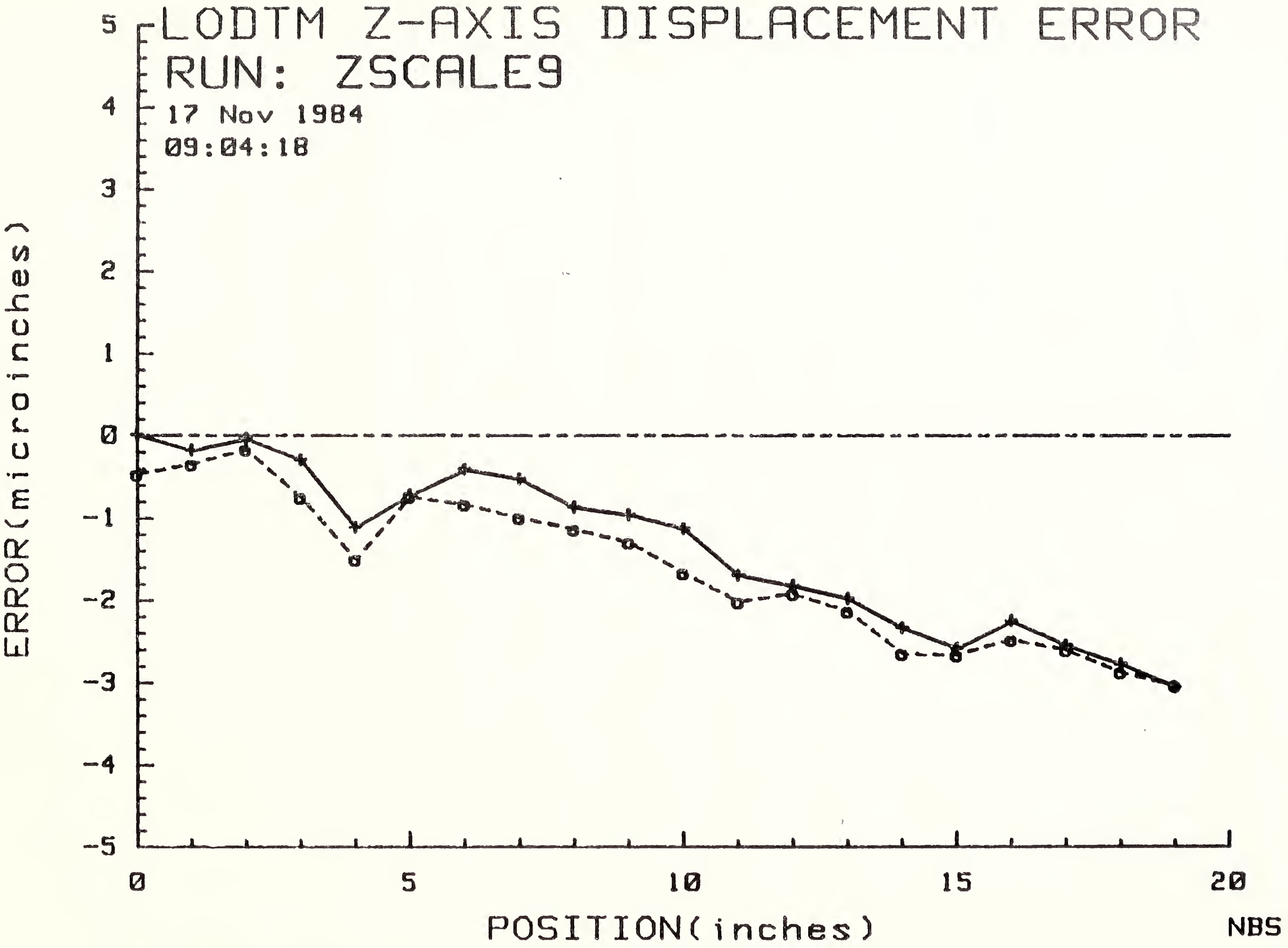
LODTM Z-AXIS DISPLACEMENT ERROR
RUN: ZSCALE9
17 Nov 1984
09:04:18
ERROR(microinches)
5
4
3
2
1
0
-1
-2
-3
-4
-5
0
5
10
15
20
POSITION(inches)
NBS

Figure 16

suspect a drift in calibration of one of the systems employed for the determination of the refractive index of air. During this period we noted in particular that the dewpoint hygrometer indicated that the relative humidity within the LODTM machine enclosure was fluctuating erratically between 40% and 60% RH which was 10-15% higher than we observed during January-February, 1984. An error of this magnitude (and direction) in relative humidity measurement would be sufficient to explain the observed systematic Z-axis displacement error.

In summary, we believe that the LODTM control system provides a Z-axis displacement error of less than 1 part in 10^7 of the commanded position. In addition we feel that any future long-distance displacement measurements using the NBS interferometer system be preceded by re-calibrations at NBS of the environmental transducers used for determination of the refractive index of air.

Following the Z-axis scale error measurement just described, we re-measured the Z-axis pitch error using a cube corner reflector offset 10 inches South of the tool bar centerline. These measurements were performed with the tool bar air bearing supply line heaters at 50% of maximum power, and no attempt was made to correct the data for thermal drift and/or hysteresis. In attempting to understand this thermal behavior, the pitch error was measured several times. Figure (17) displays the results of a typical run in this series (ZSCALE12). The thermal hysteresis of 2-3 microinch amplitude is clearly seen in this data, in addition to a systematic residual pitch error motion. The apparent angular motion of the tool bar is seen to be a gradual

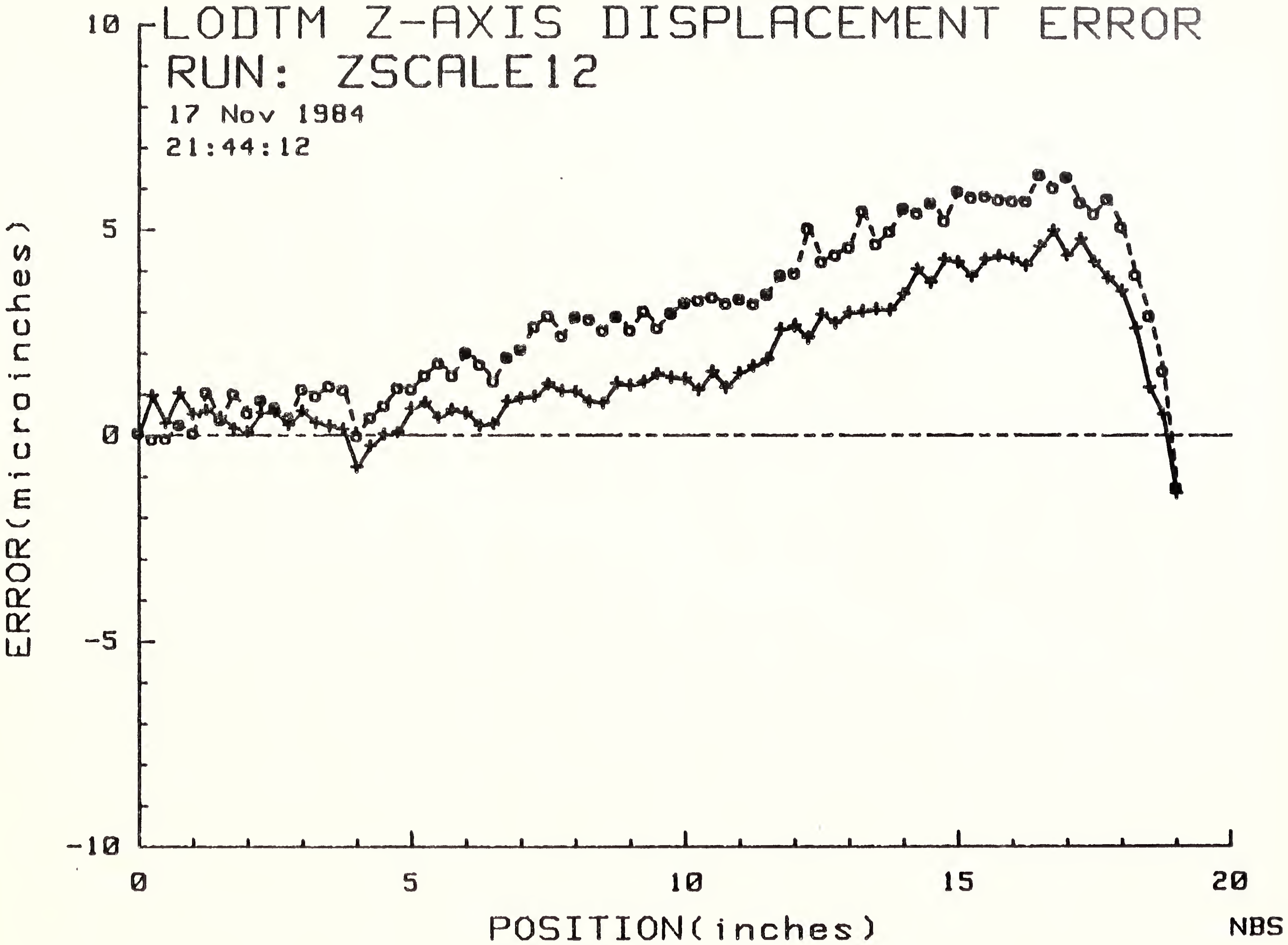
LODTM Z-AXIS DISPLACEMENT ERROR
RUN: ZSCALE12
17 Nov 1984
21:44:12
ERROR(microinches)
10
5
0
-5
-10
0
5
10
15
20
POSITION(inches)
NBS

Figure 17

counter-clockwise (viewed from the West) rotation for about 17 inches of upward Z-travel, followed by a rather abrupt clockwise rotation between 17 inches and 19 inches of travel. This latter behavior was not observed during our January-February, 1984 measurements--the reason for the change in apparent pitch motion is not known.

Because of the thermal hysteresis and our inability to model it, we proceeded to do a simple linear correction for the effects of Z-axis pitch, using the 0-17-inch portion of Fig.(17). We estimated this linear correction from a basic "eyeball" fit to the data, with the goal of making the observed pitch error agree with the linear displacement error measured on-axis [Fig. (16)]. The result of this procedure was to add to the existing linear term in the Z-axis lookup table an amount equal to 0.88 μradians of pitch in 20 inches of travel.

The Z-axis pitch was then re-measured, resulting in Fig.(18) (ZSCALE14). A comparison of Figs.(16) and (18) indicates that the new linear term in the Z-axis lookup table is now slightly too large, but the pronounced thermal hysteresis remaining in the pitch data precludes any meaningful re-adjustment. We emphasize that these measurements employed a 10" lever arm coupling the Z-axis pitch motion to the observed displacement errors. In normal machining operations on LODTM, typical tool offsets are 5 inches or less; under these conditions we conclude that Z-axis positioning errors due to angular motion of the tool bar during Z motion would be dominated by thermal hysteresis errors (except perhaps for the upper 3 inches of travel). If these errors were eliminated so that the positioning errors became

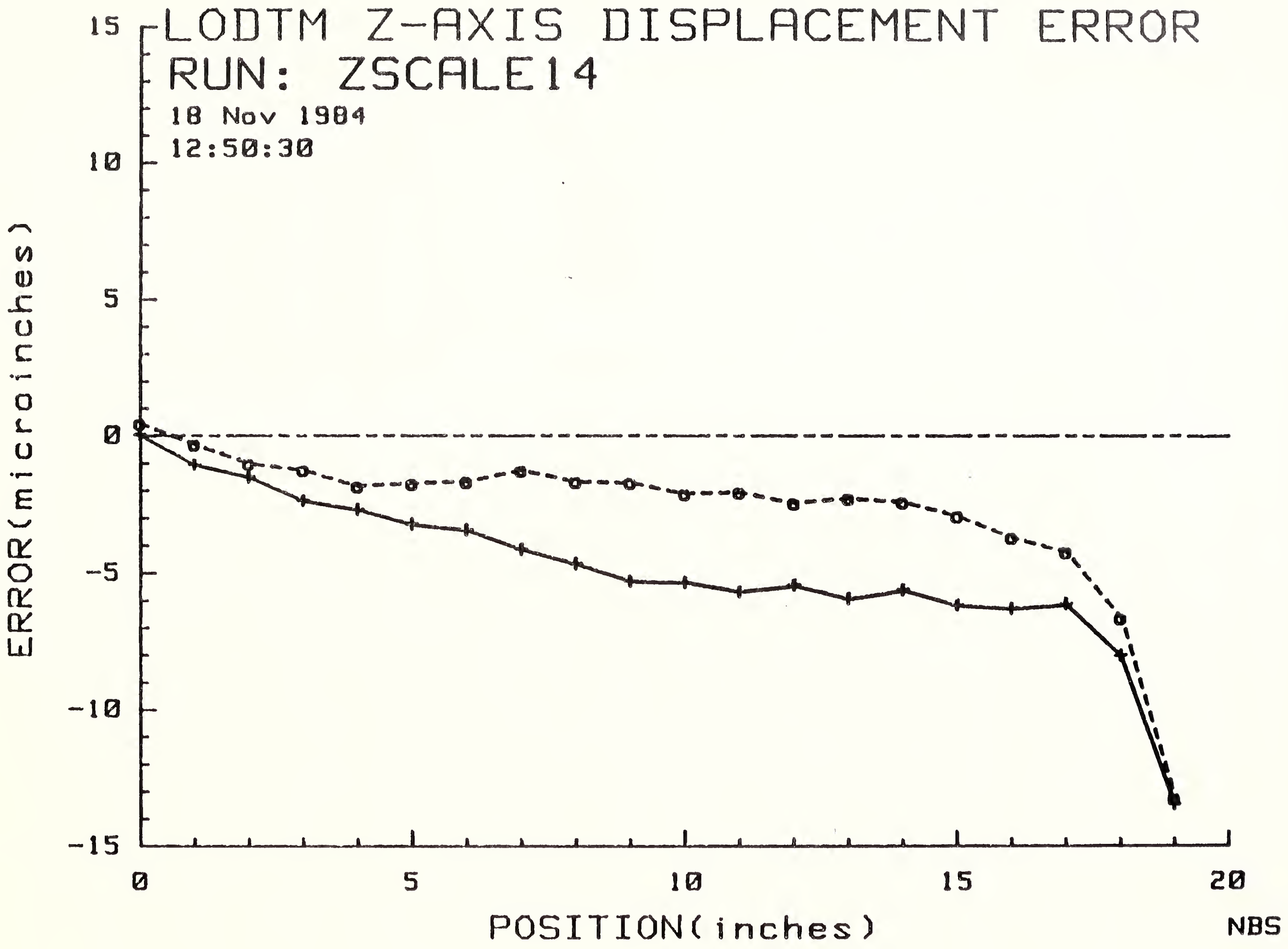
LODTM Z-AXIS DISPLACEMENT ERROR
RUN: ZSCALE14
18 Nov 1984
12:50:30
ERROR(microinches)
15
10
5
0
-5
-10
-15
0
5
10
15
20
POSITION(inches)
NBS

Figure 18

repeatable, it would be possible via parametric curve fitting and a more sophisticated lookup table to reduce pitch-related errors to a level within 1 part in 10^7 of the range of Z-axis travel.

7. Slide Straightness Errors

Because LODTM is a 2-axis machine tool, it is only necessary to measure straightness error motions in the X-Z plane. Transverse errors in the Y direction are tangent to the surface of the workpiece and cause negligible (i.e., second order) figure errors. The relevant sensitive errors on LODTM are $\delta_z(X)$, the Z (or vertical) straightness of the X-axis and $\delta_x(Z)$, the X (or horizontal) straightness of the Z-axis. In the design of the machine, these errors are sensed by laser interferometers sampling glass straightedges which act as reference surfaces. For $\delta_z(X)$, the reference straightedges are mounted on the metrology frame, while for $\delta_x(Z)$ they are kinematically attached to opposite sides of the tool bar.

Each of the LODTM straightness errors was measured in an iterative manner. That is, we first measured the error with no real-time software correction, used the resultant "map" of the figure error of the reference surfaces to fill a correction lookup table, and then re-measured the error as a check on the software correction algorithm.

7.A. Z-Straightness of the X-axis. [$\delta_z(X)$]

The Z-straightness of the X-axis, or vertical straightness, was measured over 40 inches of X-axis travel. The straightness reference for these measurements was a spare 2 inches x 6 inches x 45.5 inches glass straightedge from LODTM, which was calibrated at NBS prior to field validation. This reference surface was sampled using the NBS interferometer in the plane-mirror mode. We used an analytic computational algorithm to correct our data for errors due to gravitational sag of the reference surface. The calibration of this artifact and the procedure used for vertical straightness measurement are described in detail in Appendix C.

Following the notation of Appendix C, experimental straightness data consists of a set of displacements $d(X,\alpha)$ measured by the interferometer system at a number of positions X. The parameter α is the ratio of support separation to the length of the straightedge; for these measurements α has the fixed value of 0.538. The experimental data is related to the machine error motion $\delta_z(X)$, the calibrated shape of the reference straightedge $S(X)$, and the gravitationally-induced deformation $G(X,\alpha)$ by the relation

$$d(X,\alpha)=\delta_z(X)-S(X)-G(X,\alpha). \qquad (1)$$

The sign conventions for the quantities in Eq.(1) are the same as those introduced in Appendix C, with the exception of the machine error $\delta_z(X)$ which is taken to be positive for <u>upward</u> motion of the LODTM tool bar.

Rearrangement of Eq.(1) yields the desired error in terms of measured and computed quantities:

$$\delta_z(X)=d(X,\alpha)+S(X)+G(X,\alpha). \qquad (2)$$

Figure (19) displays the measured vertical straightness error $\delta_z(X)$ of LODTM as measured in November, 1984. In this run, the lookup table associated with the horizontal reference straightedges of LODTM was filled with zeros, so that Fig.(19) is effectively a map of the average deviation from ideal straightness of these two artifacts. We believe that the noise and associated lack of bi-directional repeatability evident in this data was caused by vertical oscillations of the fixture used to attach the interferometer to the LODTM tool bar. These oscillations were presumably excited by the 2-3 microinch, 100Hz X-axis vibration of the tool bar.

The dashed curve in Fig.(19) represents a 5-parameter polynomial fit to the experimental data. The form of the fitting function is

$$[\delta_z(X)]_{fit} = a_0 + \sum_{i=1}^{4} a_i X^i, \qquad (3)$$

with the coefficients $a_0,\ldots,a_4$ determined by a polynomial regression algorithm. The fitted straightness function corresponds to the parameter set

$a_0 = 0.088$

$a_1 = 0.620$

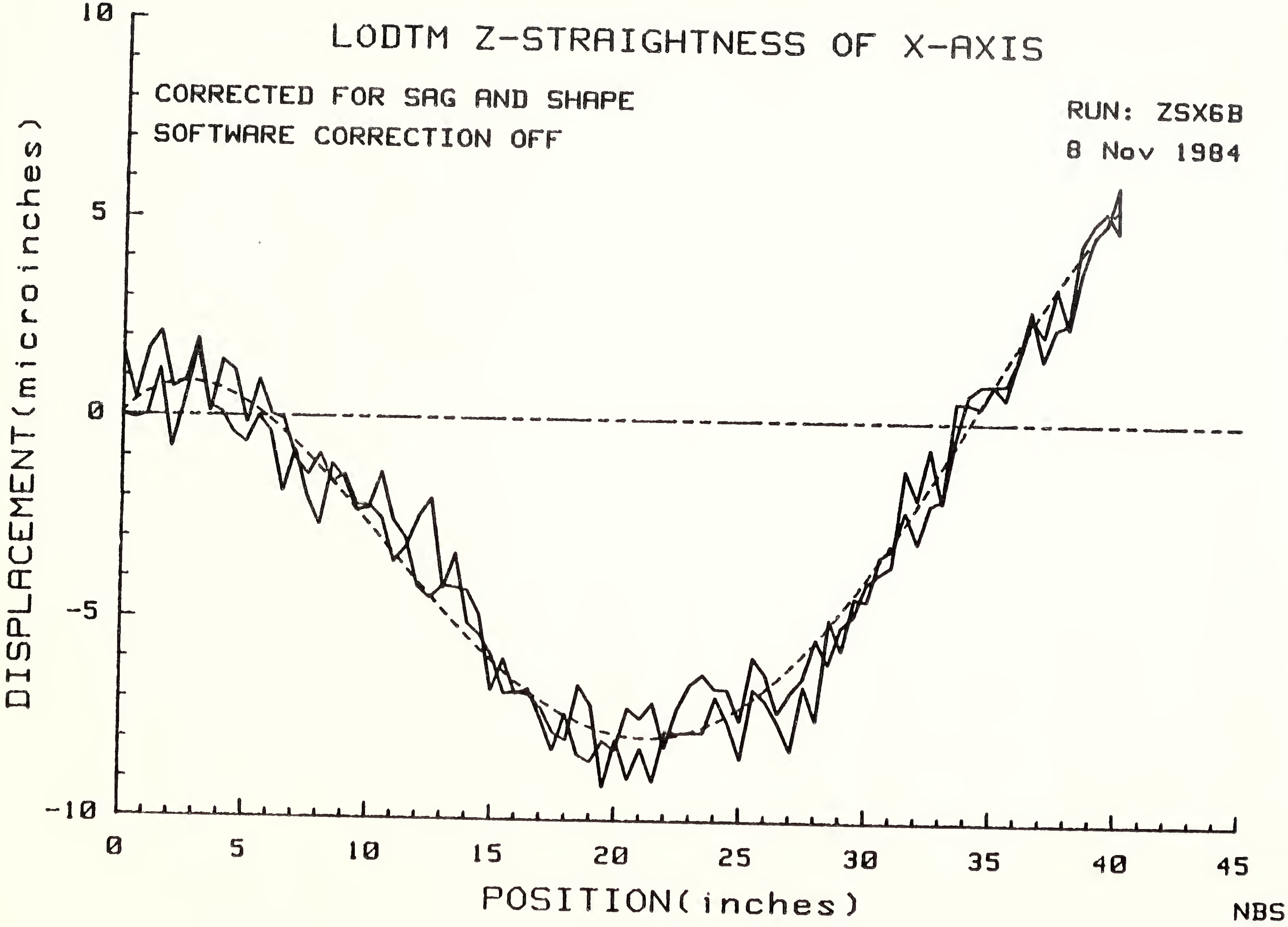
LODTM Z-STRAIGHTNESS OF X-AXIS
CORRECTED FOR SAG AND SHAPE
SOFTWARE CORRECTION OFF
RUN: ZSX6B
8 Nov 1984
DISPLACEMENT(microinches)
10
5
0
-5
-10
0
5
10
15
20
25
30
35
40
45
POSITION(inches)
NBS

Figure 19

$$a_2 = -0.1409 \qquad (4)$$

$$a_3 = 5.784 \times 10^{-3}$$

$$a_4 = -6.414 \times 10^{-5}.$$

We then proceeded to modify the LODTM correction software, using Eq.(3) and the parameter set, Eqs.(4), to generate the 1000 entries in the X-axis straightness lookup table. Following this modification we re-measured the vertical straightness, software corrected, obtaining the results shown in Fig.(20). Apart from vibrationally-induced measurement noise, it is seen that $\delta_z(X)$ has been reduced to an error of about ±2 microinches (4 μin. P-V). As we discuss in Appendix C, this error range represents the confidence limits of the analytical technique used to compute straightedge gravitational sag. Thus, as in the case of the scale errors, the vertical straightness error of the LODTM tool bar is now within the limits imposed by the measurement system.

7.B. <u>X-Straightness of the Z-axis</u>. [$\delta_x(Z)$]

The X-straightness of the Z-axis was measured over 19 inches of Z-axis travel. The straightness reference for these measurements was a 3-inch diameter precision cylindrical square approximately 20 inches in length. This artifact was mounted upon a 2-axis tilt plate, used for angular adjustments, and was centered and aligned so that its axis was very nearly collinear with the LODTM spindle axis.

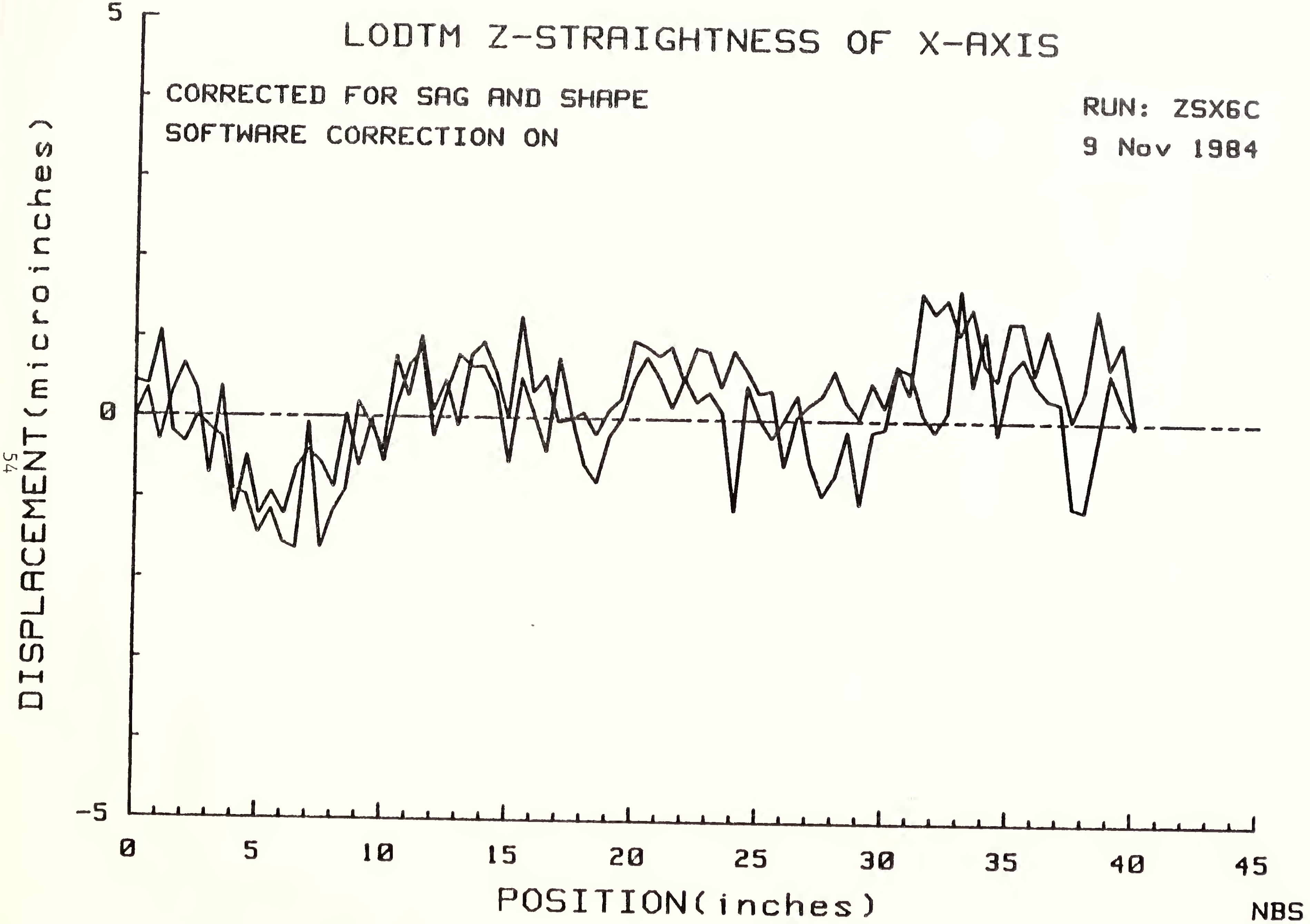LODTM Z-STRAIGHTNESS OF X-AXIS
CORRECTED FOR SAG AND SHAPE
SOFTWARE CORRECTION ON
RUN: ZSX6C
9 Nov 1984
DISPLACEMENT(microinches)
5
0
-5
0
5
10
15
20
25
30
35
40
45
POSITION(inches)
NBS

Figure 20

Horizontal (X-direction) motions of the LODTM tool bar with respect to this vertical reference artifact were measured with two NBS-designed capacitance gauges. These gauges have a cylindrical geometry, with bodies constructed of Invar in order to minimize output drift due to thermally-induced dimensional changes. The gauges were mounted to the tool bar face plate in such a way as to sample two diametrically-opposed reference lines on the gauging surface of the cylindrical square. The mounting fixture was also fabricated from Invar. A diagram of the measurement setup is shown in Fig. (21).

As discussed in Appendix C, data obtained in straightness measurements generally consists of the desired information superimposed upon a linear term due to setup and/or alignment errors. As we explain later in this section, the slopes of the linear terms in our horizontal straightness measurements may be analyzed to obtain interesting information about the parallelism of the LODTM Z-axis to the spindle rotation axis (in the static sense), and about the taper of the reference cylindrical square. For the present, however, in order to describe the straightness measurement technique, we assume that best-fit least-squares straight lines have been removed from the data.

It is necessary to adopt a sign convention for the X-straightness of Z-axis error function, $\delta_X(Z)$. We choose the following:

$$\delta_X(Z) = \begin{cases} +\text{, for motion of the tool bar to the } \underline{\text{SOUTH}} \\ \\ -\text{, for motion } \underline{\text{NORTH}} \end{cases} \qquad (5)$$

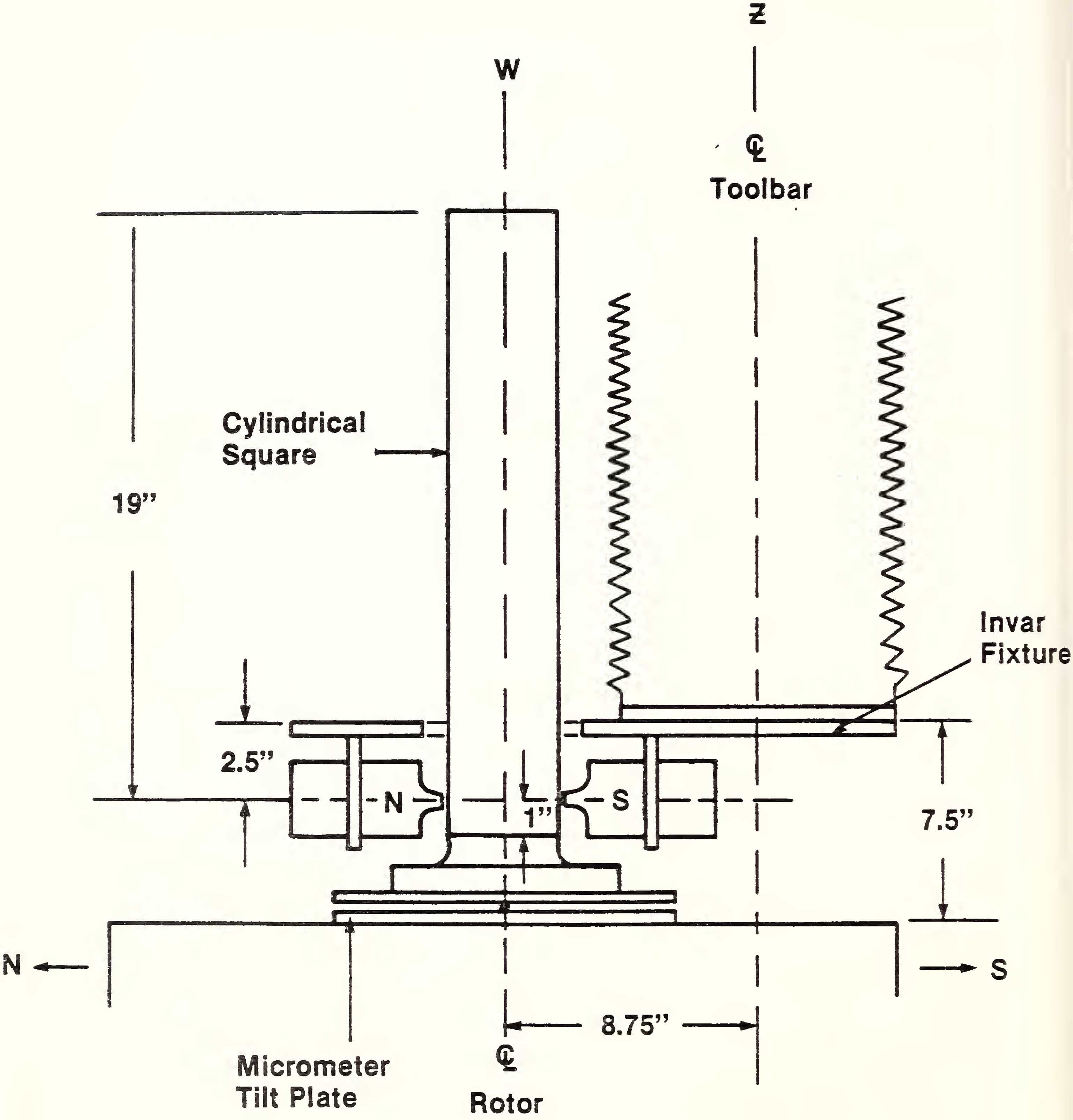
Z
W
℄
Toolbar
Cylindrical Square
19"
2.5"
N
S
1"
7.5"
Invar Fixture
N
S
8.75"
Micrometer Tilt Plate
℄
Rotor

Figure 21

Of course, when measuring straightness errors with reference artifacts it is always necessary to consider the deviations of the reference surfaces from ideal straightness. In this type of measurement it is usually possible to separate artifact errors from the errors of interest by re-orienting, or "reversing" the artifact (see Appendix C); this is the procedure followed in these measurements. The two capacitance gauges were first transported along the cylindrical square, with the latter in what is arbitrarily called the "FORWARD" orientation, and the gauge displacements recorded. The spindle was then rotated 180°, placing the cylindrical square in the "REVERSE" orientation, and a new set of displacements recorded. Accurate indexing was assured by monitoring the rotation with the 36,000 counts/revolution LODTM spindle encoder. These two sets of displacements were then used to extract $\delta_x(Z)$ and cylindrical square error as we now describe.

There are two straightness functions $C_1(Z)$ and $C_2(Z)$ which characterize the two measurement lines along the cylindrical square. By convention we associate $C_1(Z)$ with the surface sampled by the <u>South</u> capacitance gauge in the <u>Forward</u> orientation. In the <u>Reverse</u> orientation, $C_1(Z)$ is sampled by the <u>North</u> gauge. $C_2(Z)$, of course, refers to the line diametrically opposed to $C_1(Z)$, and is always sampled by the opposite gauge. By arbitrary choice, the sign conventions for these functions are

$$C_1(Z), C_2(Z) = \begin{cases} +, & \text{radially outward displacements} \\ -, & \text{radially inward displacements} \end{cases} \qquad (6)$$

The capacitance gauges respond to changes in the small (2-3 mils) gaps between their active electrodes and the conducting surfaces. Displacement data is measured relative to a zero at the start of the measurements, with the tool bar near its lower limit of travel, and is derived from measured output voltages via calibration factors for each gauge. The gauges were periodically calibrated in situ by manually stepping the LODTM tool bar in the X-direction by known amounts, using the machine's own very accurate length scales. Typical sensitivities for these gauges was 2-3 mV/microinch.

Measured displacement functions are labelled by a 2-letter descriptor, with the first letter (N or S) denoting the North or South gauge and the second letter (F or R) denoting the cylindrical square orientation (Forward or Reverse). The sign conventions are chosen so that motions of the tool bar cause identical changes in the displacement function of each gauge. This requires changing one of the gauge "polarities" in the analysis software since if the tool bar should move North or South, one gauge would get closer to the cylindrical square while the other got farther away. These sign conventions may be summarized by

$$SF(Z), NF(Z) = \begin{cases} +, & \text{tool bar motion NORTH} \\ -, & \text{tool bar motion SOUTH} \end{cases} \quad . \tag{7}$$

With these conventions, the "FORWARD" data yields the displacements

$$SF(Z) = C_1(Z) - \delta_x(Z) \tag{8}$$

$$NF(Z)=-C_2(Z)-\delta_X(Z) \tag{9}$$

while the corresponding functions for the "REVERSE" data are

$$SR(Z)=C_2(Z)-\delta_X(Z) \tag{10}$$

$$NR(Z)=-C_1(Z)-\delta_X(Z). \tag{11}$$

Equations (8-11) illustrate an interesting consequence of the use of two opposed gauges for these measurements: since there are four relations among three unknown functions, we achieve a redundant measurement of the machine error. This prrovides a useful consistency check on the data. Thus from Eqs. (9 and 10) and Eqs. (8 and 11) we have:

$$\delta_X(Z) = -\frac{1}{2}[NF(Z)+SR(Z)] \tag{12a}$$

$$= -\frac{1}{2}[SF(Z)+NR(Z)]. \tag{12b}$$

Of course, the reversal process also permits the calibration of the reference artifact, and in this case we have two such calibrations. From Eqs. (8 and 11), we have

$$C_1(Z) = \frac{1}{2}[SF(Z)-NR(Z)], \tag{13}$$

while Eqs. (9 and 10) yield

$$C_2(Z) = \frac{1}{2}[SR(Z)-NF(Z)]. \qquad (14)$$

The horizontal straightness error $\delta_x(Z)$ was measured over 12 inches of Z-axis travel during January-February, 1984, and re-measured over 19 inches of travel during November, 1984. We will concentrate in this report upon the latter measurements - the earlier ones were performed using only one capacitance gauge and were plagued by very severe thermal hysteresis.

Figures (22) and (23) display two redundant measurements of $\delta_x(Z)$ taken at 1-inch increments in both directions of Z-axis motion (i.e. "out and back"). The two measurements of Figs. (22) and (23) correspond to calculations via Eqs. (12a) and (12b), respectively. Data consistency is seen to be excellent, in the sense that if the two curves are superimposed they agree with each other within 0.5 microinch or so over the full range of motion. Also evident from the straightness data is a systematic non-repeatability related, we believe, to the thermal interactions of the air bearing pads with the tool bar structure. The air line heaters were operating at 50% of full power during this period, and no attempt was made to correct the data.

The straightness data of Figs. (22) and (23) shows a systematic motion of the tool bar to the North and then back to the South as the tool bar moves up. Similar, nearly parabolic behavior was observed over 12 inches of travel in our previous validation period, and that data was used by the

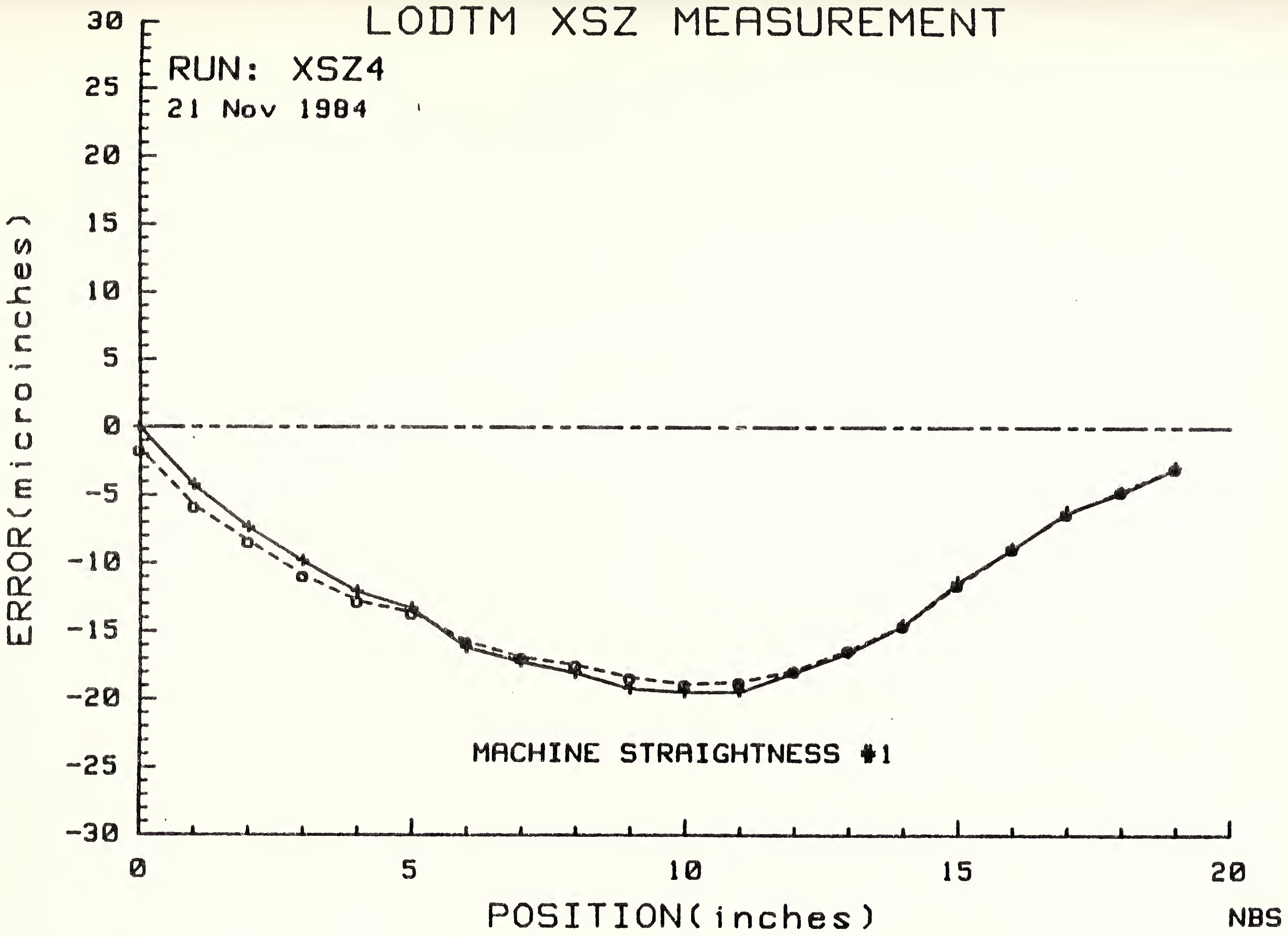
LODTM XSZ MEASUREMENT
RUN: XSZ4
21 Nov 1984
ERROR(microinches)
30
25
20
15
10
5
0
-5
-10
-15
-20
-25
-30
MACHINE STRAIGHTNESS #1
0
5
10
15
20
POSITION(inches)
NBS

Figure 22

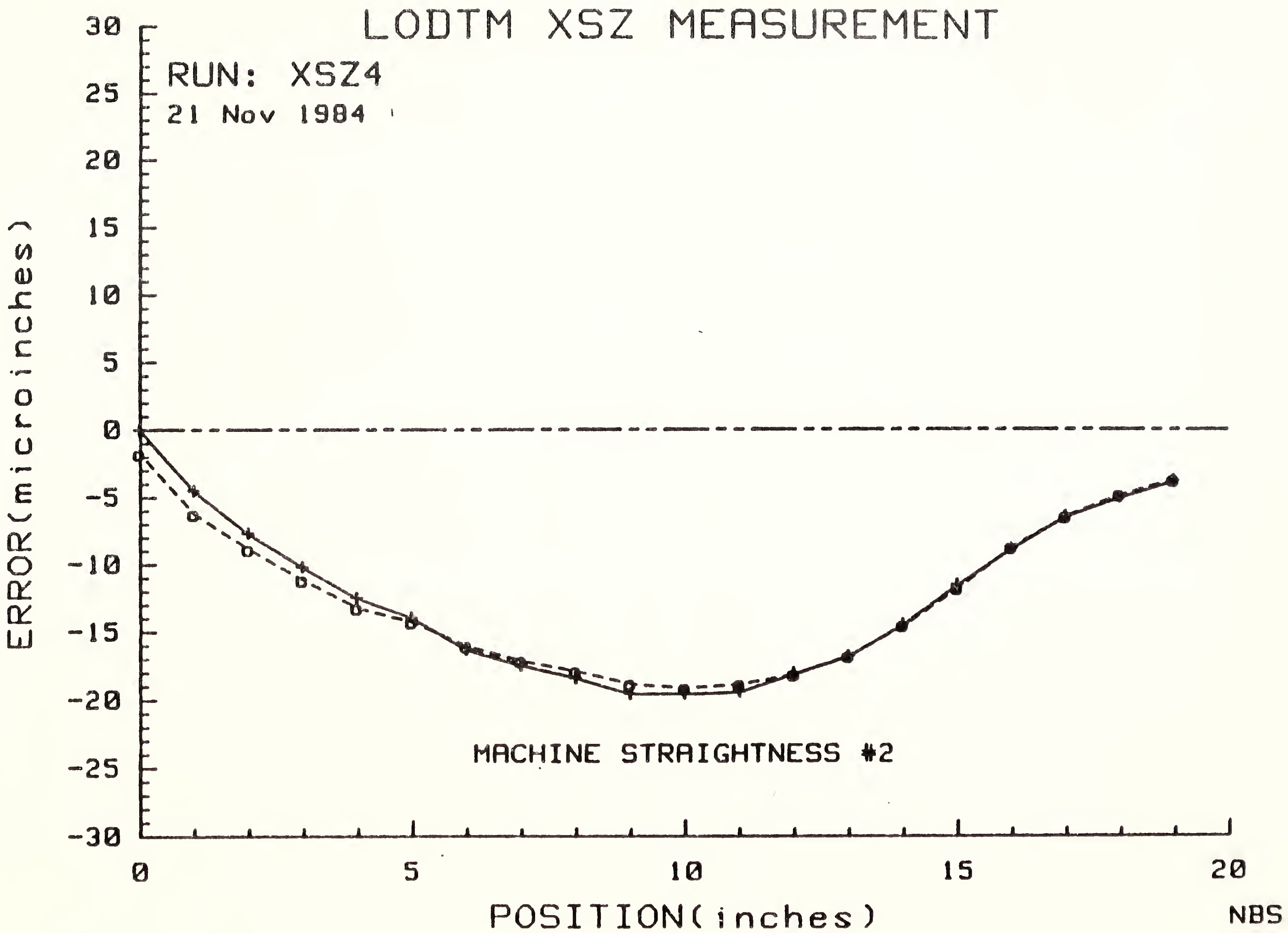
LODTM XSZ MEASUREMENT
RUN: XSZ4
21 Nov 1984
ERROR(microinches)
30
25
20
15
10
5
0
-5
-10
-15
-20
-25
-30
MACHINE STRAIGHTNESS #2
0
5
10
15
20
POSITION(inches)
NBS

Figure 23

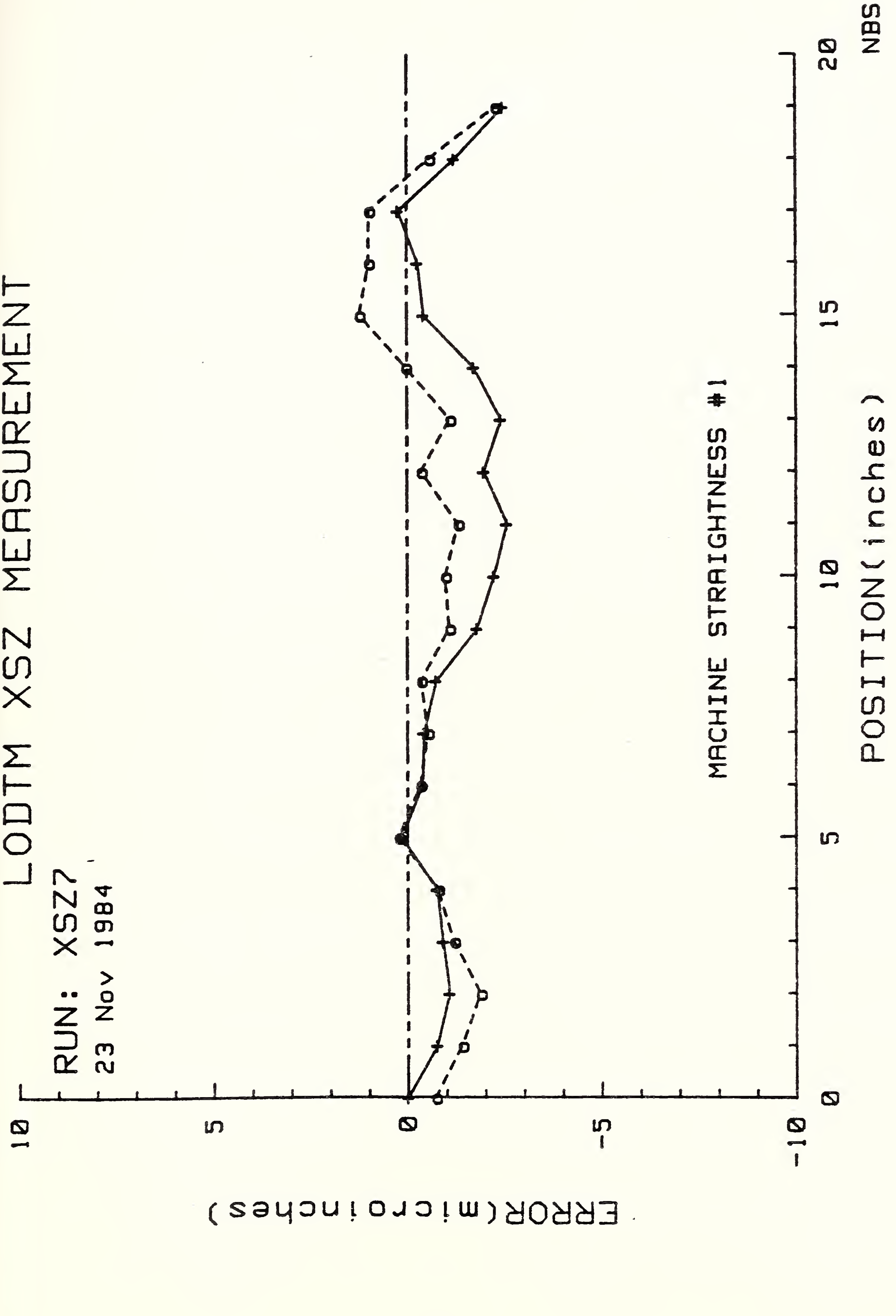
LODTM XSZ MEASUREMENT
RUN: XSZ7
23 Nov 1984
MACHINE STRAIGHTNESS #1
ERROR(microinches)
POSITION(inches)
10
5
0
-5
-10
0
5
10
15
20
NBS

Figure 24

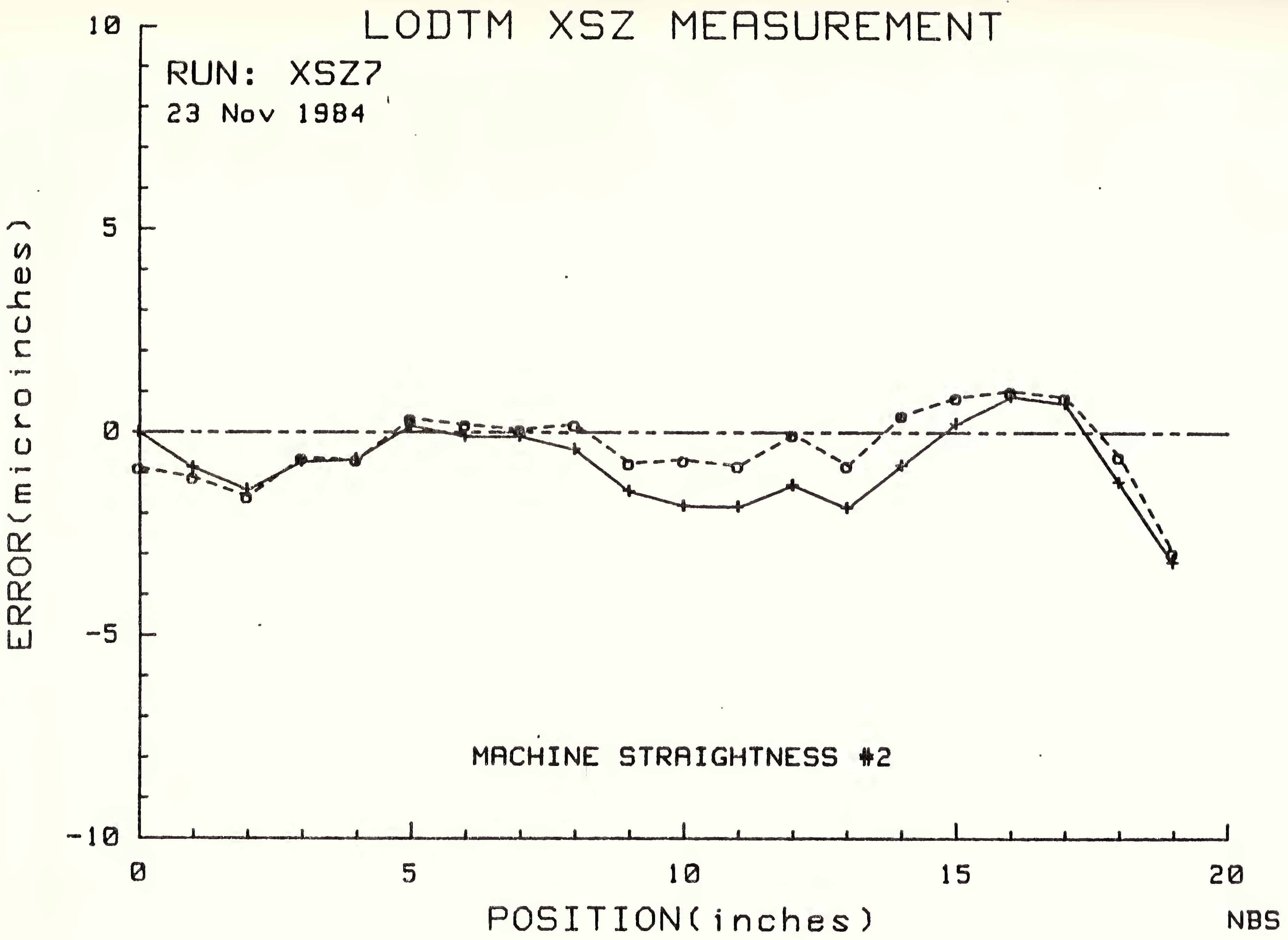
LODTM XSZ MEASUREMENT
RUN: XSZ7
23 Nov 1984
ERROR(microinches)
10
5
0
-5
-10
MACHINE STRAIGHTNESS #2
0
5
10
15
20
POSITION(inches)
NBS

Figure 25

attempt any more sophisticated software correction, so that Eq. (16) represents the $\delta_X(Z)$ correction lookup table currently implemented on LODTM.

Figures (26) and (27) display the straightness errors $C_1(Z)$ and $C_2(Z)$ of the two gauging lines sampled on the cylindrical square, computed from the data using Eqs. (13) and (14). A comparison of these figures shows this artifact to be very nearly an ideal surface of revolution. The difference in error for any particular value of Z is an estimate of the roundness error of the cylinder at that cross-section, and is on the order of 3-5 microinches or better anywhere along the gauging surface. This artifact was left at LODTM as part of the metrology system delivered by NBS, and these two surfaces have been marked on the base of the square so that it may be used in future measurements without re-calibration along these surfaces.

We now turn to a discussion of the slopes of the least-squares lines fit to the $\delta_X(Z)$ data, and the static determination of the parallelism error between the LODTM spindle rotation axis and the line of motion of the Z-axis. The relevant geometry is shown schematically in Fig. (28). In this figure, the dashed line W is the spindle axis which makes an angle α with the Z-axis when projected onto the X-Z plane. [Note: this projection operation is permissible since out-of-plane motions cause only second-order errors.] Lines C_1 and C_2 represent the two gauging surfaces of the cylindrical square, and the included angle γ between them is the taper angle of the square. The two capacitance gauges (not shown in the figure) are arranged so as to straddle the cylindrical square, and are transported along the line of the Z-axis. The top illustration (a) shows the "FORWARD" measurement

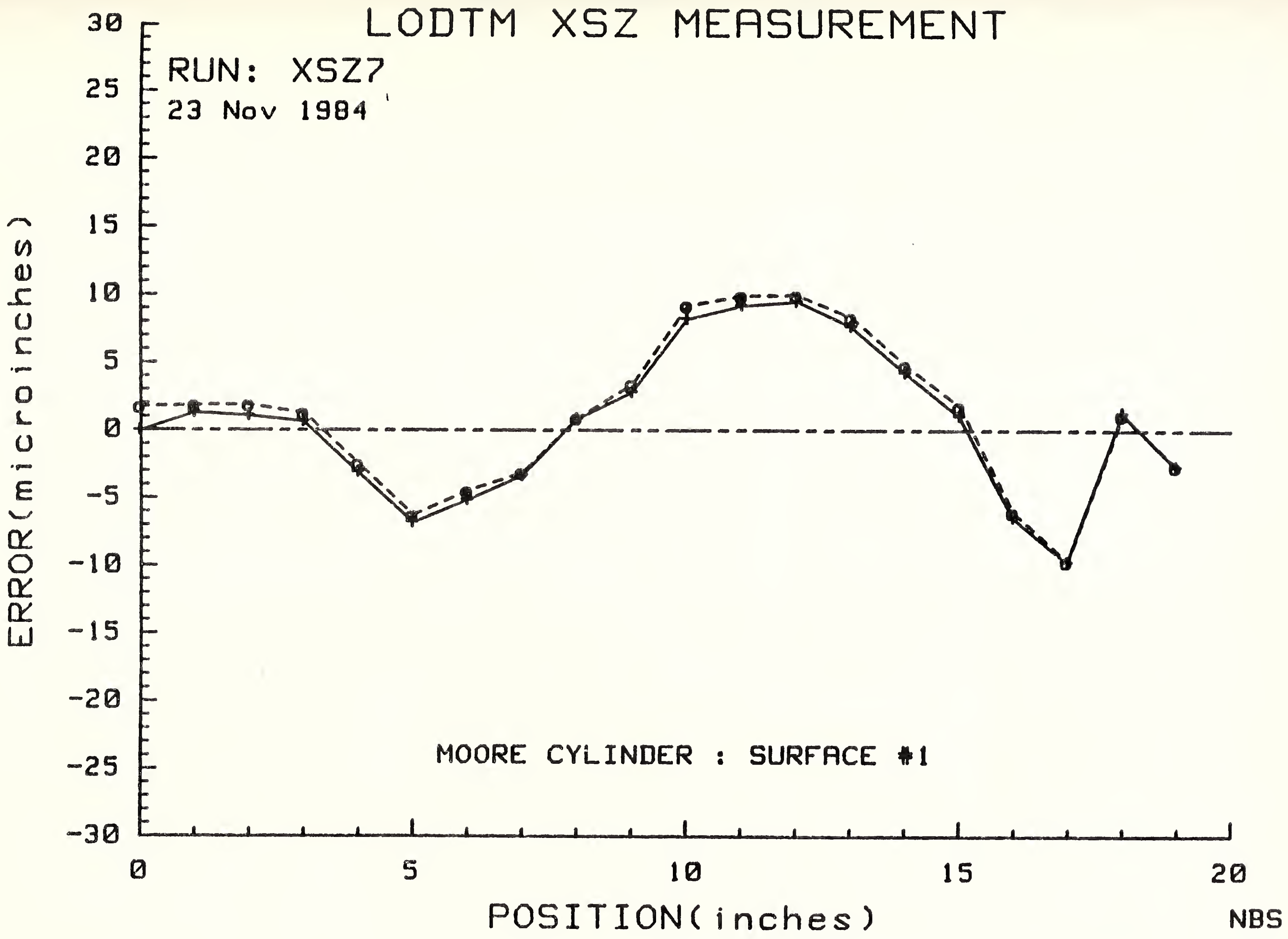
LODTM XSZ MEASUREMENT
RUN: XSZ7
23 Nov 1984
30
25
20
15
10
5
0
-5
-10
-15
-20
-25
-30
ERROR(microinches)
MOORE CYLINDER : SURFACE #1
0
5
10
15
20
POSITION(inches)
NBS

Figure 26

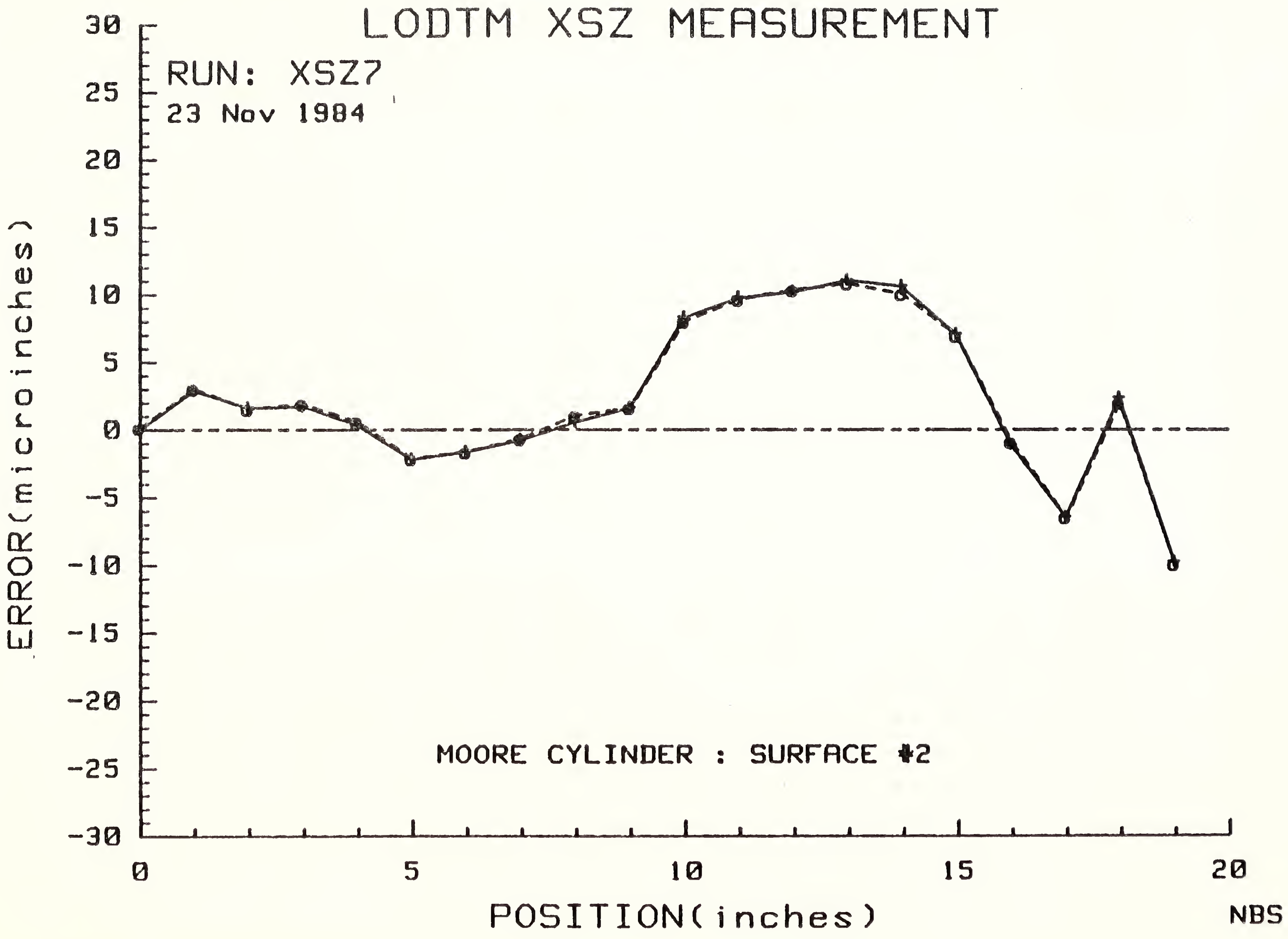
LODTM XSZ MEASUREMENT
RUN: XSZ7
23 Nov 1984
MOORE CYLINDER : SURFACE #2
ERROR(microinches)
30
25
20
15
10
5
0
-5
-10
-15
-20
-25
-30
0
5
10
15
20
POSITION(inches)
NBS

Figure 27

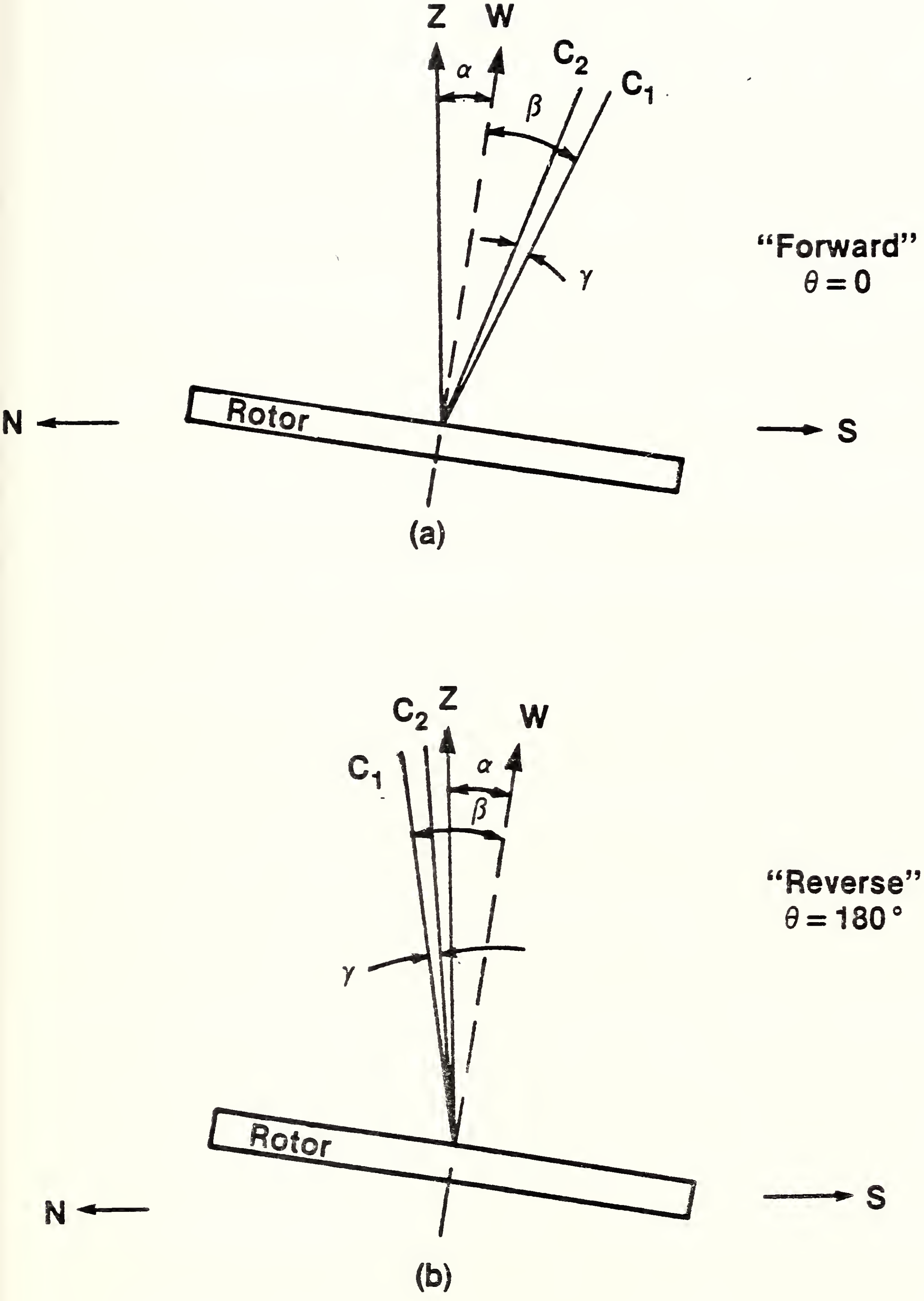
Z
W
α
C$_2$
C$_1$
β
γ
"Forward"
θ = 0
N
Rotor
S
(a)
C$_2$
Z
W
C$_1$
α
β
"Reverse"
θ = 180°
γ
Rotor
N
S
(b)

Figure 28

setup, with the rotor in an arbitrary angular position, $\theta=0$. The bottom illustration (b) shows the re-oriented "REVERSE" setup, achieved by a 180° spindle rotation. All angles in Fig. (28) are highly exaggerated for clarity.

In each measurement, the slope of the recorded data is a measure of the angle between the LODTM Z-axis and the particular sampled surface. Angle β, as shown, is defined as the angle between the spindle axis (W) and measurement line C_1. We denote the measured slopes by, for example, ϕ_{SF}, which is the slope of the SOUTH capacitance gauge data in the FORWARD orientation and so on for the rest of the data. With this convention, the angular relations may be written from an examination of Fig. (28):

$$\phi_{SF} = \alpha + \beta \tag{17}$$

$$\phi_{NF} = \alpha + \beta - \gamma \tag{18}$$

$$\phi_{SR} = \alpha - \beta + \gamma \tag{19}$$

$$\phi_{NR} = \alpha - \beta. \tag{20}$$

The angle β is determined by the setup alignment, and is of no concern here. From the relations (17-20) we have, for the cylindrical square taper:

$$\gamma = \phi_{SF} - \phi_{NF} \tag{21a}$$

$$= \phi_{SR} - \phi_{NR}, \tag{21b}$$

and for the static Z-W parallelism error:

$$\alpha = \frac{1}{2}(\phi_{SF} + \phi_{NR}) \tag{22a}$$

$$= \frac{1}{2}(\phi_{NF} + \phi_{SR}). \tag{22b}$$

During the November, 1984 validation period, in the process of developing the proper straightness correction algorithm, we measured $\delta_x(Z)$ three times, resulting in three complete realizations of the set of angular relations (17-20) from least-squares fits to the data. Using Eqs.(21) and (22), we compute the following values for γ and α:

$$\gamma = -1.96 \pm 0.10 \text{ microradians} \tag{23}$$

$$\alpha = 5.30 \pm 0.22 \text{ microradians} \tag{24}$$

We make two observations regarding these results. First, with respect to the cylindrical square taper angle γ, the negative sign indicates a taper of the opposite sense to that depicted in Fig. (28). That is, the figure of the cylindrical gauging surface is such that its mean diameter decreases with increasing distance from the base. The rate of decrease, given by Eq. (23), is about 2 microinches/inch, so that the lower end of the gauging surface is approximately 40 microinches larger in diameter than the upper end.

Second, measured Z-W parallelism error α is a large error for a high-precision machine such as LODTM, amounting as it does to more than 1 arc-second. Of course the linear error in X position with Z motion caused by such an axis alignment error could be removed by a suitable linear term in the Z-axis lookup table. We had reason, however, to expect that α would be very nearly zero, based upon our previous measurements of axis geometry. We will discuss this discrepancy in the next section.

8. Axis Geometry

There are three relevant lines in space, or axes, which characterize LODTM. These are the spindle rotation axis, denoted W, and the X and Y axes of tool bar motion. Ideally these lines would be coplanar, with W parallel to Z and the X-axis perpendicular to both Z and W. In order to assess axis alignment, it is therefore necessary to measure three angular errors: X-W squareness error, X-Z squareness error, and Z-W parallelism error. Since motions of the tool point in the Y-direction cause only second-order positioning errors in the sensitive direction and since the actual angular errors are small, we need consider only the projections of these errors onto the X-Z plane. The resultant practical axis geometry is shown schematically in Fig. (29), where it is seen that only two of the angular errors are independent. Thus, for example, if the X-W squareness error ω and the X-Z

LODTM Axis Geometry

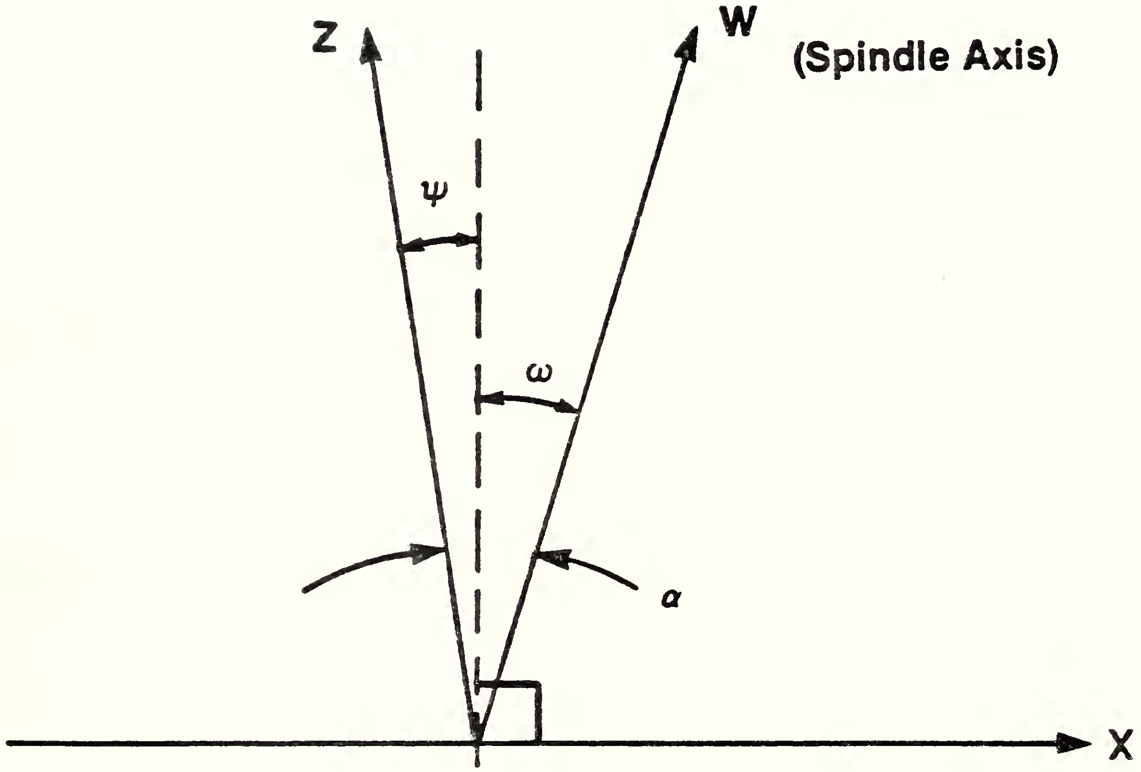

α = Z – W Parallelism Error
ω = X – W Squareness Error
ψ = X – Z Squareness Error

Figure 29

squareness error ψ are measured, then the Z-W parallelism error may be computed: $\alpha = \omega+\psi$. This relation is strictly valid only if the X-W squareness error is measured with the spindle rotating, but for a massive rotor such as that of LODTM we expect that a large change in axis direction with spindle speed would be unlikely. Fortunately, we were able to measure α independently during our measurements of spindle errors, so that the relationship above may be viewed as a useful consistency check.

8.A. X-W Squareness Error

The squareness error ω between the X-axis slide and the spindle axis was measured by a technique suggested by R. Donaldson of LLNL. The measurement apparatus was identical to that used for our $\delta_z(X)$ metrology (see Sec.7.A.), consisting of the NBS interferometer system sampling the calibrated LLNL straightedge. The principle of the technique is illustrated in Fig.(30). The straightedge was mounted so as to straddle the spindle center and the change in separation between the gauging surface and the interferometer was recorded as the interferometer was transported in the X-direction. A least-squares fit to the data yields a line whose slope is equal to the angle between the X-axis and the straightedge gauging surface. The actual squareness determination requires two such measurements, with a "reversal" to remove setup error. Fig.(30a) depicts an arbitrary "FORWARD" orientation of the straightedge, with the spindle at $\Theta=0$, and Fig.(30b) shows the "REVERSE" orientation achieved by a 180° spindle rotation. Angle β is the squareness error between the straightedge and the spindle axis resulting from the

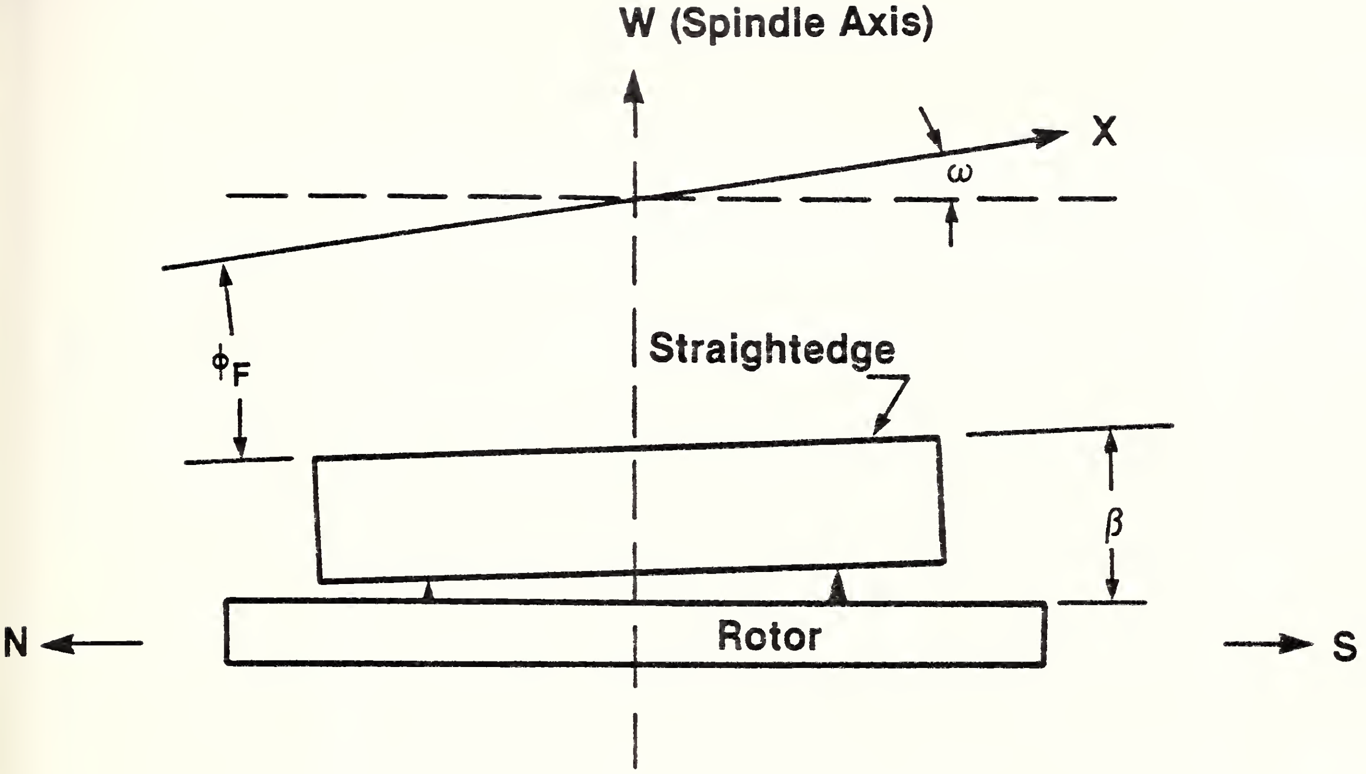

"Forward", $\theta = 0$

(a)

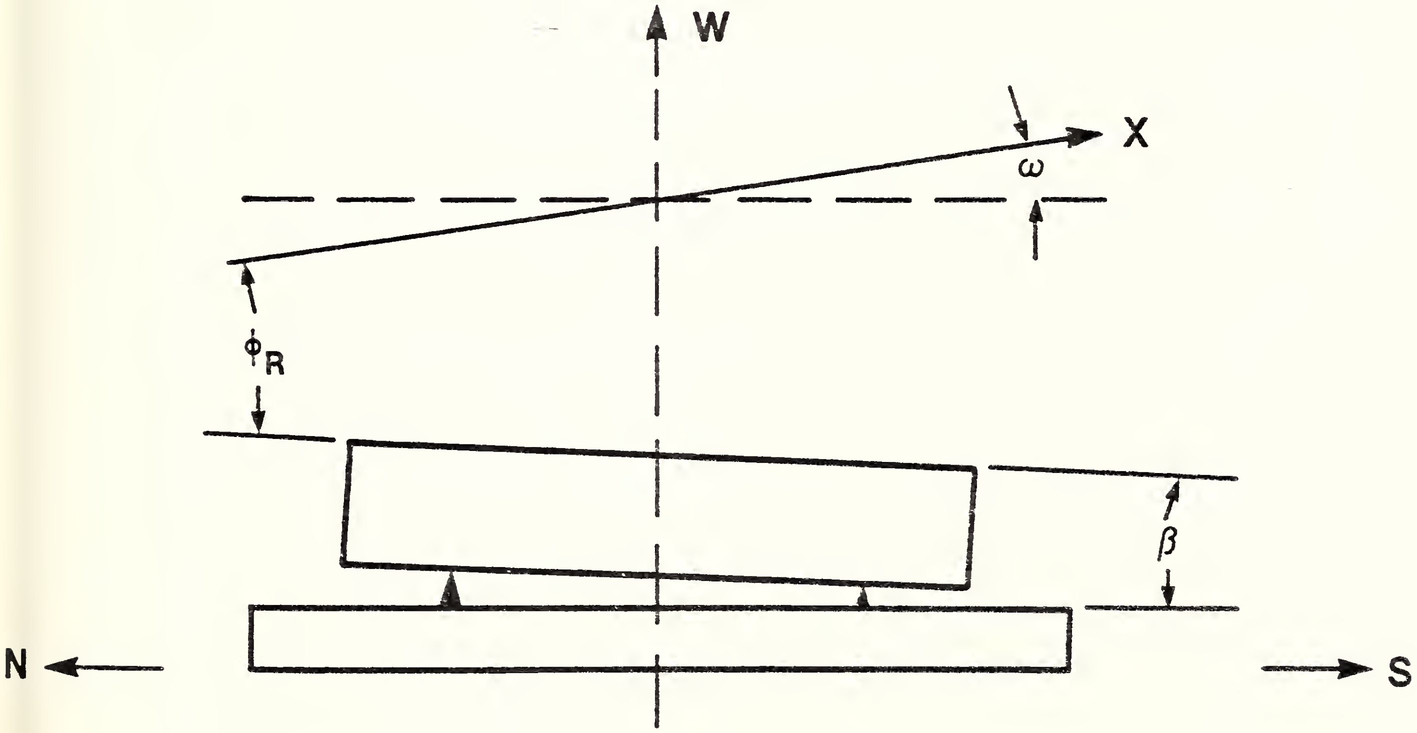

"Reverse", $\theta = 180°$

(b)

Figure 30

supporting fixtures, while angle ω is the desired X-W squareness error. We denote the measured angles in the respective orientations by ϕ_F and ϕ_R. An examination of the figures yields the relationships

$$\phi_F = \omega - \beta \tag{25}$$

$$\phi_R = \omega + \beta, \tag{26}$$

so that ω is simply

$$\omega = \frac{1}{2}(\phi_F + \phi_R). \tag{27}$$

For the actual measurements, the straightedge was centered to within 0.25-inch and the tool bar moved very nearly to the North limit of travel. With this arrangement we were able to sample 32 inches of the straightedge surface in each orientation. Since the figure error of the straightedge was known (at least to ± 2 microinches), it was possible to correct the measurement data for artifact shape. Vertical straightness errors of the LODTM X-axis were under software control via the polynomial correction algorithm described in Section 7.A. Displacements were measured at 4-inch intervals in each direction of tool bar motion.

Figure (31) shows the measured displacements in the "FORWARD" orientation after most of the linear portion has been subtracted. The most obvious feature is the nearly 25 microinch jump in the first 4 inches of travel,

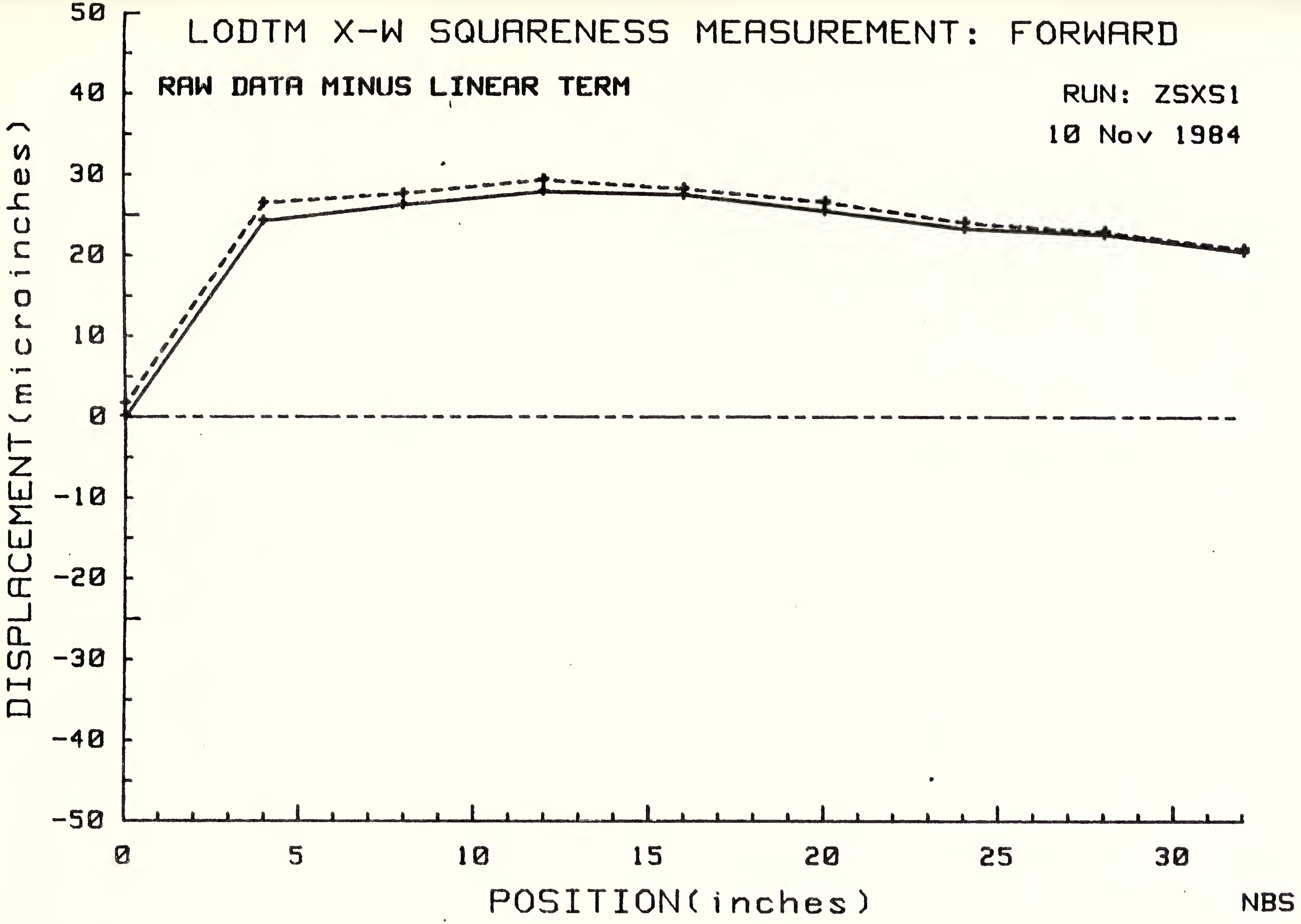
LODTM X-W SQUAREENESS MEASUREMENT: FORWARD
RAW DATA MINUS LINEAR TERM
RUN: ZSXS1
10 Nov 1984
50
40
30
20
10
0
-10
-20
-30
-40
-50
DISPLACEMENT(microinches)
0
5
10
15
20
25
30
POSITION(inches)
NBS

Figure 31

followed by a nearly linear behavior over the remainder of the range. We are certain that the reference straightedge contained no such large slope discontinuities in the first 4 inches of the sampled surface. Subsequent to this run we learned that the starting position was extremely close to the end of one of the LODTM horizontal reference straightedges and was outside the range of the vertical straightness lookup table. For this reason we have omitted the X=0 data points from the slope analysis and use only that portion of data between 4 inches and 32 inches, which amounts only to a change of origin.

Figure (32) shows the residuals of the relevant measured displacements after removal of a linear term, plotted with respect to a zero displacement at the X=4 inches position on the outward (to the South) portion of the measurement range. The solid line connects points on the way out and the dashed curve connects points on the way back. The obvious systematic non-repeatability is similar to that which characterized much of our data at LODTM, and is probably related to the tool bar air bearings. All data for this squareness measurement were taken with the air line heaters turned off. Since the Z-axis slide was not moved, the thermal model of Appendix A is not applicable to this behavior. The systematic convex nature of the residuals reflects the figure error of the reference straightedge.

Lacking an adequate model for thermal hysteresis, the data were analyzed as follows. Displacement at each position was estimated by simply averaging the samples taken in each direction of motion. These averaged data were then corrected for the shape of the reference straightedge, using a "map"

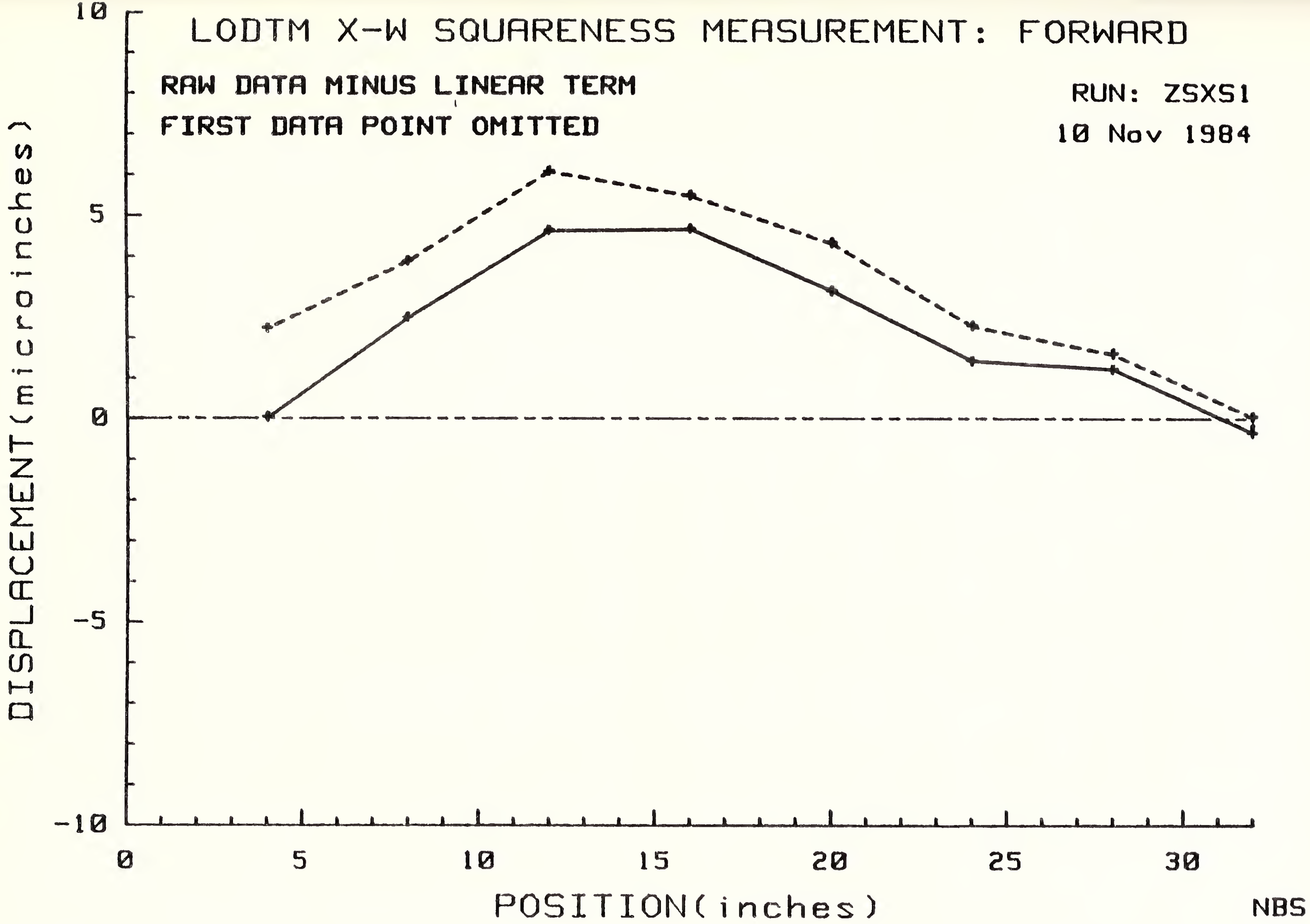
LODTM X-W SQUAREENESS MEASUREMENT: FORWARD
RAW DATA MINUS LINEAR TERM
FIRST DATA POINT OMITTED
RUN: ZSXS1
10 Nov 1984
DISPLACEMENT(microinches)
10
5
0
-5
-10
0
5
10
15
20
25
30
POSITION(inches)
NBS

Figure 32

derived from calibration data and beam calculations (see Appendix C). Finally, the averaged, corrected data were fit to a straight line using a linear least-squares algorithm.

The results of this procedure, applied to the "FORWARD" data, are shown in Fig. (33) which displays the residual deviations of the averaged data from the best-fit line. The fit is very good, with the maximum residual being no more than 0.5 microinch. The best fit slope is

$$\phi_F = \omega - \beta = +102.17 \text{ microradians.} \tag{27}$$

The positive sign means that the South end of the reference straightedge was higher than the North end in the setup.

Figure (34) shows the raw "REVERSE" displacement data, again with most of the linear trend removed. The results are, as expected, very similar to the "FORWARD" data. We applied the same analysis procedure to this data; Fig.(35) displays the deviations from the best-fit line, whose slope is

$$\phi_R = \omega + \beta = -101.38 \text{ microradians.} \tag{28}$$

The measurement uncertainties associated with Eqs.(27) and (28) are difficult to calculate with precision, due to the mixture of hysteresis, averaging, and computational errors. If we fix the X=0 end of the reference straightedge and ask for the uncertainty in the Z-position of the point at X=32 inches, then a plausible answer is about ±2 microinches. The resultant

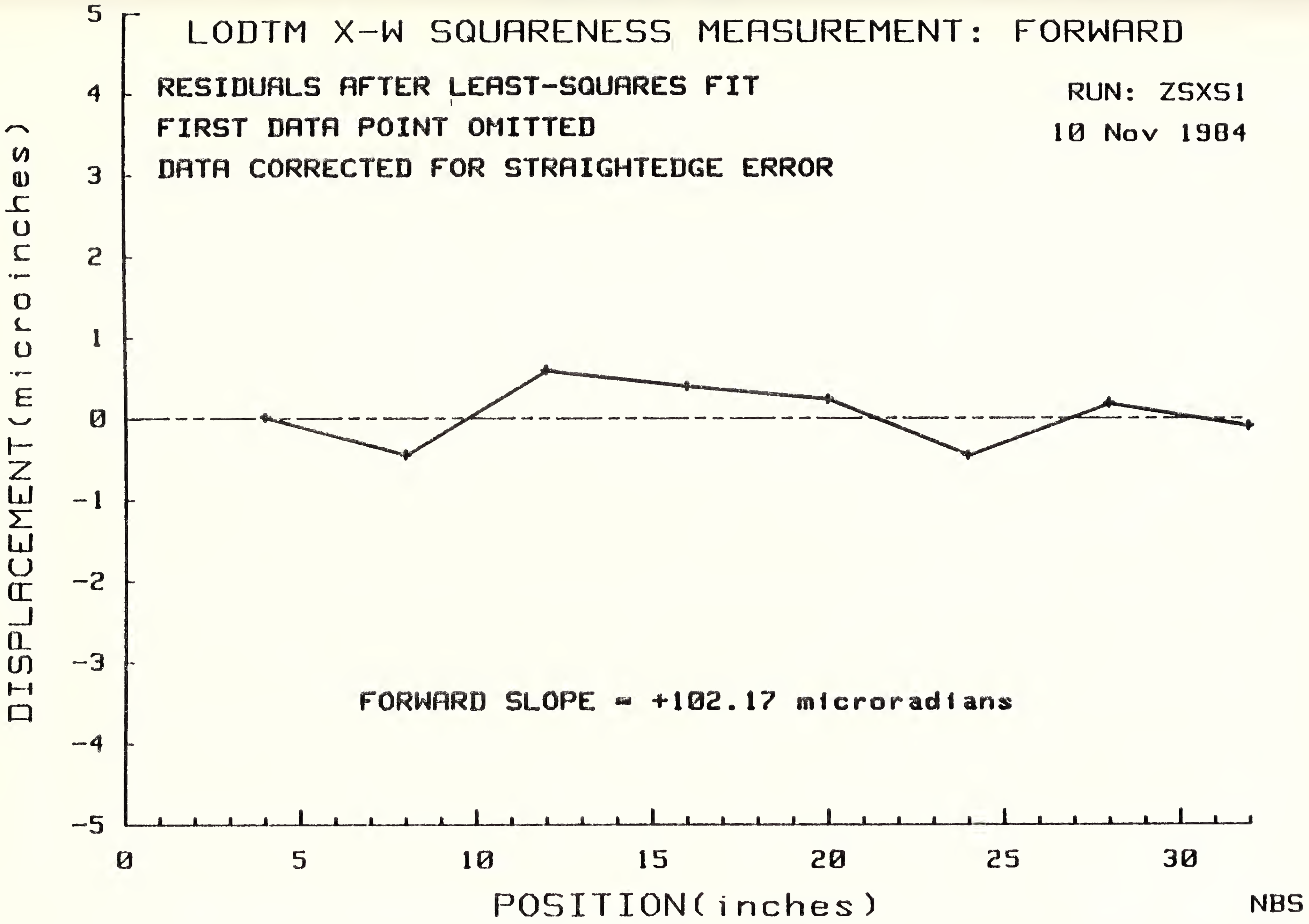
LODTM X-W SQUARENESS MEASUREMENT: FORWARD
RESIDUALS AFTER LEAST-SQUARES FIT
FIRST DATA POINT OMITTED
DATA CORRECTED FOR STRAIGHTEDGE ERROR
RUN: ZSXS1
10 Nov 1984
FORWARD SLOPE = +102.17 microradians
DISPLACEMENT(microinches)
5
4
3
2
1
0
-1
-2
-3
-4
-5
0
5
10
15
20
25
30
POSITION(inches)
NBS

Figure 33

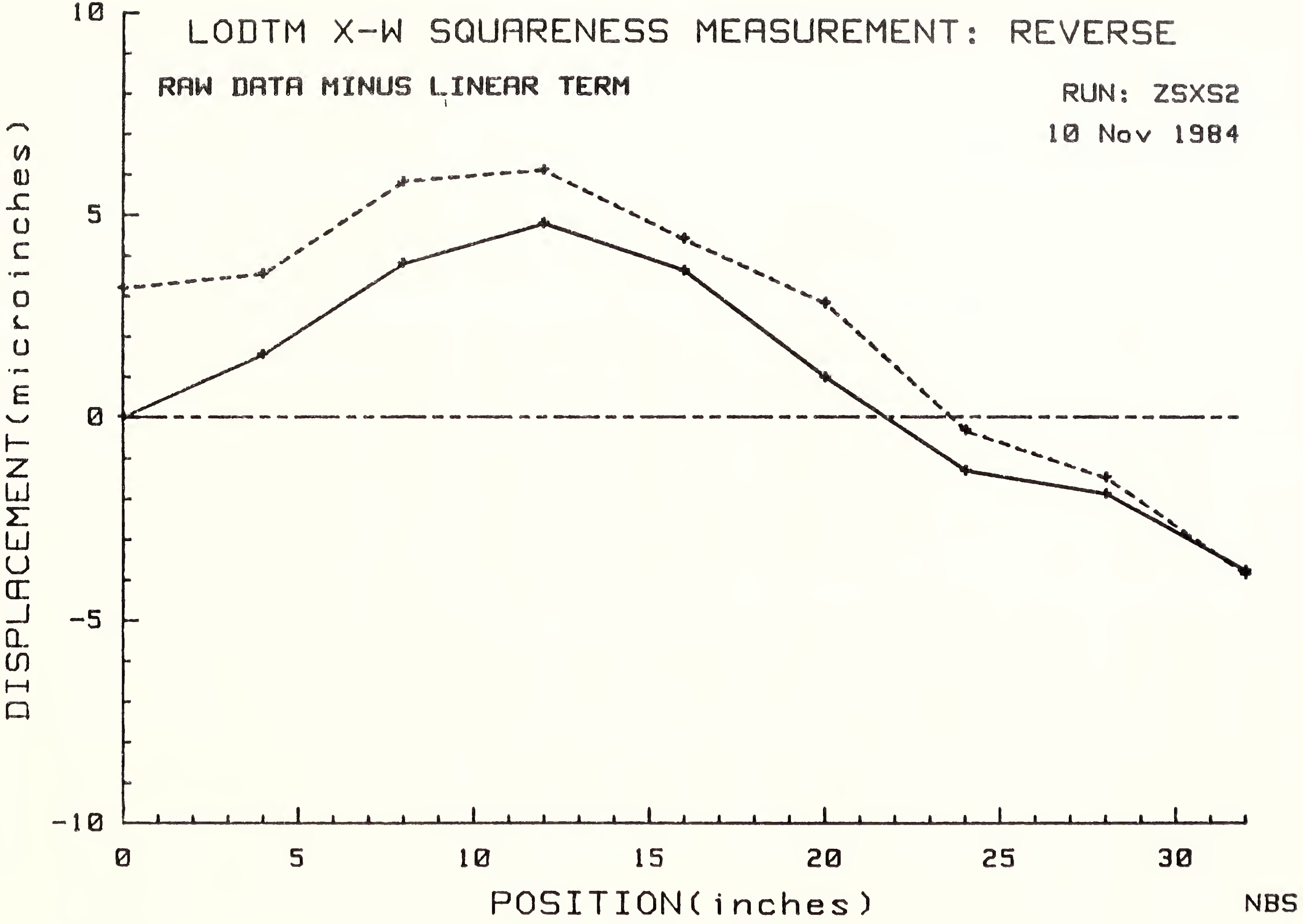
LODTM X-W SQUARENESS MEASUREMENT: REVERSE
RAW DATA MINUS LINEAR TERM
RUN: ZSXS2
10 Nov 1984
DISPLACEMENT(microinches)
10
5
0
-5
-10
0
5
10
15
20
25
30
POSITION(inches)
NBS

Figure 34

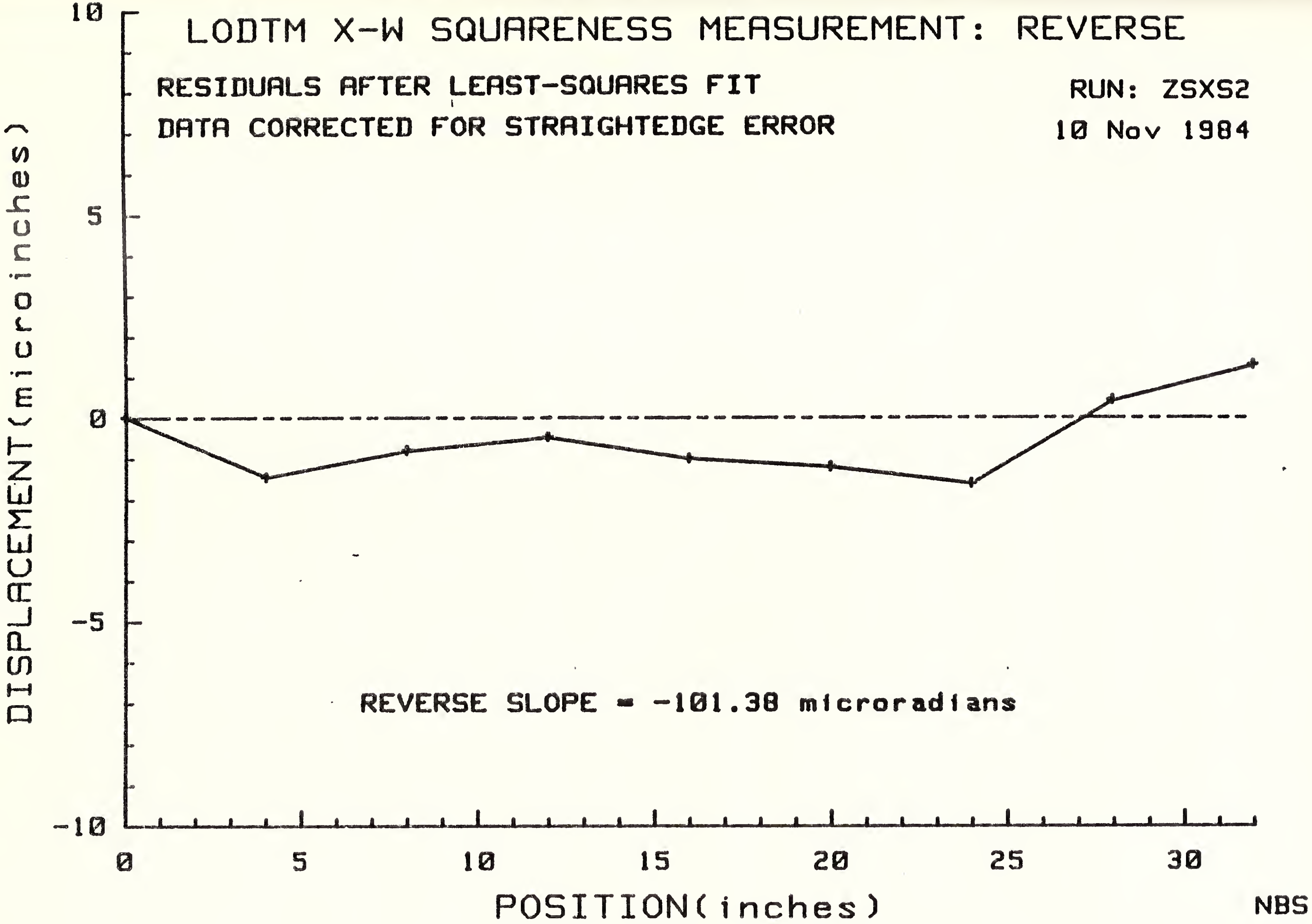
LODTM X-W SQUARENESS MEASUREMENT: REVERSE
RESIDUALS AFTER LEAST-SQUARES FIT
DATA CORRECTED FOR STRAIGHTEDGE ERROR
RUN: ZSXS2
10 Nov 1984
DISPLACEMENT(microinches)
10
5
0
-5
-10
REVERSE SLOPE = -101.38 microradians
0
5
10
15
20
25
30
POSITION(inches)
NBS

Figure 35

estimate of slope uncertainty is then ±0.06 microradians. While certainly not rigorous, we feel that this estimate is at least reasonable. Using this estimate of uncertainty for each of the measured slopes we compute for the X-W squareness error, using Eqs.(27) and (28):

$$\omega = +0.40 \pm 0.12 \text{ microradians.} \qquad (29)$$

The sign of the error is such that Fig.(30) is the correct portrayal of the relative directions of the W and X axes.

8.B. X-Z Squareness Error

The squareness error ψ between the X and Z axes slideways was measured using the NBS laser interferometer system to determine the displacement of the tool bar as it moved along the diagonal of a nearly right triangle. The technique may be understood by reference to Fig. (36) which displays the relevant geometry. The interferometer retroreflector was mounted to the tool bar, with the reference reflector on the stationary spindle surface. The system was zeroed with the retroreflector at point A. The machine then moved under program control along the diagonal d, transporting the retroreflector to point B, whose coordinates are (X,Z) with respect to A. The NBS interferometer system was then sampled 100 times (for averaging), and the diagonal d recorded. The result of this procedure is a triangle whose three sides are known. We measured d, while X and Z were measured by

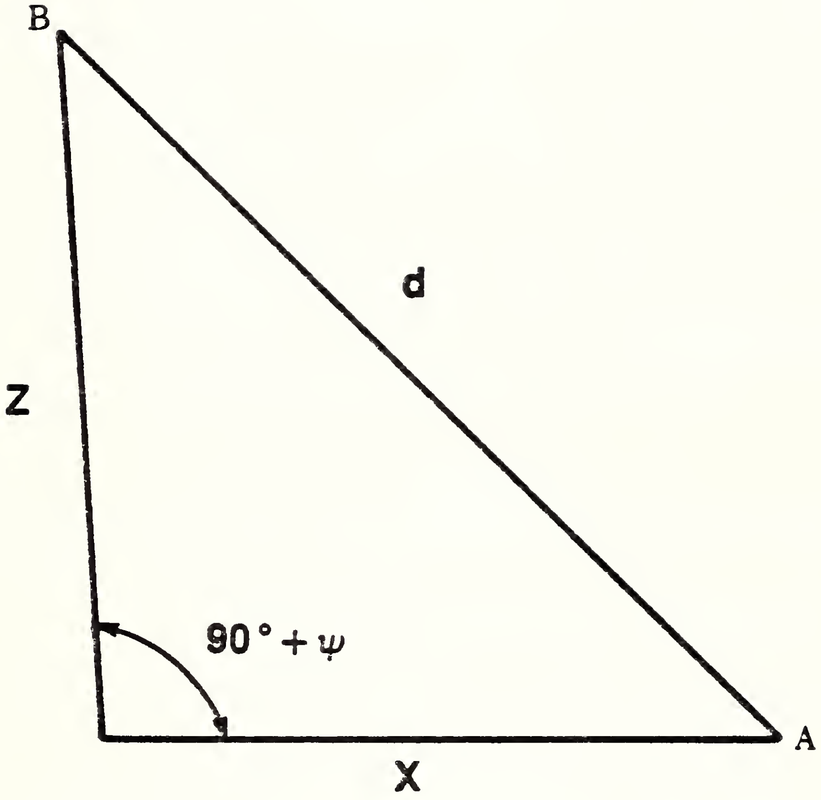

$$\sin\psi = \frac{d^2 - X^2 - Z^2}{2XZ}$$

Figure 36

LODTM's own laser scales, which we had previously determined to be very accurate.

Data analysis proceeds by using the law of cosines. From Fig.(36)

$$d^2 = X^2 + Z^2 - 2XZ\cos(\psi+90°)$$

$$= X^2 + Z^2 + 2XZ\sin\psi. \qquad (30)$$

The squareness error ψ is a very small angle, so that $\sin\psi = \psi$ with negligible error. Thus from Eq.(30)

$$\psi = \frac{d^2-X^2-Z^2}{2XZ} \qquad (31)$$

Figure (37) summarizes the average of seven measurements of ψ taken during November, 1984. The measured error is approximately +15.46 arc-seconds, or +75.1 microradians, with a standard deviation of 0.04 arc-seconds. The positive sign indicates that the tool point would move linearly to the North by about 75 microinches per inch of upward Z-axis movement were this error not corrected.

At this point the previous results were used to modify the linear term in the correction software for the Z-axis straightedges, and the X-Z squareness error was re-measured. Figure (38) shows the average of four measurements

LODTM X-Z SQUARENESS ERROR

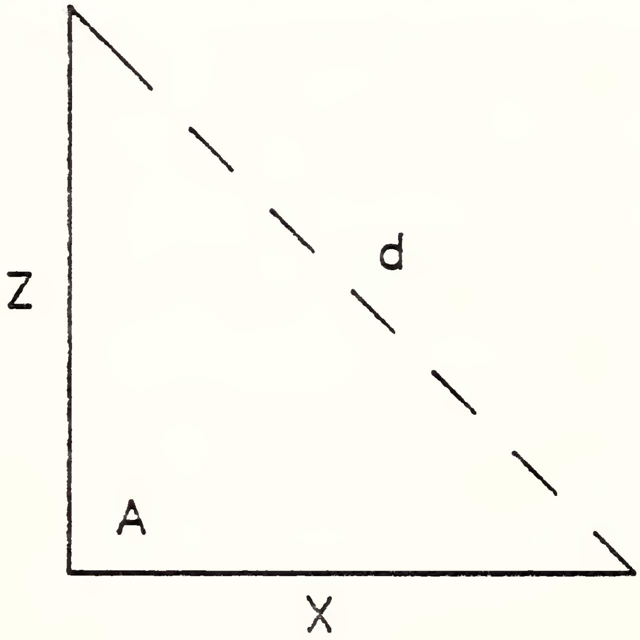

Average of 7 measurements – 13–14 Nov 1984:

(Look-up table empty)

X = 14.000000 inches
Z = 14.039000 inches
d = 19.827330 inches

A = 90.00430 degrees

Squareness Error = +75.10 microradians
= +15.46 arc-seconds

(Uncorrected for straightness and angular errors)

Figure 37

LODTM X-Z SQUARENESS ERROR

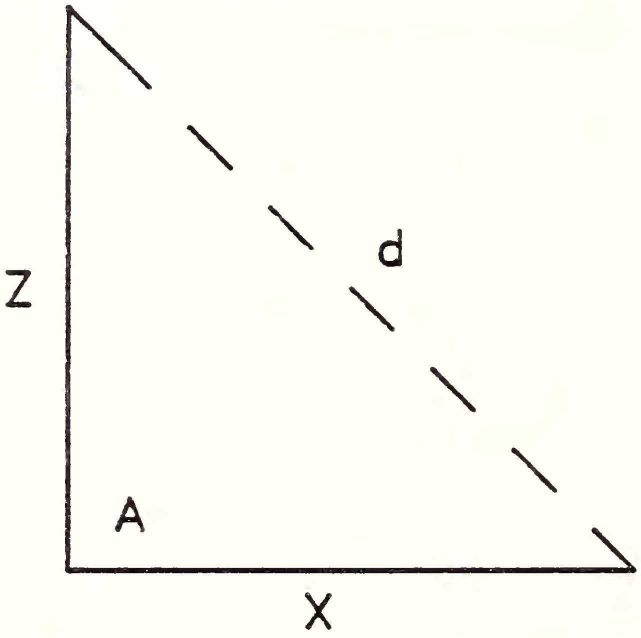

Average of 4 measurements – 14 Nov 1984:

(Look-up table loaded)

X = 14.000000 inches
Z = 14.021000 inches
d = 19.813844 inches

$A \doteq 90.00000$ degrees

Squareness Error = –0.10 microradians
= –0.02 arc-seconds

(Uncorrected for straightness and angular errors)

Figure 38

with the linear correction implemented. The average corrected X-Z squareness error is -0.02 arc-seconds (-0.10 microradians) with a standard deviation for the four measurements of 0.008 arc-seconds.

The uncertainty in this measurement may be estimated from the three quantities X,Z, and d which are used to calculate ψ. From Eq.(31)

$$\Delta\psi = \left(\frac{\partial\psi}{\partial X}\right)\Delta X + \left(\frac{\partial\psi}{\partial Z}\right)\Delta Z + \left(\frac{\partial\psi}{\partial d}\right)\Delta d, \tag{32}$$

where $$\frac{\partial\psi}{\partial X} = \frac{Z^2-X^2-d^2}{2ZX^2}, \tag{33}$$

$$\frac{\partial\psi}{\partial Z} = \frac{X^2-Z^2-d^2}{2XZ^2}, \tag{34}$$

and $$\frac{\partial\psi}{\partial d} = \frac{d}{XZ} . \tag{35}$$

Inserting the nominal values from Fig.(38), we have

$$\frac{\partial\psi}{\partial X} = \frac{\partial\psi}{\partial Z} = +0.07 \text{ microradians/microinch} \tag{36}$$

and $$\frac{\partial\psi}{\partial d} = +\ 0.10 \text{ microradians/microinch.} \tag{37}$$

At the time of these measurements the control software of LODTM was such that no pitch or straightness corrections were applied to the Z-axis motion, while the X-axis was corrected for these errors. Based upon our subsequent measurements of the relevant error terms, we can estimate their effect upon the diagonal measurement of ψ.

We first consider the error ΔX associated with Z-axis pitch and straightness errors. From the results of the pitch measurements described in Sec.6.B., we estimate that the LODTM tool bar rotated approximately 0.6 microradians in the 14 inches of Z-travel during the X-Z squareness measurements. The effect of this counter-clockwise rotation, coupled to the interferometer reference reflector by a 4-inch fixture, resulted in a 0.6 x 4 = 2.4 microinch displacement of the reflector to the South. Accompanying this pitch error was a straightness error caused by an improperly implemented $\delta_x(Z)$ lookup table (see Sec.7.B.). This error, evaluated over the appropriate 14 inches of motion, caused the reflector to move approximately 9 microinches to the North. The combined effect of these two systematic errors is such that side X of the measurement triangle shown in Fig. (38) was longer than the nominal value of 14 inches by approximately 6.6 microinches. As a result, using the sensitivity given by Eq.(36), we compute that the squareness error ψ should be altered by (6.6 microinches) x (-0.07 microradians/microinch) = -0.46 microradians. This change can be implemented in the LODTM correction software by adding 0.46 to the coefficient of the linear term in the Z-axis straightedge lookup table generating function.

The correction just described is our best estimate of the known systematic error associated with the measurement of ψ and should be used to modify the control software. The other errors of consequence are: (1) approximately ±2 microinches in ΔX due to tool bar thermal hysteresis, (2) approximately ±1 microinch in ΔZ due to $\delta_z(X)$ uncertainty, and (3) approximately ±2 microinches in Δd due to uncertainties in the NBS interferometer system. Using these values in Eq.(32) along with the sensitivities of Eqs.(36) and (37), and combining the various terms in quadrature, yields an estimated residual systematic uncertainty

$$\Delta\psi = \pm 0.3 \text{ microradians.} \tag{38}$$

In summary, the state of the machine at the end of these diagonal measurements was such that the X-Z squareness error was

$$\psi = -0.46 \pm 0.3 \text{ microradians.} \tag{39}$$

8.C. Remarks on Axis Geometry.

The measurements described in the previous two sections yield two of the three angles shown in Fig.(29): the X-W squareness error $\omega = 0.4 \pm 0.12$ microradians and the X-Z squareness error $\psi = -0.46 \pm 0.3$ microradians. The negative sign of ψ means that the angle between X and Z is acute, rather that obtuse as shown. Since ψ and ω are nearly equal in magnitude we would expect that the Z-W parallelism error α to be very small. In particular, we compute from the geometry:

$$\alpha = \omega + \psi$$

$$= -0.06 \pm 0.4 \text{ microradians.} \qquad (40)$$

A direct measurement of α, however, as described in Section (7.B.), resulted in a value of $\alpha = 5.3 \pm 0.22$ microradians. This sizeable discrepancy, amounting as it does to more than an arc-second of angular error, is much larger than can be accounted for by any reasonable increase in the measurement uncertainties. In our opinion, the most likely explanation of this behavior is an effect resulting from the nature of the LODTM slide configuration.

The linear axes of LODTM are arranged in what is commonly called a "stacked slide" configuration. That is, the Z-axis (or tool bar) is mechanically coupled to, and transported by, the X-axis carriage. The effect of this coupling is such that any pitch motion of the X-carriage will change the direction in space of the Z-axis. In order to further describe this behavior, let us assume that the machine X-axis is perfectly square to both the Z and W axes (i.e., $\omega = \psi = 0$), and that the Z-axis is perfectly parallel to the W-axis, when the tool bar is positioned above the spindle center. This situation is shown schematically in Fig.(39a). Now, as the tool point is transported in the X-direction a pitch of the X-carriage by an amount ε will rotate the Z-axis through the same angle [see Fig.(39b)]. If the Z-W

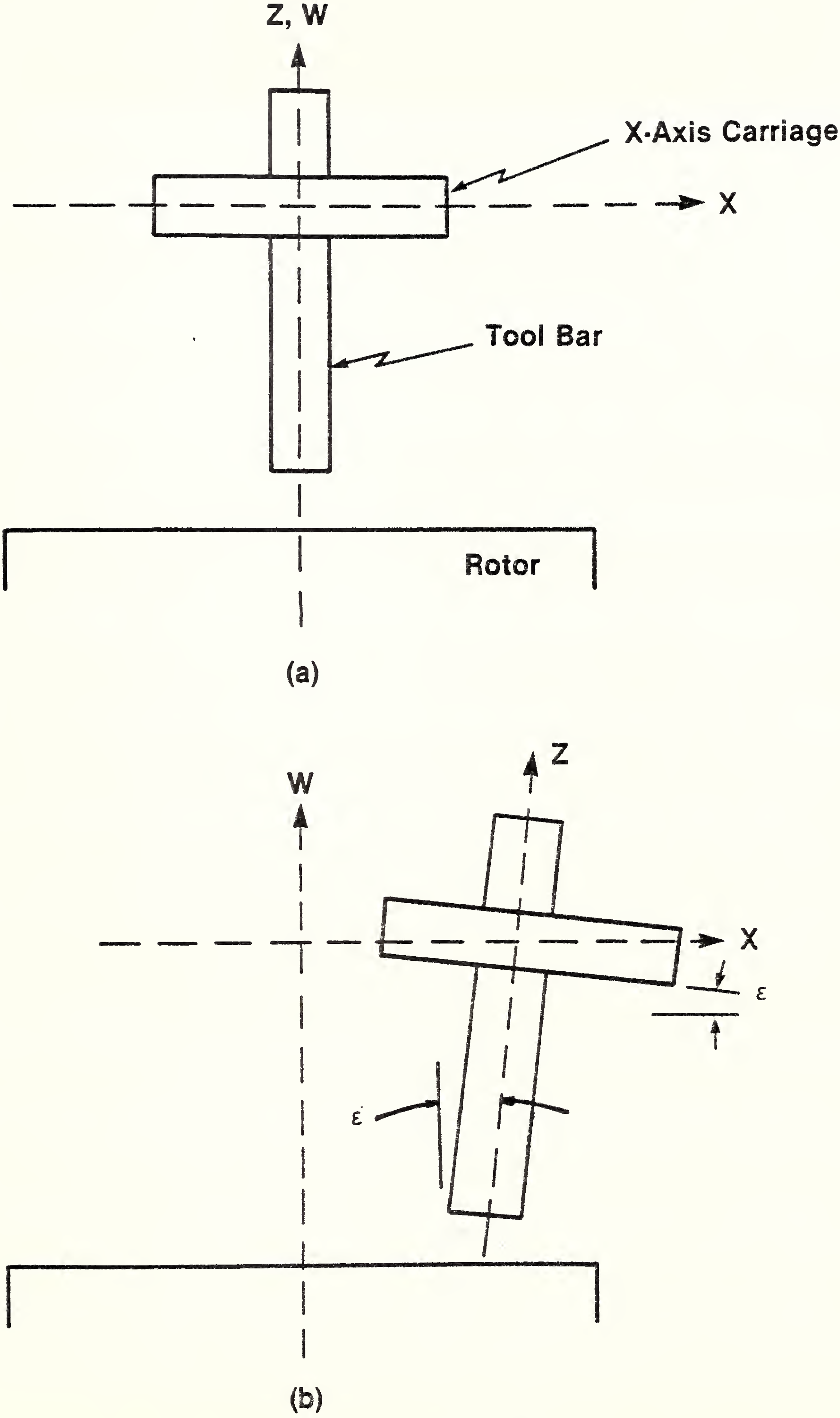

Figure 39

parallelism error α were measured with the tool bar at X_0, the result would be $\alpha = \varepsilon$. Thus, apparently, the LODTM X-W parallelism error is a function of the X-axis position. Of course, the motion control system can and does correct the tool point position in order to remove errors caused by <u>changes</u> in X-axis pitch during part machining. The initial value of the pitch, however, is a function of X-axis position upon start-up, which means that the linear term in the Z-axis straightedge error correction software is correct only for one particular location of the tool bar upon closing the positioning feedback loops.

There are several approaches which could be used to assure repeatable machine behavior. The first would entail a careful measurement of Z-W parallelism error with the machine started at a known X-axis position. The result of this measurement would be used to generate the linear term in the Z-axis correction lookup table. It would then be necessary to manually position the X-axis slide at this same location every time the machine was brought on-line, assuming, of course, that the pitch motion of the X-slide is a repeatable function.

Another approach would involve using our measurements of the X-axis pitch error to assign a linear correction coefficient based upon tool point location, when the coordinates of the latter are entered into the RTC prior to part machining. This pitch error can be deduced from Fig.(7). Dividing the measured error by 10 inches (the Z tool offset) yields the X-axis pitch error directly in microradians. If the Z-W parallelism error is known at some X-position, then the value at some other position can be computed using

Fig.(7). This approach would require re-coding of the LODTM position correction software to include the X-axis pitch error function.

A third approach would employ an auxiliary tool set station mounted to the LODTM metrology frame at height Z_0 above the existing station. This auxiliary station would need to be sensitive only to X-direction tool offsets. The reference geometry of this system would then be recorded by the following procedure. First, measure the parallelism error at some known location and use the result to initialize the correction software at that location. Then, zero the coordinate system at the lower tool set station and find the X-axis location of the upper tool set station. Following an emergency stop or other loss of servo control, the machine could then be restarted at any location and the tool set stations re-measured. Any change in the X-position of the upper station with respect to the lower, divided by the height difference Z_0, would then be a measure of uncompensated parallelism error and could be used to re-compute the lookup table.

9. Spindle Errors

Spindle rotation errors of LODTM were measured during the November, 1984 validation period. The relevant errors are radial error motion, axial error motion, and tilt error motion. Since these error motions may depend upon spindle rotation rate, each was measured at 25 RPM and 50 RPM. These values represent, according to the LODTM staff, realistic lower and upper limits on spindle speeds to be used in actual part machining.

Our original intention was to measure each of the spindle error motions twice - once with all spindle software correction terms turned off and again with these terms turned on. The first measurements would then yield the "raw" spindle errors, while the second would be used to verify the software correction algorithms. When this was done, however, it became apparent that the uncorrected spindle errors were, in every case, smaller that the "corrected" ones. We subsequently discovered several problems with both the hardware (spindle capacitance gauges) and software used to correct for spindle error motions. In order to avoid complicating this discussion with data of marginal utility, we shall present only the results obtained for the "raw", uncorrected spindle errors.

9.A. Radial Error Motion

Radial error motions of the LODTM spindle were measured at 25 and 50 RPM at two axial locations. These two locations correspond to effective tool positions 7.5 inches and 21.5 inches above the rotor surface. The hardware used for these measurements was identical to that used for the Z-axis straightness measurements, consisting of a 3-inch diameter precision cylindrical square and two Invar capacitance gauges. The setup is shown in Fig.(21).

Error data was acquired using a commercial two-channel digital oscilloscope coupled to the metrology system computer via an IEEE-488 parallel interface bus. A capacitance gauge was connected to the positive differential input of each channel, while a precision voltage reference source supplied +10VDC to the two negative inputs. By thus "bucking" most of the nominal 10 volt gauge output, oscilloscope sensitivity was increased for higher resolution. By operating each input differential amplifier at ±1 volt full scale, the least-count of the 12-bit ADC corresponded to a change in gauge output of approximately 0.24 mV. For these gauges, this represents a displacement sensitivity of about 0.1 microinch.

In order to obtain spindle data which was synchronous with angular position, we used buffered TTL pulses derived from the LODTM spindle encoder. The oscilloscope was triggered by the encoder top-dead-center (TDC) pulse which defines the zero-angle ($\Theta = 0$) spindle location, in order to initiate data collection. Subsequent A/D conversions and oscilloscope memory steps were commanded by pulses derived from the encoder angular position pulse stream. The 36,000 encoder pulses per revolution entered a selectable divide-by-N circuit whose output comprised the command pulses. Most of our measurements were performed using N=100, resulting in error motion data in one-degree increments of spindle angular position or 360 points per revolution. The digital oscilloscope has a memory capacity of 7936 points per channel so that a complete run resulted in 7936/360 ≈ 22 revolutions of error motion data for each of the two capacitance gauges.

We denote the spindle radial error motion by $S(\Theta)$ and the roundness error of the cylindrical square by $C(\Theta)$. In order to separate spindle error from artifact error, we used the elegant reversal technique proposed by Donaldson [4]. In this method, error motion data is acquired using two orientations of the cylindrical square which differ by a 180° rotation. The use of two gauges, also 180° apart, effectively provides the necessary gauge reversal and, as in the case of the Z-axis straightness measurements (Sec. 7.B.), provides redundant information as a check on data consistency. The way in which cylinder reversal works will become apparent as we describe the reduction and analysis of the capacitance gauge data.

As usual, it is necessary to adopt sign conventions for the relevant error functions. We choose the following:

$$S(\Theta) = \begin{cases} +, & \text{for spindle radial motion to the } \underline{\text{SOUTH}} \\ -, & \text{otherwise} \end{cases} \qquad (41)$$

$$C(\Theta) = \begin{cases} +, & \text{for displacements } \underline{\text{out}} \text{ of the surface} \\ -, & \text{otherwise} \end{cases} \quad . \qquad (42)$$

The first set of data is acquired with the cylindrical square in an arbitrary "FORWARD" orientation. The gauges measure changes in the gap between their active electrodes and the cylinder surface as functions of angular position Θ. The raw (non-centered) displacement functions for the SOUTH and NORTH gauges respectively are written

$$FS_{raw}(\Theta) = A\sin\Theta + B\cos\Theta + S(\Theta) + C(\Theta) \qquad (43)$$

and

$$FN_{raw}(\Theta) = -A\sin\Theta - B\cos\Theta - S(\Theta) + C(\Theta+\pi). \qquad (44)$$

The first two terms in each expression represent the first-harmonic (i.e., once-per-revolution) cylinder centering error. These terms are arbitrarily written with positive signs for the SOUTH gauge, and the signs reversed for the NORTH gauge (i.e., if S and C were both identically zero, then the motion seen by the NORTH gauge would be exactly opposite to that seen by the SOUTH gauge). This once-per-revolution component of the error data cannot cause workpiece errors since it is in principle possible to mount a perfectly circular test artifact in such a way that this component would be reduced to zero. A more complete discussion of this "fundamental radial error motion" may be found in Refs. [2] and [3].

The raw displacement data was reduced by a two-parameter least-squares algorithm in order to determine the centering error coefficients A and B. These numbers determine the location of the cylindrical square axis (at the cross-section being sampled) with respect to the LODTM spindle axis. The polar coordinates (r_c,Θ_c) of this location are

$$r_c = (A^2 + B^2)^{1/2} \qquad (45)$$

and

$$\Theta_c = \tan^{-1} (A/B). \qquad (46)$$

Once A and B were computed, corrections $A\sin\theta + B\cos\theta$ were subtracted from the SOUTH gauge data and added to the NORTH gauge data, yielding the centered functions of interest. The results, for the "FORWARD" cylinder orientation, are

$$FS(\theta) = +S(\theta) + C(\theta) \tag{47}$$

and

$$FN(\theta) = -S(\theta) + C(\theta+\pi). \tag{48}$$

The cylindrical square was then rotated 180° with respect to the spindle and the entire process repeated. Then for the "REVERSE" orientation we have

$$RS(\theta) = +S(\theta) + C(\theta+\pi) \tag{49}$$

and

$$RN(\theta) = -S(\theta) + C(\theta). \tag{50}$$

Equations (47-50) are the central results of this procedure and yield, upon inspection, the desired functions:

$$S(\theta) = [FS(\theta)-RN(\theta)]/2 \tag{51a}$$

$$= [RS(\theta)-FN(\theta)]/2 \tag{51b}$$

and

$$C(\theta) = [FS(\theta)+RN(\theta)]/2 \tag{52a}$$

$$C(\theta+\pi) = [RS(\theta)+FN(\theta)]/2. \tag{52b}$$

Since these functions are periodic, we can replace Θ with $\Theta+\pi$ in Eq.(52b) in order to get an alternative relation:

$$C(\Theta+2\pi) = C(\Theta) = [RS(\Theta+\pi) + FN(\Theta+\pi)]/2. \qquad (52c)$$

These expressions (51-52) illustrate the redundancy which results from the use of two capacitance gauges.

The first measurements of spindle radial motion were performed at a gauge height of 7.5 inches above the rotor surface. Figures (40) and (41) show polar plots of the radial motion at 25 RPM, computed from the data using Eqs. (51a) and (51b), respectively. These plots may be interpreted as views of the spindle rotor from above, with SOUTH at the three o'clock position. This position is also the location of $\Theta=0$ when the spindle is at "top dead center." The angle Θ increases counterclockwise; since the spindle rotated in a clockwise direction during these measurements, increasing values of Θ were sampled by the gauges aligned with the N-S axis which is the sensitive direction for radial errors. Figure (42) shows the difference in the two determinations of radial motion which is seen to be zero within a noise level of a few tenths of a microinch. Such difference plots, of which this one is typical, were used primarily as consistency checks on the capacitance gauge data.

The single trace of Fig.(40) represents the average of 22 revolutions of data. In order to assess the degree of "random" or non-repeatable error we

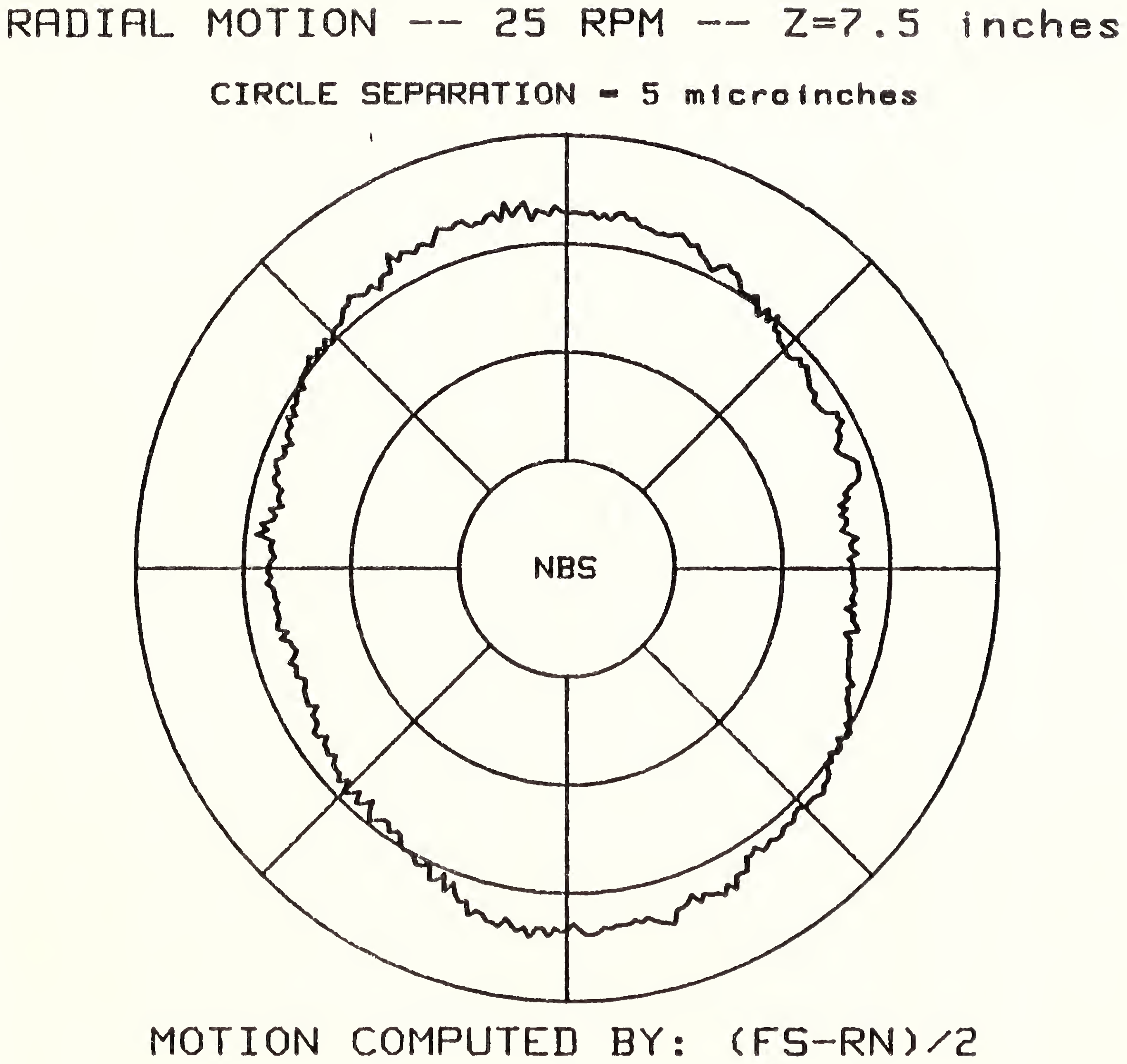
RADIAL MOTION -- 25 RPM -- Z=7.5 inches
CIRCLE SEPARATION = 5 microinches
NBS
MOTION COMPUTED BY: (FS-RN)/2

Figure 40

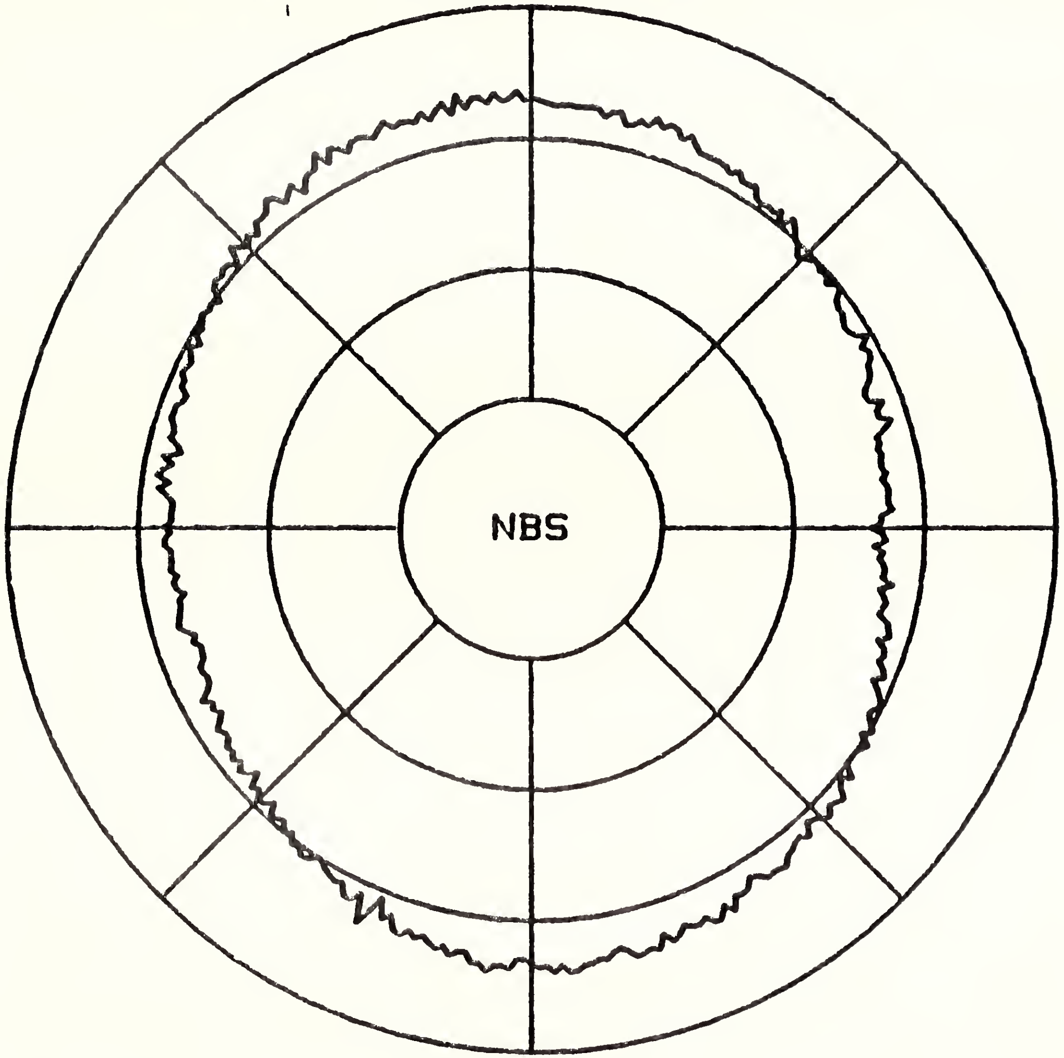

RADIAL MOTION -- 25 RPM -- Z=7.5 inches

CIRCLE SEPARATION = 5 microinches

MOTION COMPUTED BY: (RS-FN)/2

Figure 41

RADIAL MOTION -- 25 RPM -- Z=7.5 inches

CIRCLE SEPARATION = 2 microinches

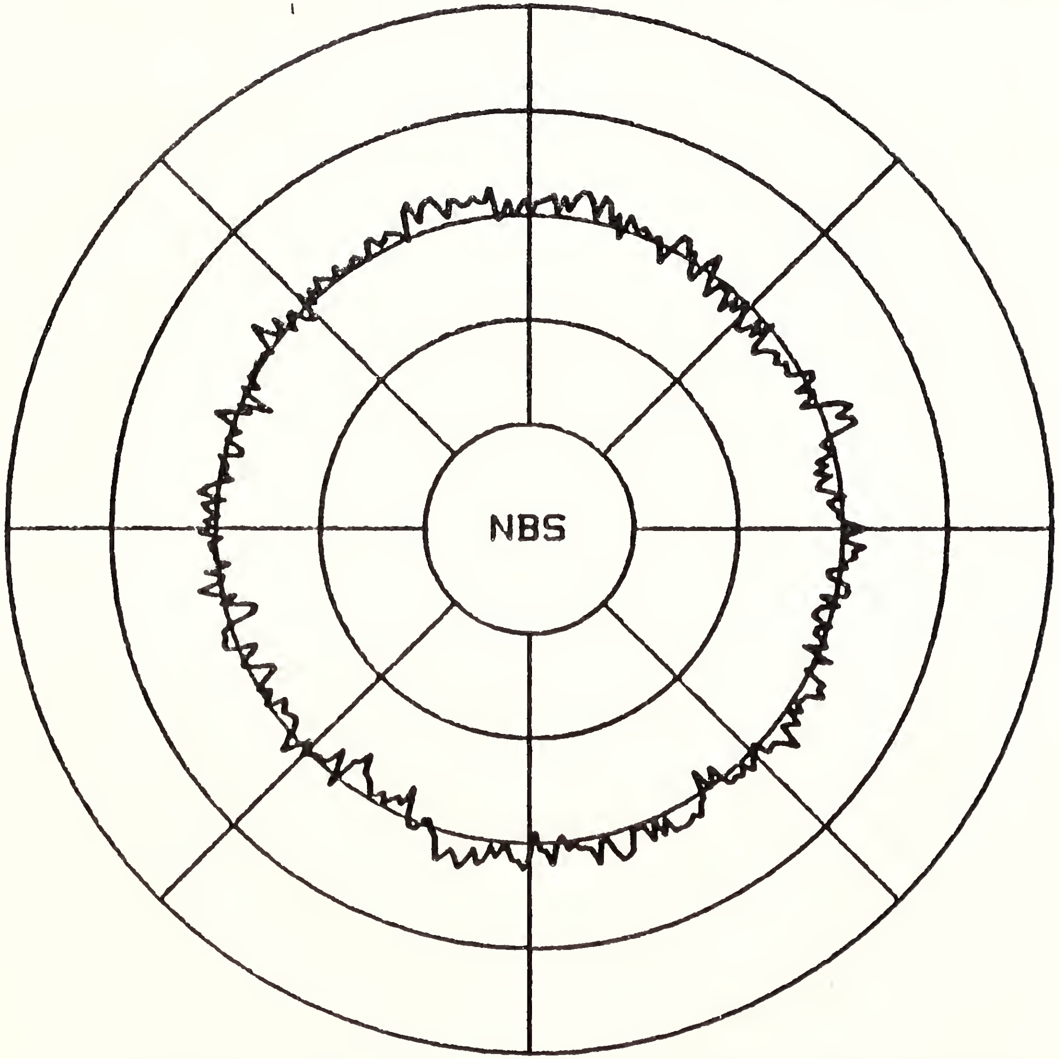

DIFFERENCE OF COMPUTED MOTIONS

Figure 42

should strictly display, in addition to this average, the maximum and minimum values of radial motion at each angular position. We chose not to do so for the following reason. The vibration of the LODTM tool bar, to which we refer several times in this report, coupled rather strongly to the cantilevered fixture used to hold the gauges in these measurements. The result, observed with the spindle at rest, was a nearly sinusoidal, ≈100Hz "noise" component of 5-6 microinch P-V amplitude. The effect of such a background would be to mask (and probably dominate) the non-repeatable rotation errors of interest. Therefore, all of the spindle error motion data presented here will be averaged data. In our opinion, a very good estimation of spindle "random" error motions can be obtained by measurement and analysis of error signals from the LODTM spindle capacitance gauges, which are attached to the metrology frame. These measurements are described later in this section.

As seen from Fig.(40), the P-V radial error motion at Z=7.5 inches and 25 RPM is about 4 microinches, and is quite systematic. The nearly elliptical shape of the polar plot suggests a dominant twice-per-revolution or second harmonic systematic error. This behavior is much more evident if the error is displayed on a linear plot, as shown in Fig.(43). The solid curve in this figure is the averaged radial error motion data, while the dashed curve is the result of fitting the measurement data to a finite Fourier series in the angular position. This expansion takes the form

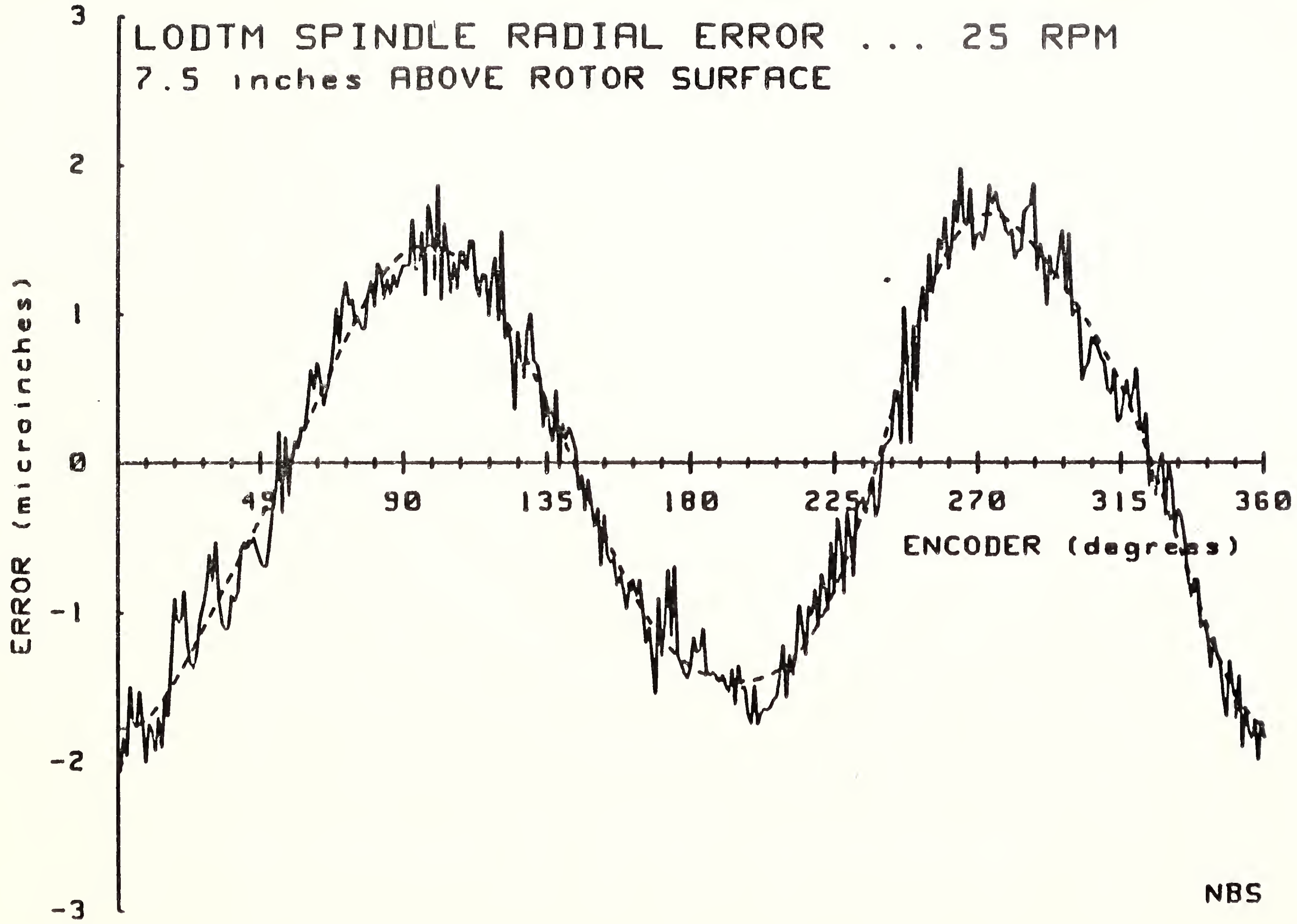
LODTM SPINDLE RADIAL ERROR ... 25 RPM
7.5 inches ABOVE ROTOR SURFACE
ERROR (microinches)
3
2
1
0
-1
-2
-3
45
90
135
180
225
270
315
360
ENCODER (degrees)
NBS

Figure 43

$$S(\Theta) = A_0 + \sum_{k=1}^{N} (A_k \cos k\Theta + B_k \sin k\Theta). \qquad (53)$$

The best-fit A and B coefficients for this data, and for the remainder of the measured spindle error motions, are tabulated later in this section.

Figure (44) displays the radial error motion at 50 RPM, again at Z=7.5 inches. Figure (45) is a linear plot of this data, together with the resultant Fourier analysis. Comparison with the 25 RPM data shows the same general shape with a somewhat (≈0.5 microinch) greater P-V amplitude at 50 RPM. Such a dependence of radial error on rotation rate is often observed in spindle error measurements.

Following these measurements, the tool bar was moved upwards by 14 inches, so that the effective "tool point" was 21.5 inches above the rotor surface, and a new set of radial error motion data was collected. Figures (46) and (47) show the resultant errors for speeds of 25 and 50 RPM respectively, while Figs. (48) and (49) are the corresponding linear plots and Fourier series fits.

Tables 2 and 3 show the coefficients of the Fourier series fits to the radial error motion data, for Z=7.5 inches and Z=21.5 inches respectively. These coefficients were determined from Eq.(53) with N=10. This choice of highest harmonic was arbitrary, and, as the tabular results indicate, is more than adequate to characterize the radial error motions of LODTM. In

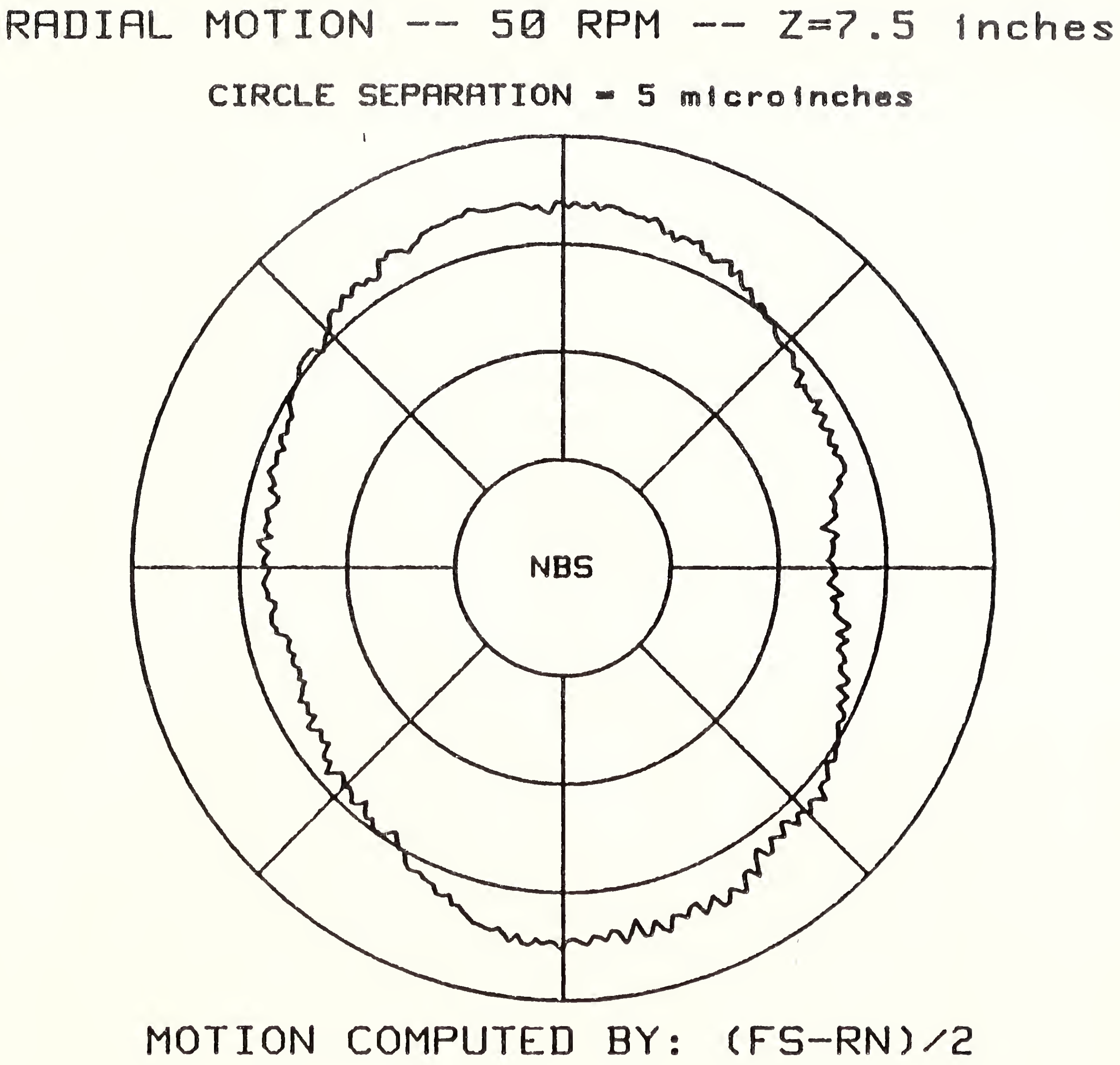
RADIAL MOTION -- 50 RPM -- Z=7.5 inches
CIRCLE SEPARATION = 5 microinches
NBS
MOTION COMPUTED BY: (FS-RN)/2

Figure 44

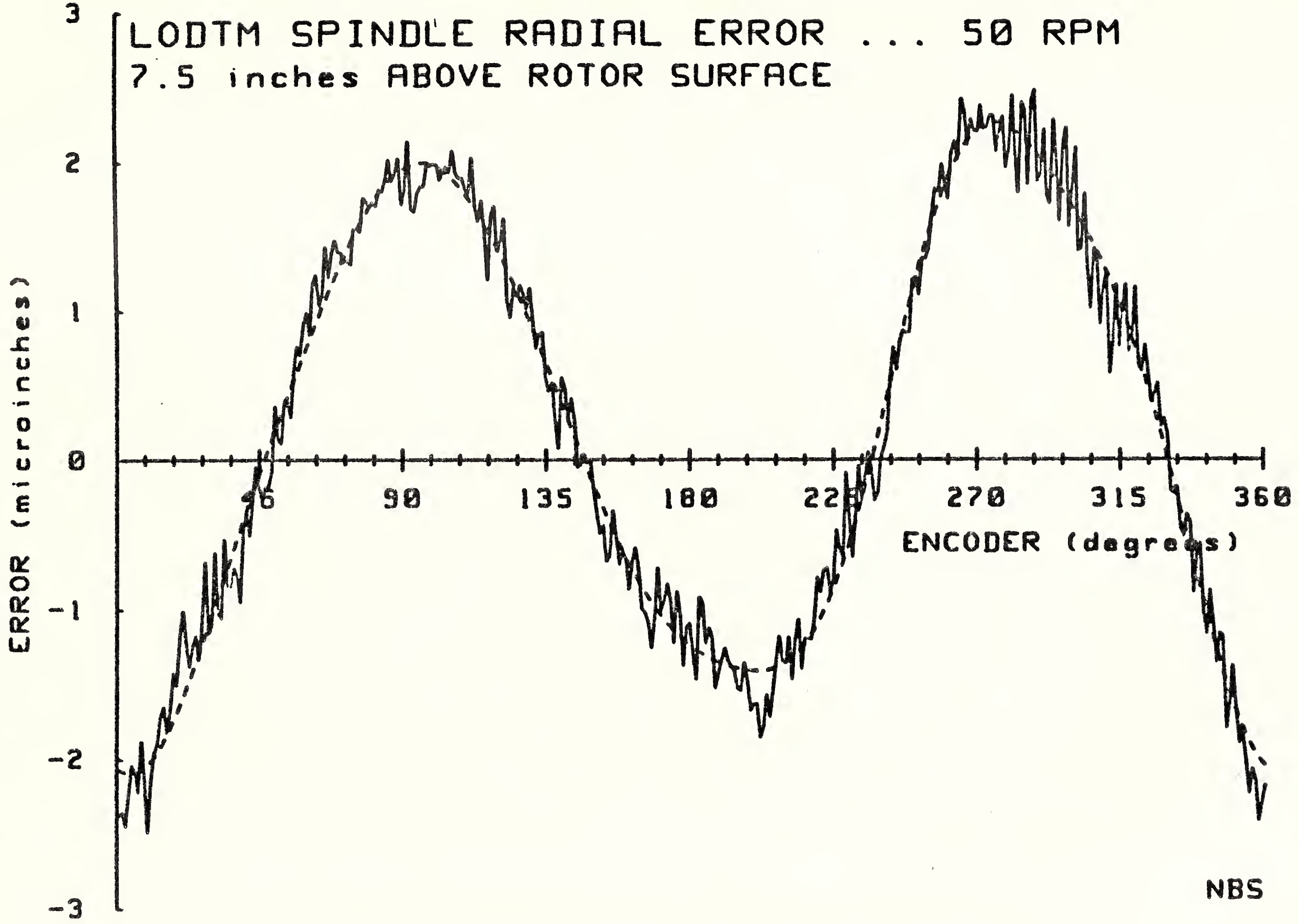
LODTM SPINDLE RADIAL ERROR ... 50 RPM
7.5 inches ABOVE ROTOR SURFACE
ERROR (microinches)
3
2
1
0
-1
-2
-3
45
90
135
180
225
270
315
360
ENCODER (degrees)
NBS

Figure 45

RADIAL MOTION -- 25 RPM -- Z=21.5 inches

CIRCLE SEPARATION = 5 microinches

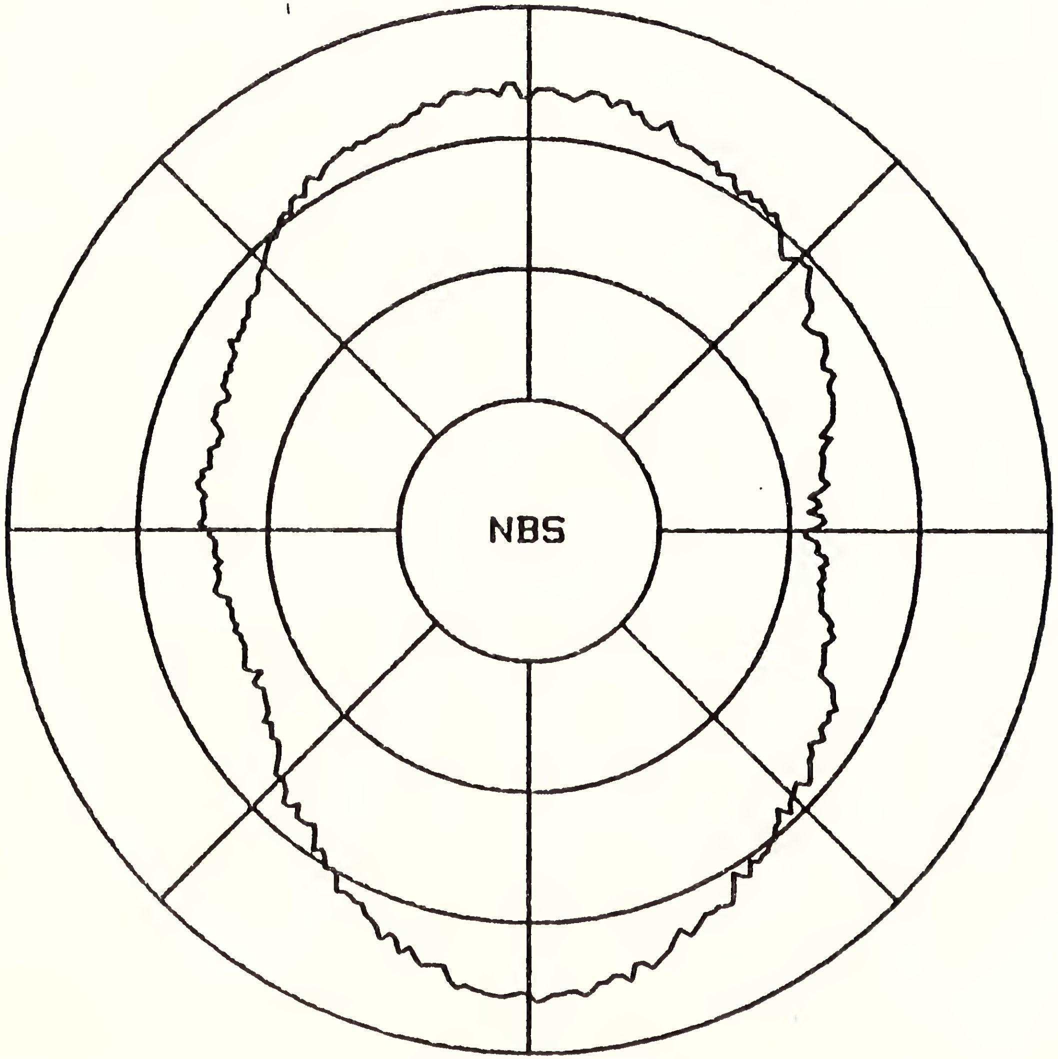

MOTION COMPUTED BY: (RS-FN)/2

Figure 46

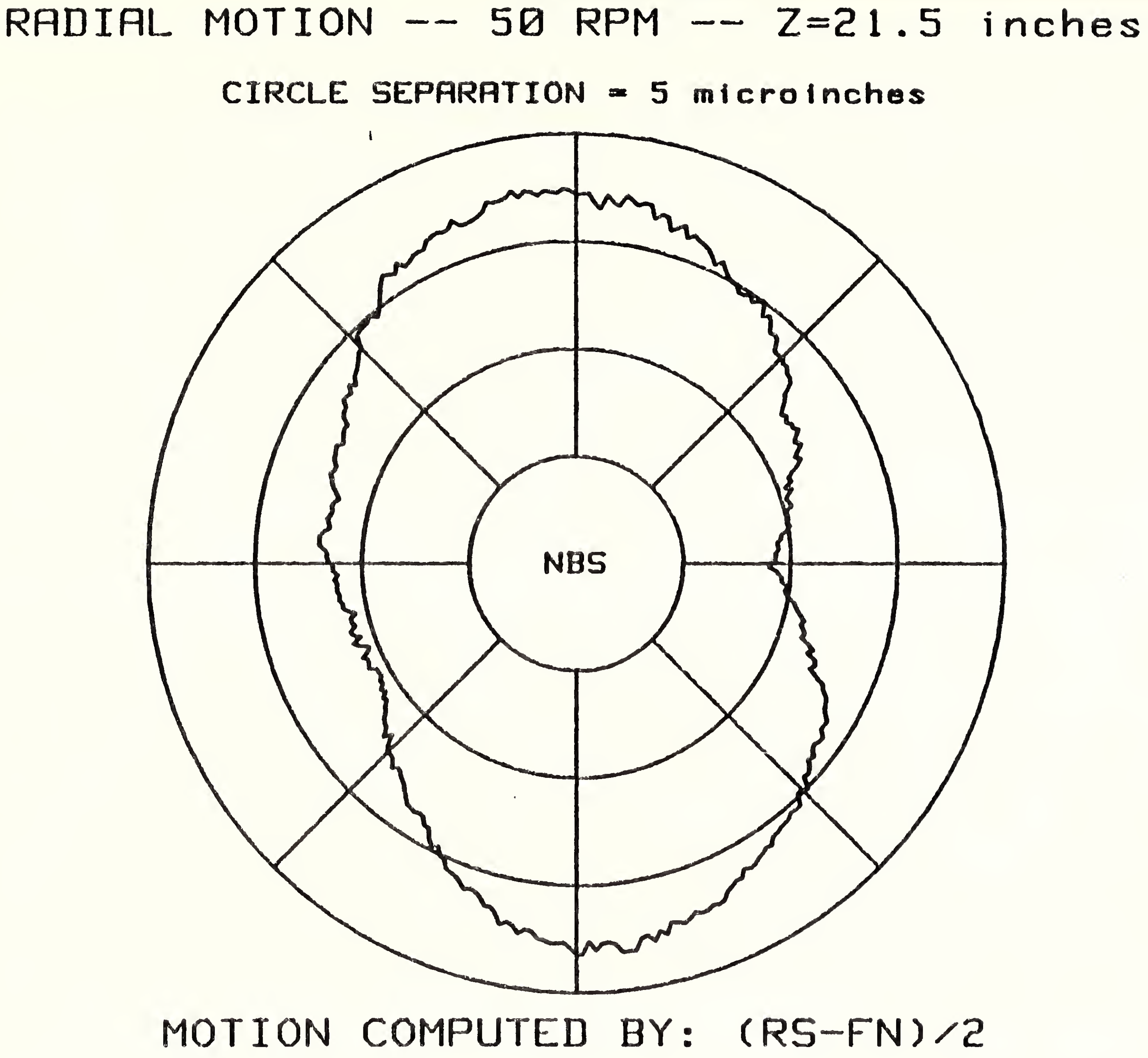
RADIAL MOTION -- 50 RPM -- Z=21.5 inches
CIRCLE SEPARATION = 5 microinches
NBS
MOTION COMPUTED BY: (RS-FN)/2

Figure 47

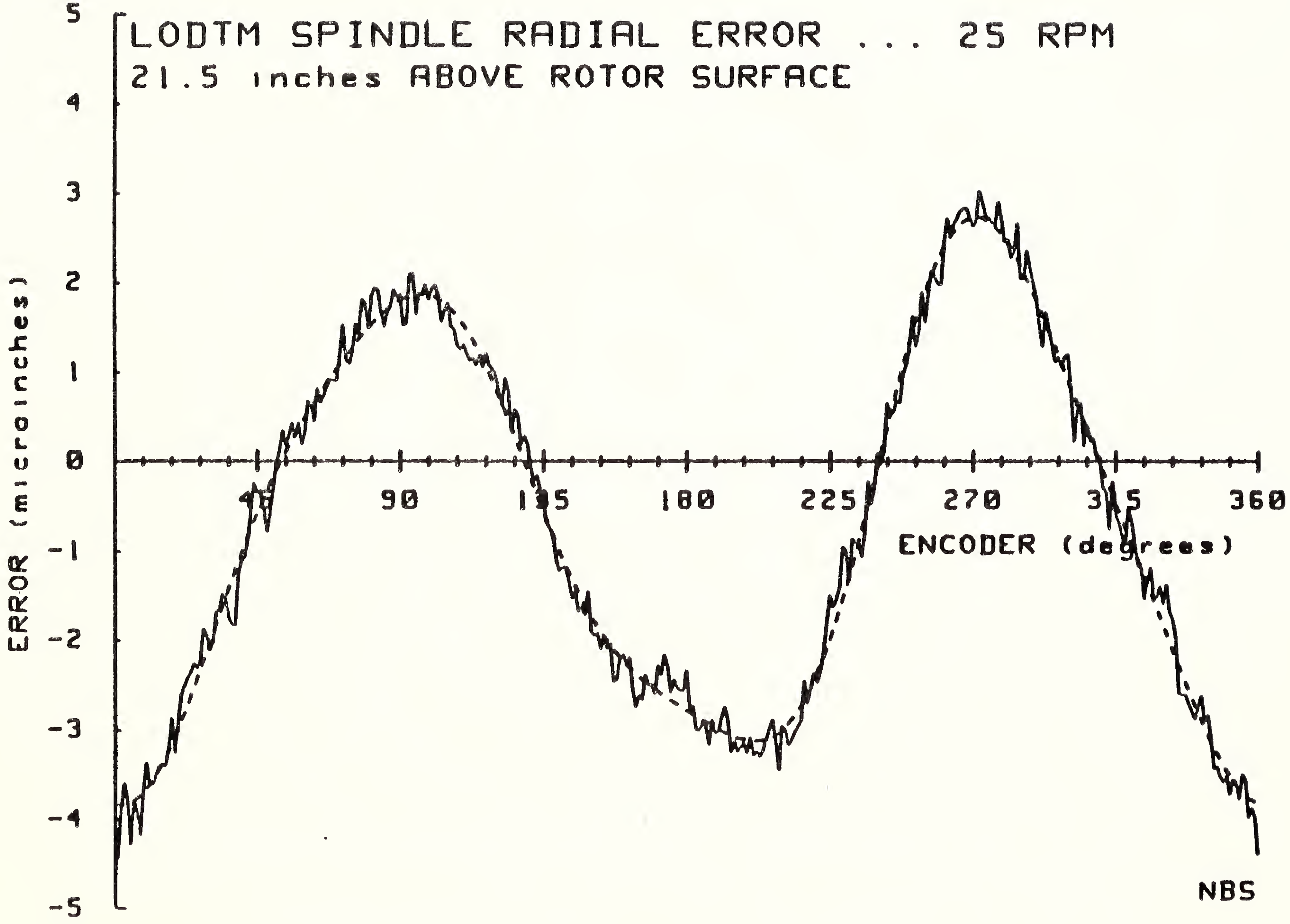
LODTM SPINDLE RADIAL ERROR ... 25 RPM
21.5 inches ABOVE ROTOR SURFACE
ERROR (microinches)
5
4
3
2
1
0
-1
-2
-3
-4
-5
45
90
135
180
225
270
315
360
ENCODER (degrees)
NBS

Figure 48

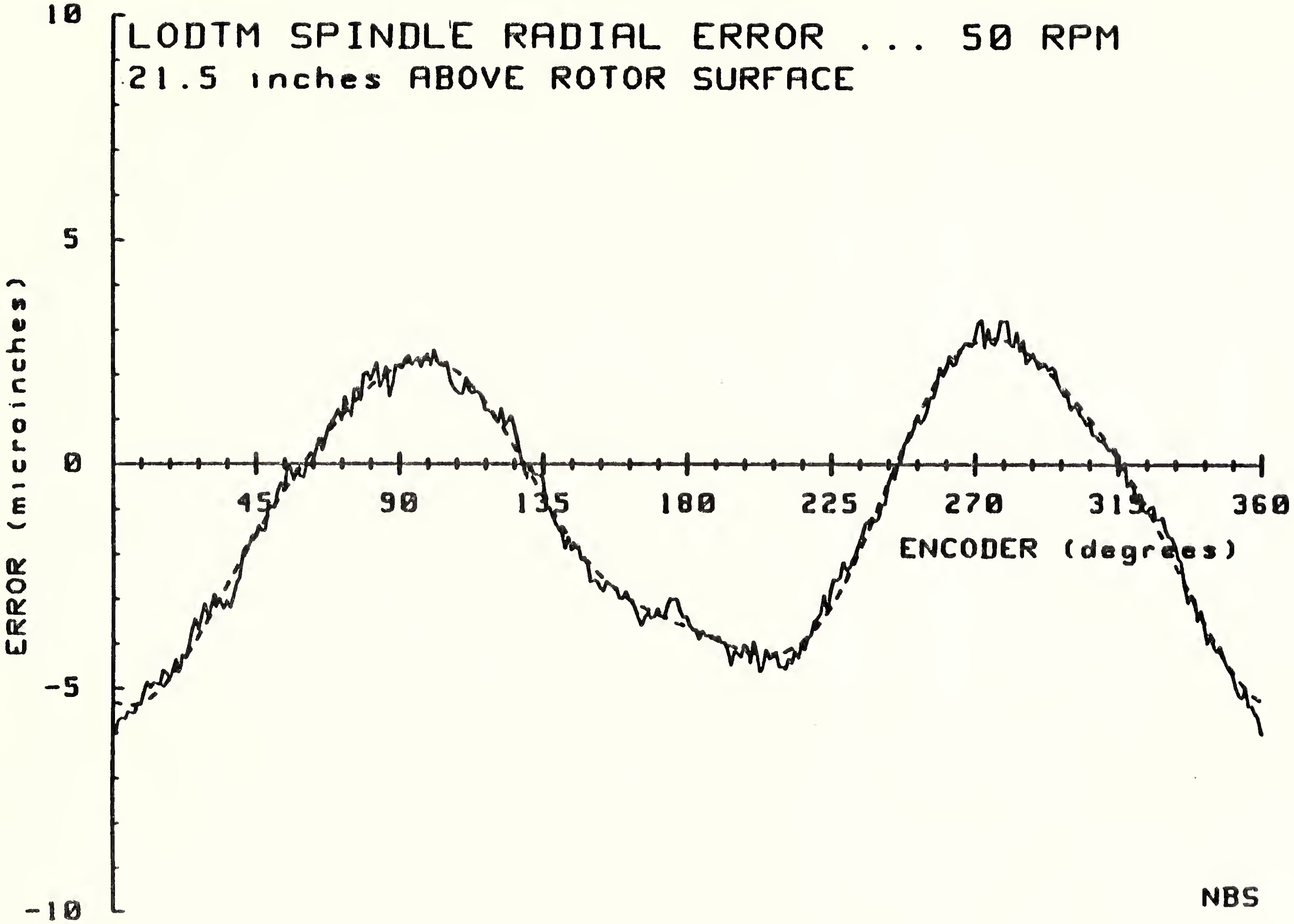
LODTM SPINDLE RADIAL ERROR ... 50 RPM
21.5 inches ABOVE ROTOR SURFACE
10
5
0
-5
-10
ERROR (microinches)
45
90
135
180
225
270
315
360
ENCODER (degrees)
NBS

Figure 49

LODTM SPINDLE RADIAL MOTION

Fourier Components

Z = 7.5 inches

k	A_k (microinches)		B_k (microinches)	
	25 RPM	50 RPM	25 RPM	50 RPM
0	-0.04	0.20	---	---
1	---	---	---	---
2	-1.49	-1.81	-0.49	-0.62
3	-0.11	-0.27	0.10	0.07
4	0.03	0.02	0.01	-0.02
5	-0.09	-0.14	-0.03	-0.06
6	-0.06	-0.06	0.05	0.04
7	-0.06	-0.07	0.06	0.06
8	-0.01	-0.03	0.00	0.00
9	-0.06	-0.08	-0.01	-0.02
10	-0.04	0.01	0.02	0.02

Table 2

LODTM SPINDLE RADIAL MOTION

Fourier Components

Z = 21.5 inches

k	A_k (microinches)		B_k (microinches)	
	25 RPM	50 RPM	25 RPM	50 RPM
0	-0.71	-1.16	---	---
1	---	---	---	---
2	-2.76	-3.43	-0.39	-1.02
3	-0.30	-0.51	0.33	0.14
4	0.19	0.17	-0.02	-0.02
5	-0.25	-0.33	-0.13	-0.14
6	-0.03	-0.04	-0.01	0.01
7	-0.11	-0.15	0.03	0.05
8	0.04	0.03	0.00	0.04
9	-0.01	-0.03	0.02	0.02
10	-0.03	-0.04	0.01	0.03

Table 3

each case, essentially all of the observed error is accounted for by the first three or four terms in Eq.(53), with the second-harmonic (k=2) contribution by far the predominant.

We make two observations concerning these results. First, it is clear that the uncorrected LODTM spindle has a remarkably small radial error motion for its size, and could be used in its present state for all but the most precise fabrication work. Second, because of the very simple and systematic form of these errors and the lack of high harmonic content, analytic corrections could be implemented in the control software and radial errors removed from the workpiece by command corrections to the X-axis slide servo, which has ample frequency response to handle these 4-5 Hz maximum bandwidth error motions.

Finally, in Figs. (50) and (51) we display the roundness errors of the cylindrical square at the locations corresponding to Z=7.5 inches and Z=21.5 inches respectively. A complete analysis of these errors showed them to be independent of spindle speed (as expected) and independent of the mode of computation. [i.e., using either Eq.(52a) or (52b-c)]. As suggested by the Z-axis straightness data (Sec.7.B.), these figures show that this mechanical artifact is a very good one, with P-V roundness errors of approximately 5 microinches at the two measured cross-sections.

9.B. Axial Error Motion

CYLINDRICAL SQUARE ERROR -- 25 RPM -- Z=7.5 inches

CIRCLE SEPARATION = 5 microinches

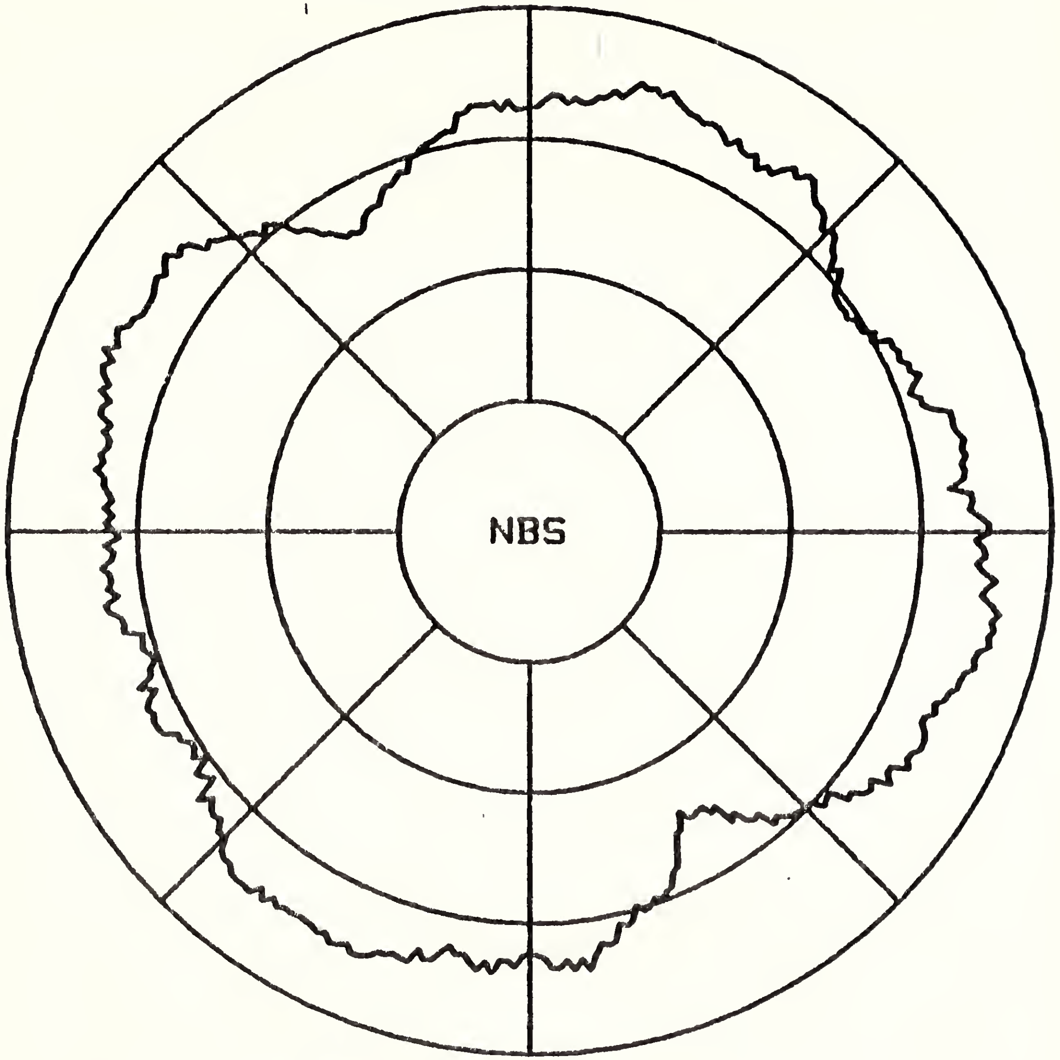

ERROR COMPUTED BY: (FS+RN)/2

Figure 50

CYLINDRICAL SQUARE ERROR -- 25 RPM -- Z=21.5 inches

CIRCLE SEPARATION = 5 microinches

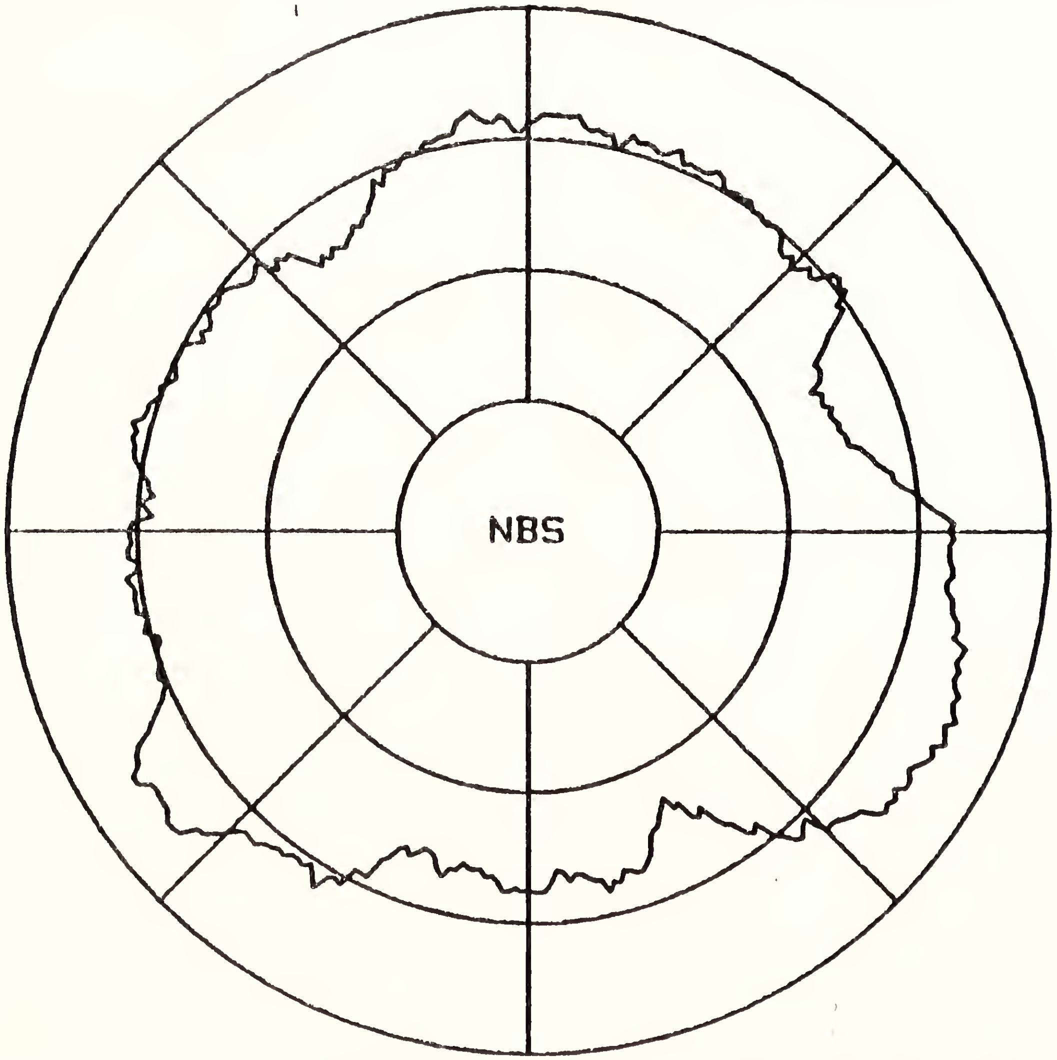

ERROR COMPUTED BY: (RS+FN)/2

Figure 51

The axial errors of the LODTM spindle were measured using a 2-inch diameter precision tungsten carbide ball as a test artifact. Motions of the ball along the X and Z directions were monitored using the two Invar capacitance gauges mounted on an L-shaped fixture. The set-up was functionally identical to that used for X-Z drift tests as described in Sec. 1 and shown schematically in Fig.(1).

The error motion of interest, in the axial or Z direction, was measured by the vertically-oriented Z-axis gauge. The X-axis gauge provided centering information on the test ball. Unlike radial motion errors, a once-per-revolution or first-harmonic axial motion is a direct source of workpiece figure error. For this reason it is necessary to use great care in both gauge alignment and ball centering when measuring axial motion. It is straightforward to show that if the test ball is off center by an amount r and the Z-axis gauge off center (i.e. off axis) by an amount Δ, then the measurement data will contain an undesirable first-harmonic component of P-V amplitude $2r\Delta/R$, where R is the radius of the test ball. This apparent motion is indistinguishable from real axial error motion and must therefore be minimized. By direct measurement and adjustment during set-up, Δ was reduced to 0.001 inch or less, while analysis of the X-axis gauge data yielded ball centering error of less than 20 microinches. Thus, for R=1 inch, the resultant undesired apparent motion was ≈ 0.04 microinches. This is a negligible error.

The measured axial motion, at spindle speeds of 25 and 50 RPM respectively, is shown in Figs.(52) and (53). The 50 RPM data is noticeable smoother than

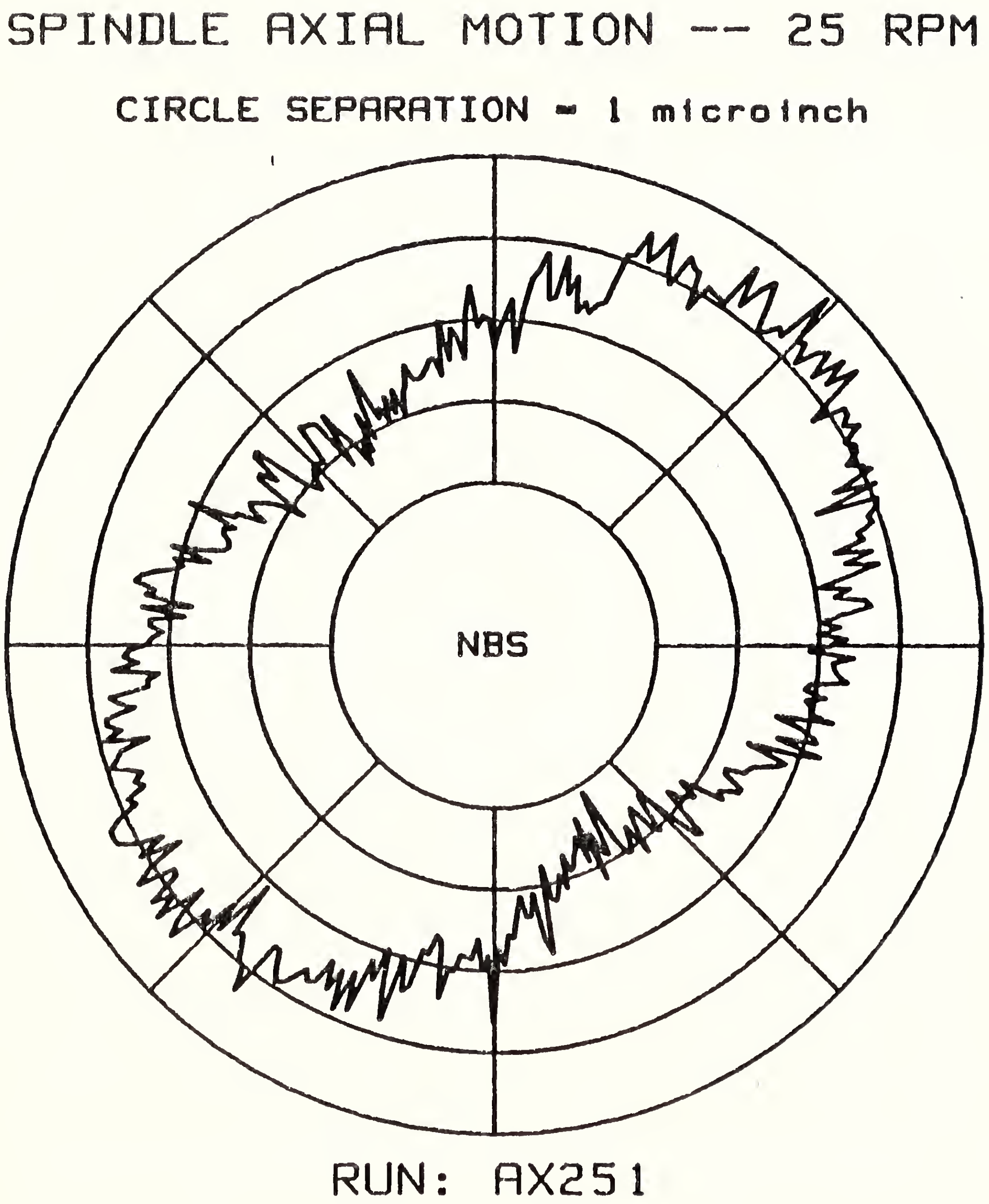
SPINDLE AXIAL MOTION -- 25 RPM
CIRCLE SEPARATION = 1 microinch
NBS
RUN: AX251

Figure 52

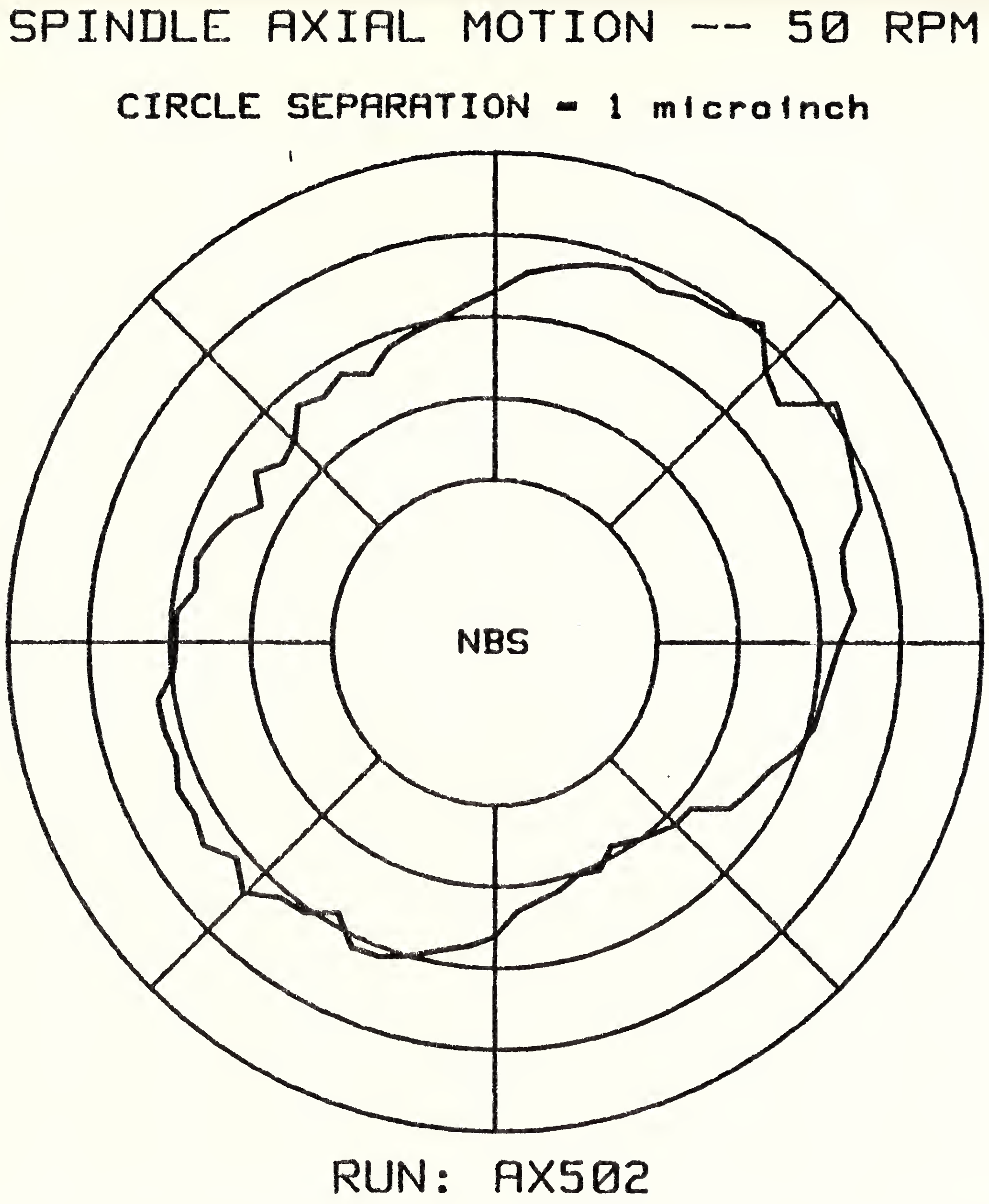
SPINDLE AXIAL MOTION -- 50 RPM
CIRCLE SEPARATION = 1 microinch
NBS
RUN: AX502

Figure 53

that at 25 RPM because of increased averaging. The axial motion at 50 RPM was measured every 5 degrees of angular position, so that each point represents the average of 110 samples. The 25 RPM data is averaged over only 22 revolutions.

Figures (54) and (55) show linear plots of the axial errors, together with dashed lines representing Fourier series curve fits described by Eq.(53). As in the case of the radial errors, the dominant contributions to the axial motions are second-harmonic in nature. The general shape of the axial motion is preserved at the two measured speeds, with a tendency towards decreasing amplitude as the speed increases. It should also be noted that the magnitude of these errors is quite small, being no more than about 3 microinches P-V at 25 RPM. The coefficients of the harmonic terms in the Fourier series, Eq.(53), for the axial motion are given in Table 4 for 25 RPM (N=10) and 50 RPM (N=5).

9.C. Tilt Error Motion

Once the radial error motion of the LODTM spindle is known at two axial locations, it is a straightforward matter to compute the spindle angular, or tilt, motion in the sensitive direction. Denoting the radial error motions at the low and high positions, respectively, by $S_L(\Theta)$ and $S_H(\Theta)$, and the axial separation of these locations by Z_0, the tilt error motion $T(\Theta)$ is given by

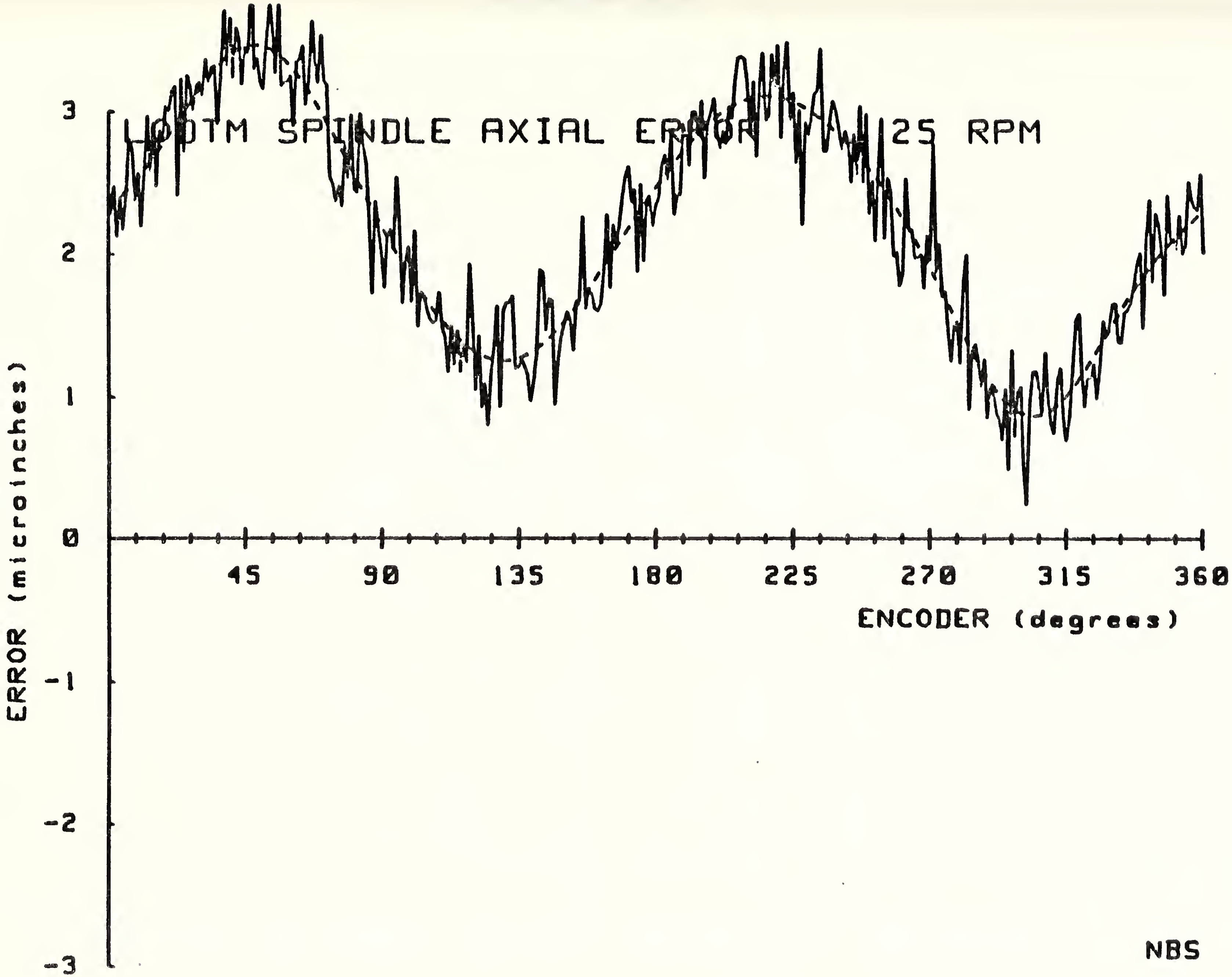
LODTM SPINDLE AXIAL ERROR 25 RPM
ERROR (microinches)
3
2
1
0
-1
-2
-3
45
90
135
180
225
270
315
360
ENCODER (degrees)
NBS

Figure 54

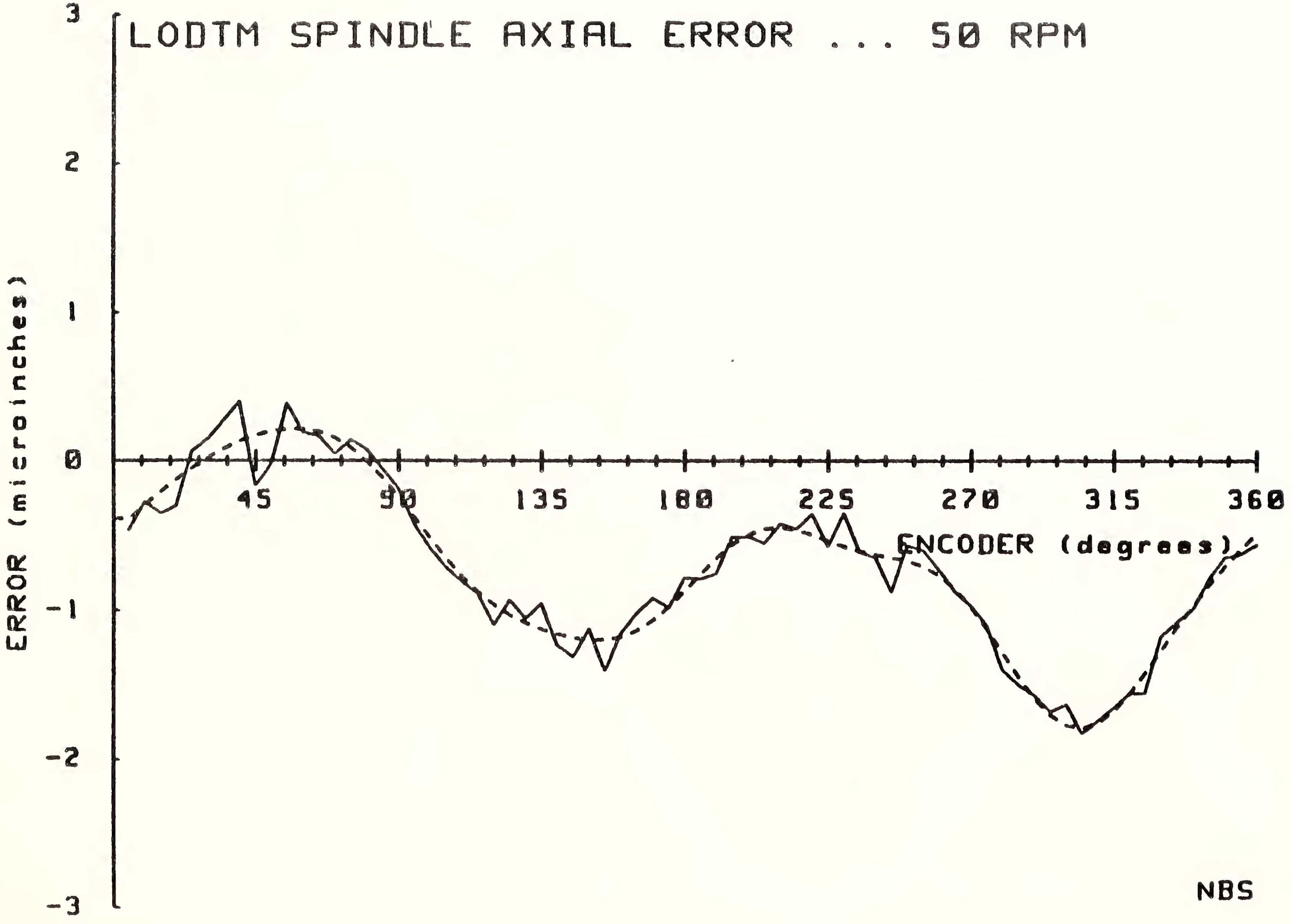
LODTM SPINDLE AXIAL ERROR ... 50 RPM
ERROR (microinches)
3
2
1
0
-1
-2
-3
45
90
135
180
225
270
315
360
ENCODER (degrees)
NBS

Figure 55

LODTM SPINDLE AXIAL MOTION

Fourier Components

k	A_k (microinches)		B_k (microinches)	
	25 RPM	50 RPM	25 RPM	50 RPM
0	2.21	-0.72	---	---
1	-0.02	0.13	0.14	0.41
2	0.20	0.00	1.03	0.63
3	-0.03	0.06	-0.03	-0.03
4	0.01	0.07	-0.11	-0.04
5	-0.03	0.01	-0.08	-0.07
6	-0.02		-0.03	
7	-0.01		0.01	
8	0.01		0.00	
9	-0.01		-0.01	
10	-0.02		-0.05	

Table 4

$$T(\Theta) = \frac{S_H(\Theta) - S_L(\Theta)}{4.85Z_0} \quad . \qquad (54)$$

In this expression, S_H and S_L are in microinches, Z_0 = 14 inches, and the factor of 4.85 in the denominator is included to yield $T(\Theta)$ in arc-seconds.

The resultant tilt error motions, at spindle speeds of 25 and 50 RPM, are shown in Figs.(56) and (57). Total P-V error at both speeds is of the order of 0.04 arc-seconds or about 0.2 microradians. The Fourier components for the tilt error may be computed from Eq.(54), along with the fit coefficients tabulated in Tables 2 and 3.

9.D. Spindle Capacitance Gauges

In the course of our measurements of the LODTM spindle error motions, we recorded the output signals of the spindle capacitance gauges which are intended to be used for real-time correction of the tool point position. There are four of these gauges altogether; one pair (North and South) is sensitive to radial, or X, spindle motion and another pair (again, North and South) is sensitive to axial, or Z, motion. By appropriate addition or subtraction of the outputs of these gauges, all components of the spindle error motion may be measured during part machining. Of course, in order to actually implement this dynamic correction procedure, each of the

SPINDLE TILT MOTION -- 25 RPM

CIRCLE SEPARATION = .02 arc-seconds

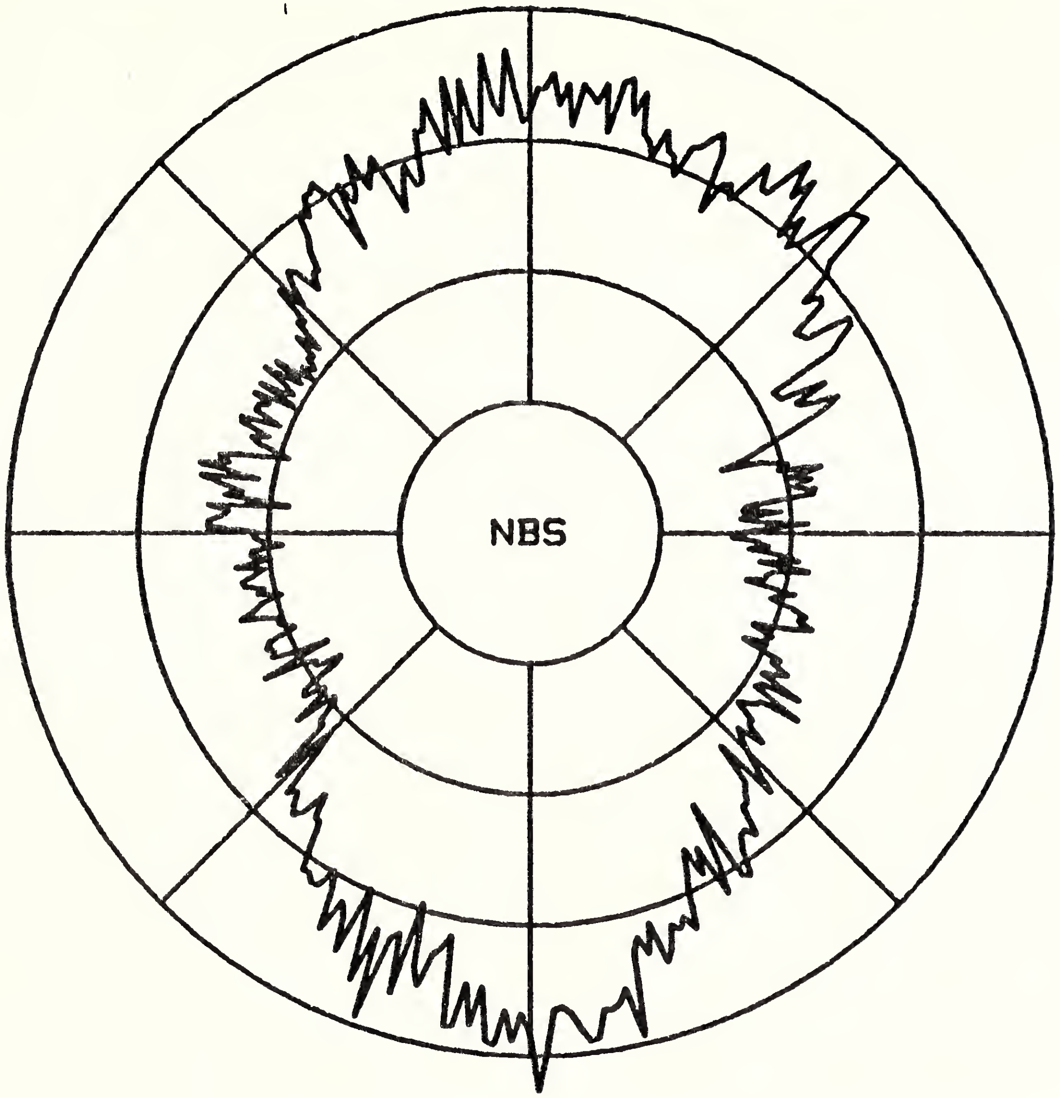

Figure 56

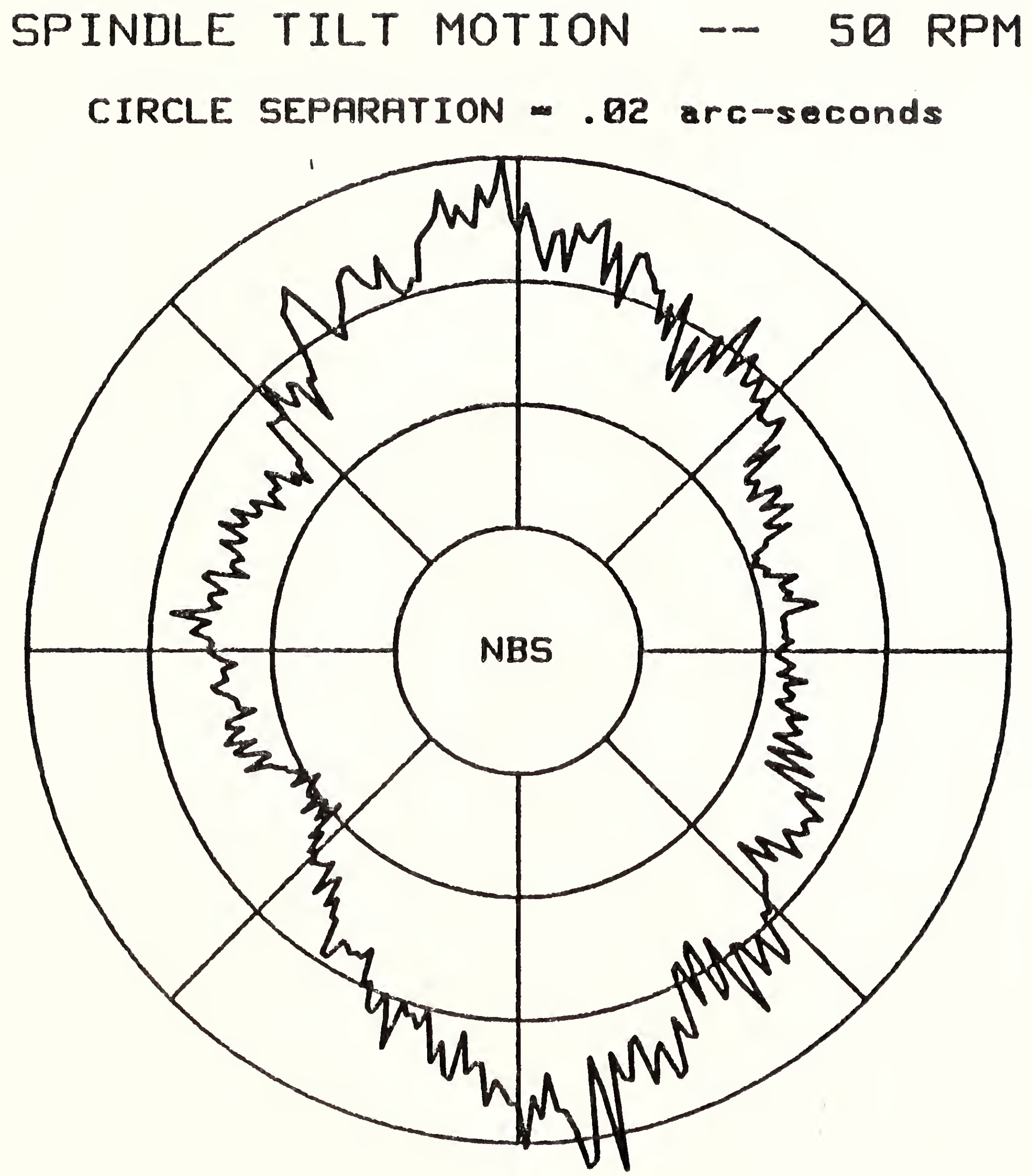
SPINDLE TILT MOTION -- 50 RPM
CIRCLE SEPARATION = .02 arc-seconds
NBS

Figure 57

capacitance gauges must be accurately calibrated. Furthermore, it is necessary to correct the gauge outputs for apparent motions caused by form errors of the nominally circular gauging surfaces machined into the spindle rotor.

The original procedure, as envisaged by the LODTM staff, was to perform the gauging surface calibrations (groove shapes) at very low spindle speed and to store this data in the form of capacitance gauge lookup tables. As we discovered, however, this procedure will not work because the gauge outputs are sensitive functions of spindle speed. This speed dependence is illustrated by Figs.(58-61). Figures (58) and (59) show, respectively, the output signals of the South-X and South-Z spindle capacitance gauges at two rotational speeds. In each figure the solid curve is the output at 2 RPM and the dashed curve is the output at 50 RPM. The spindle speed dependence is evident from these figures, and is more clearly shown by the differences plotted in Figs. (60) and (61). At the time of these measurements, (December, 1984) the displacement sensitivities of the South-X and South-Z capacitance gauges were, respectively, 30.0 mV/microinch and 22.5 mV/microinch, according to calibration data supplied by the staff of LODTM. From Fig. (60) we see that the P-V change output between 2 RPM and 50 RPM is for the South-X, approximately 1.2V which corresponds to an apparent change in radial motion of approximately 40 microinches. For the South-Z gauge, the P-V change in output is about 0.35 V, yielding an apparent change in axial and/or tilt motion of nearly 16 microinches. Corresponding results for the two North capacitance gauges were essentially the same.

While it is possible in principle for these changes to represent actual behavior of the LODTM spindle rotor, the small changes in actual motion

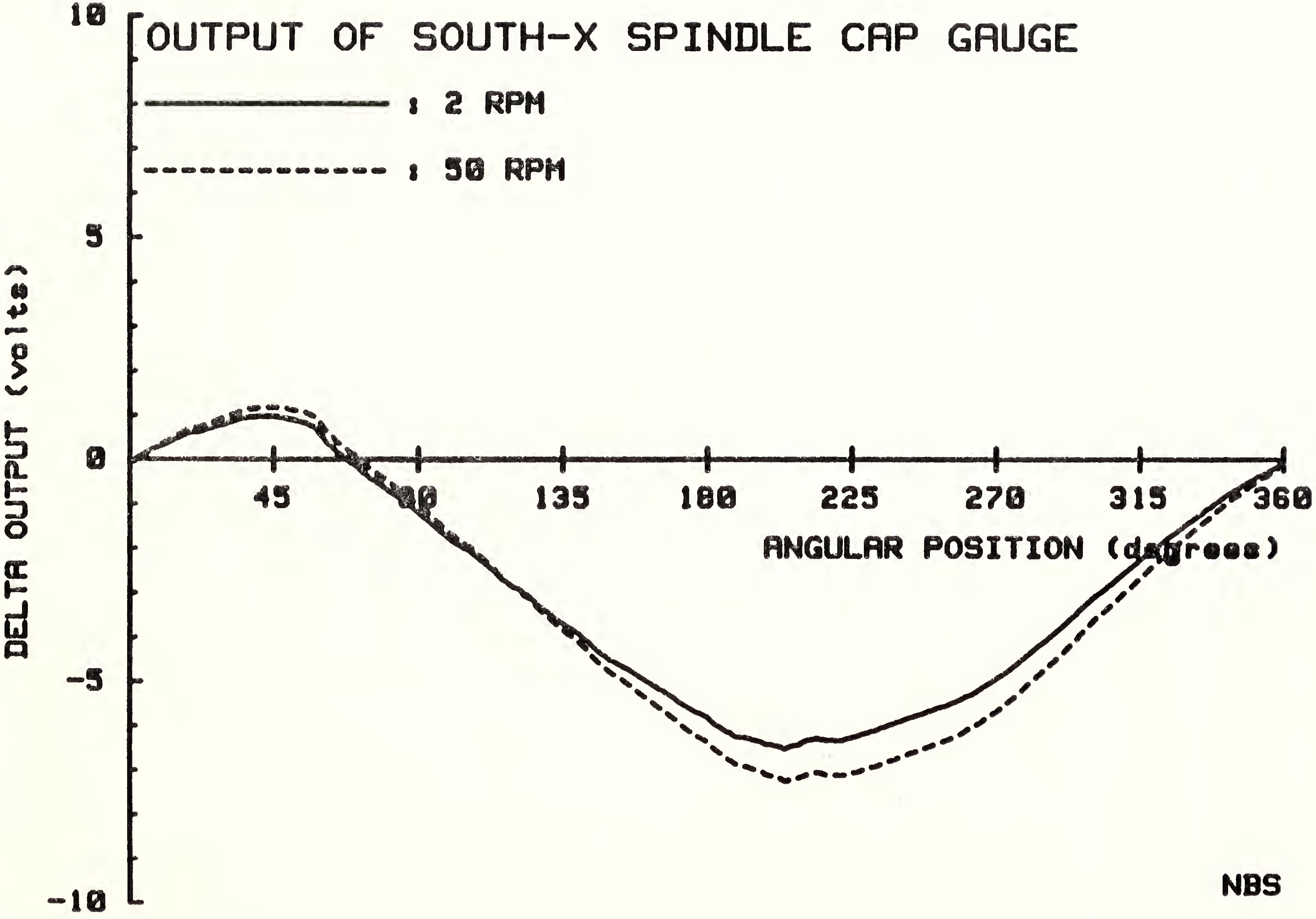
OUTPUT OF SOUTH-X SPINDLE CAP GAUGE
: 2 RPM
: 50 RPM
10
5
0
-5
-10
DELTA OUTPUT (volts)
45
90
135
180
225
270
315
360
ANGULAR POSITION (degrees)
NBS

Figure 58

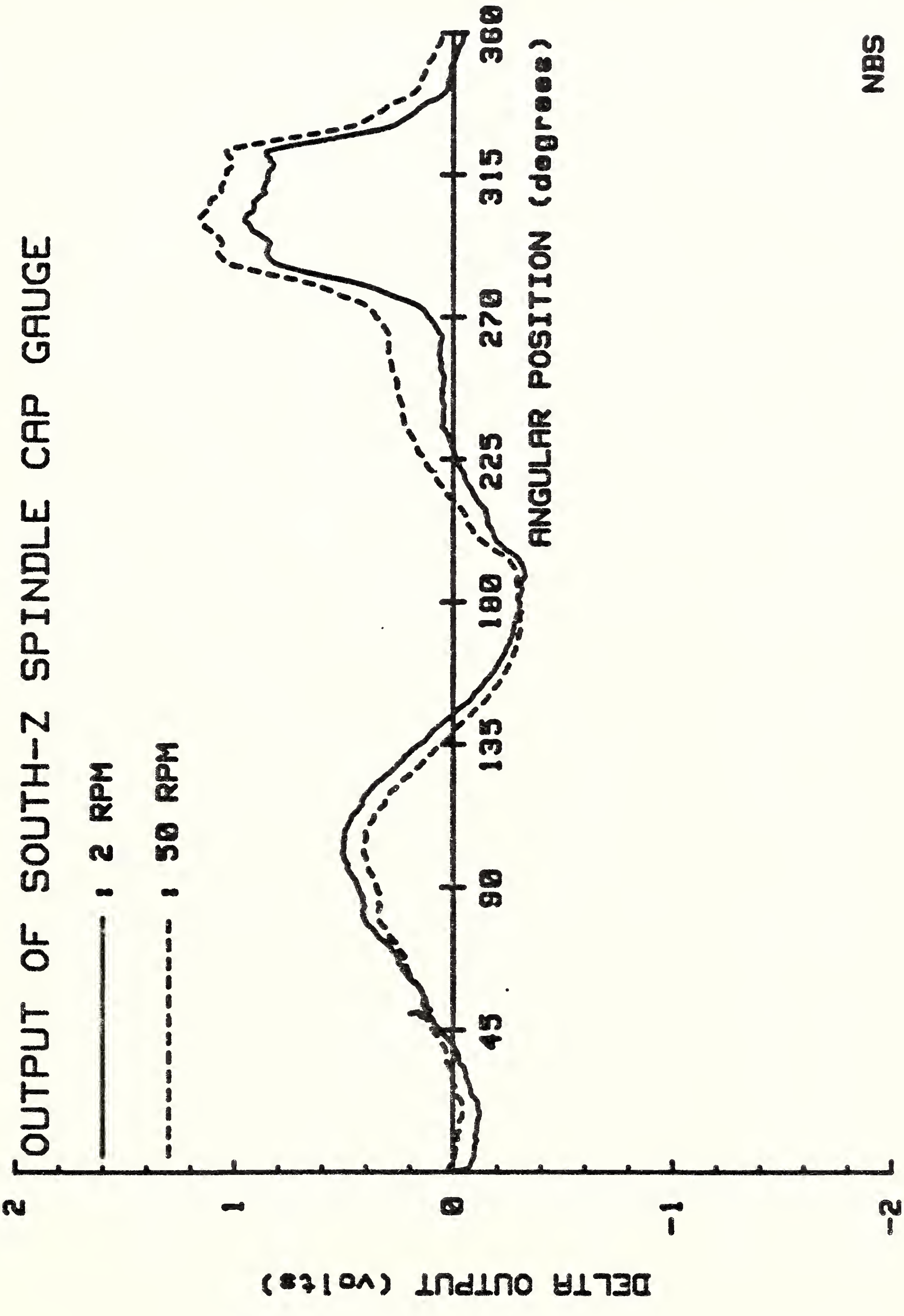
OUTPUT OF SOUTH-Z SPINDLE CAP GAUGE
2 RPM
50 RPM
DELTA OUTPUT (volts)
2
1
0
-1
-2
ANGULAR POSITION (degrees)
45
90
135
180
225
270
315
360
NBS

Figure 59

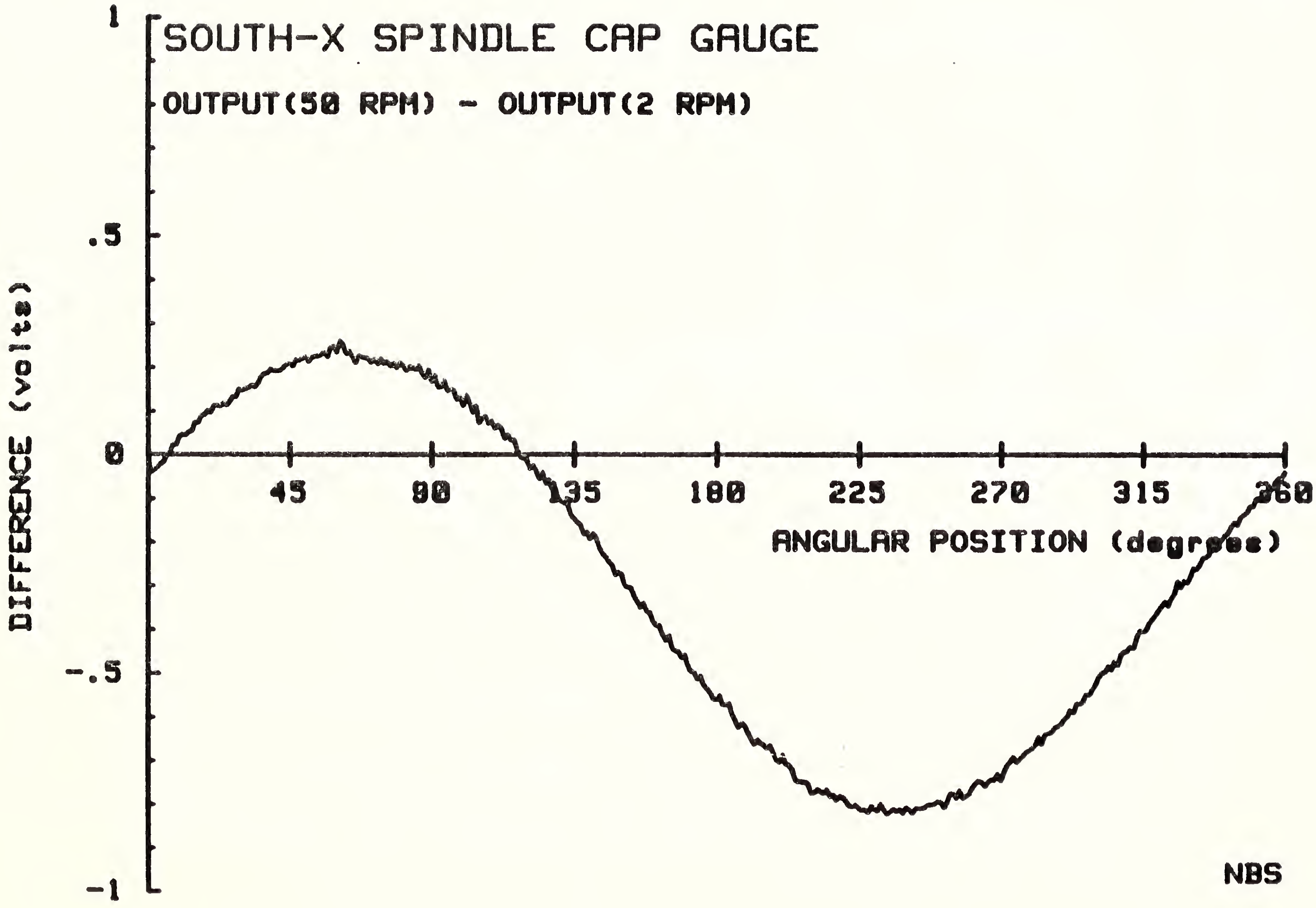
SOUTH-X SPINDLE CAP GAUGE
OUTPUT(50 RPM) - OUTPUT(2 RPM)
DIFFERENCE (volts)
1
.5
0
-.5
-1
45
90
135
180
225
270
315
360
ANGULAR POSITION (degrees)
NBS

Figure 60

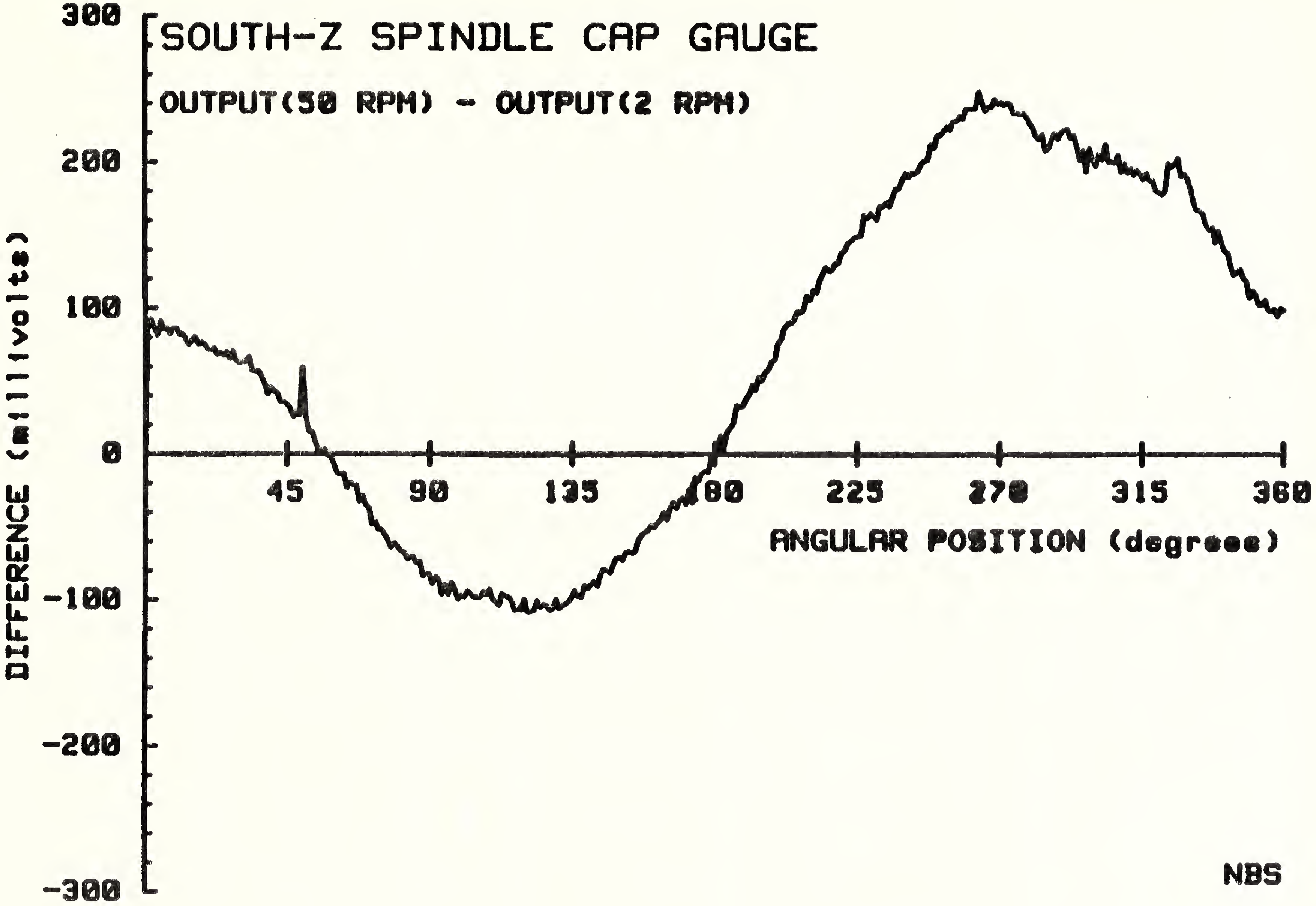
SOUTH-Z SPINDLE CAP GAUGE
OUTPUT(50 RPM) - OUTPUT(2 RPM)
300
200
100
0
-100
-200
-300
DIFFERENCE (millivolts)
45
90
135
180
225
270
315
360
ANGULAR POSITION (degrees)
NBS

Figure 61

between 25 and 50 RPM suggest, in our opinion, a dynamic change in capacitance gauge output caused by some combination of groove centrifugal distortion and hydrodynamic interaction of the gauges with the air in the sensing grooves. At any rate, we believe that these results make it mandatory to do the necessary groove shape calibrations at actual machining spindle speeds.

9.E. Spindle Random Motion / Capacitance Gauge Noise

In an effort to estimate the "random", or non-repeatable components of the spindle error motion, in this section we present further analyses of the output signals of the LODTM spindle capacitance gauges.

The first observation concerns the calibration factors of the X-axis gauges, which were supplied by the LODTM staff. These numbers appear to be inconsistent. To see the source of this inconsistency, we consider the following set of relations between the gauge error signals and the terms which affect their outputs. For an arbitrary set of sign conventions, these relations are

$$XS(\theta) = A\sin\theta + B\cos\theta + R(\theta) + GX(\theta) + Snoise(\theta) \qquad (55)$$

$$XN(\theta) = -A'\sin\theta - B'\cos\theta - R(\theta) + GX(\theta+\pi) + Nnoise(\theta) \qquad (56)$$

Here, XS and XN represent the displacements indicated by the South and North X-axis gauges, $R(\Theta)$ is the spindle radial motion, and $GX(\Theta)$ is the form error of the X-axis capacitance gauge groove. The first two terms in each expression represent first-harmonic "centering error"; in a case where $R(\Theta) = GX(\Theta) = 0$, and for noise-free gauges, we would expect $A = A'$ and $B = B'$. Any deviation from this condition would indicate the non-repeatable noise signals of the gauges; non-repeatable radial motion has been included in $R(\Theta)$.

Using a 2-parameter least-squares algorithm, we determined the coefficients A,A',B, and B' for the gauge signals at 50 RPM, using the calibration factors as determined by the LODTM staff (South-X: 30 mV/microinch and North-X: 34 mV/microinch). The results were: $A = 77.6$, $B = 109.1$, $A' = 58.8$, and $B' = 81.9$, where all units are microinches. From these results we see that $A/A' = B/B' = 1.33$, so that for a given radial displacement of the spindle rotor the motion indicated by the South gauge would be some 30% greater than that of the North gauge. There is no way from this data to decide whether one or both of the gauges was improperly calibrated, but it does suggest a careful review and check of the calibration procedure.

In order to proceed with the analysis, we arbitrarily increased the South-X gauge sensitivity from 30 mV/microinch to ≈40 mV/microinch so that Eqs.(55) and (56) would yield a consistent set of centering error coefficients. We also assume correct calibration factors for the Z-axis gauges, whose outputs are not amenable to the centering error analysis. This latter result is due to the mixture of axial and tilt motion in the outputs of the Z-axis gauges.

Figures (62-65) show the measured peak-valley output spread for each of the LODTM capacitance gauges at 50 RPM. At each angular position ($\Delta\Theta$ = 1 degree) the indicated value is just the difference between the maximum and minimum gauge output voltage divided by the appropriate sensitivity, as recorded over 22 spindle revolutions. In each case the P-V spread is about 2 microinches, being slightly greater for the North-X gauge. The latter effect may be due to a vibration of the North end of the LODTM metrology frame which we observed very briefly but did not systematically study.

These measurements indicate a "random" or non-repeatable error signal of ≈±1 microinch from each of the LODTM capacitance gauges at 50 RPM. The crucial question is how much of this error is due to spindle non-repeatability and how much is inherent gauge noise. Relations (55) and (56) suggest a way to estimate the latter. By adding the equations we have (taking A=A' and B=B')

$$XS(\Theta) + XN(\Theta) = GX(\Theta) + GX(\Theta+\pi) + Snoise(t) + Nnoise(t). \qquad (57)$$

In this expression the arguments of the noise functions are written as t, the time of gauge sampling, since they are not strictly functions of Θ. By averaging both sides of this equation over many revolutions, the noise terms tend to zero and we get an approximation to the function $GX(\Theta) + GX(\Theta+\pi)$. This function is shown in Fig.(66), averaged over 22 revolutions at 50 RPM, and is clearly seen to have period π. Replacing Θ with $\Theta+\pi$ in Eq.(57) yields

$$XS(\Theta+\pi) + XN(\Theta+\pi) = GX(\Theta+\pi) + GX(\Theta+2\pi) + Snoise(t') + Nnoise(t'), \qquad (58)$$

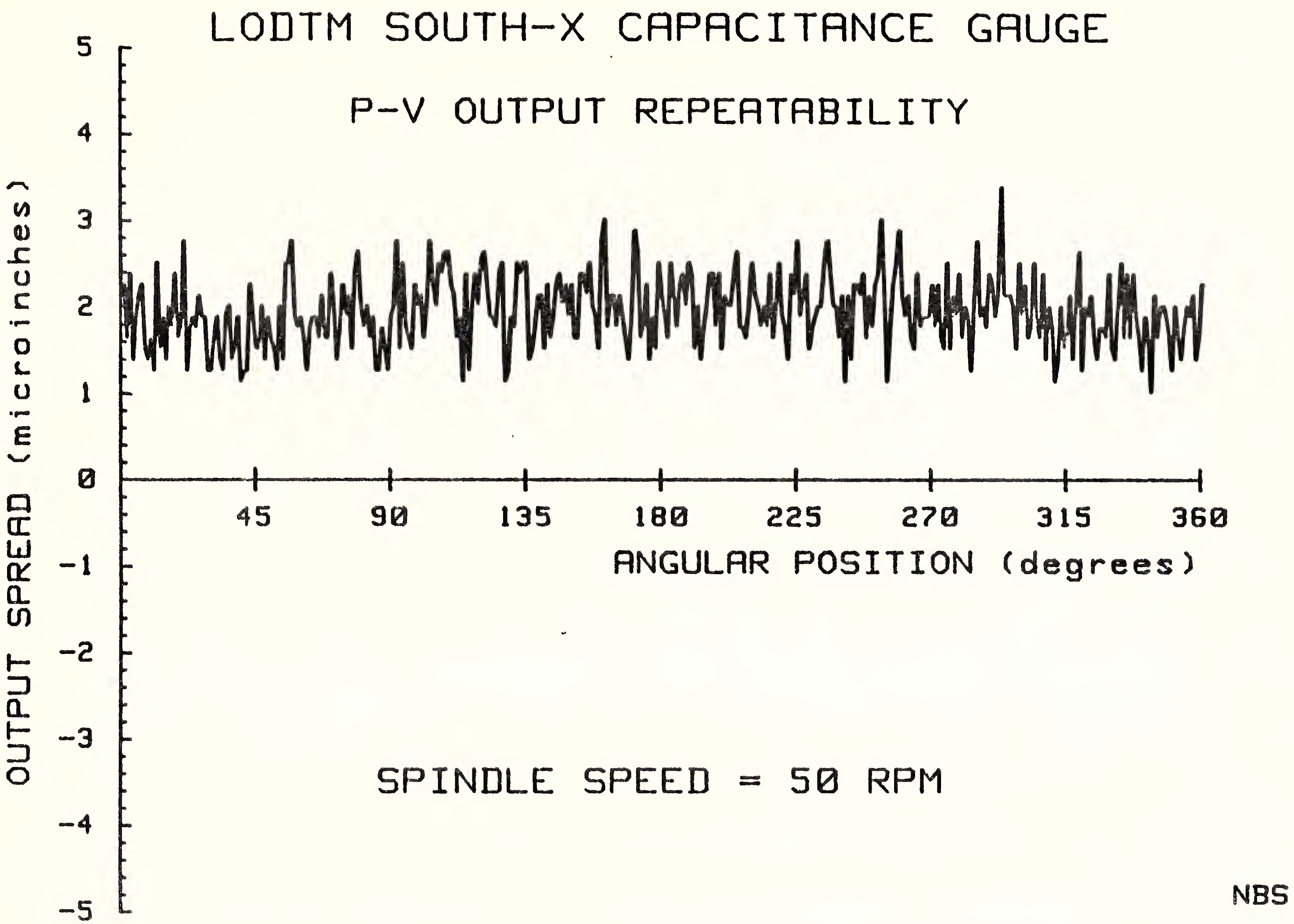
LODTM SOUTH-X CAPACITANCE GAUGE
P-V OUTPUT REPEATABILITY
OUTPUT SPREAD (microinches)
5
4
3
2
1
0
-1
-2
-3
-4
-5
45
90
135
180
225
270
315
360
ANGULAR POSITION (degrees)
SPINDLE SPEED = 50 RPM
NBS

Figure 62

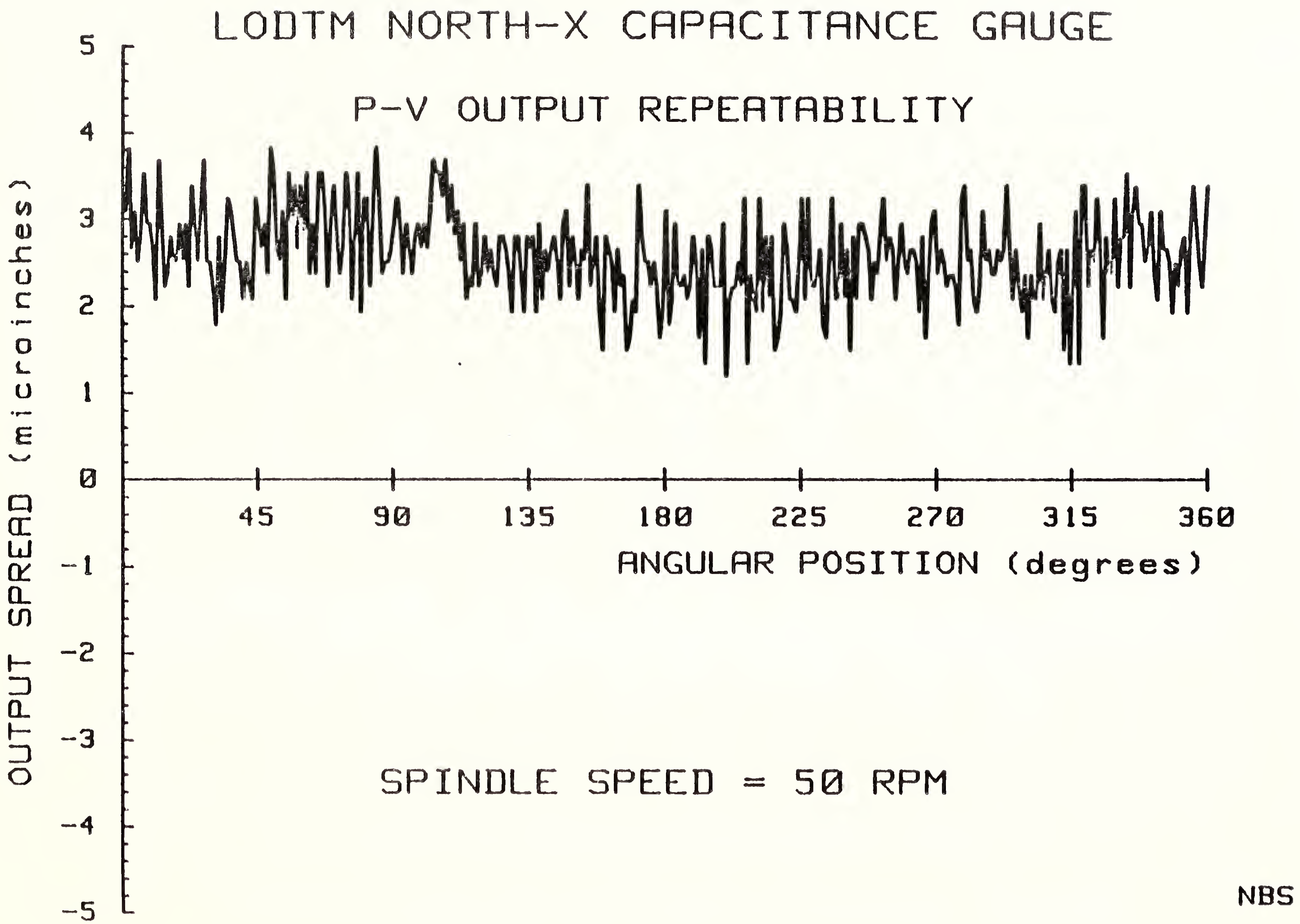
LODTM NORTH-X CAPACITANCE GAUGE
P-V OUTPUT REPEATABILITY
OUTPUT SPREAD (microinches)
5
4
3
2
1
0
-1
-2
-3
-4
-5
45
90
135
180
225
270
315
360
ANGULAR POSITION (degrees)
SPINDLE SPEED = 50 RPM
NBS

Figure 63

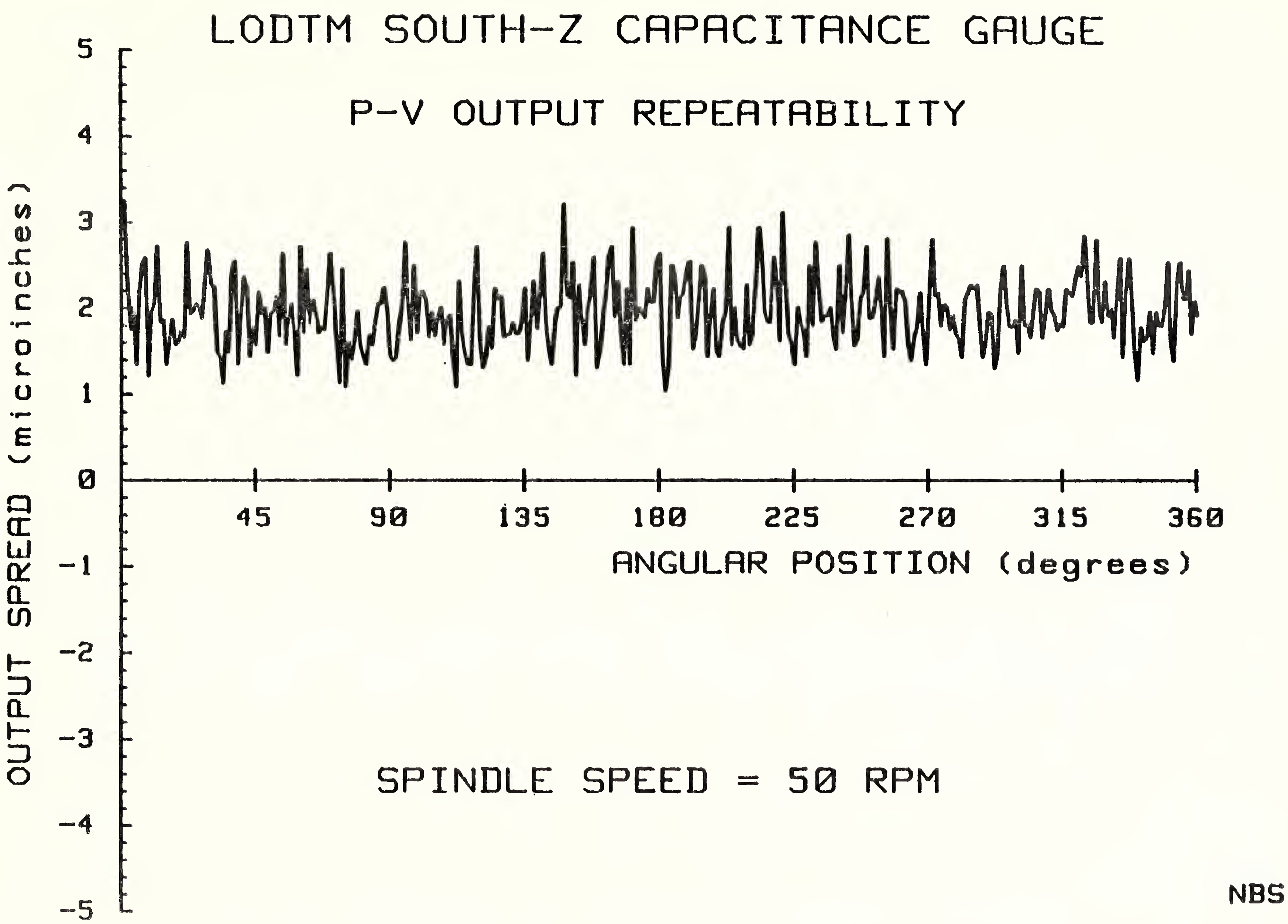
LODTM SOUTH-Z CAPACITANCE GAUGE
P-V OUTPUT REPEATABILITY
OUTPUT SPREAD (microinches)
5
4
3
2
1
0
-1
-2
-3
-4
-5
45
90
135
180
225
270
315
360
ANGULAR POSITION (degrees)
SPINDLE SPEED = 50 RPM
NBS

Figure 64

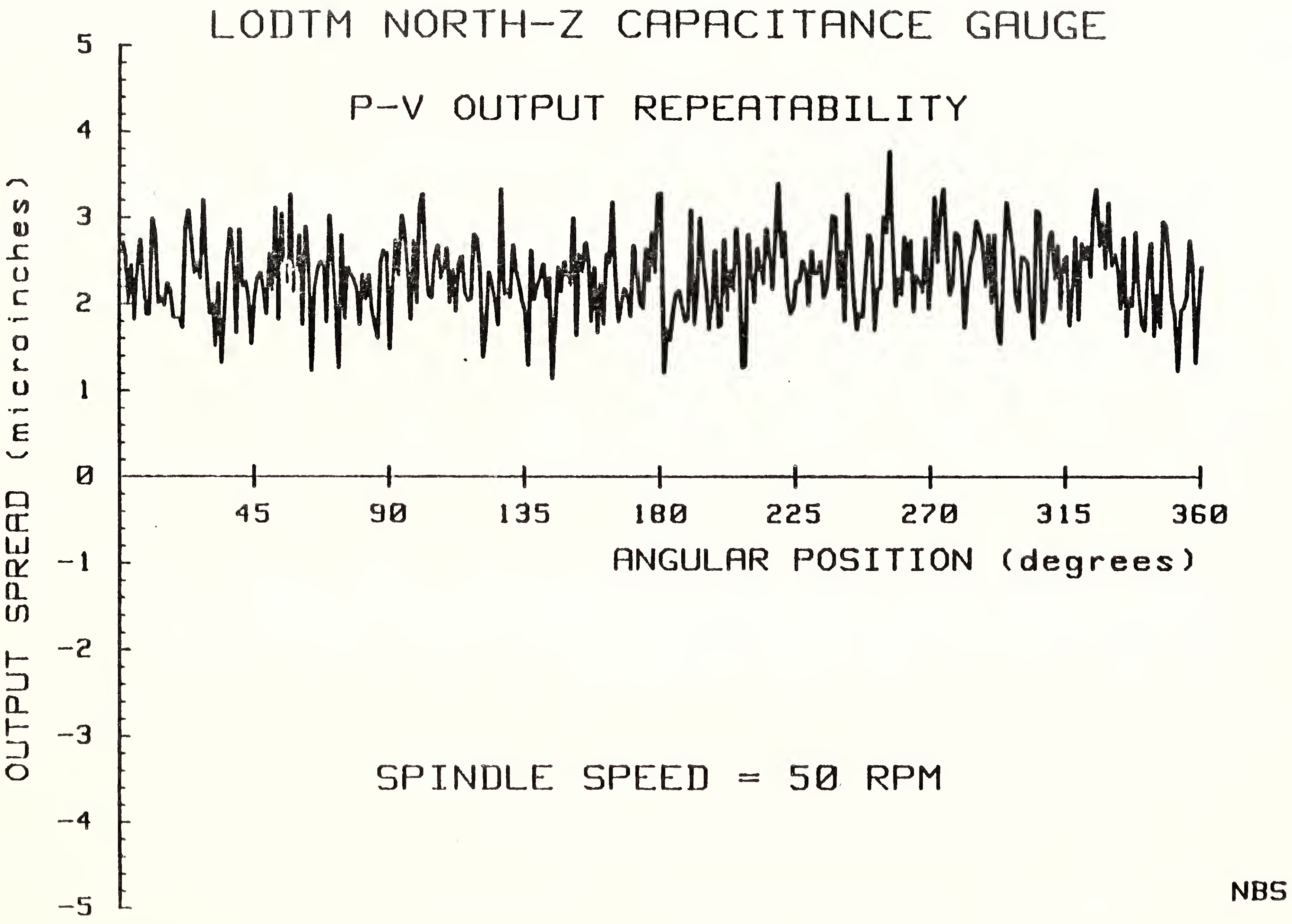
LODTM NORTH-Z CAPACITANCE GAUGE
P-V OUTPUT REPEATABILITY
OUTPUT SPREAD (microinches)
5
4
3
2
1
0
-1
-2
-3
-4
-5
45
90
135
180
225
270
315
360
ANGULAR POSITION (degrees)
SPINDLE SPEED = 50 RPM
NBS

Figure 65

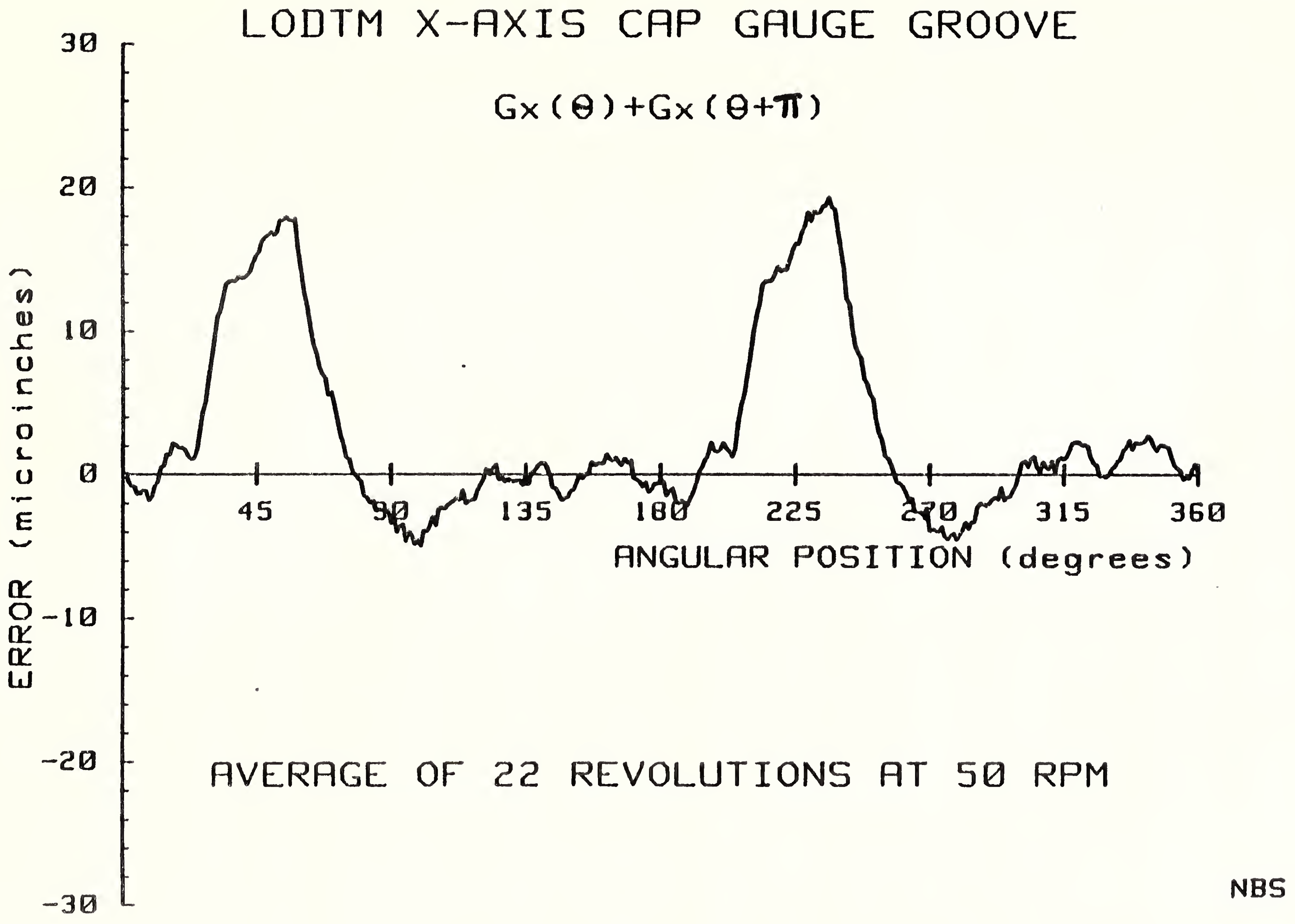
LODTM X-AXIS CAP GAUGE GROOVE
Gx(θ)+Gx(θ+π)
30
20
10
0
-10
-20
-30
ERROR (microinches)
45
90
135
180
225
270
315
360
ANGULAR POSITION (degrees)
AVERAGE OF 22 REVOLUTIONS AT 50 RPM
NBS

Figure 66

and since $GX(\Theta+2\pi) = GX(\Theta)$, subtracting (58) from (57) gives

$$XS(\Theta)+XN(\Theta)-[XS(\Theta+\pi)+XN(\Theta+\pi)]=\mathrm{Snoise}(t)-\mathrm{Snoise}(t')+\mathrm{Nnoise}(t)-\mathrm{Nnoise}(t').(59)$$

The left-hand side of (59) can be evaluated from the measurement data and used to estimate the noise level in the correction signal XS+XN. If the noise signals at t and t' are uncorrelated, then the right-hand side of (59) will have a P-V amplitude of about twice the correction signal noise level of interest.

In Fig.(67) we show one-half of the LHS of Eq.(59) for one revolution of the measured data. The noise level is ≈±2 microinches which suggests that the non-repeatability observed in the X-axis gauge signals is primarily due to gauge noise. If this is in fact correct, then it is an important observation since this noise component is comparable to the radial error motion which the capacitance gauges were designed to sense and correct. In our opinion, this question of gauge noise should be more thoroughly investigated prior to the implementation of spindle error compensation as planned in the LODTM design.

As discussed above, the foregoing analysis cannot be readily applied to the Z-axis gauges because of the mixture of error terms. The measured non-repeatable signals from these gauges, however, are nearly the same as for the X-axis gauges which suggests the possibility of comparable inherent noise levels.

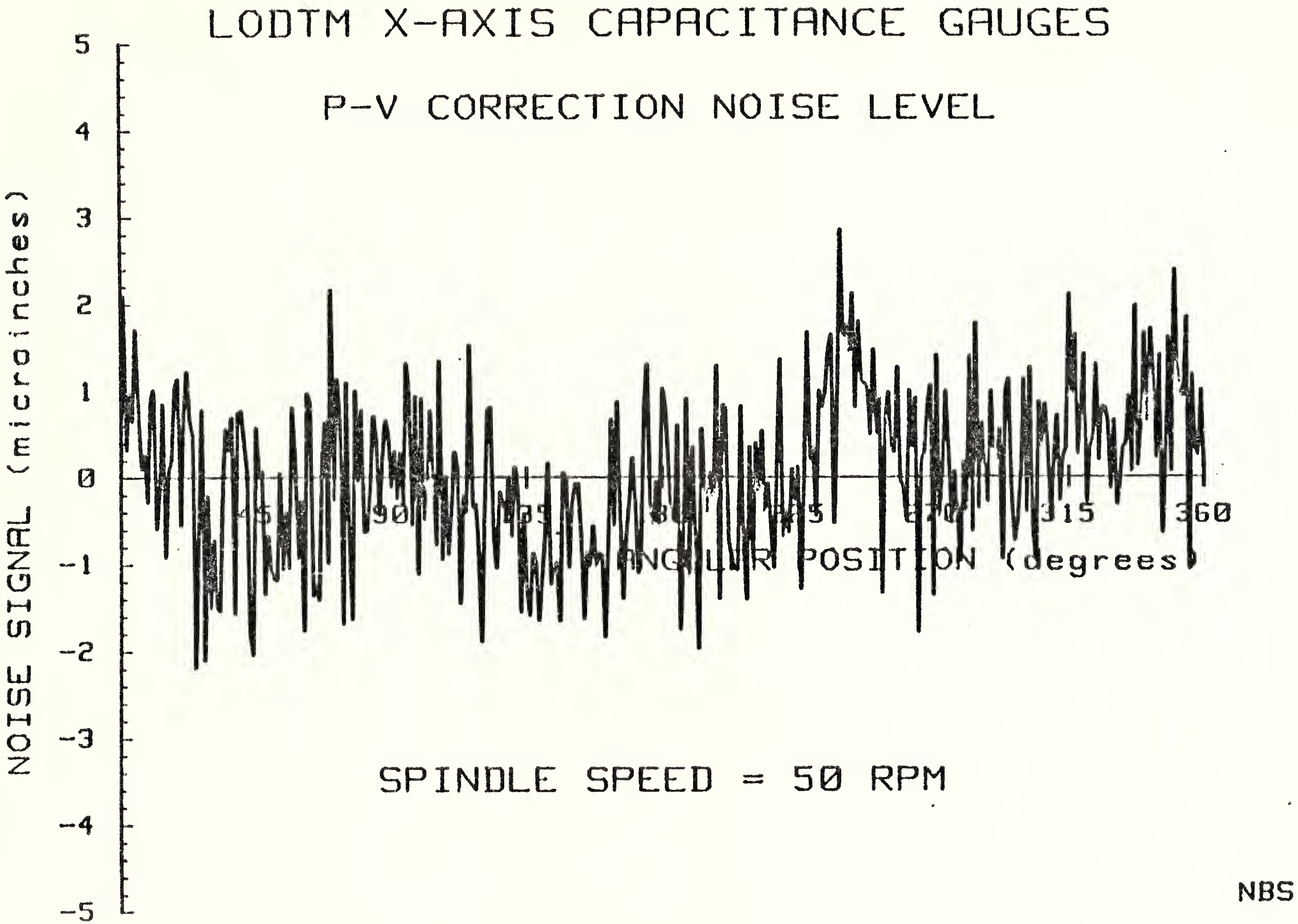
LODTM X-AXIS CAPACITANCE GAUGES
P-V CORRECTION NOISE LEVEL
NOISE SIGNAL (microinches)
5
4
3
2
1
0
-1
-2
-3
-4
-5
45
90
135
180
225
270
315
360
ANGULAR POSITION (degrees)
SPINDLE SPEED = 50 RPM
NBS

Figure 67

9.F. Dynamic Z-W Parallelism Error

In Section (7.B.) we described the slope analysis of X-straightness of Z data to yield a static measurement of the angle α between the spindle (W) axis and the Z-axis. The result was $\alpha = 5.3 \pm 0.22$ microradians. In the course of our measurements of radial spindle error motion, we were able to measure α dynamically. This is, of course, the real parallelism error of interest since LODTM is always used with the spindle rotating when cutting parts and it is an often-observed phenomenon for a spindle axis of rotation to change its direction in space as a function of rotation speed. The static measurement would be of direct interest were LODTM to be used as a measuring machine.

The dynamic measurement of α was realized by analysis of radial motion data at 25 and 50 RPM and was accomplished as follows. We averaged the DC output of one of the capacitance gauges (the North gauge) over the 22 samples obtained at spindle top dead center ($\theta=0$). The difference between these averages obtained at Z=7.5 inches and Z=21.5 inches yields the change in gap between the gauge and the cylindrical square at the two axial locations. We then corrected this observed change for the effects of setup and artifact errors. The centering errors at the two locations were obtained as a routine part of the radial motion analysis, and yielded the orientation of the cylindrical square with respect to the spindle axis. The data was further reduced by including the taper and straightness errors of the cylindrical square.

The results of this procedure were (a) 25 RPM: α=2.6±0.4 microradians and (b) 50 RPM: α=2.9±0.4 microradians. The measurement uncertainties are 3σ values resulting from the ≈± 1 microinch standard deviations observed in the gauge averaging process. The direction of the error is the same as in the static case; that is, the spindle axis is tilted toward the South with respect to the Z-axis.

We make two comments concerning these results. First, the Z-W parallelism error appears to be sensibly independent of rotation speed between 25 and 50 RPM, although we sampled only these two values. Second, the dynamic error is significantly different from the static result (≈0.6 arc-second) and is subject to the same sensitivity to machine start-up position, as discussed in Section (8.C.).

10. Fast Tool Servo Tests

The test methods and procedures used to determine the displacement response of the Fast Tool Servo (FTS) are described in three separate sections. The first section covers the NBS-built capacitance gauges, the second section discusses the linearity tests of the FTS for static displacements and the third section covers the FTS dynamic tests.

During all testing described below, both the air temperature in the very close proximity of the capacitance gauge's sensing gap and the room's barometric pressure were continually monitored. The room air temperature was 20.4 ± 0.1°C and during any one test run varied less than ±0.04°C.

10.A. NBS Capacitance Gauges

During the last several years NBS has developed and built [7] a family of very sensitive, wideband capacitance gauges with a small sensing area (1/16 - 1/8 inch diameter). The minimal sensitivity of the gauge used in these tests, for an offset of approximately 2200 μin, was 3.7 mV/μin. The output amplifier of the gauge electronics provided 20 dB of gain.

The capacitance gauges were calibrated against a flat polished surface using the NBS Moore 5 coordinate measuring machine (CMM). The Moore 5 was used under computer control, which permits its coordinate position to be read using a laser interferometer displacement measuring system. The positioning resolution of the CMM is 0.5 μin, and that of the laser system is 0.4 μin. The gauge was placed in a fixture comprised of two rotary tables mounted perpendicular to each other. This fixture made it easy to align the gauge's sensing surface parallel to the polished target surface prior to the start of the calibration run.

The instrument block diagram for the measurements on the CMM is shown in Figure (68). The CMM's table moved in the X-direction only. The computer-controlled experiment moved the table relative to the target the desired number of displacement increments. Both the number of increments and their

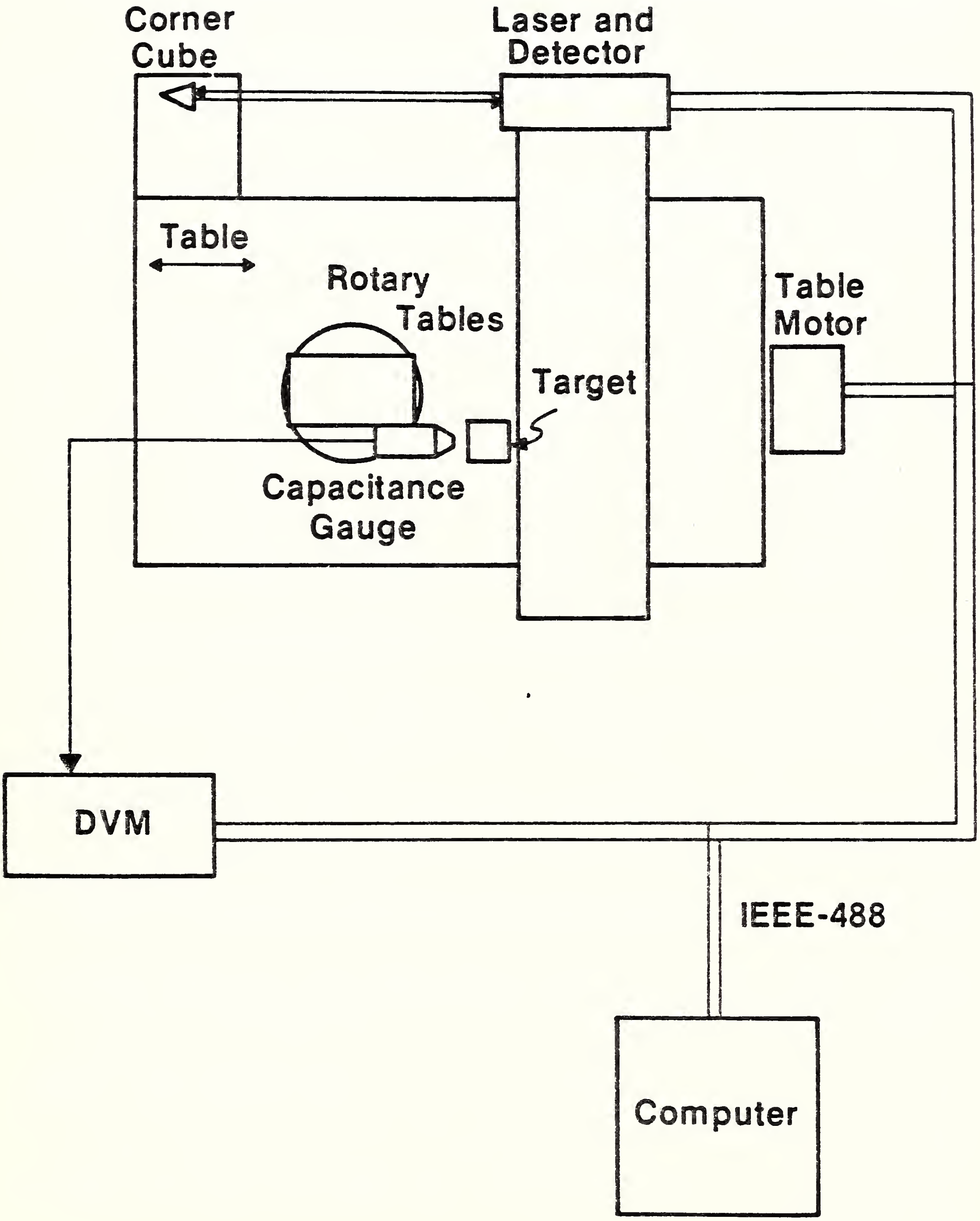
Corner Cube
Laser and Detector
Table
Rotary Tables
Table Motor
Target
Capacitance Gauge
DVM
IEEE-488
Computer

Figure 68

magnitude were entered into the program prior to the start of the test. An additional parameter was entered to give the number of complete cycles the test was to run. One cycle consisted of two runs. During the first run the gauge (table) moved away from the surface and during the second run the gauge moved toward the surface. For each run the laser displacement and the corresponding gauge output voltage were recorded. The results of each run were curve-fit using a polynominal of the form

$$V = \sum_{n=1}^{N} C_n (d_0 + d)^{-n} \tag{60}$$

where d is the change in displacement, V is the gauge output voltage, d_0 is the gauge's nominal offset distance, and C_n are the constants determined from the curve-fitting procedure. The value of N was either 4 or 5 depending on the magnitude of the total displacement range over which the data were recorded. The Marquardt [8] curve-fitting procedure was used to determine the C_n. Typical results from the curve-fitting procedure are shown in Table 5. These results, which are for the case of N = 4, yield a mean and standard deviation of the absolute values of the differences between the measured data and the fit data of 1.7 mV, and 2.5 mV respectively. These statistical values approximately correspond to 0.42 μin and 0.62 μin, respectively. It is also seen that over the range of ± 15 μin the gauge is fairly linear.

Typical Results of Curve-Fitting Eq. (60) to NBS Capacitance Gauge Calibration Data

	Changes in Gauge Output Voltage at various Offset Voltages (mV)				
Displacement (μin)	11.5 V	11.0 V	10.5 V	10.0 V	9.5 V
-15	76.009	68.090	62.202	57.656	53.887
-10	50.519	45.291	41.398	38.385	35.883
- 5	25.183	22.595	20.664	19.167	17.920
- 1	5.025	4.511	4.127	3.829	3.581
0	0.000	0.000	0.000	0.000	0.000
1	- 5.019	- 4.507	- 4.125	- 3.827	- 3.579
5	-25.035	-22.496	-20.595	-19.115	-17.879
10	-49.923	-44.894	-41.125	-38.180	-35.716
15	-74.669	-67.196	-61.583	-57.194	-53.512

Table 5

To obtain an estimate of the repeatability and stability of the capacitance gauge and, indirectly, the curve-fitting procedure, the gauges were calibrated five times over a period of 9 months. Each calibration run was performed with either the same or different position increments and with either the same or different nominal offset distance from the sensing surface. Typical results for the sensitivity at a distance corresponding to 10.0 V are shown in Table 6. The percentage standard error of the sensitivity is 0.46%, which corresponds to an uncertainty of 0.87 μin in 50 μin. Even though this uncertainty is small, the NBS gauge was calibrated just prior to the start of the static and dynamic tests and only the results of these two runs (#5 in Table 6) were used.

The form of Eq. (60) is not convenient in actual usage of the capacitance gauge in the tests, since we are interested in displacement as a function of voltage. Therefore, in the computer programs that were used to run the experiments described in the next two sections the following form was used:

$$d_o + d = \sum_{n-1}^{N} C'_n V^{-n} \qquad (61)$$

The constants C'_n were also determined by the Marquardt method. The C'_n were determined for each run of data set #5 and the results averaged prior to insertion in Eq. (61). The results obtained from this inverse curve-fit

Typical Repeatability of the Sensitivity of
the NBS Capacitance Gauge

		Test Conditions		Numerical Curve-Fit		
Data Set	Sensitivity at 10.0 V (mV/μin)	Voltage range (V)	Increment (μin)	Offset (μin)	# data points	N (Eq. 60)
#1	3.809	11.5 - 4.5	100	2500	77	5
	3.810					
	3.807					
	3.804					
	3.805					
	3.797					
#2	3.753	11.5 - 9.5	10	2500	52	4
	3.739					
	3.776					
	3.761					
#3	3.804	11.5 - 1.3	25	2200	302	5
	3.803					
	3.811					
	3.794					
#3a	3.770	11.5 - 4.5	25	2200	125	5
	3.763					
	3.782					
	3.763					
#4	3.698	11.5 - 5.5	10	2200	202	5
	3.750					
	3.743					
	3.799					
#5	3.918	11.6 - 8.8	10	2200	72	4
	3.829					
mean	3.787					
std dev.	0.041					

Table 6

yield sensitivity and error values that are very closely the reciprocal of the results obtained from Eq. (60).

10.B. Static Displacement Tests

Prior to the performance of the dynamic tests, a series of static tests were run to get an indication of the linearity and repeatability of the FTS and its associated electronics together with the NBS capacitance gauge and its instrumentation and curve-fitted voltage/displacement response.

The FTS and NBS capacitance gauges were mounted in a steel, L-shaped fixture in a manner that duplicated the mounting on LODTM itself. The entire fixture was then placed on a large, thick, steel-topped table of honeycombed construction. The target for the NBS capacitance gauge was a polished disk on one surface with a concentric cylindrical rod protruding from its back surface. This rod was inserted into the FTS in place of the diamond cutting tool and held by means of a set screw.

The schematic diagram of the instrumentation configuration is shown in Figure (69). The entire test was under computer control, with all instruments interfaced using the IEEE-488 protocol. The air temperature was monitored with a thermistor calibrated at NBS. It was attached to a digital ohmmeter which was read prior to each measurement. The output voltage of the NBS capacitance gauge was monitored with a 6-digit DC digital voltmeter (DVM). The voltage output from the barometric pressure sensor and the

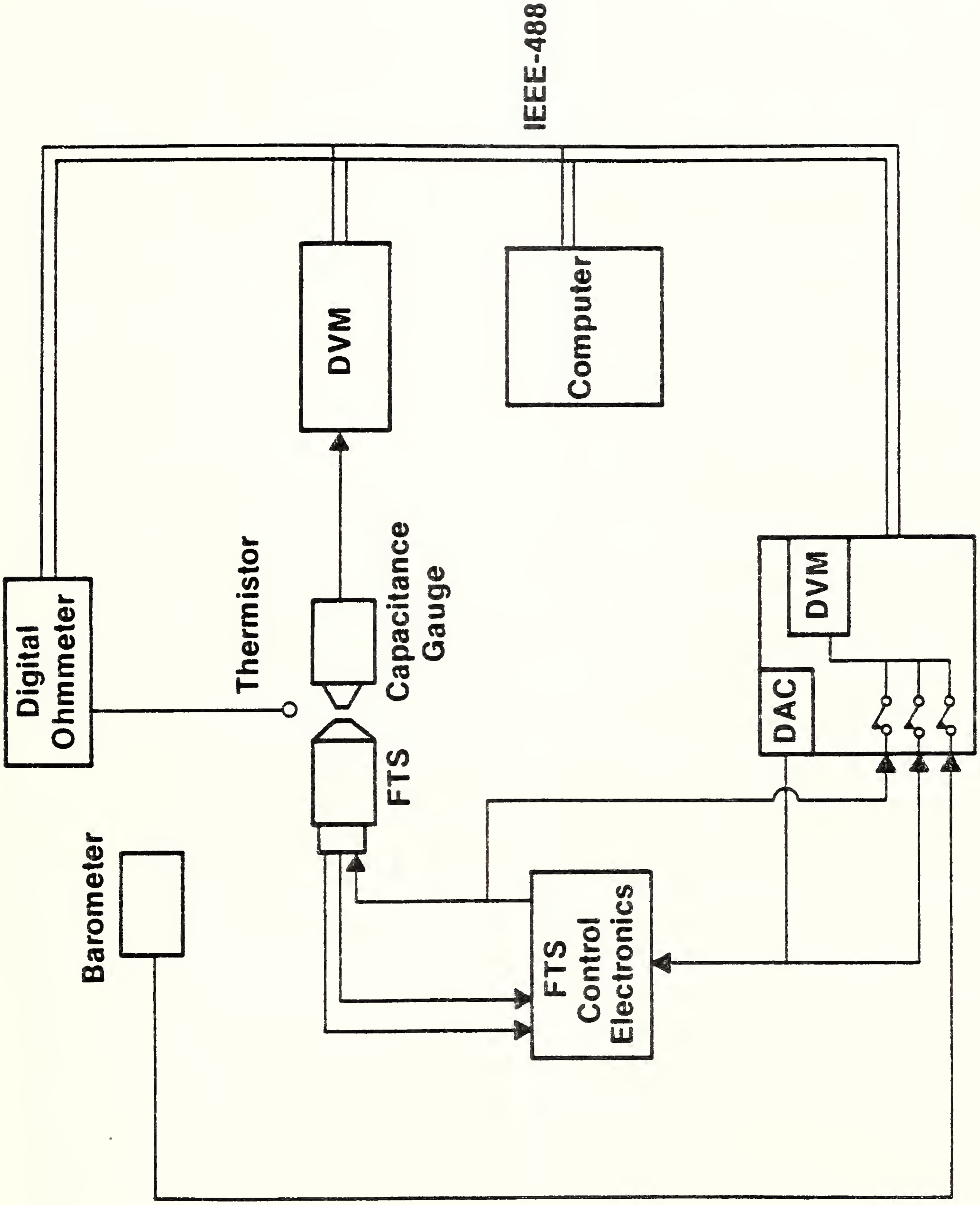
IEEE-488
Digital Ohmmeter
DVM
Computer
Thermistor
Capacitance Gauge
FTS
DVM
DAC
Scanner
Barometer
FTS Control Electronics

Figure 69

voltages from the various intermediate stages of the FTS electronics were monitored with a scanner, which incorporated a DVM. The scanner also had a programmable digital-to-analog converter(DAC), which was used to provide the DC voltages to drive the FTS.

The test procedure used in these tests was as follows. The output of the DAC was set to 0.000V and the output voltage of the NBS capacitance gauge was read. Then the DAC was set to V_0 volts and the capacitance gauge again read. At each of these voltages the corresponding displacements were determined using Eq. (61). The difference of these two displacement values gave the static displacement response of the FTS for that value of input voltage, V_0. The values of V_0 ranged from ±10 V in increments of 0.5 V in the following manner: 0.0 V to 10.0 V to -10.0 V to 0.0 V. It should be mentioned that this procedure eliminates the effects of drift on the measurements. A different test method has to be used to monitor drift. No drift tests were performed on the FTS.

A typical result of these tests is shown in Figure (70). The repeatability is outstanding so that most data points, which are represented by plus signs, fall on top of each other. There are 78 data points plotted in Figure (70). The linearity of the response, typified by the negligible standard deviation of the randomly distributed data points about the fitted line of 0.04 μin, is excellent. This test was run three times, twice on one day and once on the next day. The results are summarized in Table 7. The actual repeatability of the individual displacement values to the applied

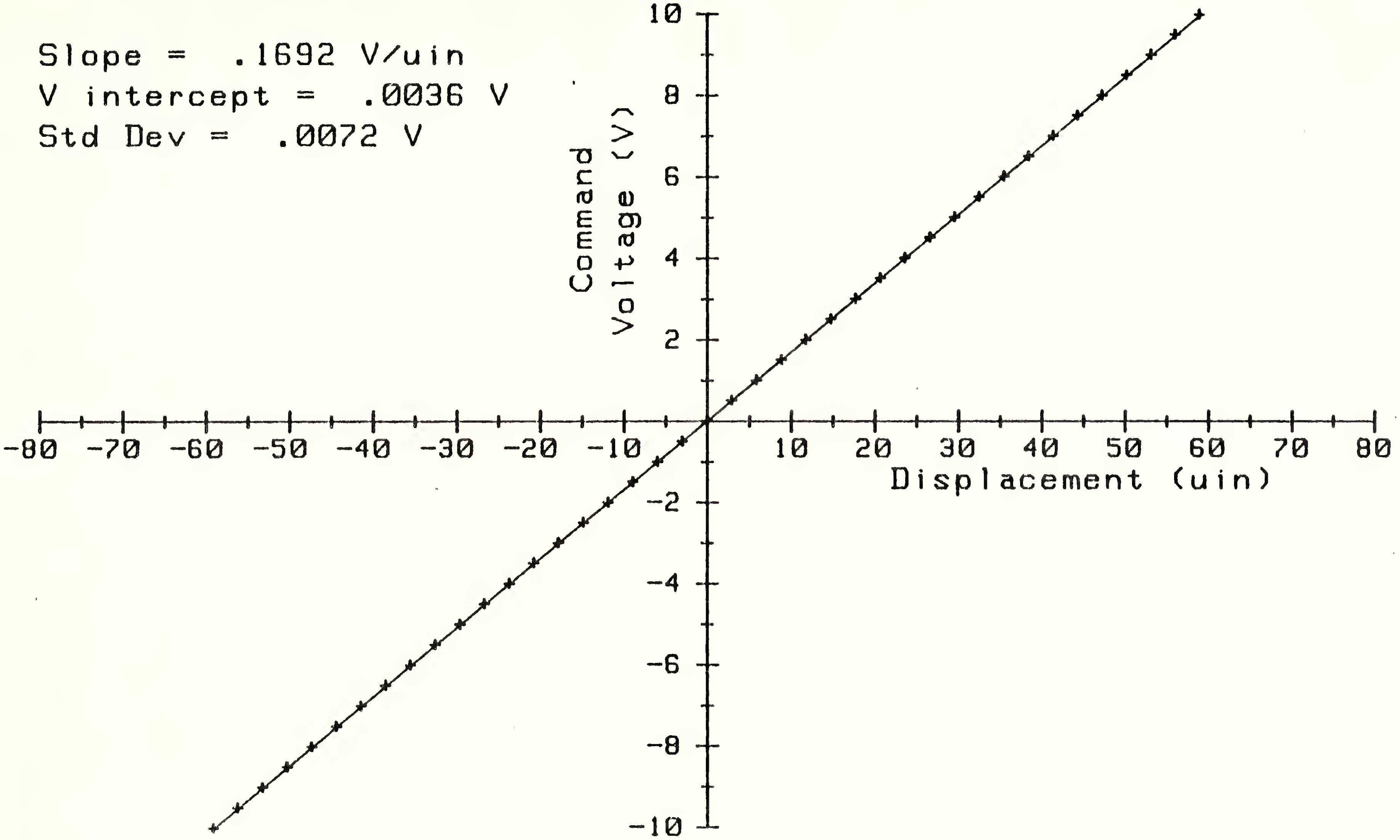
Slope = .1692 V/uin
V intercept = .0036 V
Std Dev = .0072 V
Command
Voltage (V)
10
8
6
4
2
-2
-4
-6
-8
-10
-80
-70
-60
-50
-40
-30
-20
-10
10
20
30
40
50
60
70
80
Displacement (uin)

Figure 70

Linearity and Repeatability of FTS Static Response

	Run #1	Run #2	Run #3
Slope (V/μin)	0.1691	0.1692	0.1692
V-intercept (V)	0.0033	0.0000	0.0036
Standard Deviation (V)	0.0066	0.0314	0.0072

Table 7

voltages is within ±0.03 μin, for the most part, with a few differences as large as ±0.05 μin.

These highly reproducible results indicated that the FTS and the NBS instrumentation were properly working and that the dynamic tests could now be performed.

10.C. Dynamic Displacement Tests

The mechanical test setup used in the dynamic tests was the same as that used in the static tests with one additional feature: the L-shaped fixture was clamped at three points to the rigid, steel-topped table. The instrumentation block diagram is given in Figure (71). The differences in the dynamic instrumentation setup and the static setup are that the DAC is replaced by a frequency synthesizer and the dynamic ouput of the NBS capacitance gauge is recorded with a lock-in amplifier. The lock-in amplifier is used for two reasons: its low frequency response (0.2 Hz), and its narrow filtering capabilities with its corresponding long averaging times. The output of the lock-in amplifier is in volts rms.

The maximum harmonic output amplitude of the frequency synthesizer was 10.0 V peak-to-peak. In order to get the amplitude of the signals to the maximum 20.0 V peak-to-peak, an amplifier (shown in Figure (71) with dotted lines) was used to obtain FTS displacements above 30 μin. The amplifier's amplitude frequency response was virtually uniform from 1 Hz to 200 Hz with

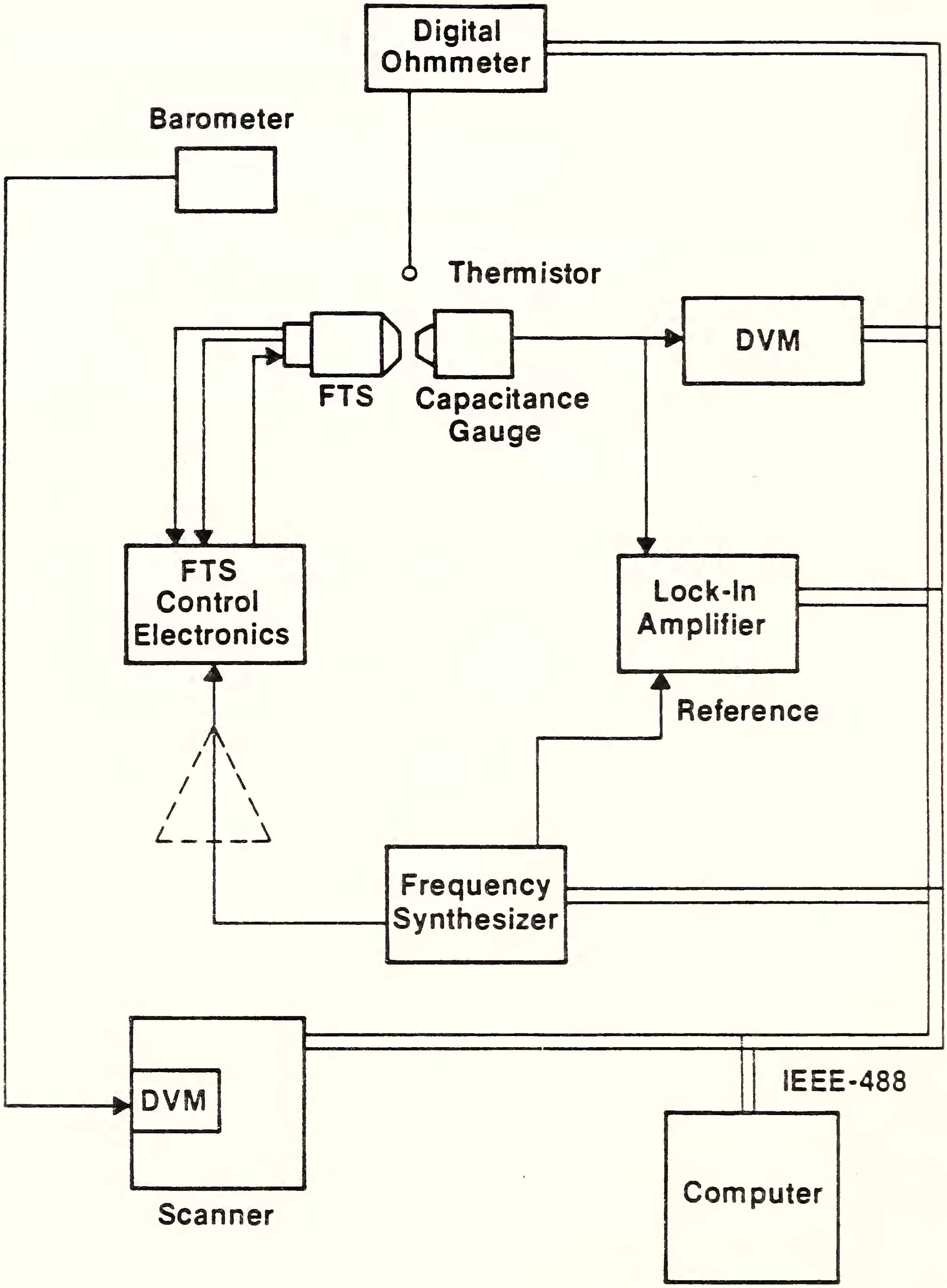
Digital
Ohmmeter
Barometer
Thermistor
DVM
FTS
Capacitance
Gauge
FTS
Control
Electronics
Lock-In
Amplifier
Reference
Frequency
Synthesizer
DVM
Scanner
IEEE-488
Computer

Figure 71

a slight attenuation of 0.02 dB, or a 0.2% decrease in the amplitude of the signal. Since this corresponds to 0.1 μin in 50 μin, this error is well within the experimental error and was, therefore, neglected. However, the output of the amplifier at DC was approximately -0.1 dB relative to its output from 1 Hz to 200 Hz. This difference is taken into account in the subsequent data by increasing the values of the measured nominal static displacement by 1.0%. The frequency synthesizer could also be used as a DC voltage source between ±10.0 V.

The lock-in amplifier had a microprocessor-controlled feature that determined, without operator intervention, the proper voltage range and phase angle to obtain the maximum rms recording of the input voltage. This feature made it extremely easy to program the lock-in amplifier for complete computer control.

The dynamic tests were conducted at frequencies from 1 to 200 Hz with the following frequency resolution: from 1-10 Hz, every 1 Hz; from 10-100 Hz, every 5 Hz; and from 100-200 Hz, every 20 Hz. Each of these frequency sweeps was conducted at the following seven nominal static displacement amplitudes: 4.6, 9.2, 18.4, 27.6, 36.5, 45.6, and 54.7 μin. At each nominal static displacement and at each frequency the following test protocol was used, which virtually eliminated any effects of drift. The output voltage of the frequency synthesizer was set to 0.0 VDC and the capacitance gauge's output voltage read with the DVM exactly as was done in the static tests. The frequency synthesizer then puts out a DC voltage of magnitude V_0 and the capacitance gauge's output voltage was again read by the DVM. These two voltages were converted to displacements using Eq.(61), and their difference, D_0, recorded. Lastly, the frequency synthsizer put out a harmonic signal of frequency f and amplitude V_0, the same amplitude as the DC voltage. The output of the capacitance gauge was then read with the lock-in amplifier. Since the lock-in amplifier does not respond to DC and its output is rms, the voltage used to convert the lock-in's output to a displacement is

$$V = V_0 - V_L\sqrt{2} \tag{62}$$

where V_L is the rms voltage from the lock-in amplifier. The negative sign in Eq.(62) is arbitrary since the change in voltage during one cycle is both + and - around V_0. The voltage, V, given by Eq.(62) is converted into a corresponding peak displacement, D, using Eq.(61). The difference $D-D_0$ at each frequency is the measure of the frequency distortion of the dynamic amplitude response of the FTS.

As was done in the static test, three runs as function of frequency at each of the seven nominal static displacements were made to get an indication of the repeatability of the FTS system and the NBS measuring system in the dynamic environment. The results are tabulated in Tables 8 and 9. It is seen that the results repeat to within ±0.02 μin everywhere except, inexplicably, for run #3 at a nominal static displacement of 54.7 μin. The average of the three runs at each of the seven nominal static displacements is plotted in Figure (72).

Repeatibility of FTS Dynamic Response for Three Runs as a Function of Frequency and Peak Displacement Amplitude

	DD-SD (uin)											
	SDn= 4.6 uin			SDn= 9.2 uin			SDn=18.4 uin			SDn=27.6 uin		
Frequency (Hz)	#1	#2	#3	#1	#2	#3	#1	#2	#3	#1	#2	#3
1.0	-.01	.02	-.01	.07	.07	-.02	.19	.19	.17	.17	.27	.19
2.0	.03	.02	.03	.06	.04	.06	.11	.16	.18	.22	.15	.17
3.0	.02	.01	.03	.06	.06	.07	.17	.15	.19	.22	.23	.27
4.0	.03	.03	.02	.08	.07	.09	.19	.19	.21	.26	.26	.28
5.0	.04	.04	.03	.10	.09	.09	.22	.22	.21	.32	.32	.34
6.0	.04	.03	.04	.10	.10	.10	.25	.26	.26	.36	.38	.34
7.0	.05	.04	.05	.11	.11	.13	.26	.28	.29	.40	.39	.40
8.0	.05	.03	.03	.12	.12	.11	.27	.27	.28	.39	.39	.44
9.0	.05	.04	.04	.13	.10	.13	.26	.26	.25	.39	.39	.37
10.0	.03	.05	.05	.13	.12	.12	.25	.26	.28	.40	.39	.41
15.0	.05	.03	.03	.12	.12	.11	.25	.27	.28	.41	.41	.44
20.0	.04	.04	.04	.13	.10	.10	.28	.29	.28	.43	.40	.42
25.0	.04	.03	.02	.11	.11	.12	.32	.27	.27	.42	.44	.46
30.0	.06	.05	.06	.14	.12	.13	.30	.34	.32	.50	.46	.47
35.0	.04	.06	.06	.13	.12	.12	.31	.32	.35	.51	.50	.52
40.0	.05	.03	.03	.13	.14	.12	.35	.32	.36	.52	.54	.53
45.0	.05	.07	.04	.13	.14	.14	.38	.35	.35	.56	.57	.58
50.0	.02	.07	.06	.15	.15	.14	.37	.37	.36	.61	.60	.59
55.0	.06	.05	.05	.15	.14	.14	.38	.41	.38	.64	.61	.64
60.0	.05	.06	.05	.17	.15	.15	.41	.40	.42	.68	.68	.64
65.0	.07	.07	.05	.16	.17	.18	.42	.42	.40	.72	.71	.72
70.0	.06	.07	.06	.16	.15	.17	.45	.44	.46	.74	.73	.74
75.0	.08	.06	.06	.18	.21	.17	.46	.48	.46	.81	.80	.78
80.0	.09	.06	.06	.19	.19	.20	.46	.49	.50	.81	.81	.80
85.0	.08	.08	.06	.20	.19	.19	.51	.54	.53	.86	.85	.82
90.0	.07	.08	.07	.20	.19	.21	.54	.54	.53	.90	.89	.88
95.0	.10	.08	.09	.20	.21	.23	.53	.53	.53	.92	.92	.91
100.0	.08	.07	.07	.21	.22	.22	.59	.58	.58	.97	.99	1.00
120.0	.09	.09	.09	.26	.27	.24	.67	.67	.67	1.16	1.15	1.18
140.0	.13	.12	.11	.29	.28	.28	.75	.79	.74	1.34	1.33	1.31
160.0	.13	.13	.12	.32	.32	.32	.89	.87	.89	1.53	1.53	1.55
180.0	.14	.16	.13	.36	.37	.35	1.01	1.03	1.01	1.76	1.75	1.76
200.0	.16	.15	.15	.42	.41	.42	1.14	1.14	1.14	2.02	2.01	1.98

SD = Static Displacement
DD = Peak Dynamic Displacement
SDn= Nominal SD

Table 8

Repeatibility of FTS Dynamic Response for Three Runs as a Function of Frequency and Peak Displacement Amplitude

Frequency (Hz)	DD-SD (uin)								
	SDn=36.9 uin			SDn=46.1 uin			SDn=55.2 uin		
	#1	#2	#3	#1	#2	#3	#1	#2	#3
1.0	.03	.42	-.03	.16	.20	.54	.05	.13	.68
2.0	.22	.19	.27	.41	.40	.50	.50	.65	.47
3.0	.29	.29	.27	.42	.50	.48	.70	.66	.46
4.0	.39	.39	.36	.54	.57	.59	.77	.68	.55
5.0	.41	.46	.44	.69	.63	.67	.88	.79	.65
6.0	.48	.52	.50	.75	.74	.76	.91	.89	.71
7.0	.50	.55	.51	.84	.75	.79	1.03	.97	.74
8.0	.55	.57	.55	.75	.81	.77	1.04	1.02	.78
9.0	.57	.55	.50	.76	.76	.78	.99	.94	.73
10.0	.53	.55	.51	.82	.79	.79	.99	1.00	.75
15.0	.53	.56	.53	.79	.82	.86	1.10	1.00	.80
20.0	.56	.59	.59	.85	.86	.89	1.13	1.11	.86
25.0	.63	.65	.66	.88	.94	.95	1.17	1.18	.99
30.0	.69	.67	.67	.99	.98	1.01	1.25	1.23	1.14
35.0	.72	.75	.73	1.09	1.05	1.05	1.41	1.35	1.23
40.0	.75	.75	.76	1.15	1.11	1.13	1.41	1.40	1.34
45.0	.81	.82	.82	1.21	1.18	1.19	1.49	1.50	1.41
50.0	.84	.85	.87	1.23	1.25	1.26	1.55	1.55	1.47
55.0	.90	.91	.93	1.31	1.30	1.33	1.67	1.66	1.56
60.0	.94	.97	.98	1.44	1.38	1.40	1.77	1.74	1.62
65.0	1.00	1.00	1.01	1.49	1.45	1.48	1.85	1.84	1.71
70.0	1.07	1.06	1.08	1.55	1.53	1.57	1.92	1.93	1.83
75.0	1.09	1.13	1.13	1.60	1.60	1.62	2.02	1.98	1.87
80.0	1.16	1.18	1.19	1.69	1.68	1.68	2.14	2.14	1.96
85.0	1.21	1.23	1.25	1.75	1.76	1.79	2.21	2.19	2.05
90.0	1.28	1.30	1.29	1.83	1.86	1.86	2.34	2.34	2.23
95.0	1.32	1.34	1.35	1.90	1.90	1.93	2.47	2.43	2.19
100.0	1.39	1.38	1.43	2.01	1.99	2.02	2.50	2.48	2.39
120.0	1.64	1.64	1.68	2.33	2.35	2.37	3.00	2.98	2.88
140.0	1.90	1.87	1.95	2.69	2.70	2.70	3.31	3.29	3.13
160.0	2.15	2.16	2.21	3.08	3.10	3.11	3.93	3.91	4.44
180.0	2.45	2.47	2.49	3.49	3.53	3.47	4.73	4.71	4.82
200.0	2.80	2.80	2.80	3.93	3.96	3.97	5.23	5.23	5.23

SD = Static Displacement
DD = Peak Dynamic Displacement
SDn= Nominal SD

Table 9

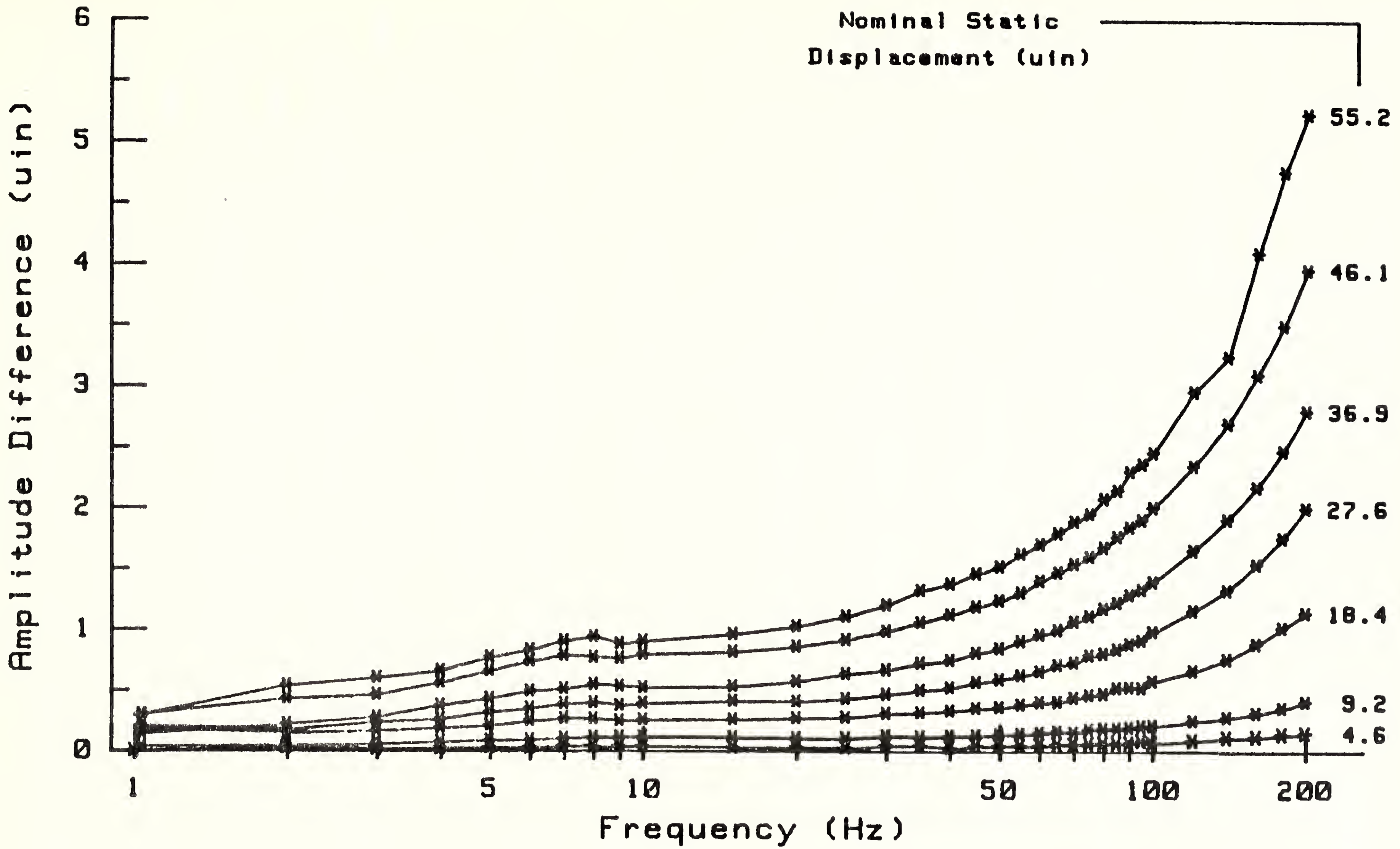
Nominal Static
Displacement (uin)
55.2
46.1
36.9
27.6
18.4
9.2
4.6
Amplitude Difference (uin)
0
1
2
3
4
5
6
1
5
10
50
100
200
Frequency (Hz)

Figure 72

10.D. Discussion

The results indicate that the FTS static and dynamic repeatability from run to run is better than 0.05 μin in almost all cases. The deviation from linearity of the static displacement as a function of input voltage to a maximum of either ±10.0 V is better than 0.05 μin. The tests used to obtain these results were performed in such a way that any effects of drift were removed. No drift tests were performed by NBS. The results of the dynamic tests indicate that the desired bandwidth of 100 Hz for the FTS can be met with qualifications: for a frequency distortion of less than 1.0 μin the peak dynamic displacement has to be less than approximately 28 μin; for a distortion of 2.0 μin the peak displacement can be as high as 46 μin.

ACKNOWLEDGEMENTS

Many persons contributed substantially to the success of the LODTM field validation effort. At NBS, we thank Bob Hocken and Tom Charlton for numerous helpful discussions. Fieldwork at LODTM would not have been possible without the dedicated and skilled assistance of Ralph Veale and Bruce Borchardt. The capacitance gauges were designed and constructed by Bill Penzes with the support of the NBS instrument shops. The NBS interferometer system was realized with the help of Mike Huff and Toni Savoy. Special thanks go to Howard Layer for the design and fabrication of the laser heterodyne circuitry. Leon Carroll provided valuable assistance during calibration of the LLNL reference straightedge. Lewis Greenspan did much of

the data reduction and analysis for the FTS validation testing. We also thank Charles Summers for the excellent and timely fabrication of many of our special fixtures. Chuck Giauque and C.J. Johnson were responsible for the safe transportation of our metrology instrumentation to LLNL.

In addition to our colleagues at NBS, we owe a large debt of gratitude to the staff of LODTM who graciously supported our efforts in the field. In particular, Bob Donaldson and Steve Patterson provided invaluable technical advice and assistance in all aspects of the machine validation, together with Dennis Atkinson, Ray McClure, and Ted Saito. Detailed guidance with respect to the many electronic, optical, mechanical, and software subsystems of LODTM, without which we would have faced enormous obstacles, was provided by Jerry Chrislock, Doug Baird, Dave Hopkins, Jeff Roblee, Al Maddux, Bob Wade, and Dick Grayson. Ray Ewing coordinated the many transfers of measurement hardware between NBS and LLNL. During November and December, 1984, George Weinert aided us in our day-to-day measurement activities. Finally, for administrative aid and assistance, many thanks to Pat Flowers, Dorothy Pontsler, and Corrine Wells.

We would like to extend a special note of appreciation to Alan Hopkins, of the Air Force Wright Aeronautical Laboratory, who did a superb job of coordinating this work within the constraints imposed by the schedule requirements of the many agencies and contractors who comprise the Alpha laser program.

Finally, we thank Wendy King of NBS for her skill and patience in typing this report.

This work was supported by the Defense Advanced Research Projects Agency under ARPA Order 4404.

REFERENCES

1. R.R. Donaldson and S.R. Patterson, "Design and Construction of a Large, Vertical Axis Diamond Turning Machine", Proc. SPIE 433, 62 (1983)

2. H.K. McCue, "The Motion Control System for the Large Optics Diamond Turning Machine", Proc. SPIE 433, 68 (1983)

3. R.R. Donaldson, Technology of Machine Tools, Vol.5, Machine Tool Accuracy, Sec. 9.14, "Error Budgets", UCRL-52960-5 (1980)

4. R.R. Donaldson, "A Simple Method for Separating Spindle Error from Test Ball Roundness Error", Annals of the CIRP, Vol. 21/1 (1972)

5. J.B. Bryan and P. Vanherck, "Unification of Terminology Concerning the Error Motion of Axes of Rotation", Annals of the CIRP, Vol. 24/2 (1975)

6. ANSI Standard B89.3.4-198X, "Axes of Rotation", Draft 101

7. E.L.R. Corliss and W.B. Penzes, "Low Noise Broadband Modulated Preamplifiers for a Variety of Transducers", App. Acoustics 16, 67 (1983)

8. J.C. Nash, Compact Numerical Methods for Computers: Linear Algebra and Function Minimization, John Wiley and Sons, NY (1979), Ch.17

APPENDIX A

INTRODUCTION

Many of our measurements of the positioning errors of the LODTM tool bar were characterized by a systematic non-repeatability or hysteresis, dependent upon the direction of tool bar motion, feedrate, total measurement time, fixturing, and range of travel. This behavior was most pronounced when the tool bar was moved in the Z-direction during the measurement. The cause of these effects was ultimately traced to the air bearings which act to constrain and guide the tool bar in the Z-direction. Evidently, expansion of the air supplied to these bearings from ≈100 psi supply pressure to atmospheric pressure is accompanied by a significant decrease in temperature due to Joule-Thompson throttling. Thus the air bearings, and the tool bar itself in the neighborhood of the bearings, are cooled below the nominal machine temperature of 20°C. There are two principal consequences of this temperature gradient. First, the tool bar itself can be thermally deformed, or warped, and second, any tooling or fixturing bolted to the tool bar mounting plate can experience thermal expansion or contraction as the tool bar moves in Z.

The coupling of these temperature gradients to our measurement instrumentation is well illustrated by Fig.(A1). This data was obtained using a capacitance gauge attached to the tool bar with an aluminum plate and gauging against a precision cylindrical square. Prior to the start of this

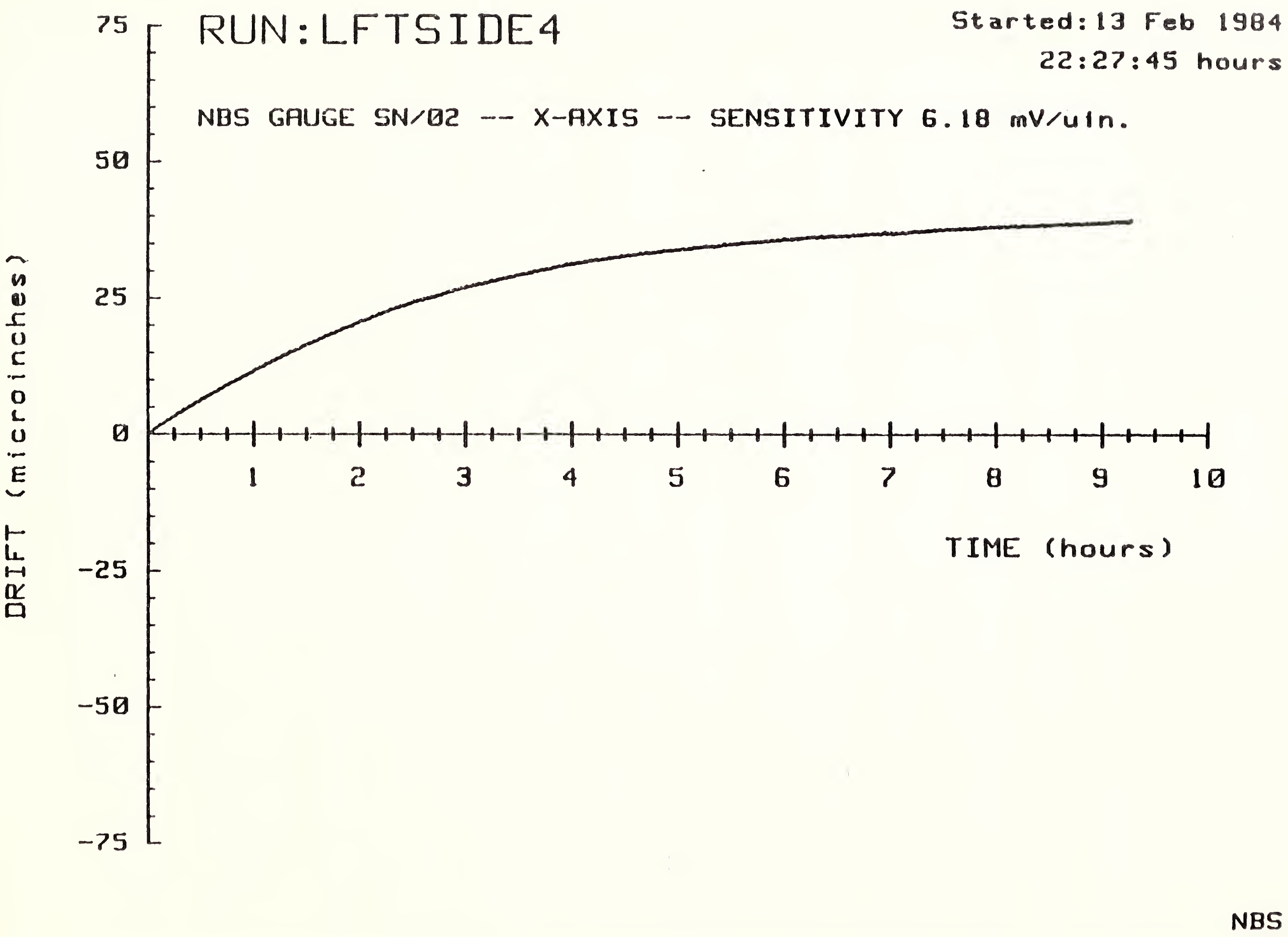
RUN:LFTSIDE4
Started:13 Feb 1984
22:27:45 hours
NBS GAUGE SN/02 -- X-AXIS -- SENSITIVITY 6.18 mV/uin.
DRIFT (microinches)
75
50
25
0
-25
-50
-75
1
2
3
4
5
6
7
8
9
10
TIME (hours)
NBS

Figure A1

experiment, the tool bar was near its lower limit of travel and the gauge was in equilibrium with respect to the cylindrical square as verified by a drift test of approximately one hour. The tool bar was then moved rapidly (2 inches/minute) upward by 12 inches and an immediate drift test begun, resulting in Fig.(A1). The data shows an apparently exponential drift with a time constant of ≈3 hours and asymptotic displacement of ≈40 microinches. The direction of motion is such as to require a contraction of the aluminum mounting plate or, equivalently, a cooling of the tool bar mounting plate. Subsequent to this measurement we attached a calibrated thermistor to the mounting plate in order to directly monitor its temperature. We observed that the mounting plate cooled by approximately 0.4°C when moved from its lower limit of travel to 19 inches upward in Z.

Based upon these observations, we developed a simple, physically plausible model of the tool bar face plate temperature as a function of its position history. We proceed to described this model, and its use in correcting some of our error data.

THE THERMAL MODEL

The basic observation leading to the thermal model is that the temperature of the tool bar mounting plate is a function of Z-position. We make no attempt at a first-principles understanding of the thermal behavior of the tool bar mounting structure. In order to completely define the model, we make the following assumptions:

1. The tool bar face plate equilibrium temperature is a linear function of Z-position:

$$T_{eq}(Z) = T_0 - \frac{\Delta T}{Z_0}.Z \quad , \Delta T>0. \tag{A1}$$

   Here, T_{eq} denotes the temperature which would exist at the face plate if one waited long enough at any position Z. We take Z to be positive upward, so that T_0 is the face plate equilibrium temperature at the lower limit of travel. The quantity $\Delta T/Z_0$ represents the constant temperature gradient between two positions a distance Z_0 apart.

2. If the face plate is at equilibrium temperature at some position Z_1 and the tool bar moved rapidly to a new position Z_2, then the face plate will approach the new equilibrium temperature exponentially with a time constant τ which is independent of position.

3. The effect of temperature changes upon measurement data depends upon an effective length parameter. This parameter is a characteristic of the material and dimensions of the fixture attached to the tool bar.

All measurements involving Z-axis motion started near the lower limit of travel (Z=0). The tool bar moved under computer control in steps of uniform size. At each measurement point a programmed dwell allowed time for data sampling. A complete measurement sequence consisted of such moves up to a maximum height and then back to Z=0, with each point sampled twice (i.e.,"out and back").

The observed thermal effects upon experimental data clearly depend upon the position history of the tool bar. For the measurement sequence just described, tool bar velocity is a simple function of time:

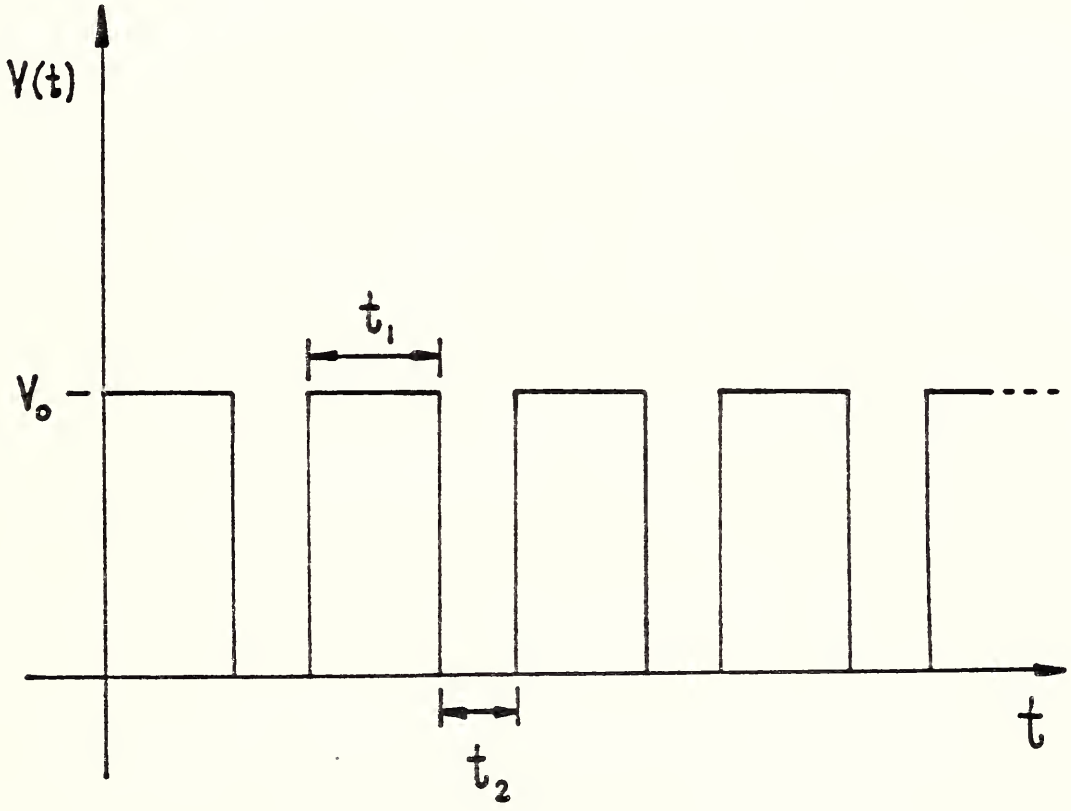

Here,

t_1=time to move between points

$= \Delta Z/V_0$,

where ΔZ is the step size and V_0 the programmed feedrate, and

t_2=programmed dwell time.

Integration of V(t) yields the tool bar position function Z(t):

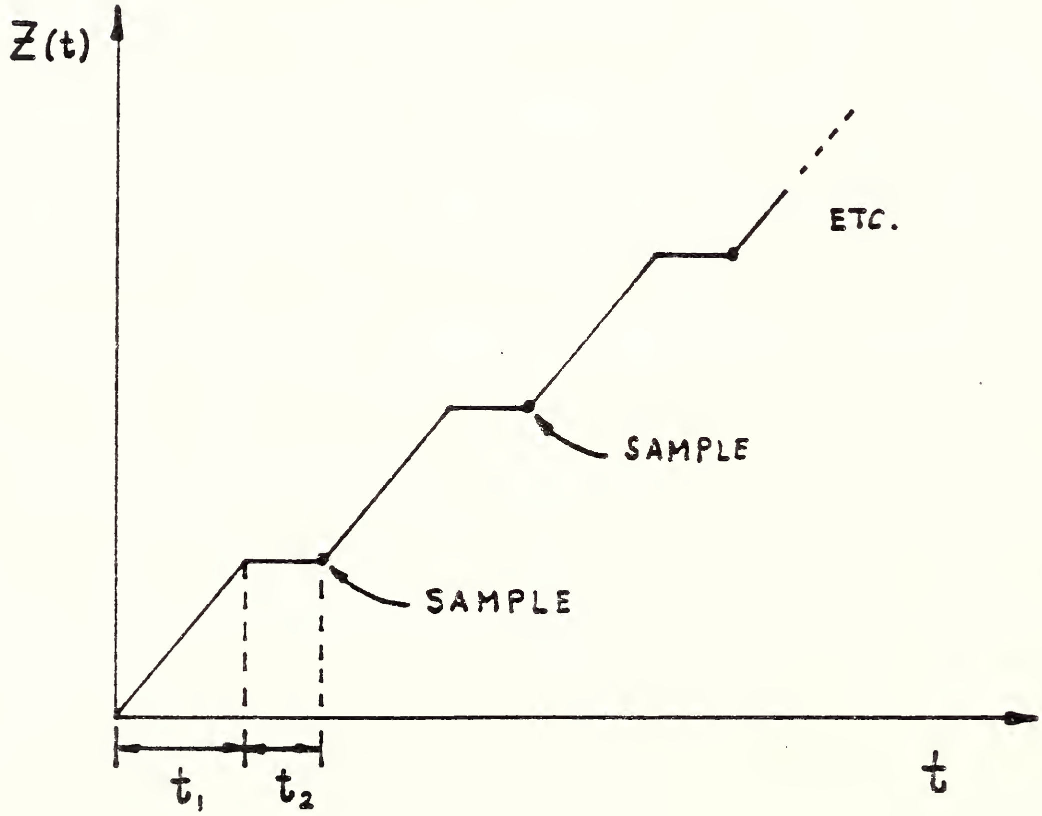

The general problem may be addressed with reference to the following diagram, which depicts a typical sequence of events.

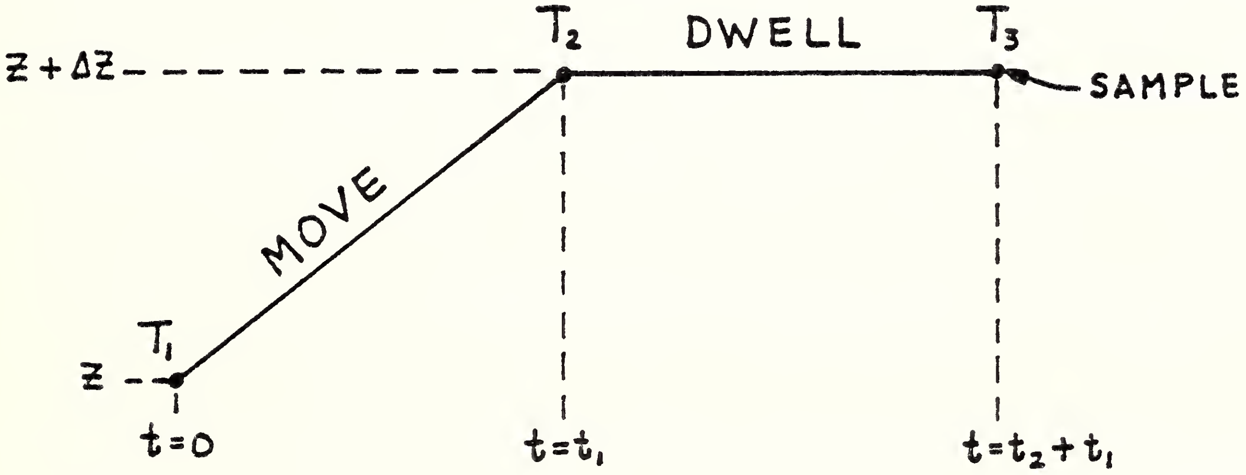

At time t=0 the tool bar begins to move from Z to Z+ΔZ at feedrate V_0. The face plate temperature is T_1. After a time $t_1 = \Delta Z/V_0$, the tool bar arrives at position Z+ΔZ and comes to rest. At this moment the face plate temperature is T_2. After a dwell of duration t_2 the datum is sampled, at which time the face plate temperature is T_3. The basic problem is to compute T_3, given T_1 and the assumed properties of the face plate temperature field.

The fundamental thermal relaxation equation is

$$\frac{dT}{dt} = -k(T-T_{eq}) \quad , \tag{A2}$$

where $k = 1/\tau$ = a reciprocal time constant and T_{eq} is the face plate temperature as $t \to \infty$. The model algorithm consists of using Eq.(A2) twice, first to find T_2 given T_1 and then to find T_3 given T_2. We call the path from $T_1 \to T_2$ a MOVE, and the path from $T_2 \to T_3$ a DWELL. The solution to the relaxation equation is different for the two paths.

A. MOVES, $T_1 \to T_2$.

Using Eq.(A1) for T_{eq}, the relaxation equation (A2) becomes

$$\frac{dT}{dt} = -k(T - T_0 + \frac{V_a \Delta T}{Z_0} t). \tag{A3}$$

Since our only concern is with changes in face plate temperature, we simplify by setting $T_0 = 0$. Then Eq.(A3) becomes

$$\frac{dT}{dt} = -k \ (T + \frac{V_a \Delta T}{Z_0} t). \tag{A4}$$

Now, replacing k with $1/\tau$, and defining a parameter $\alpha = V_0 \Delta T/Z_0$, we may rewrite Eq.(A4) as

$$\frac{dT}{dt} = -\frac{1}{\tau}(T + \alpha t). \qquad (A5)$$

The solution to Eq.(A5) consistent with the initial condition $T(0)=T_1$ is

$$T(t) = (T_1 - \alpha\tau)e^{-t/\tau} - \alpha(t - \tau), \qquad (A6)$$

which may be verified by insertion into Eq.(A5). Thus, for a MOVE of duration t_1 we have

$$T(t_1) = T_2 = (T_1 - \alpha\tau)e^{-t_1/\tau} - \alpha(t_1 - \tau). \qquad (A7)$$

We simplify the notation by defining a MOVE function as the right-hand side of Eq.(A7), so that

$$T_2 = M(T_1,\alpha,\tau,t_1). \qquad (A8)$$

B. DWELLS, $T_2 \rightarrow T_3$.

This is a simpler problem than for a MOVE, since the equilibrium temperature is constant during a DWELL. We have

$$\frac{dT}{dt} = - \frac{1}{\tau} (T - T_{eq}),$$

with $T_{eq} = - Z\Delta T/Z_0$ = constant. The solution is a simple exponential relaxation:

$$T(t) = T_{eq} + (T_2 - T_{eq})e^{-t/\tau}, \qquad (A9)$$

so that for a DWELL of duration t_2 we have

$$T(t_2) = T_3 = T_{eq} + (T_2 - T_{eq})e^{-t_2/\tau}. \qquad (A10)$$

By analogy with the MOVE function, Eq.(A8), we now define a DWELL function D as the right-hand side of Eq.(A10):

$$T_3 = D(T_2, Z, \Delta T/Z_0, \tau, t_2). \qquad (A11)$$

DATA CORRECTION

For a typical data run, the following parameters are assumed to be fixed:

τ = relaxation time constant

$\Delta T/Z_0$ = temperature gradient

t_2 = programmed dwell time

ΔZ = programmed step size.

The correction algorithm then proceeds by iteration. We have

$$T_3 = D(T_2, Z), \text{ other parameters fixed,} \qquad (A12)$$

and

$$T_2 = M(T_1, \alpha, t_1), \ \tau \text{ fixed.} \qquad (A13)$$

Note: the parameters $\alpha = V_0 \Delta T/Z_0$ and $T_1 = \Delta Z/V_0$ are taken to be variables and are adjusted to maximize the bi-directional repeatability of the experimental data. The reason for this has to do with the LODTM controller. If V_0 were known exactly, then α and t_1 would be fixed. The LODTM control panel has a 0 → 100% feedrate override potentiometer whose position was not recorded in our experimental log books. Fitted values gave feedrates of 80-90% of the programmed values.

Combining Eqs.(A12) and (A13) yields

$$T_3 = D[M(T_1, \alpha, t_1), Z] \ , \ \alpha = V_0 \Delta T/Z_0 . \qquad (A14)$$

This is the central result of the procedure. Starting at the beginning of a data run (T_1 = 0), Eq.(A14) gives the temperature (T_3) at the first data point. This value of T_3 then becomes the initial temperature ($T_3 \rightarrow T_1'$) of the next MOVE/DWELL sequence and (A14) used again to find T_3'. Then $T_3' \rightarrow T_1'$, and so on. At the upper limit of travel the tool bar motion changes direction, which is simply accomplished by letting $\alpha \rightarrow -\alpha$ (i.e., $V_0 \rightarrow -V_0$). In this manner we bootstrap our way out and back.

The above procedure yields the calculated face plate temperature at each point in the measurement cycle. These temperatures are then multiplied by an adjustable length parameter and the result either added to, or subtracted from, the experimental data. The size of the length parameter depends upon the characteristic dimensions of the mounting fixture and the material from which it is fabricated.

The results of this data correction model are well illustrated by Figs.(A2-A4). Figure (A2) shows the raw data from one of our early measurements of the X-straightness of the Z-axis. The solid curve connects points sampled on the way up in Z, and the dashed curve connects points sampled on the way down. The effect of thermal hysteresis in this data is obvious. Figure (A3) displays the thermal drift during this run, computed by repeated application of Eq.(A14) and optimized with respect to α and t_1. Figure (A4) shows the corrected data, obtained by subtracting (A3) from (A2). The effect of the thermal model is such that bi-directional repeatability is reduced to less than 0.5 microinches at all measured points.

In addition to the Z-axis straightness data, this algorithm was also used to remove thermal drift from our early Z-axis scale and pitch errors, prior to

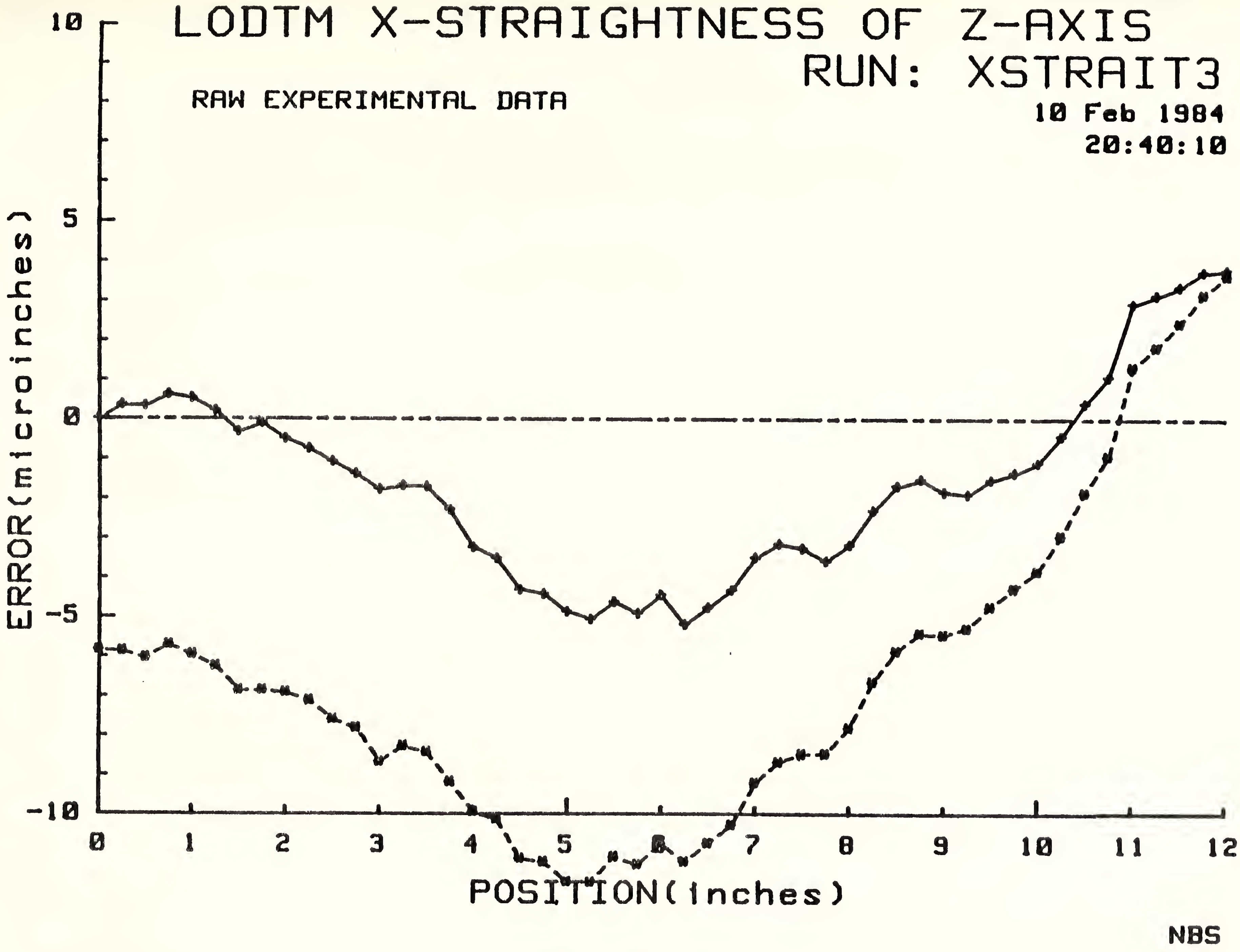
LODTM X-STRAIGHTNESS OF Z-AXIS
RUN: XSTRAIT3
RAW EXPERIMENTAL DATA
10 Feb 1984
20:40:10
ERROR(microinches)
10
5
0
-5
-10
0
1
2
3
4
5
6
7
8
9
10
11
12
POSITION(inches)
NBS

Figure A2

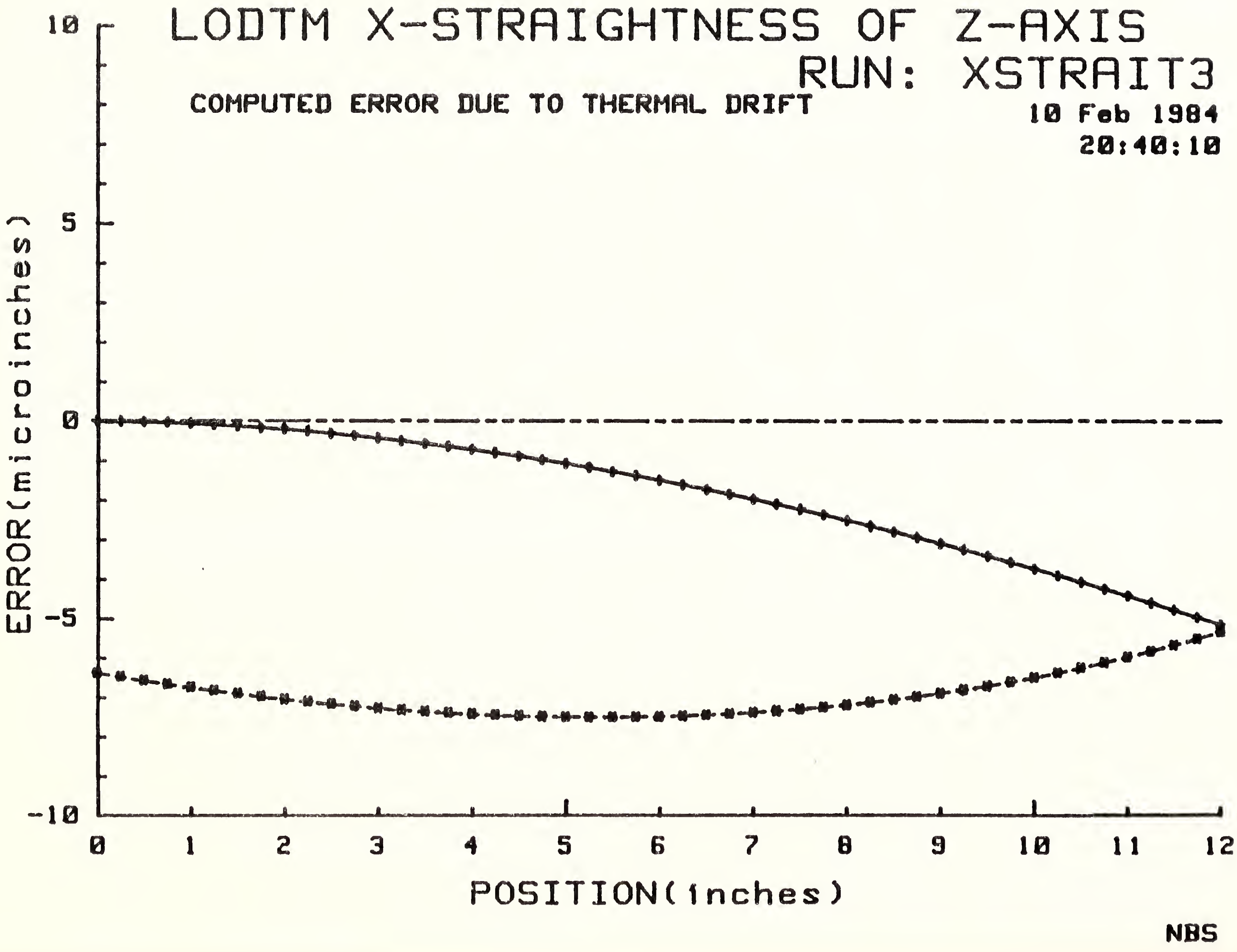
LODTM X-STRAIGHTNESS OF Z-AXIS
RUN: XSTRAIT3
COMPUTED ERROR DUE TO THERMAL DRIFT
10 Feb 1984
20:40:10
ERROR(microinches)
10
5
0
-5
-10
0
1
2
3
4
5
6
7
8
9
10
11
12
POSITION(inches)
NBS

Figure A3

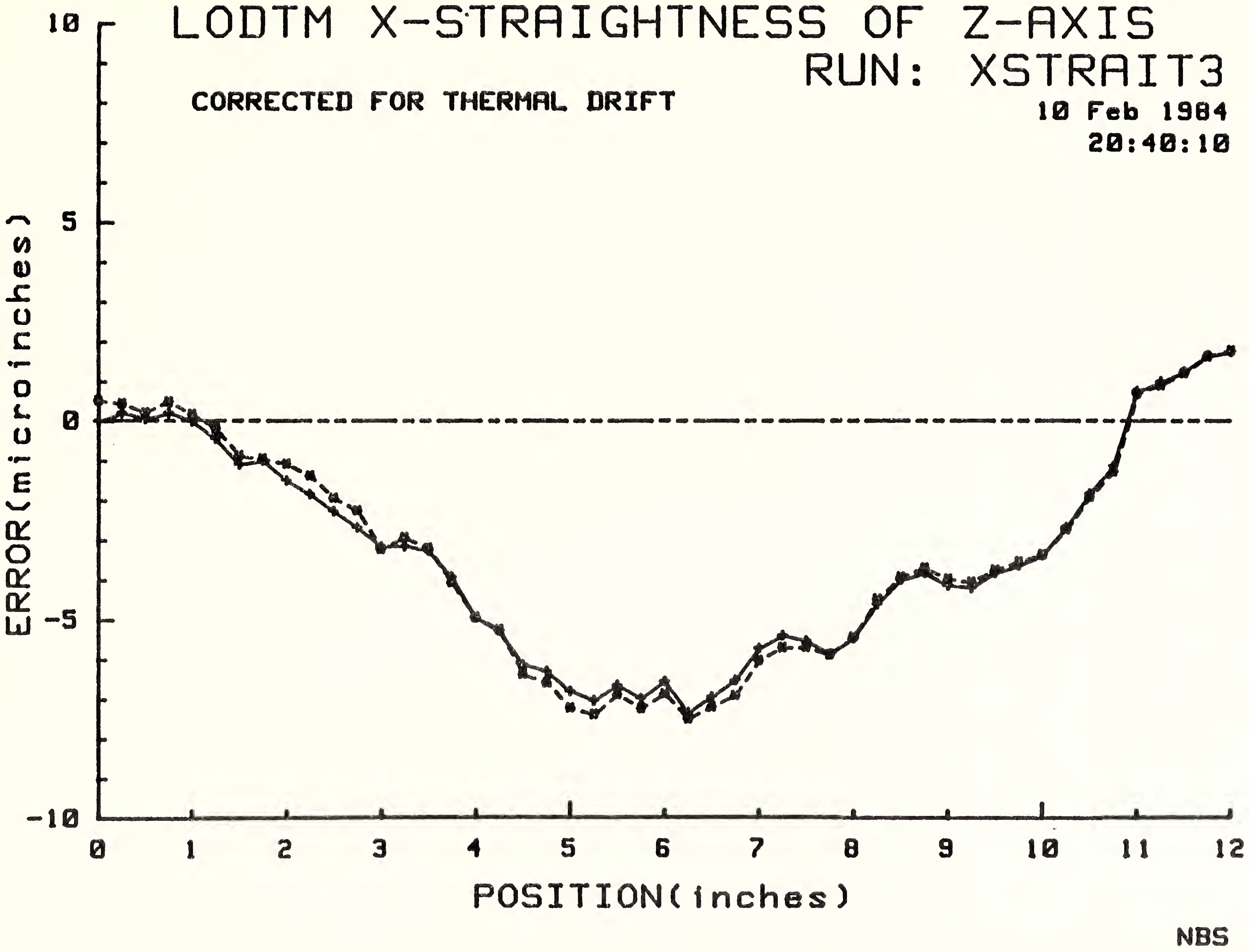
LODTM X-STRAIGHTNESS OF Z-AXIS
RUN: XSTRAIT3
CORRECTED FOR THERMAL DRIFT
10 Feb 1984
20:40:10
10
5
0
-5
-10
ERROR(microinches)
0
1
2
3
4
5
6
7
8
9
10
11
12
POSITION(inches)
NBS

Figure A4

the installation of heaters on the air supply lines to the tool bar air bearings. Since the effect of these heaters was to keep the tool bar face plate essentially isothermal, the model described here is not applicable to later data which, however, still displayed marked hysteresis. The cause of this behavior is not known, but is most likely due to thermal deformation of the tool bar and/or the kinematic mounting structures of the Z-axis straightedges.

APPENDIX B

This appendix is a reprint of a paper which describes in detail the design and operation of the NBS interferometer system. The equation and figure numbers refer only to the appendix itself, not to the main body of this report.

Reprinted from Applied Optics, Vol. *24*, page 808, March 15, 1985

High-accuracy displacement interferometry in air

W. Tyler Estler

The absolute accuracy of laser interferometers employed in displacement metrology is limited by two dominant factors: uncertainties in the source vacuum wavelength and the refractive index of the ambient air. In this paper we describe an interferometer system designed to minimize these uncertainties. Based on a commercial interferometer, the new system features direct measurement of the vacuum wavelength by frequency comparison with a portable iodine-stabilized He–Ne laser. The refractive index of air is computed from accurately measured values of pressure, temperature, and relative humidity. Combined with a desktop computer, the interferometer system permits the automated field measurement of displacement errors (such as those associated with precision machine tools) with an absolute accuracy of 8.5 parts in 10^8. Performance of the interferometer in field metrology is illustrated by the results of recent validation testing of the large optics diamond turning machine (LODTM) at Lawrence Livermore National Laboratory. These results highlight the need for new measurements of the absolute refractive index of standard air in order to reduce a limiting uncertainty on such measurements of ±5 parts in 10^8.

I. Introduction

The past decade has seen the evolution of a new class of numerically controlled machine tools, called diamond turning machines, which are capable of the direct machining of precision optical elements. General features of these machines include laser interferometric length scales, real-time correction of kinematic positioning errors, and extensive environmental controls. An excellent review of the fabrication of machined optics is given by Brown *et al.*[1]

As the size and accuracy of diamond turning machines have increased, very severe demands have been placed on the metrology instrumentation employed to measure their positioning accuracy. The large optics diamond turning machine (LODTM), constructed at the Lawrence Livermore National Laboratory, will serve to illustrate these demands. Design goals for the LODTM include an estimated surface-normal figure error of 1.1-μin. (28-nm) rms on reflective metal optics of 64-in. (1.6-m) diameter and 20-in. (0.5-m) height.[2] The machine tool bar, which positions the diamond tool with respect to the rotating workpiece, moves in two dimensions (X and Z) with ranges of motion of 44 in. (1.1 m) and 20 in. (0.5 m), respectively. To measure the positioning error of the tool bar over its full range of travel in X, to an accuracy within the design error budget, thus requires a displacement measurement with an absolute accuracy of about two parts in 10^8.

In this paper we describe a laser interferometer system developed at the National Bureau of Standards (NBS) for use in field tests of the kinematic positioning accuracy of the LODTM. While the linear axes of the LODTM are controlled by laser interferometers within flexible evacuated bellows, field test instrumentation must of necessity operate in the open air of the machine enclosure. As will be shown, our present knowledge of the refractive index of air places a fundamental limitation on the accuracy achievable in such conditions.

II. Displacement Interferometry

The basis of nearly all long-travel measurements in precision machine tool metrology is the Michelson interferometer and its variants. The central component of the current NBS interferometer is a commercial instrument manufactured by Hewlett-Packard (HP).[3,4] The source is a Zeeman-stabilized He–Ne laser which emits reference and measurement beams separated in frequency by ~2 MHz and of orthogonal linear polarizations. Displacements of the moving reflector appear as phase information on a rf carrier and are detected by standard heterodyne techniques. Such ac implementations of the Michelson interferometer offer excellent noise immunity and high resolution. When used with a plane-mirror reflector and quarterwave plate, the least count of the instrument corresponds to a displacement resolution of $\lambda/64$ or ~0.4 μin. (0.01 μm) for λ near 25 μin. (633 nm).

The length scale of a displacement interferometer operating in air is given by

---

The author is with U.S. National Bureau of Standards, Center for Manufacturing Engineering, Automated Production Technology Division, Gaithersburg, Maryland 20899.

Received 8 November 1984.

$$\lambda_{\text{air}} = \lambda_{\text{vac}}/n_{\text{air}}, \tag{1}$$

where λ_{vac} is the wavelength of the source in vacuum and n_{air} is the refractive index of air. The vacuum wavelength is simply related to the source frequency f_0:

$$\lambda_{\text{vac}} = c/f_0, \tag{2}$$

where the speed of light in vacuum is

$$c = 299,792,458 \text{ m/s, exactly.} \tag{3}$$

The result (3) is a consequence of the October, 1983, redefinition of the meter by the International Bureau of Weights and Measures (BIPM).

It follows from Eqs. (1)–(3) that the absolute accuracy of a laser interferometer in air is determined by the uncertainties in the source frequency and the refractive index of air. In the NBS interferometer system, these uncertainties are minimized by (a) direct measurement of f_0 by frequency comparison with an iodine-absorption stabilized He–Ne laser, and (b) calculation of n_{air} using accurately measured values of environmental parameters.

III. Vacuum Wavelength

While the metrology Zeeman laser is frequency stabilized, the long-term stability is specified to be only one part in 10^7. Of the several techniques which have been employed for length control of He–Ne laser resonators,[5] stabilization based on resonant absorption in molecular iodine vapor has proved to be by far the superior. Frequency reproducibility of such devices of different design details have been demonstrated to be a few parts in 10^{11} or better.[6] The absolute frequencies of two of the I_2 hyperfine components (i and g) of such a laser have recently been measured directly at NBS, with an absolute uncertainty of 1.6 parts in 10^{10}.[7]

In the interferometer system described here, we employ a portable I_2-stabilized He–Ne laser, designed at NBS,[8] to measure the frequency f_0 of the metrology laser. Light from the stabilized laser and one frequency component of the metrology laser are coincident on a high-speed avalanche photodiode and rf amplifier. The resultant difference (or beat) frequency is monitored by an accurate frequency counter. Since the frequency of the stabilized laser is accurately known for each component (we typically lock the laser on the h component), this measurement yields the frequency of the metrology laser, and hence the vacuum wavelength, with a comcomitant accuracy (about two parts in 10^{10}).

Such heterodyne measurements over a period of months have demonstrated that our particular commercial laser is exceptionally stable. We have never observed this laser to drift more than ±1 MHz from its lock point in any 24-hour period, which corresponds to a short-term frequency stability of about ±2 parts in 10^9.

IV. Refractive Index of Air

In principle, one might consider directly measuring the refractive index of the ambient air and using the results to continuously correct, in real time, the interferometer displacement measurements. We decided that the development of such a tracking refractometer, accurate to 0.1 ppm or better, was a significant research problem in its own right and chose, therefore, to calculate the refractive index using accurately measured values of the relevant environmental parameters.

Fortunately, the refractive index of air is a very well-known function of atmospheric pressure (P), air temperature (T), water vapor partial pressure or relative humidity (H), and carbon dioxide concentration by volume (y). The emission spectra of atoms and molecules, measured in air, were the primary pieces of experimental data which led to the great successes of quantum mechanics earlier in this century. Considerable effort was devoted to determining the effects of the ambient air on measured spectral line wavelengths.

An empirical equation due to Edlén[9] is generally used in metrology. Recently, Jones[10] of NBS combined a precise determination of the density of moist air with Edlén's formulation to yield another, somewhat simpler representation. For a vacuum wavelength of $\lambda = 0.6329912714\ \mu\text{m}$ typical of an iodine-stabilized He–Ne laser, Jones's result is

$$n(P,T,H,y) = 1 + A - B, \tag{4}$$

where

$$A = 78.603[1 + 0.540(y - 0.0003)]P/TZ \times 10^{-8}, \tag{5}$$

$$B = (0.00042066 f e_s H) \times 10^{-8}. \tag{6}$$

In these equations P is in pascals, T in kelvins, H in percent, and y is the fractional CO_2 concentration by volume. Three additional factors occur in Jones's representation: Z is a compressibility factor which reflects the departure of moist air from ideal gas behavior, f is an enhancement factor related to the effective saturation vapor pressure of water in air, and e_s is the saturation vapor pressure of pure water vapor over a plane surface of pure liquid water. Tables of Z, f, and e_s are included in the Appendix of Jones's paper.

By computing the partial derivatives of $n(P,T,H,y)$ with respect to each of its arguments and evaluating the resulting expressions at near-standard conditions ($P = 101325$ Pa, $T = 293.15$ K, $H = 25\%$, and $y = 0.00034$), the sensitivity of the refractive index to changes in the ambient environment may be determined. Table I displays the change in each parameter which causes a change of +1 part in 10^8 in the refractive index.

Table I. Environmental Parameters Which Affect the Refractive Index of Air; Sensitivities are Computed from Eqs. (4)–(6)

Parameter	Nominal value	Change for which $\Delta n = +1$ part in 10^8
Pressure	101.3 kPa (760 mmHg)	+3.73 Pa (+0.028 mmHg)
Temperature	20.0°C	−0.01°C
Humidity	40%	−1%
Carbon dioxide concentration	340 ppm	+67 ppm

It is important to realize that even were P, T, H, and y known exactly, there would still remain a systematic uncertainty in n_{air}. Since Edlén's equation and Jones's reformulation are empirical expressions, they can be no more accurate than the original experimental data which went into their derivations. Edlén estimates the absolute uncertainty to be ±5 parts in 10^8. Apart from this fundamental limit on achievable accuracy, there are technical limits on the measurements of environmental parameters. We proceed to discuss these measurements and to estimate the resulting total error budget.

V. Pressure Compensation

As atmospheric pressure increases so does air density, resulting in a concomitant increase in refractive index. A change ΔP of +3.73 Pa (0.028 mmHg) causes a change Δn_{air} of +1 part in 10^8 (see Table I). This sensitivity is quite significant for several reasons. During periods of rapid climatic change (a passing cold front, for example), atmospheric pressure may fluctuate by hundreds of Pa in the course of a machine tool calibration. Furthermore, when measuring the scale errors of a vertically translating axis, it may be necessary to correct for the decrease in pressure with altitude. Near the earth's surface this gravitationally induced pressure gradient is approximately −13 Pa (−0.1 mmHg) per meter, resulting in a decrease in n_{air} of more than three parts in 10^8 for each meter of vertical translation.

In our present interferometer system we measure atmospheric pressure using a flexible diaphragm capacitance-type transducer [Rosemount model 1201F1A3AIA, range 80–110 kPa (600–825 mmHg)][3] which produces a nearly linear 0–5-VDC output over its measurement range. The analog output results in a very high resolution; in practice, however, our resolution is 0.67 Pa (0.005 mmHg), determined by the least count of the digital voltmeter used to sample the transducer. The principal advantage of this type of pressure sensor is the very small combined error due to hysteresis and nonrepeatability, amounting to ±2.7 Pa (±0.02 mmHg).

The transducer was calibrated by the Temperature and Pressure Measurements and Standards Division of NBS, employing gas lubricated piston gauges. The calibration included ten pressures over the design range, with both increasing and decreasing pressures. The data were analyzed and a residual ±0.07% nonlinearity was removed by fitting to a fifth-order polynomial function which is used by the system data collection/analysis computer to convert the measured analog signal to atmospheric pressure.

The resulting error in n_{air} due to pressure measurement error may be estimated by combining the hysteresis/nonrepeatability error with a possible 0.005% systematic error arising from calibration uncertainty. This procedure yields, at a nominal pressure of 101.3 kPa,

$$(\Delta n_{\mathrm{air}}/n_{\mathrm{air}})_P = \pm 2 \times 10^{-8}. \qquad (7)$$

VI. Temperature Compensation

As air is heated at constant pressure, the resultant expansion causes both density and refractive index to decrease. The sensitivity of n_{air} to temperature changes is −1 part in 10^8 for $\Delta T = +0.01$ K (see Table I). Significant measurement errors can arise, even in exceptionally well-controlled laboratory environments, due to thermal gradients in the ambient air. In addition to the expected vertical temperature stratification we have observed gradients of several tenths of a kelvin between points a meter or so apart in a horizontal plane in a laboratory whose mean temperature was controlled to ±0.05 K. For highest accuracy in displacement interferometry, these observations imply that air temperature must be measured at many points along the measurement beam and an average be computed for data correction.

We measure air temperature with an array of semiconductor thermistor sensors (Victory Engineering model 41U1A401).[3] The sensors are mounted in open aluminum shrouds for protection against mechanical damage and are typically spaced every 8–10 cm along the measurement laser beam.

There are many advantages to the use of thermistors rather than such alternatives as thermocouples or platinum resistance thermometers. Thermistors have very large negative temperature coefficients so that small changes in air temperature are quite easily measured. Our thermistors have a nominal resistance $R(T)$ of ~12 kΩ at 20°C and a temperature coefficient dR/dT of nearly 5%/K. The digital multimeter used to sample them has a least count of ±1 Ω, which yields a resolution of ~2 mK. The small (2.3-mm) diameter of the sensors leads to a fast response to temperature changes, with time constants of <6 sec in still air.

Thermistors have in the past been avoided in precision applications because of concerns about their stability aginst drift. Recent studies,[11,12] however, have shown that bead thermistors such as ours, particularly when they are aged prior to use, are actually very stable, with drift rates generally <1 mK/100 days. Our thermistors were aged for more than 1½ years prior to mounting in their air shrouds.

While the sensors are designed to be matched and interchangeable, the matching tolerance is specified to be only ±0.2 K. To attain the accuracy required of the laser system, each thermistor had to be accurately calibrated. Four of them were calibrated at five points in the temperature range 292.15–294.15 K (19.0–21.0°C) by the Temperature and Pressure Measurements and Standards Division of NBS. These calibrations employed direct comparisons with standard platinum resistance thermometers and are accurate to ±5 mK. The calibration data were used in a least-squares algorithm to derive an analytic resistance vs temperature function for each thermistor. These functions take the form

$$R(T) = R_0 \exp(b/T), \qquad (8)$$

where T is in kelvins and R_0 and b are constants, different for each thermistor, determined by the algorithm. The form of Eq. (8) follows naturally from the

Boltzmann distribution of electrons thermally excited into the conduction band of a doped semiconductor. The four calibrated thermistors were subsequently used as temperature transfer standards for the calibration of an additional twenty. The transfer calibrations were carried out in our own laboratory by means of a commercial thermostated water bath containing a deep reservoir of stirred, electrically insulating paraffin oil. We estimate the accuracy of these calibrations to be ±0.01 K, based on the maximum departure from the mean temperature of any of the four transfer standards which surrounded the thermistor being calibrated.

The use of thermistors in high precision applications requires several precautions. The physical mounting must be very secure to prevent strain-induced resistance changes, and such mounting should always precede calibration. If long lead wires are used, significant errors can be caused by the lead resistance. For this reason we use a 4-wire resistance measurement technique in which two pairs of lead wires are attached to the thermistor leads. A constant current is passed through the thermistor via one pair of leads and the resultant voltage drop is sensed by the second pair. Since a modern digital voltmeter has a very high input impedance and draws essentially zero current, no voltage drop occurs in the sensing leads and they can cause no error.

A further potential source of error arises from thermistor self-heating. A resistor with resistance R ohms carrying a current of I amperes generates heat (called Joule heat) at a rate of I^2R Watts. This causes the resistor's temperature to rise until, at equilibrium, losses due to conduction, convection, and radiation equal the rate of heat production. A thermistor used to measure air temperature therefore rides at a higher temperature than ambient. In certain applications, such as hot-bead anemometry, this phenomenon serves a very useful purpose but it must obviously be minimized in precision thermometry. The straightforward way to do so is by minimizing the current used in sampling the resistance. Thermistors are characterized by a dissipation constant, which in the case of our devices is 2 mW/K. This means that in order to dissipate 2 mW of Joule power a thermistor must heat to 1 K above ambient temperature, resulting in a 1 K measurement error. We sample our thermistors with a current of 10 μA which would, if applied continuously, cause a temperature error of ~2 mK. Since sampling takes <0.1 s, the actual error must be much smaller than this.

We estimate the uncertainty in the measured of air temperature to be ±0.01 K. The corresponding uncertainty in refractive index due to temperature error is

$$(\Delta n_{\mathrm{air}}/n_{\mathrm{air}})_T = \pm 1 \times 10^{-8}. \tag{9}$$

VII. Humidity Compensation

Water vapor is ~15% less refractive than dry air.[9] Therefore, as water vapor partial pressure (or relative humidity) increases at constant total pressure, the refractive index decreases. The magnitude of the effect is $(\Delta n_{\mathrm{air}}/n_{\mathrm{air}}) = -1 \times 10^{-8}$ for $\Delta H = +1\%$, at temperatures near 20°C (see Table I).

Until recently, measurements of relative humidity with accuracies of 1% or better were nearly impossible, being more typically 5–10% using devices ranging from horsehair hygrometers and wet/dry bulb thermometers to chilled-cup dew-point instruments and hygroscopic crystal sensors. A modern development, based on the chilled-cup technique, lends itself ideally to accurate humidity measurement in an automated metrology system.

The principle of the chilled-mirror dew-point hygrometer is both simple and elegant. The sensing element is a mirrored metallic surface mounted atop a thermoelectric cooling stage. The mirror is cooled below ambient temperature until, at the dew point, a thin layer of condensation forms on the surface and is detected by a small light source/photodetector combination which monitors the surface reflectance. By closing a feedback loop using the photodetector output as an error signal, the current to the cooling stage is servoed to keep the condensation layer constant. The stage and mirror thus track the dew point, whose temperature is measured by a platinum resistance thermometer embedded in the mirror.

To determine relative humidity, ambient temperature must be known as well as dew-point temperature. In our instrument (EG&C Environmental Equipment model 911)[3] ambient temperature is measured by a second platinum resistance thermometer mounted in the inlet to the sampling system which draws air across the mirror surface. The two thermometers have matched temperature coefficients so that the functional conversion from resistance to temperature is the same for both of them. Once the dew point and ambient temperatures are known, relative humidity may be determined by reference to a psychrometric chart. With the model 911, the relevant portions of the chart are contained in a programmable read-only memory (PROM), and the computation is performed automatically. The output of the device is a 0–10 VDC analog signal directly proportional to the relative humidity.

The instrument was calibrated at the factory against a standard hygrometer which had itself been calibrated by the Thermal Processes Division of NBS. The nominal measurement accuracy is ±0.5% relative humidity, yielding an index uncertainty of

$$(\Delta n_{\mathrm{air}}/n_{\mathrm{air}})_H = \pm 0.5 \times 10^{-8}. \tag{10}$$

VIII. Role of Carbon Dioxide

Carbon dioxide is ~50% more refractive than standard air,[9] so that an increase in CO_2 concentration causes an increase in n_{air}. The sensitivity is $\Delta n_{\mathrm{air}} = +1 \times 10^{-8}$ for $\Delta y = 0.000067$ (67 ppm) (see Table I).

A recent review article by Revelle[13] surveys the present state of knowledge of the concentration of CO_2 in the earth's atmosphere. Continuous measurements, in connection with the International Geophysical Year (IGY), have been made for more than 20 years at stations in Hawaii and Antarctica. A graph of CO_2 con-

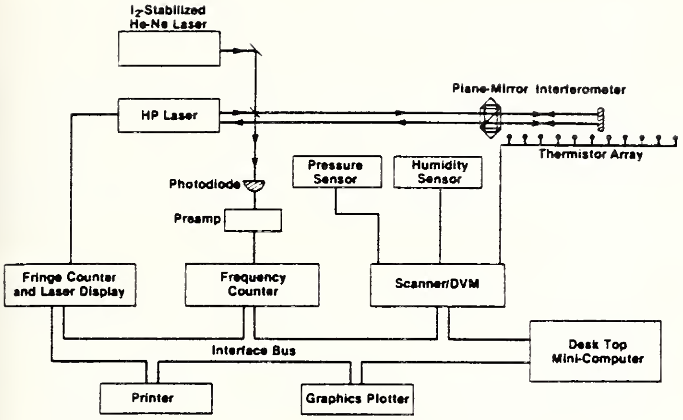

Fig. 1. Schematic diagram of the interferometer system.

centration vs time displays an increasing exponential behavior presumably associated with the combustion of fossil fuels. The present value of y, estimated from this graph, is ~340 ppm and is increasing at ~1.4 ppm/year. In light of these observations, we consider it to be very unlikely that variations in y could be large enough to cause significant errors in our interferometer system (a change of 67 ppm represents a ±20% change in concentration). For this reason we have adopted a constant value of 340 ppm for y and assume no measurement error due to changes in CO_2 concentration.

IX. Resultant Accuracy

Since the heterodyne frequency measurement yields an essentially exact value for the laser vacuum wavelength, the accuracy of displacement measurements is dependent only on errors in the determination of the refractive index. To arrive at a worst-case estimate, we simply add the systematic errors due to the environmental parameters to the absolute uncertainty given by Edlén. The result is

$$(\Delta n_{\mathrm{air}}/n_{\mathrm{air}})\mathrm{total} = \pm 8.5 \times 10^{-8}. \tag{11}$$

We believe that Eq. (11) represents a realistic limit on the possible accuracy of optical interferometric displacement measurements in air. Any substantial improvement must await new experiments which will refine by an order of magnitude the absolute value of the refractive index of standard air.

X. Interferometer System

A block diagram of the completed interferometer system is shown in Fig. 1. The actual displacement measurement is performed by the metrology laser, using plane mirror interferometer optics which provide resolution doubling. In a typical machine calibration the plane mirror reflector is attached to the translating element (which in the case of a diamond turning lathe would be the tool bar), and the remote interferometer, which consists of a polarizing beam splitter, two cube corner retroreflectors, and a quarterwave plate, is mounted on a fixed machine member (i.e., the stationary spindle faceplate). The laser fringe counter is zeroed with the optics nearly in contact in order to minimize dead-path errors, which are zero drifts due to uncompensated changes in refractive index along the beam path between the optics.

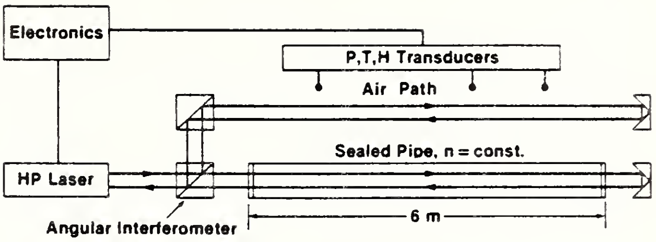

"ΔX" = $2.4 \times 10^{8}\ \Delta n(P,T,H)$ microinches

Fig. 2. Schematic diagram of the optical geometry used to test compensation of the interferometer system for changes in the refractive index of air.

The machine then begins a sequence of programmed moves to a randomly selected set of points along the measurement axis. At each point the machine controller sends an in-position signal to the desk-top computer which integrates the metrology system. The computer communicates with the system components via a standard parallel interface bus (IEEE-488). First, the frequency counter is sampled yielding the beat frequency between the two lasers and subsequently the metrology laser vacuum wavelength. Then the environmental parameters are determined by scanning the thermistor array and the pressure and humidity transducers. The conversions of the sensor signals to the appropriate variables (P, T, or H) are performed by the system software using stored calibration data. The computer uses these to compute the refractive index from Eqs. (4)–(6) and proceeds to sample the laser fringe counter. The actual fringe count contains a random component due to air turbulence in the beam path; this effect is reduced by averaging a large number (100–200) of laser readings taken in rapid succession.

The measured values of vacuum wavelength and n_{air} are then used to correct the metrology laser display. To perform this correction it is necessary to know the wavelength used by the display electronics in the fringe count to displacement conversion, which consists of an assumed vacuum wavelength contained in an onboard ROM, divided by an internal value for n_{air}. The latter parameter may be programmed into the display via the interface bus (we choose $n = 1$) while the former may be obtained from the laser manufacturer.

XI. Test of Environmental Compensation

To test the real-time correction capability of the interferometer system, we employ the arrangement shown schematically in Fig. 2. The optical geometry is basically a modified Michelson interferometer in which a second reflection renders the measurement and reference beams parallel. This is accomplished using the angular interferometer and reflector supplied with the metrology laser system. The two beam paths in Fig. 2 are 240 inches (6 m) in length. The lower beam, which we refer to as the reference beam, passes through a plastic pipe whose ends are sealed by plane glass windows. Since the air within the pipe has constant density and moisture content, the refractive index along the reference path is also constant. The upper beam propagates through the open air of the laboratory, so that changes in the environmental parameters will cause corresponding changes in the apparent length (optical path) of this arm of the interferometer. If, for example, atmospheric pressure should increase at constant temperature, the resultant increase in air density would cause the laser wavelength to decrease along the measurement path, making this path appear to lengthen. The metrology laser system is operated in the displacement mode and measures a fictitious change Δx in the length of the air path, where

$$\begin{aligned}\Delta x &= 2.4 \times 10^8\, \Delta n(P,T,H) \text{ microinches,}\\ \Delta x &= 6 \times 10^6\, \Delta n \text{ micrometers.}\end{aligned} \tag{12}$$

Because of the parallel beam paths, the measurement is insensitive to any actual relative displacement of the optics which might occur due to temperature changes or tidal strains. The absence of angular movements was assured by running the interferometer without the sealed pipe so that the paths were identical. The apparatus is also insensitive to small changes in the laser wavelength since the difference in optical path between the two beams is at most a few parts in 10^4. For this reason it is unnecessary to use the iodine-stabilized laser in compensation testing. A subtle effect is due to thermal expansion of the sealed pipe which lowers the density of the entrapped air and causes a change in optical path of the reference arm. The effect is very small, however, being of the order of one part in 10^8 per kelvin.

The open path is instrumented with an array of thermistors and the pressure and humidity transducers. A test run is started by zeroing the metrology laser, sampling P, T, and H, and computing the initial value of the refractive index. The interferometer is then sampled periodically along with the environmental parameters, and a displacement is computed using Eq. (12). The computed value is then subtracted from the actual reading. If the measured changes in refractive index were exact, the result after subtraction would be zero.

The results of one compensation test experiment are shown in Figs. 3–7. This run lasted approximately two days, during which the data were sampled every 15 minutes. Figures 3–5 display, respectively, the atmospheric pressure, temperature, and relative humidity during the experiment. Laboratory temperature, as shown in Fig. 4, was controlled to better than 0.1 K except for a short interval in the neighborhood of 25 hours after the start. The somewhat erratic behavior at this time was caused by visitors to the laboratory who examined the apparatus and radiantly heated the thermistor array.

Figure 6 shows the interferometer data. The solid line is the apparent change in length of the measurement path. The dashed line, which is nearly coincident with the time axis, is the result after subtraction of the computed apparent displacement using Eq. (12). A comparison of Figs. 3 and 6 shows that such an interferometer system makes an excellent (though expensive) barometer. The nearly 6-mmHg (800-Pa) range of pressure variation during the experiment accounts for nearly all the apparent change in length of the measurement path. Since the length of the path is 240 inches (6 m), an apparent displacement of 240 microinches (6 μm) represents a change in refractive index of 1 ppm. The total range during this run was nearly 2 ppm.

Figure 7 provides a magnified view of the data after correction. We note essentially no remaining systematic behavior, which indicates that the coefficients in Edlén's equation for n_{air} are very well determined. The random fluctuations evident in the corrected data are due to air turbulence along the beam path. The rms random error associated with these fluctuations is ~2.5 microinches or one part in 10^8. This value represents the limit of our ability to correct interferometric data for changes in the refractive index of air. While this demonstrates that our measurements of P, T, and H are precise, we stress that this experiment does not test the absolute accuracy of Edlén's equation, to which an arbitrary constant could be added without affecting our results.

XII. Performance in Field Metrology

The laser interferometer system described above has recently been used to measure the static positioning errors of the LODTM tool bar, as a part of a field validation of the machine's performance by the Machine Tool Metrology Group of NBS.

Tool bar positioning errors were measured over a total range of travel of 19.5 in. (0.5 m) in Z and 40 in. (1 m) in X. In each case, the moving reflector was attached to a fixture bolted to the tool bar, while the reference reflector and associated optics were fixtured to the (nonrotating) spindle rotor. The errors were measured at 0.5-in. (13-mm) intervals over the full range of travel, with each point being sampled twice (once in each direction of tool bar motion).

The results of these measurements are shown in Figs. 8 and 9 for the X and Z axes, respectively. At each point, the displacement error is the difference between the displacement measured by the laser interferometer system and the commanded machine position. The solid lines indicate data taken in the forward direction and the dashed lines correspond to data taken in the reverse direction. Each point represents the average of 100 samples of the interferometer system. The lack of exact bidirectional repeatability is due primarily to air turbulence in the laser beam bath. This effect could be reduced by increasing the number of samples.

As Figs. 8 and 9 indicate, the motion control system of the LODTM linear axes is exceptionally accurate. We stress that in each case the measured machine errors are well within the approximately one part in 10^7 absolute accuracy of the NBS interferometer system. It is interesting that both error plots may be imagined to have slight positive slopes of $\sim 3 \times 10^{-8}$. If the positioning errors of the LODTM were really zero, this observation would imply that the refractive index of air,

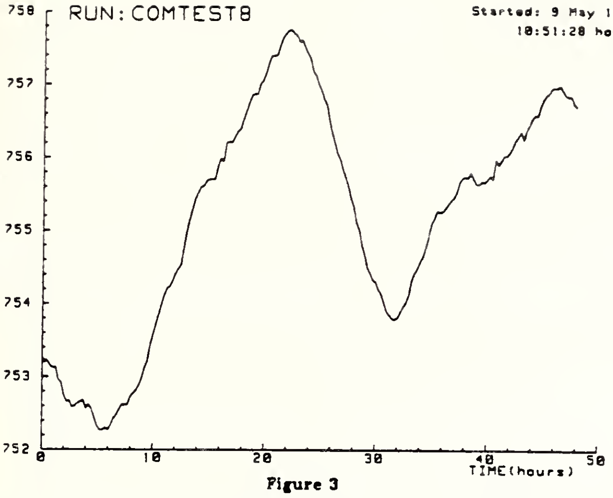

Figure 3

Fig. 3. Variation of atmospheric pressure during test of refractive-index compensation.

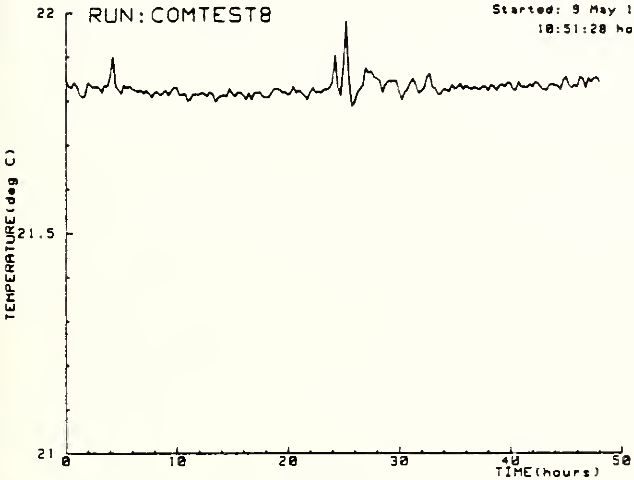

Figure 4

Fig. 4. Variation of air temperature during test of refractive-index compensation.

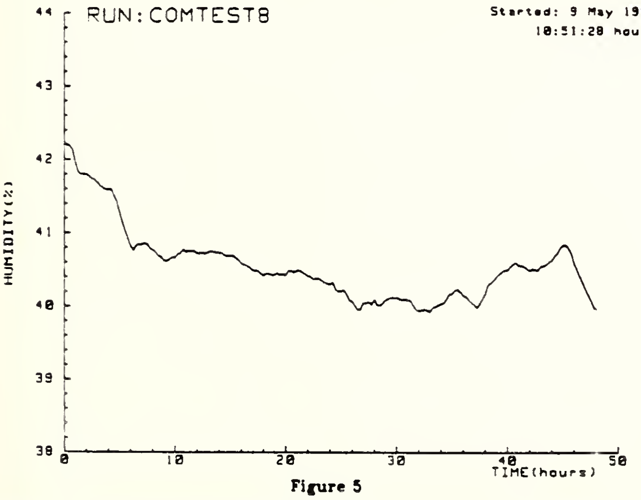

Figure 5

Fig. 5. Variation of relative humidity during test of refractive-index compensation.

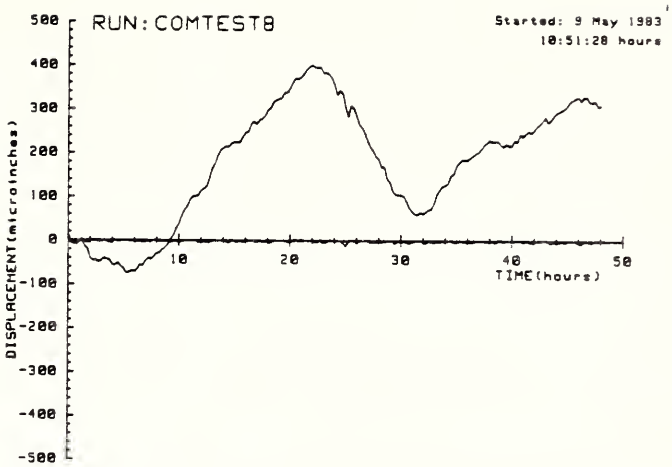

Fig. 6. Displacement measured by the interferometer system during test of refractive-index compensation. The solid curve is the fictitious displacement measured along the open air path caused by changes in the refractive index of the ambient air. The dashed curve, which is nearly coincident with the time axis, is the result after subtraction of the displacement computed using Eq. (12) in the text.

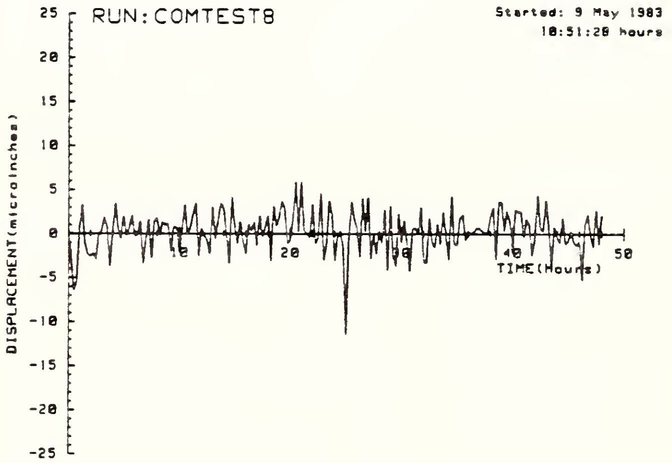

Fig. 7. Magnified view of the data after correction from the test of refractive-index compensation. The random behavior is due to air turbulence along the measurement path. The rms value of this random error is ~2.5 microinches or one part of 10^8.

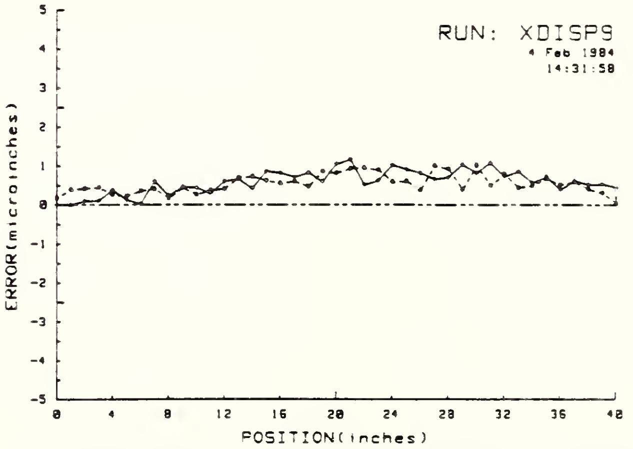

Fig. 8. Linear displacement error of the LODTM X axis. The data are completely within the approximately one part in 10^7 calculated error of the NBS interferometer system.

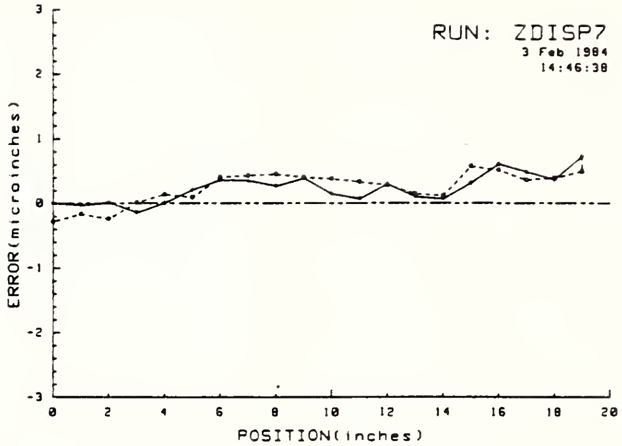

Fig. 9. Linear displacement error of the LODTM Z axis. As with the X axis, the data are within the calculated error of the NBS interferometer system.

as computed by Edlén's formula, is too small by the same factor. This error is within Edlén's estimate of a $\pm 5 \times 10^{-8}$ uncertainty in n_{air}.

While we do not claim to have improved on Edlén's formulation, we feel strongly that our field measurement experience has highlighted a demonstrable need in precision length metrology for improved measurements of the absolute refractive index of air.

References

1. N. J. Brown, R. R. Donaldson, and D. C. Thompson, "Fabrication of Machined Optics for Precision Applications," Proc. Soc. Photo-Opt. Instrum. Eng. **381**, 48 (1983).
2. R. R. Donaldson, "Technology of Machine Tools," Vol. 5, UCRL-53960-5 (1980), Sec. 9.14.
3. The identification of commercial instruments is given only for the sake of clarity. In no instance does such identification imply recommendation or endorsement by the National Bureau of Standards, nor does it imply that the particular equipment described is necessarily the best available for the described purpose.
4. Hewlett-Packard model 5528A laser measurement system; see Hewlett-Packard J. **34**, No. 4 (Apr. 1983).
5. R. J. Hocken and H. P. Layer, "Lasers For Dimensional Measurement," Ann. CIRP **28/1**, 303 (1979).
6. J. M. Chartier, J. Helmcke, and A. J. Wallard, "International Intercomparison of the Wavelength of Iodine-Stabilized Lasers," IEEE Trans. Instrum. Meas. **IM-25**, 450 (1976).
7. D. A. Jennings *et al.*, "Direct Frequency Measurement of the I_2-Stabilized He–Ne 473-THz (633-nm) Laser," Opt. Lett. **8**, 136 (1983).
8. H. P. Layer, "A Portable Iodine Stabilized Helium-Neon Laser," IEEE Trans. Instrum. Meas. **IM-29**, 358 (1980).
9. B. Edlen, "The Refractive Index of Air," Metrologia **2**, 71 (1966).
10. F. Jones, "The Refractivity of Air," J. Res. Natl. Bur. Stand. **86**, 27 (1981).
11. S. W. Wood, B. W. Mangum, J. J. Filliben, and S. D. Tillet, "An Investigation of the Stability of Thermistors," J. Res. Natl. Bur. Stand. **83**, 247 (1978).
12. T. J. Edwards, "Observations on the Stability of Thermistors," Rev. Sci. Instrum. **54**, 613 (1983).
13. R. Revelle, "Carbon Dioxide and World Climate," Sci. Am. **247**, No. 2, 35 (Aug. 1982).

The author would like to thank Robert J. Hocken and Thomas Charlton of the National Bureau of Standards, Center for Manufacturing Engineering, for valuable discussions. Howard Layer, of the NBS Length and Mass Measurements and Standards Division, provided essential information on iodine-stabilized lasers and constructed the laser heterodyne circuitry. Fieldwork at the LODTM was performed with the able assistance of Ralph Veale and Bruce Borchardt of the NBS Machine Tool Metrology Group and was graciously supported in all aspects by the LODTM technical staff.

This work was supported by the Defense Advanced Research Projects Agency under ARPA order 4404.

APPENDIX C

This appendix is a pre-print of a paper which describes in detail the calibration procedure for the optical straightedge used for straightness measurements on LODTM, as well as the algorithm used to correct for gravitational distortion. Equation and figure numbers refer only to the appendix itself, not to the main body of this report.

Calibration and use of optical straightedges in the metrology of precision machines

W. Tyler Estler
National Bureau of Standards
Center for Manufacturing Engineering
Automated Production Technology Division
A107 Metrology
Gaithersburg, Maryland 20899

Abstract. We describe techniques used to measure straightness errors of precision machines. These measurements employ a dimensionally stable mechanical reference surface that is sampled with a laser interferometer—hence the term optical straightedge. The figure error of the reference surface and the straightness error motion of a coordinate measuring machine carriage in a horizontal plane are each measured with an estimated accuracy of 0.5 μin. (13 nm) over 40 in. (1 m) of travel. When measuring straightness error in a vertical plane, the results are complicated by deformation of the reference surface by gravitational forces. We use a computational algorithm, based upon simple beam theory, to correct straightness data for this distortion. While inadequate for accuracies better than about 2 μin. (50 nm), we believe that the algorithm, which may be tested using an uncalibrated straightedge, may be improved using finite-element calculations of gravitational sag.

Subject terms: surface metrology; coordinate measuring machines; diamond turning; machine tools; precision engineering; straightness.

Optical Engineering 24(3), 372-379 (May/June 1985).

CONTENTS

1. Introduction
2. Straightness error motions
3. Straightedge calibration and horizontal straightness
4. Vertical straightness and gravitational sag
5. Acknowledgments
6. References

1. INTRODUCTION

The Machine Tool Metrology Group of the National Bureau of Standards (NBS) is engaged in the characterization and measurement of the positioning errors of machine tools and coordinate measuring machines. Most recently we have been concerned with the extension of traditional measurement techniques, and the development of new ones, in order to permit the field validation of ultraprecise machines designed for the fabrication of reflective metal optics. These machines, such as the large optics diamond turning machine (LODTM) at Lawrence Livermore National Laboratory (LLNL), are capable of the direct machining of aspheric optical elements with figure accuracies approaching 1 μin. (25 nm) rms over surfaces greater than 60 in. (1.5 m) in diameter.[1,2]

In this paper we describe the techniques used to measure a class of kinematic positioning errors known as straightness errors. These measurements employ optical gauging of precision mechanical straightedges and are limited in their accuracies by one's knowledge of the deviations from ideal straightness of such artifacts. In the following sections we describe (a) the use of an optical straightedge in machine straightness metrology, (b) the calibration technique used to measure straightedge figure error, and (c) our approach to the problem of gravitational distortion of a straightedge when used to measure vertical straightness errors. The techniques are illustrated by the results of two particular straightness measurements on an NBS 5-axis computer-controlled coordinate measuring machine.

2. STRAIGHTNESS ERROR MOTIONS

We consider a machine tool or coordinate measuring machine carriage designed to transport a workpiece, tool, or probe along a linear axis. For definiteness, we assume that the direction of motion is along the machine x-axis. It is customary to assume that such a carriage moves as a rigid body with five of its six degrees of freedom constrained so as to move in pure translation along the desired direction by precisely the desired amount. In a real machine none of these assumptions is strictly valid, and the degree to which it departs from them comprises a large part of the discipline of machine tool metrology. By careful design employing kinematic constraints, it is

---

Invited Paper ME-101 received Aug. 10, 1984; revised manuscript received Dec. 5, 1984; accepted for publication Dec. 8, 1984; received by Managing Editor Feb. 1, 1985.

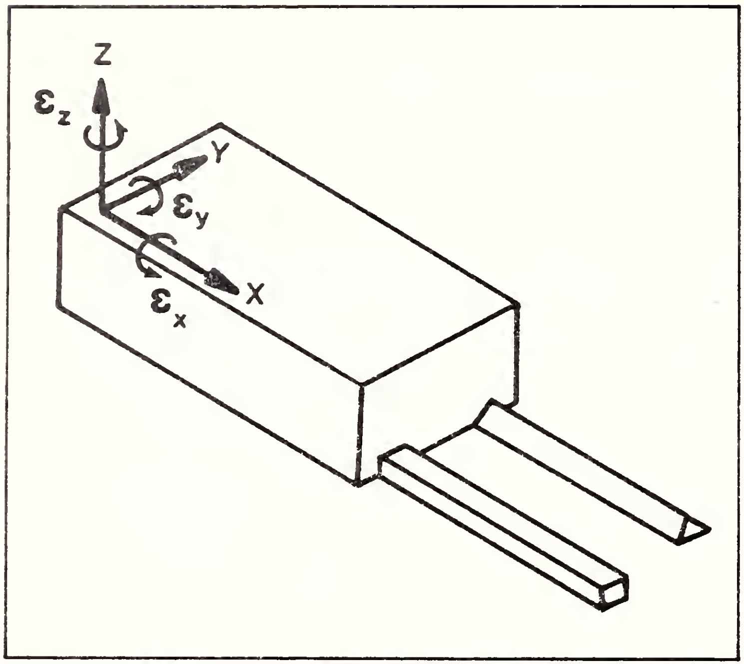

Fig. 1. A typical machine carriage designed for linear motion along the x-axis. There are error motions associated with each of the six degrees of freedom.

possible to minimize carriage distortion so that positioning errors between tool and workpiece are determined primarily by the machine's rigid body geometry.

Figure 1 shows schematically such a machine carriage. For such a rigid body there are six error terms, one for each degree of freedom. Three of these are rotation errors about the machine's Cartesian axes. These are denoted as $\epsilon_x(x)$, $\epsilon_y(x)$, and $\epsilon_z(x)$, where the rotation axis is indicated by the subscript and the dependence upon carriage position is displayed explicitly. On a real linear carriage these rotations are very small and are commonly referred to as roll, pitch, and yaw, respectively. The three remaining terms correspond to displacement errors. The difference between the actual position of the carriage in the direction of motion and the commanded position, denoted $\delta_x(x)$, is commonly known as "positioning error" or "scale error." Motions of the carriage in the y and z directions are called straightness errors. We refer to the quantities $\delta_y(x)$ and $\delta_z(x)$ as the "y-straightness of the x-axis," and the "z-straightness of the x-axis," respectively. In the case where the x and y axes define a horizontal plane, it is common for $\delta_y(x)$ to be called "horizontal straightness" and for $\delta_z(x)$ to be called "vertical straightness."

A more precise definition of straightness error is due to Bryan[3]: "slide straightness error is the non-linear movement that an indicator sees when it is either stationary and reading against a perfect straightedge supported on a moving slide or moved by the slide along a perfect straightedge which is stationary." As Bryan explains, the term "non-linear" refers to the fact that it is not necessary to align the reference straightedge so that it is perfectly parallel to the axis of motion. Straightness errors are the residuals obtained after subtraction of the best-fit straight line from measurement data.

While it is not obvious, the distinction between moving the indicator or the straightedge is a very important one because of the presence of angular motion. The choice of which method to use is dictated by the function of the machine carriage. A more complete description of this distinction, and of machine tool errors in general, may be found in Ref. 4.

Several techniques have been developed for the measurement of straightness errors,[4] including gauging against a taut wire, laser "straightness" interferometers, alignment telescopes, fluid reference surfaces, and, of course, mechanical straightedges. Most of these techniques become difficult and then impossible as the desired accuracy approaches a few microinches. It is our opinion that the highest accuracy can be obtained with a dimensionally stable, carefully calibrated optical straightedge. As will be shown, with good machine repeatability and thermal control, horizontal straightness error measurement and straightedge calibration can be achieved nearly simultaneously with an accuracy of better than 1 μin. (25 nm). In measuring vertical straightness a complication arises: deformation of the straightedge under its own weight. We have developed a computational technique to deal with this phenomenon, which, while inadequate for measurements of better than a few microinches, may be improvable by more refined computation.

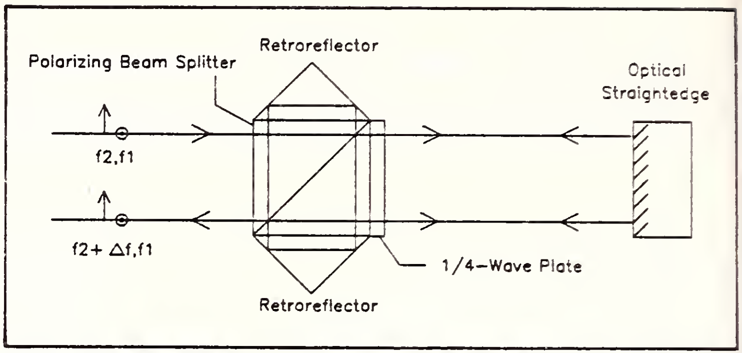

Fig. 2. Optical geometry used to sample the straightedge. Two orthogonal linearly polarized beams, with frequencies f_1 and f_2, are incident from the left. Component f_1 circulates within the beam splitter/retroreflector structure and returns to a detector. Component f_2 travels twice to the gauging surface and also returns to the detector. Motions of the gauging surface toward or away from the beam splitter cause frequency shifts Δf in the beat frequency at the detector. Displacements are measured by comparing the counts from this detector with counts from a reference detector that measures $f_1 - f_2$. In our measurements the straightedge is transported past the interferometer in a direction normal to the plane of the figure.

3. STRAIGHTEDGE CALIBRATION AND HORIZONTAL STRAIGHTNESS

The optical straightedge used in this work is one of the spare optical reference artifacts procured during construction of LODTM. Two similar straightedges are installed on LODTM and serve as horizontal reference planes for the detection and software correction of vertical straightness errors. The straightedge was kindly provided on loan to NBS by LLNL and the staff of LODTM. It is made of Zerodur (registered trademark of Schott Glaswerke, Mainz, Federal Republic of Germany),* a glass-ceramic material of low thermal expansion coefficient and excellent dimensional stability.[5] It is rectangular in cross section, with dimensions 2 in. (50 mm)×6 in. (150 mm), and is approximately 45.5 in. (1.16 m) long. One of the two-inch faces is precision-lapped and coated with a reflective layer of aluminum. The term "optical straightedge" refers to this gauging surface, which is sampled using a commercial laser interferometer system together with air refractive index correction instrumentation developed at NBS.[6] The basic optical geometry, shown in Fig. 2, is identical with that employed for position control of precision x-y stages used in microlithography. Interferometer resolution is 0.4 μin. (10 nm); in practice we average over many samples in order to achieve an effective resolution of about 0.1 μin. (2.5 nm).

All measurements described here were performed on the NBS Moore No. 5 coordinate measuring machine (CMM) (Moore Special Tool Co., Inc., Bridgeport, CT).† This is a fixed-bridge machine whose geometry is shown schematically in Fig. 3. The ranges of motion of the x, y, and z axes are 48 in. (1.22 m), 24 in. (0.61 m), and 10 in. (0.25 m), respectively. All machine slides consist of precision roller bearings in double-vee guideways, lead screw drives, and retrofitted laser interferometric length scales. Only the x-axis was

---

*The identification of commercial materials and instruments is given only for the sake of clarity. In no instance does such identification imply endorsement by the NBS, nor does it imply that the particular material or equipment described is necessarily the best available for the described purpose.

†Please see previous disclaimer footnote.

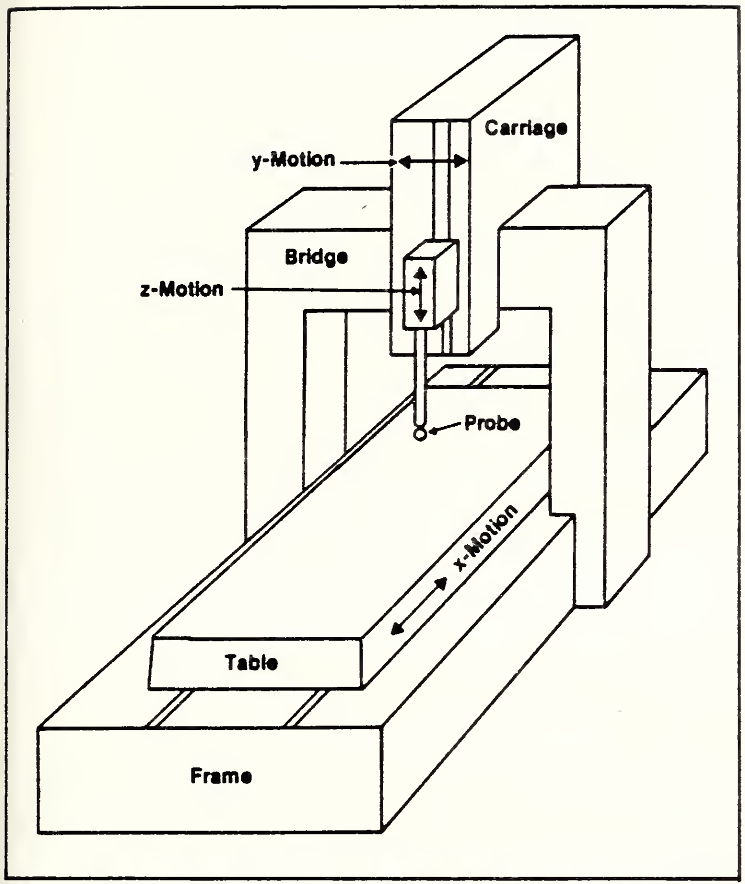

Fig. 3. Schematic diagram showing the geometry of the Moore 5Z coordinate measuring machine.

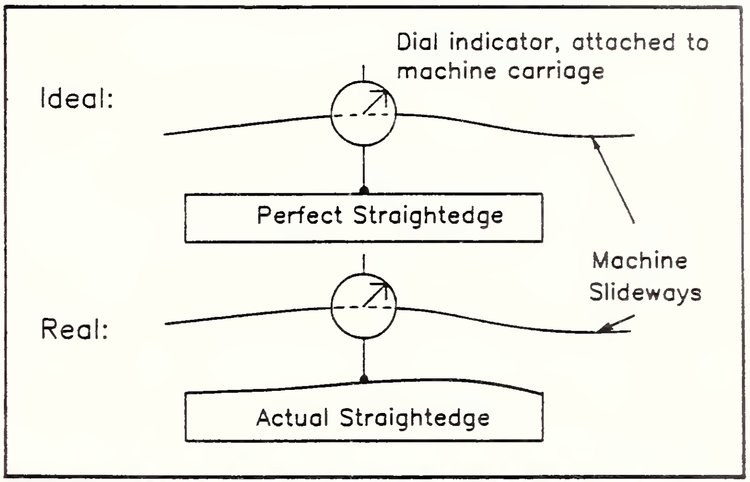

Fig. 4. The basic conceptual problem in straightness measurements using a mechanical artifact. No real straightedge is really straight.

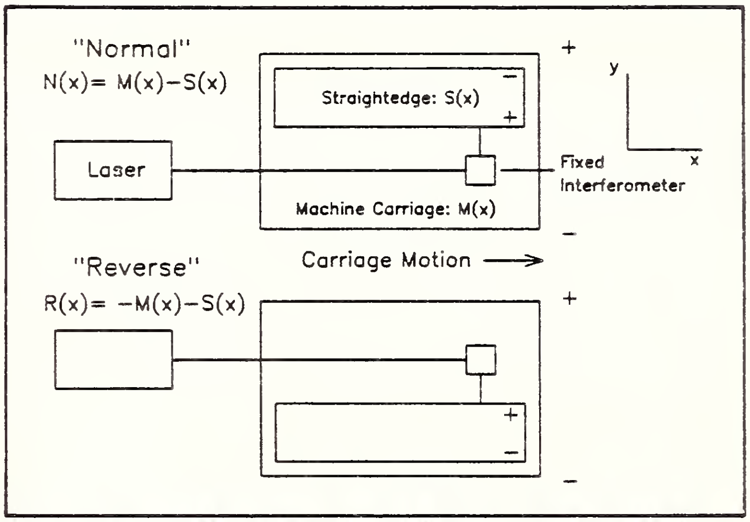

Fig. 5. The principle of straightedge reversal. Two measurements with different straightedge orientations are sufficient to remove the artifact figure error and to determine its shape S(x).

employed; the optical straightedge was mounted on the worktable and transported past the fixed interferometer, which was attached to the machine quill.

The basic conceptual problem associated with straightness measurement using a mechanical artifact is illustrated in Fig. 4. No real straightedge is perfectly straight, so that errors in the shape of the reference artifact become mixed with the machine errors that one is trying to measure. Fortunately, this problem is readily solved by a technique known as straightedge reversal, which is both simple and elegant. The principle is illustrated in Fig. 5. In this figure the dial indicator is replaced by a laser interferometer, so as to depict more accurately the setup actually used for the measurements. For notational simplicity, the horizontal straightness error $\delta_y(x)$ to be measured is replaced by the function M(x) (for machine), and we denote the shape of the optical gauging surface by S(x). It is necessary to adopt a sign convention for these functions; we choose the following:

$$M(x) = \begin{cases} +, \text{ for motion of the machine carriage in the } +y \text{ direction} \\ -, \text{ otherwise} \end{cases} \tag{1}$$

$$S(x) = \begin{cases} +, \text{ for displacements } \textit{out} \text{ of the gauging surface} \\ -, \text{ otherwise .} \end{cases} \tag{2}$$

Straightedge reversal consists of two measurement setups. The straightedge is first supported on its side with the gauging surface in a vertical plane, in what is arbitrarily called the "normal" orientation, and a data run is taken with the interferometer (see top illustration of Fig. 5). The system polarity is such that positive displacements correspond to increasing distance between the interferometer optics and the straightedge gauging surface. The result of this measurement is a set of displacements N(x) evaluated at a chosen number of nominal carriage positions. With the sign conventions of Eqs. (1) and (2), we have

$$N(x) = M(x) - S(x) \ . \tag{3}$$

In the second step, the straightedge is rotated 180° about its long axis, and the interferometer optics is arranged so as to sample the reoriented gauging surface. This is called the "reverse" orientation, shown in the bottom illustration of Fig. 5. With this setup we obtain a new set of displacements R(x), which differs from N(x) since the effect of the reversal is to change the sign of the machine straightness contribution. Thus,

$$R(x) = -[M(x) + S(x)] \ . \tag{4}$$

The results of these measurements are sufficient to determine both the machine horizontal straightness and the artifact calibration, since from Eqs. (3) and (4) we have

$$M(x) = \frac{N(x) - R(x)}{2} \tag{5}$$

and

$$S(x) = -\frac{[N(x) + R(x)]}{2} \ . \tag{6}$$

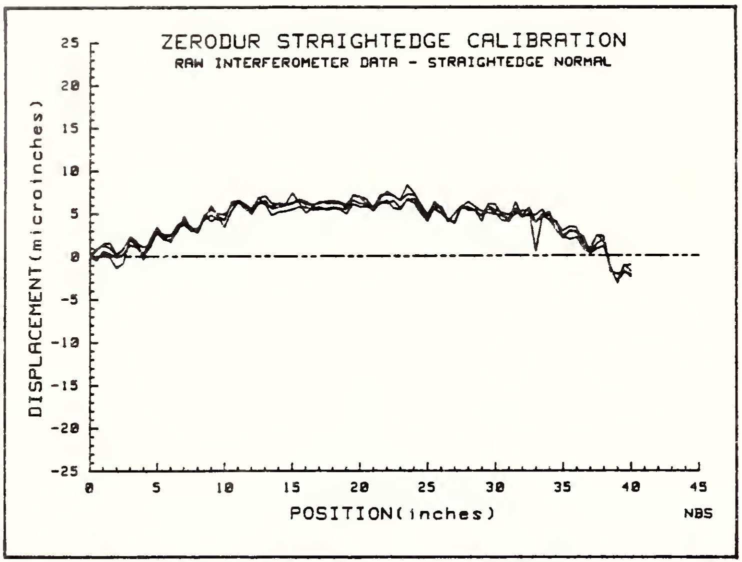

Fig. 6. The results of four passes with the straightedge in the "normal" orientation. The cause of the low-lying point near 33 in. in one of the runs is not known.

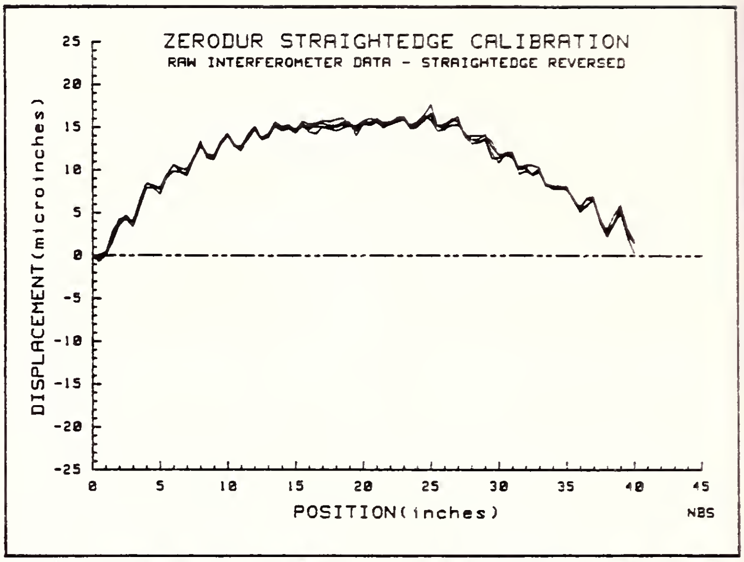

Fig. 7. The results of four passes with the straightedge in the "reverse" orientation. The repeatable nature of the machine's error motions is remarkable.

This procedure was used to measure the horizontal straightness error of the Moore 5Z CMM over 40 in. (1 m) of x-axis travel and to determine the figure error of the optical straightedge. The straightedge was mounted upon two symmetrically placed "line" supports consisting of 1/16 in. (1.6 mm) diameter hardened steel dowel pins. These pins were located near the so-called "Airy points" in order to minimize gravitational distortion of the straightedge. We assume that any bending of the straightedge causes negligible distortion of the gauging surface when measuring horizontal straightness.

It is necessary to use reasonable care in the setups for these measurements in order to assure that the two sampling laser beams track the same portions of the straightedge in each configuration. This requires that (a) the gravitational sag and (b) the difference in height between the ends of the straightedge in both orientations each be small compared to the diameters of the sampling beams, which are approximately 0.25 in. (6.6 mm). The choice of support locations reduced the sag to a maximum value of about 24 μin. (0.6 μm), so that condition (a) was easily satisfied. The height difference (b) was determined by the support fixtures and in each case was less than 0.005 in. (0.13 mm), so that condition (b) was also satisfied.

The raw data, minus linear terms due to misalignment, are shown in Figs. 6 and 7 for the "normal" and "reverse" orientations, respectively. Each run consists of four passes, with the displacement sampled at 0.5 in. (13 mm) intervals. Measured displacements represent the average of 200 interferometer samples at each location. As the data indicate, the error motions of the Moore machine are very systematic, repeating themselves to within 0.5 μin. (13 nm) or less on the average. Figure 8 displays the average of the four passes in the "normal" (solid line) and "reverse" (dashed line) orientations.

Figure 9 shows the horizontal straightness of the Moore machine x-axis, computed from the data using Eq. (5). The peak-to-valley departure from ideal straightness is approximately 6 μin. (150 nm), which is exceptionally good for a machine with no active compensation for straightness error. The pronounced periodic behavior that is evident in the figure is probably due to lead screw periodic error. We believe that the relatively smooth area between 15 and 20 inches represents an area of the screw that has been lapped by its own nut to be relatively free of periodic error. It is this position of the machine table that is exercised most frequently in normal use in metrology at NBS.

The shape of the optical straightedge, computed using Eq. (6), is displayed in Fig. 10. This artifact is seen to have a very systematic shallow depression of about 12 μin. (300 nm) amplitude, which presumably resulted from the lapping process during manufacture. We believe that the small "ripples" of 0.5 μin. (13 nm) or less in amplitude are residuals from the nonrepeatability noise in the raw

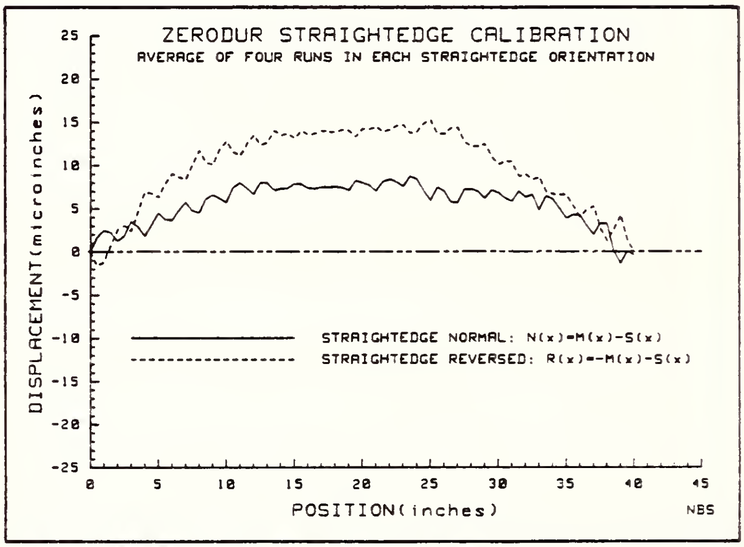

Fig. 8. Averaged horizontal straightness data from which machine straightness M(x) and straightedge figure error S(x) are computed.

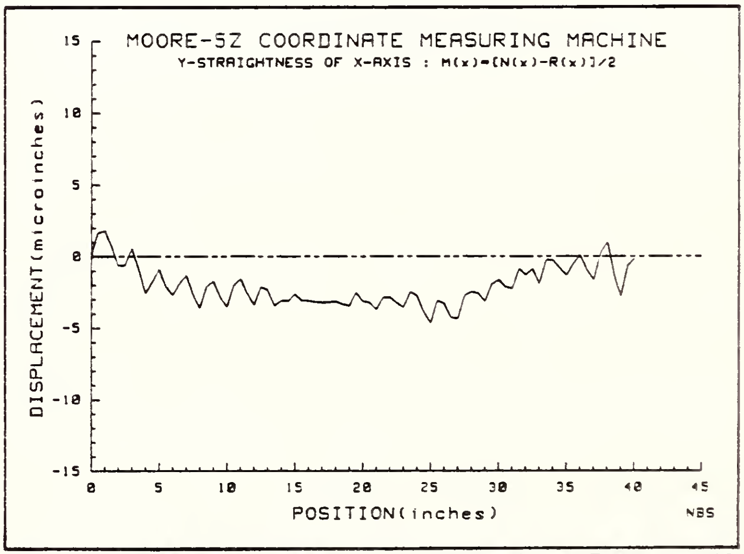

Fig. 9. Horizontal straightness error motion of the Moore 5Z table over 40 in. of x-axis travel. The maximum peak-to-valley error is about 6 μin. The periodic behavior is probably due to lead screw error.

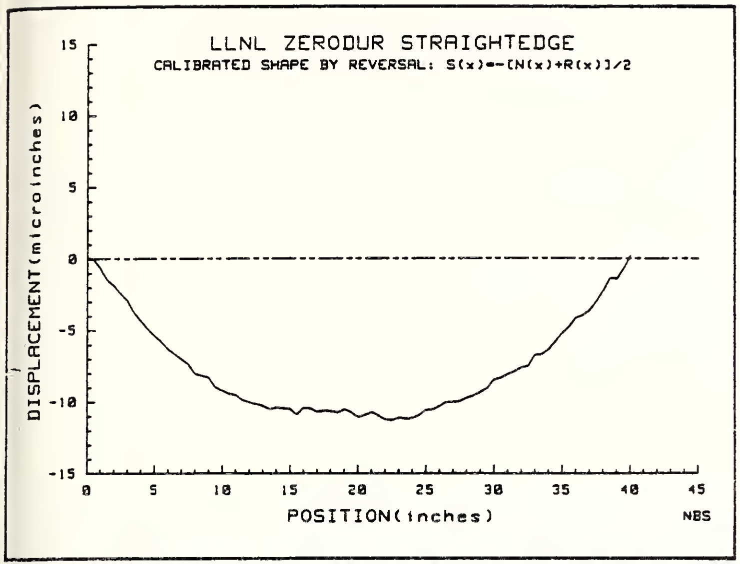

Fig. 10. The figure error S(x) of a 40 in. section of the Zerodur optical straightedge. The surface has a very systematic depression of about 12 μin. or one-half a wavelength of light from a He-Ne laser. We believe that the localized fine structure is due to noise in the measurement data and is not a property of the straightedge.

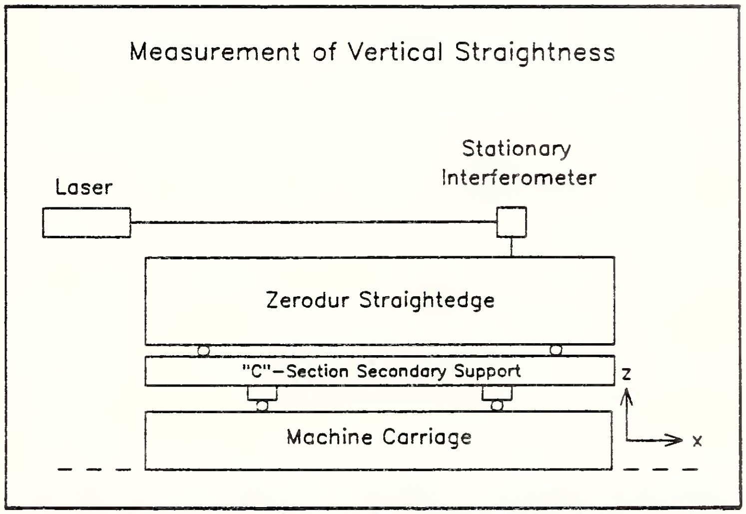

Fig. 11. The straightedge support geometry used for vertical straightness measurements. The C-section subsupport assures that the machine carriage is always loaded in the same way as the straightedge support points are shifted.

data and are not localized fine structure on the straightedge itself.

We estimate the absolute accuracy of these measurements to be approximately 0.5 μin. (13 nm), based upon the repeatability of the Moore machine, its measurement history, and the frequency calibration and refractive index compensation of the laser interferometer system.

4. VERTICAL STRAIGHTNESS AND GRAVITATIONAL SAG

We now turn to the problem of measuring the z-straightness $\delta_z(x)$, or vertical straightness, of the Moore CMM x-axis carriage. When mounted on parallel line supports with the gauging surface horizontal, the optical straightedge will be deformed by gravity due to its own weight. Depending upon the location of the supports, this gravitational sag can dominate and mask nearly completely the vertical straightness errors of a precision machine such as the Moore 5Z. (Of course, the same type of deformation occurs when measuring horizontal straightness, but, as mentioned in the previous section, we believe that this has a negligible effect on the shape of the vertical gauging surface.) Furthermore, the effect of gravitational sag cannot be eliminated by the reversal technique: if the straightedge is inverted, both the machine straightness and the gravitational terms in the interferometer data change signs. The fact that the straightedge is not really straight to begin with only serves to further complicate the situation.

In our search for a solution to this problem we have explored several alternatives to simple symmetrically located line supports. One might consider eliminating the optical straightedge altogether and replacing it with a large plane reflecting surface of fluid. A simple calculation is sufficient to show that such a surface will depart from ideal flatness by about 0.1 μin./in. (100 nm/m) due to the earth's curvature. A fluid surface large enough to replace the optical straightedge would thus deviate from straightness by more than 3 μin. (75 nm). This offers no real improvement for vertical straightness measurements since gravitational sag can be reduced to a value only slightly larger by an optimal choice of support locations.

While it is true that the shape of such a fluid reference surface is quite simple to calculate, we feel that instabilities in the fluid induced by accelerations of the moving machine elements as well as tilting of the machine structure with shifting loads would make such a measurement very difficult and time-consuming.

An interesting idea (which does not work) is to immerse the straightedge in a dense fluid so as to remove most of its weight from the line supports. While mercury is an obvious choice, safety considerations led us to consider acetylene tetrabromide ($C_2H_2Br_4$), which is dense enough to float optical glasses. The problem with this idea stems from the hydrostatic forces exerted by the fluid on the ends of the straightedge, which create a bending moment. Calculation shows that the effect of these forces would be to bow the straightedge by approximately 6 μin. (150 nm), which is comparable to the gravitational distortion the technique was envisaged to eliminate. This method is also subject to the fluid instabilities described above. (Note: we do not recommend the use of organic halides as buoyant fluids; while probably safer than mercury, such fluids are reactive with some common metals, such as aluminum, and are toxic inhalation hazards.)

Gravitational distortion can be reduced by use of multiple line supports. Some care must be exercised in the design of such a system to ensure that each support is equally loaded. R. Donaldson of LLNL has designed a device with eight equally spaced kinematic supports,* which a finite-element calculation indicates reduces surface sag to less than 0.1 μin. (2.5 nm). A prototype has been constructed at LLNL but has not yet been employed for straightness measurements.

With this background, we decided in the interests of time and expense to attempt to calculate the gravitational sag with symmetrically placed line supports, using the analytic results of simple beam theory. This approach has the advantage of easy implementation on a small computer and can be tested for validity by varying the support locations. In applying this scheme to our measurements of vertical straightness, we make the following assumptions:

(a) The optical straightedge is a homogeneous elastic beam of constant rectangular cross section and constant material properties.

(b) The gravitational sag of a perfect straightedge is an analytic function $G(x, \alpha)$, which may be calculated exactly from simple beam theory. Here, $\alpha = L/L_0$, where L = support separation and L_0 = length of the straightedge.

(c) The resultant shape of a real straightedge when supported vertically is $S(x) + G(x, \alpha)$, where S(x) is the "natural" shape of the gauging surface as determined by the reversal technique.

Figure 11 shows the setup used for vertical straightness measurements on the Moore CMM. The straightedge support structure is more elaborate than that used for horizontal measurements, due to the variable loading of the machine worktable as the straightedge line supports are changed to new locations. The optical straightedge and its supporting dowel pins ride on a steel C-section channel that is itself supported on steel parallels and another pair of dowel pins.

---

*R. R. Donaldson, personal communication.

Because of table deformations, the machine straightness depends upon the size and location of applied forces. The C-section substructure keeps them constant, regardless of the location of the straightedge supports.

As in the case of horizontal straightness, it is necessary to adopt a sign convention for the functions involved in the data analysis. We choose

$$\delta_z(x) = \begin{cases} +, \text{ for motion of the machine carriage in the } +z \text{ direction} \\ -, \text{ otherwise} \end{cases} \tag{7}$$

$$G(x,\alpha) = \begin{cases} +, \text{ for displacement upward } (+z) \\ -, \text{ otherwise ,} \end{cases} \tag{8}$$

and we keep the same convention for S(x), Eq. (2), together with the same interferometer polarity. The displacement $d(x,\alpha)$ measured by the laser system is then given by

$$d(x,\alpha) = -\delta_z(x) - G(x,\alpha) - S(x) \ , \tag{9}$$

so that the z-straightness of the x-axis, for known gravitational sag, is

$$\delta_z(x) = -d(x,\alpha) - G(x,\alpha) - S(x) \ . \tag{10}$$

Equation (10) is the central result of this procedure, and it suggests a straightforward way to test the correctness of the computational algorithm. Consider using the arrangement of Fig. 11 to measure vertical straightness with two different support separations L_1 and L_2. Each measurement yields a determination of $\delta_z(x)$ with a different value of $\alpha = L/L_0$, and if $G(x,\alpha)$ is calculated exactly, then these determinations will result in the same function. Using Eq. (10) twice, we thus examine the difference

$$\delta_z(x)\Big|_{\alpha=\alpha_1} - \delta_z(x)\Big|_{\alpha=\alpha_2} = \left[d(x,\alpha_2) - d(x,\alpha_1) + G(x,\alpha_2) - G(x,\alpha_1)\right] \ . \tag{11}$$

This function should vanish for a correct model of $G(x,\alpha)$ within the inherent machine repeatability. It is interesting to note that Eq. (11) is independent of S(x), so that computational algorithms may be tested without prior straightedge calibration.

The deformation of a symmetrically supported straightedge, bending under its own weight, is a well-known problem in the theory of simple beams. We follow the formalism described by Rolt.[7] The geometry is depicted in Fig. 12, which shows one-half of the straightedge. Point B locates one of the supports, at distance L/2 from the center. The distance $y = G(x,\alpha)$, $\alpha = L/L_0$, is the desired deflection and is given by the following formulae.

Between A and B,

$$G(x,\alpha) = \frac{wL_0^4}{384EI}\left[12\left(\frac{1}{2}-\alpha\right)\eta^2 + \eta^4\right] \ . \tag{12}$$

Between B and C,

$$G(x,\alpha) = \frac{wL_0^4}{384EI}\left[4\alpha^3 - 1 + 4\eta(1-3\alpha^2) + (1-\eta)^4\right] \ . \tag{13}$$

In these expressions, $\eta = 2x/L_0$, w = weight/unit length, E = Young's modulus, and I = moment of inertia of a cross section about the median plane $= bh^3/12$, where b and h are the beam width and height, respectively. Inserting the known dimensions of the Zerodur optical straightedge, Eqs. (12) and (13) become

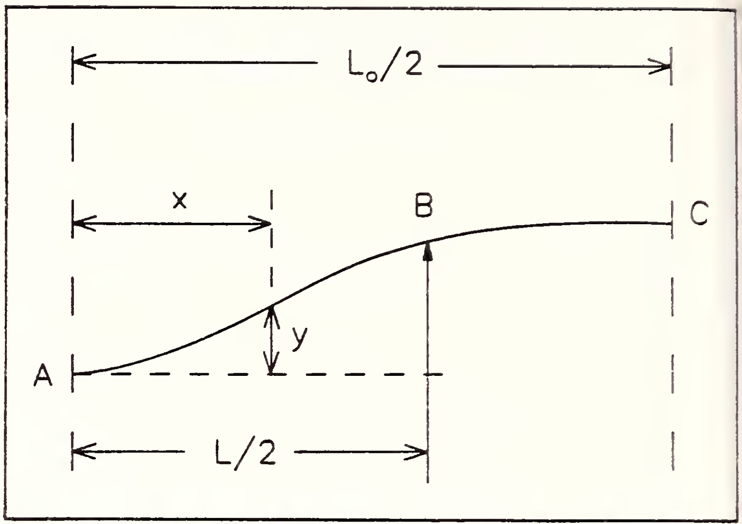

Fig. 12. The geometry employed for the analytical model of straightedge gravitational deformation with symmetrically placed line supports. This diagram depicts one-half of the straightedge with one support at B. (After Rolt, Ref. 7).

$$G(x,\alpha) = 309.27\,\beta\left[12\left(\frac{1}{2}-\alpha\right)\eta^2 + \eta^4\right] \quad \text{between A and B ,} \tag{14}$$

and

$$G(x,\alpha) = 309.27\,\beta\left[4\alpha^3 - 1 + 4\eta(1-3\alpha^2) + (1-\eta)^4\right] \quad \text{between B and C .} \tag{15}$$

The units have been chosen so that Eqs. (14) and (15) give deflections in microinches. The parameter β in these expressions is the ratio of the weight/unit length to Young's modulus. Using accepted values for the density and Young's modulus of Zerodur, $\rho = 0.091 \ \text{lb}\cdot\text{in}^{-3}$ and $E = 13.2\times10^6 \ \text{lb}\cdot\text{in}^{-2}$,[8] we find $\beta = 0.0827 \ \mu\text{in}$. Since in our opinion neither of these quantities is known to better than a few percent for a particular Zerodur artifact, and since computed deflections are directly proportional to β, we chose to allow β to be a free parameter that is optimized to yield the best agreement among the three straightness measurements to be described.

In Fig. 13 we show the gravitational sag of the straightedge as computed using Eqs. (14) and (15) for three symmetric support locations: Case 1, $\alpha_1 = 0.538$; Case 2, $\alpha_2 = 0.720$; and Case 3, $\alpha_3 = 0.938$. The curves have been shifted vertically so that the ends of the straightedge are at z = 0 in each case, and the sign of the displacement has been chosen so as to permit a natural visualization of the distortion. Only the central 45 in. (1.1 m) are shown, corresponding to the region of the gauging surface actually used in the measurements. It is clear from this figure that straightedge sag can cause serious errors in vertical straightness measurements on precision machines, particularly for supports near the ends ($\alpha \simeq 1$). On the other hand, a judicious choice of support locations can reduce these errors to less than 10 μin. Figure 14 shows a magnified view of the sag when $\alpha = 0.538$. In this view it is easy to visualize the supports near x = 11 in. and x = 34 in.; these locations are close to the so-called "Airy points" ($\alpha = 0.577$), where the ends become horizontal; these are the traditional support locations for line standards of length. The peak-to-valley deviation from perfect straightness in Fig. 14 is less than 6 μin. (150 nm).

The interferometer data $d(x,\alpha)$ for the three measurement cases are shown in Fig. 15. A comparison of these data with the curves of Fig. 13 shows clearly how gravitational distortion of the optical straightedge can dominate and conceal the straightness error of a precision machine. In order to extract the vertical straightness $\delta_z(x)$,

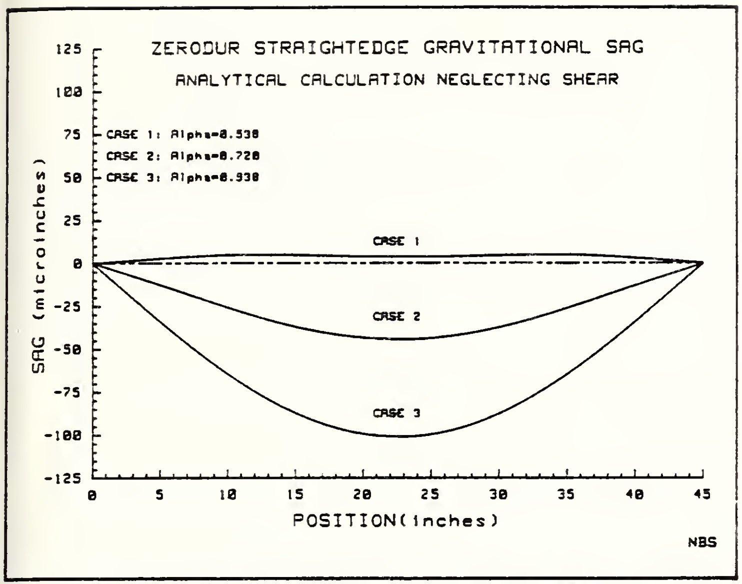

Fig. 13. Computed gravitational sag of the Zerodur straightedge for three positions of the symmetrical supports. The parameter α is the support separation as a fraction of the total length L_0 of the straightedge. Depending upon the location of the supports, the total distortion ranges from about 6 μin. to more than 100 μin.

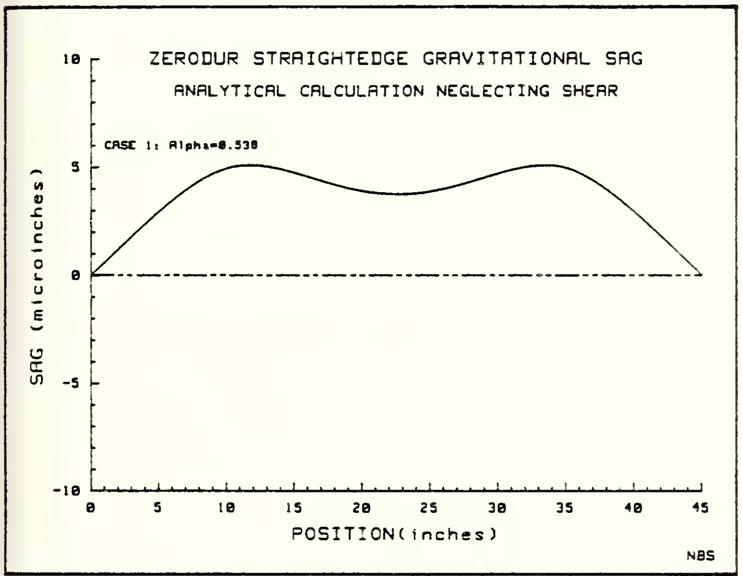

Fig. 14. A magnified view of the gravitational sag computed for Case 1, $\alpha = 0.538$. The two line supports are located near $x = 11$ in. and $x = 34$ in. This is nearly the minimum straightedge distortion that can be achieved with two simple supports.

we use Eq. (10) along with the shape function S(x) determined by the reversal technique. Since the vertical straightness data were taken over 45 in. of x-axis travel while S(x) was measured over only 40 in., we used a seventh-degree polynomial fit of S(x) and analytic continuation to extend the shape function to 45 in. We considered this to be a reasonable procedure, given the highly systematic nature of the 40 in. calibration. The results of these three determinations of $\delta_z(x)$ are shown in Fig. 16. If the analytic calculations of $G(x, \alpha)$ were exact, these should all be identical straightness functions within the machine repeatability, and on the scale of this figure the results look encouraging. The Moore 5Z CMM is seen to have a pronounced "valley" in its x-axis guideways. This may be due to a natural wearing and "erosion" of the guideways during the 15 yr period since its installation at NBS. The peak-to-valley amplitude of this vertical straightness error is about 40 μin. (1 μm), which is much worse than the horizontal straightness error but still quite small for an uncorrected machine of its size.

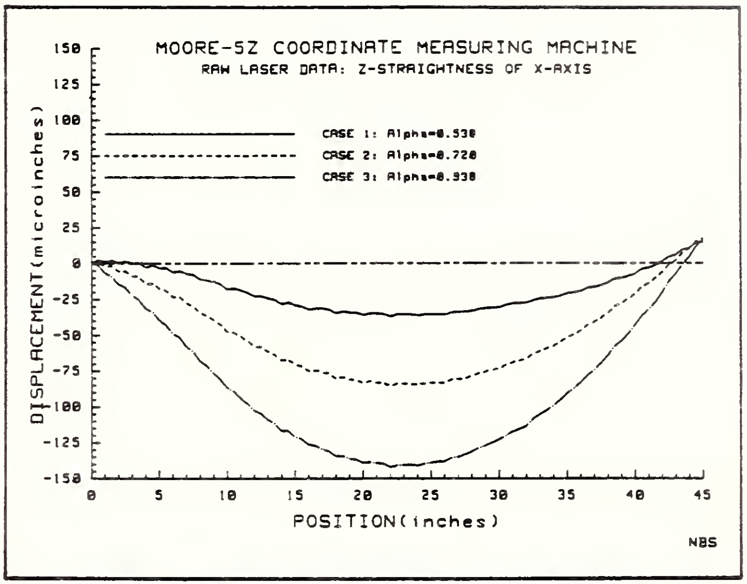

Fig. 15. Laser measurement data obtained with the setup shown in Fig. 11, with three positions of the line supports. Each curve represents the average of six runs, and in each case a least-squares straight line has been subtracted to remove the effect of tilt. A comparison of these data with the calculated gravitational sags shown in Fig. 13 shows how such distortions can mask the straightness errors of a precision machine.

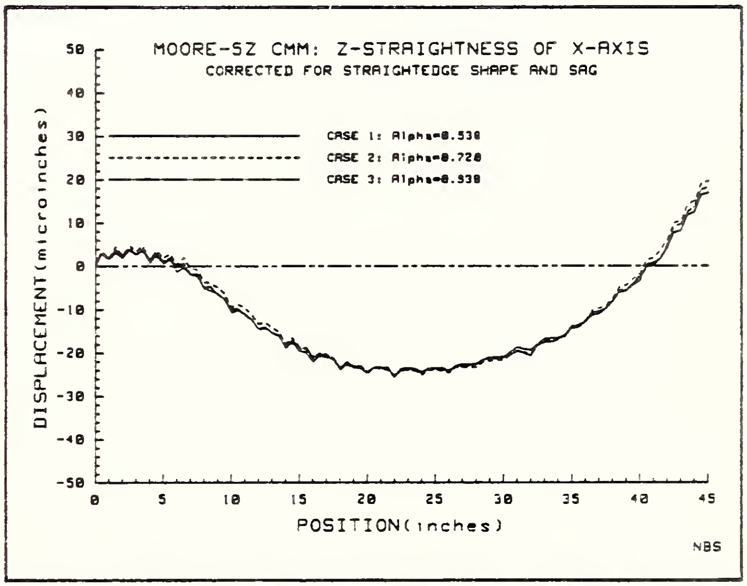

Fig. 16. Three measurements of the vertical straightness of the Moore 5Z x-axis, computed from the laser data of Fig. 15 using simple beam theory and Eq. (10). If our computational algorithm were exact, these three functions would be identical within the random errors of the measurements.

The real test of our analytic calculation is displayed by the differences of computed straightness functions shown in Fig. 17. The value of β that minimized these differences is 0.0841 μin., which differs from the accepted value of 0.0827 μin. by about 1.7%. For any particular pair of cases, the residual error is about 2 μin. (50 nm). On the one hand these results may be viewed as quite successful, since the total sag and shape errors removed by the computation are, in Case 3, greater than 110 μin. (2.8 μm). On the other hand, however, the residual errors are only a factor of two or so smaller than would be obtained by supporting the straightedge at its minimum-deflection points and using no correction at all [still assuming, of course, that the reversal calibration S(x) remains a simple additive function]. We believe that these results represent a fairly realistic limit on what can be achieved using simple beam theory, with its neglect of shear forces. We also feel that submicroinch vertical straightness accuracy could be realized with our technique given a more refined calculation

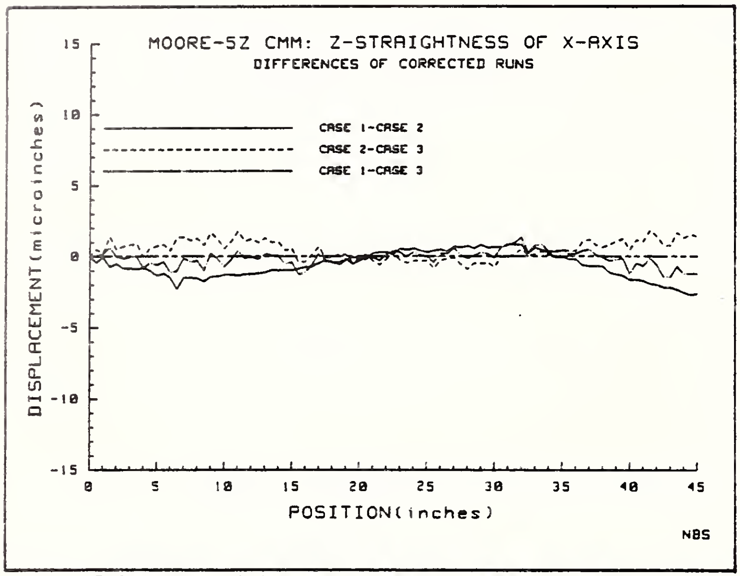

Fig. 17. Differences of the vertical straightness functions of Fig. 16. Only two of these differences are independent. It is clear that our measurement algorithm fails below the level of about 2 μin.

of gravitational distortion. Recently, R. Donaldson and J. Roblee of LLNL have completed several finite-element calculations of beam deflections with our support geometries.† We are presently engaged in a reanalysis of our vertical straightness data using the results of these new calculations.

5. ACKNOWLEDGMENTS

I would like to thank my colleagues Robert Hocken, Thomas Charlton, and Edward Magrab of the NBS Center for Manufacturing Engineering for useful discussions and help with experimental design. Robert R. Donaldson of LLNL provided valuable theoretical and experimental guidance, together with helpful comments on the manuscript. Jeff Roblee, also of LLNL, performed the finite-element calculations.

This work was supported by the Defense Advanced Research Projects Agency under ARPA Order 4404.

6. REFERENCES

1. N. J. Brown, R. R. Donaldson, and D. C. Thompson, in *Symposium on Optical Surface Technology*, H. Walter, ed., Proc. SPIE 381, 48 (1983).
2. R. R. Donaldson, *Technology of Machine Tools*, Vol. 5, Machine Tool Accuracy, Sec. 9.14, UCRL-52960-5 Lawrence Livermore National Laboratory, Livermore, Calif. (1980).
3. J. B. Bryan, Precision Engineering, 1(3) 129 (July 1979).
4. R. J. Hocken, *Technology of Machine Tools*, Vol. 5, Machine Tool Accuracy, Sec. 3, UCRL-52960-5 Lawrence Livermore National Laboratory, Livermore, Calif. (1980).
5. J. W. Berthold, S. F. Jacobs, and M. A. Norton, Metrologia 13, 9 (1977).
6. W. T. Estler, Appl. Opt. (March 1985).
7. F. H. Rolt, *Gauges and Fine Measurements*, Vol. II, p. 340, Macmillan and Co., London (1929).
8. ZERODUR Glass Ceramics. Technical brochure from Schott Optical Glass, Inc., Duryea, PA 18642.

---

†R. R. Donaldson, personal communication.

NBS-114A (REV. 2-80)

U.S. DEPT. OF COMM. **BIBLIOGRAPHIC DATA SHEET** *(See instructions)*	1. PUBLICATION OR REPORT NO.	2. Performing Organ. Report No.	3. Publication Date

4. TITLE AND SUBTITLE

Validation Metrology of the Large Optics Diamond Turning Machine

5. AUTHOR(S)

W. Tyler Estler and Edward B. Magrab

6. PERFORMING ORGANIZATION *(If joint or other than NBS, see instructions)*

NATIONAL BUREAU OF STANDARDS
DEPARTMENT OF COMMERCE
WASHINGTON, D.C. 20234

7. Contract/Grant No.

ARPA ORDER 4404

8. Type of Report & Period Covered

FINAL

9. SPONSORING ORGANIZATION NAME AND COMPLETE ADDRESS *(Street, City, State, ZIP)*

Defense Advanced Research Projects Agency
1400 Wilson Boulevard
Arlington, VA 22209

10. SUPPLEMENTARY NOTES

☐ Document describes a computer program; SF-185, FIPS Software Summary, is attached.

11. ABSTRACT *(A 200-word or less factual summary of most significant information. If document includes a significant bibliography or literature survey, mention it here)*

We present the results of field validation measurements designed to test the positioning accuracy and kinematic performance of the Large Optics Diamond Turning Machine (LODTM), constructed at Lawrence Livermore National Laboratory. Field measurements were performed during January-February and November, 1984, and are sufficient to characterize the capabilities of LODTM when used as a measuring machine. No part cutting tests were done. Measured errors include those due to machine drift, position repeatability, laser length scales, slide straightness, tool bar angular motions, axis geometry, and spindle motion. The static and dynamic performance of the Fast Tool Servo was assessed by bench tests at NBS. We also identify those aspects of machine behavior which are potentially problematic in fabriaction of large optics with figure errors within the design specifications of LODTM.

12. KEY WORDS *(Six to twelve entries; alphabetical order; capitalize only proper names; and separate key words by semicolons)*

diamond turning; machine tools; metrology; optics; precision engineering; servo systems

13. AVAILABILITY

☐ Unlimited
☒ For Official Distribution. Do Not Release to NTIS
☐ Order From Superintendent of Documents, U.S. Government Printing Office, Washington, D.C. 20402.
☐ Order From National Technical Information Service (NTIS), Springfield, VA. 22161

14. NO. OF PRINTED PAGES

15. Price